

# Trapped nonneutral plasmas, liquids, and crystals (the thermal equilibrium states)

Daniel H. E. Dubin and T. M. O'Neil

*Department of Physics, University of California at San Diego, La Jolla, California 92093*

Plasmas consisting exclusively of particles with a single sign of charge (e.g., pure electron plasmas and pure ion plasmas) can be confined by static electric and magnetic fields (in a Penning trap) and also be in a state of global thermal equilibrium. This important property distinguishes these totally unneutralized plasmas from neutral and quasineutral plasmas. This paper reviews the conditions for, and the structure of, the thermal equilibrium states. Both theory and experiment are discussed, but the emphasis is decidedly on theory. It is a huge advantage to be able to use thermal equilibrium statistical mechanics to describe the plasma state. Such a description is easily obtained and complete, including for example the details of the plasma shape and microscopic order. Pure electron and pure ion plasmas are routinely confined for hours and even days, and thermal equilibrium states are observed. These plasmas can be cooled to the cryogenic temperature range, where liquid and crystal-like states are realized. The authors discuss the structure of the correlated states separately for three plasma sizes: large plasmas, in which the free energy is dominated by the bulk plasma; mesoscale plasmas, in which the free energy is strongly influenced by the surface; and Coulomb clusters, in which the number of particles is so small that the canonical ensemble is not a good approximation for the microcanonical ensemble. All three cases have been studied through numerical simulations, analytic theory, and experiment. In addition to describing the structure of the thermal equilibrium states, the authors develop a thermodynamic theory of the trapped plasma system. Thermodynamic inequalities and Maxwell relations provide useful bounds on and general relationships between partial derivatives of the various thermodynamic variables.

[S0034-6861(99)00801-6]

## CONTENTS

I. Introduction	88	B. Numerical experiments on mesoscopic plasmas	115
II. Confinement and Constants of the Motion	90	C. Large plasmas	121
A. Confinement geometry	90	1. The correlation function of the one-component plasma	121
B. Constants of the motion	91	2. Correlation energy	123
C. Confinement theorem	92	3. Free energy, the freezing transition, and correlation pressure	126
D. Constraint on the mean-square radius of the plasma	92	4. Thermodynamic functions for a large trapped plasma	127
III. Mean-field Description of Thermal Equilibrium States	94	5. Effect of correlations on the plasma edge	131
A. Boltzmann distribution	94	D. Analytic models of mesoscopic plasmas	134
B. Experimental observation of thermal-equilibrium states	96	1. Cylindrical shell model	134
1. Electron plasmas	96	2. Planar shell model	137
2. Ion plasmas	97	3. Intershell correlations	139
C. Self-consistent potential, Debye shielding, and imaginary neutralizing charge	98	4. Mesoscopic to large-plasma transition	141
D. Infinitely long column	100	5. Limits of large and small aspect ratio: inhomogeneous Coulomb chains and discs	143
E. Finite-length column	101	E. Coulomb clusters	146
F. Small spheroidal plasmas	102	1. Constant rotation frequency	147
G. Centrifugal separation	106	2. Constant angular momentum	150
H. Generalization of the confinement geometry	107	V. Thermodynamics of Nonneutral Plasmas	152
1. Inhomogeneous but cylindrically symmetric magnetic field	107	A. The $TdS$ equation	153
2. Rotating wall	108	B. Maxwell relations	155
IV. Strong Correlation	111	C. Derivatives at constant $T$ and $\omega$ vs derivatives at constant $E$ and $L$	155
A. Microcanonical and canonical ensembles	111	D. Thermodynamic inequalities	156
1. Mesoscopic plasmas, large plasmas, and Coulomb clusters	112	E. Fluctuations	160
2. Spatial and reduced distribution functions	112	F. Adiabatic processes	161
3. Relation to a one-component plasma	113	G. Thermodynamic approach to transport	162
4. Infinite homogeneous one-component plasma and the coupling parameter $\Gamma$	113	1. Direction of evolution	162
		2. Evolution equations	163
		3. Temperature and frequency stability	164
		VI. Discussion	166
		Acknowledgments	169
		References	169

## I. INTRODUCTION

This paper discusses plasmas with a single sign of charge that are confined in Penning traps. These traps typically have cylindrical symmetry, with radial confinement provided by a uniform axial magnetic field and axial confinement by electrostatic fields. Examples of plasmas that have been confined in recent experiments include pure electron plasmas, positive-ion plasmas of one or more species, positron plasmas, and electron-antiproton plasmas. These plasmas are totally unneutralized, and in that sense they are a subset of the more general class of nonneutral plasmas.

Plasmas with a single sign of charge provide some unique research opportunities that are not available with neutral (or quasineutral) plasmas. In principle these plasmas can be confined forever by static electric and magnetic fields, and in practice very long confinement times (hours and even days) are routinely achieved. They can be confined by such fields and also be in a state of thermal equilibrium. Since recombination cannot occur, they can be cooled to the cryogenic temperature range, where liquid and crystal-like states are predicted and observed.

The thermal equilibrium states are the focus of the paper. At first one might think that the existence of such states is an obvious and trivial property shared by all plasmas, but that is not the case. A neutral (or quasineutral) plasma cannot be confined by static electric and magnetic fields and also be in a state of thermal equilibrium. Consequently, a confined neutral plasma cannot be in a state of minimum free energy; there is always free energy to drive instabilities, and these instabilities have plagued the confinement of neutral plasmas. In contrast, a confined plasma with a single sign of charge that is in a state of thermal equilibrium is guaranteed to be stable and quiescent. In general, a system that is in or near thermal equilibrium tends to be controllable and predictable. Furthermore, the effect of small controlled deviations from thermal equilibrium can be investigated with precision. Thermal equilibrium states are routinely observed for both pure electron plasmas and pure ion plasmas.

From a theoretical perspective, it is a huge advantage to be able to use thermal equilibrium statistical mechanics to describe the plasma state. Such a description is easily obtained and is very complete; for example, it includes the detailed structure of the sheath at the plasma surface and of the microscopic order. It should also be noted that the evolution to thermal equilibrium may be so complicated that we cannot follow it in detail; for example, it may involve a turbulent phase. Nevertheless, the resulting thermal equilibrium state is determined by constants of the motion that are preserved during the evolution, so the thermal equilibrium state can be predicted from the initial conditions.

We are discussing here a cloud of unneutralized charges, and the reader may wonder why we call this cloud a plasma. The reason is that it exhibits many of the collective phenomena associated with neutral plas-

mas. For example, a pure electron plasma exhibits electron-plasma oscillations (Langmuir oscillations) that are essentially the same as those exhibited by a neutral plasma. The reason for this is easy to understand. Electron-plasma oscillations occur at such a high frequency in a neutral plasma that the ions do not participate in the motion. Likewise, the other modes that involve only the electrons in a neutral plasma are supported by a pure electron plasma. In addition, a nonneutral plasma exhibits the phenomenon of Debye shielding. To be precise, we refer to a weakly correlated cloud of charges as a plasma only when the cloud is large in all its dimensions compared to the Debye length,  $\lambda_D = (kT/4\pi n e^2)^{1/2}$ . Here,  $T$  is the temperature of the charges and  $n$  is the density. The name *nonneutral plasma* came into usage with the publication of Davidson's monograph, *Theory of Nonneutral Plasmas* (1974).

Clouds of unneutralized charges have been confined for long times in various kinds of traps: Penning traps, rf or Paul traps, Kingdon traps, and storage rings (Kingdon, 1923; Penning, 1936; Paul and Steinwedel, 1953). However, clouds that are large and dense enough to be called a plasma have typically been confined in Penning traps. Furthermore, we shall observe that charged-particle confinement in radio-frequency Paul traps can be approximately described by an effective ponderomotive potential, leading to thermal equilibrium identical to that of Penning traps. Consequently, we consider only Penning traps and their natural generalizations.

In Sec. II, we use an idealized model of the trap to construct confinement theorems. For the idealized trap, the plasma cannot escape. Of course, a real trap has imperfections—most importantly, field and construction errors that break the cylindrical symmetry—so the plasma is gradually lost. Nevertheless, the loss time can be long compared to the time for Coulomb interactions to bring the charges into thermal equilibrium with each other.

In Sec. III, we review the mean-field (or Boltzmann) description of the thermal equilibrium states. The main difficulty in obtaining such a description is in solving Poisson's equation for the self-consistent electric potential. A plasma is by definition a collection of charges that can substantially modify (Debye shield) the trap potential. Fortunately, the thermal equilibrium states have a simple universal character. The plasma rotates rigidly (without shear) about the direction of the magnetic field, and the density is nearly uniform out to some surface of revolution and there drops to zero on the scale of the Debye length. For the important case of a small plasma in a quadratic trap potential, the surface of revolution is a spheroid (ellipse of revolution), and a complete analytic solution is possible. For a multispecies plasma, centrifugal separation can be important, with different species residing in concentric rings. In this section, we also discuss generalizations of the Penning trap that admit thermal equilibrium states.

When the plasma is cooled correlations between the charges become important. A measure of the strength of correlations is the coupling parameter  $\Gamma = e^2/akT$ , or,

equivalently, the plasma expansion parameter  $1/n\lambda_D^3 = 4\pi\sqrt{3}\Gamma^{3/2}$ . Here,  $a$  is the Wigner-Seitz radius (i.e.,  $4\pi na^3/3 \equiv 1$ ). The coupling parameter is simply the ratio of the interaction energy between neighboring charges,  $e^2/a$ , to the random energy per degree of freedom,  $kT$ . Correlations are weak when  $\Gamma \ll 1$  and strong when  $\Gamma \gg 1$ . A large range of  $\Gamma$  values is experimentally accessible, and thermal equilibrium states are observed for both weakly correlated and strongly correlated plasmas. For a strongly correlated cloud of charges, the Debye length is smaller than the interparticle spacing and effectively loses its meaning. For this case, we require the cloud to be much larger than the interparticle spacing. It is worth noting here that some authors limit the definition of plasma to include only the case of weak correlation. These authors have in mind neutral plasmas. When correlations (collisions) become strong in an electron-ion plasma, the collisional drag between electrons and ions effectively destroys modes such as Langmuir oscillations. One is left with acoustic modes in which the electrons and ions move together, so the system loses much of its distinctive character as a plasma. However, for the nonneutral plasmas under consideration here, Langmuir oscillations survive into the regime of strong correlation. As the correlated system of charges begins to resemble a crystal, the Langmuir oscillations simply evolve into phonons.

The Boltzmann distribution is a one-particle distribution and cannot describe the effect of correlations. In Sec. IV, we review the  $N$ -particle (Gibbs) description of the thermal equilibrium states. Because the mean-field potential is large compared to the interaction potential for neighboring charges, the correlations cause only small changes in the gross (mean-field) shape of the plasma, as established in Sec. III. Instead, they simply establish order within that shape.

A standard theoretical model for the study of correlations is the one-component plasma (OCP). An OCP is a system of classical point charges that is embedded in a uniform neutralizing background charge. We shall see that the Gibbs distribution for a magnetically confined single-species plasma is the same as the Gibbs distribution for an OCP (of finite size). Thus the magnetically confined plasmas provide a laboratory realization of an OCP, at least for thermal equilibrium properties. In addition, the theory that was developed to describe the effect of correlations in an infinite OCP can be applied to magnetically confined plasmas, if these plasmas are large enough to manifest bulk properties.

The Gibbs distribution for an infinite homogeneous OCP can be scaled so that it depends only on  $\Gamma$ , that is, the nature of the thermal equilibrium state is determined by  $\Gamma$ . For  $\Gamma \ll 1$  the system of charges is a weakly correlated plasma, for  $\Gamma \gg 2$  the system begins to exhibit the local order characteristic of a fluid, and for  $\Gamma = 174$  there is a phase transition to a bcc crystal state.

However, in many experiments on strongly correlated nonneutral plasmas, the number of trapped particles is not sufficiently large for us to treat the plasma as infinite and homogeneous. Consequently, the correlation prop-

erties of the plasma are substantially affected by finite-size effects. We identify three size regimes that display qualitatively different correlation behavior: Coulomb clusters, which consist of only a few trapped charges ( $N \leq 10$ ); mesoscopic plasmas (also referred to by some authors as microplasmas), which are larger than the clusters but are still strongly influenced by finite-size effects; and large plasmas, which are sufficiently large to be treated as infinite and homogeneous. Only for large plasmas is a transition to a bcc lattice observed.

For mesoscopic plasmas, a bcc lattice in the crystalline phase is no longer expected; instead the crystal structure displays sensitive dependence on the overall shape and size of the plasma. Over a broad parameter range the plasma crystal consists of concentric shells of charge, which can be thought of as lattice planes that have been deformed by the external confinement potential into shells. For other parameters, the plasmas can be compressed into one-dimensional lines of charge (Coulomb chains) or two-dimensional discs. In Sec. IV we compare numerical simulations and analytic theory of mesoscopic plasmas to experimental results that probe the shell structure. We also review the thermal equilibrium properties of the infinite OCP and compare these properties to recent experiments on large, strongly correlated plasmas. Finally, we describe some aspects of strongly correlated Coulomb clusters. At low temperatures these small collections of charges form simple geometrical configurations that can be predicted on the basis of a minimum-energy principle.

In Sec. V we consider the thermodynamics of nonneutral plasmas. A thermodynamic description of the plasma state has many advantages. Using thermodynamics we can uncover a number of connections between seemingly unrelated physical properties. For example, thermodynamic derivatives are connected by Maxwell relations; the second law imposes bounds on measurable quantities; and  $TdS$  equations allow a general description of the dynamical evolution of the plasma between different thermal equilibrium states, including the evolution caused by complex transport phenomena.

In Sec. VI we conclude with a brief discussion of several topics that could have been included in a review of thermal equilibrium properties, but were not for lack of space. For those readers who would like to learn more about nonneutral plasmas, we also briefly touch upon several other active areas of research in nonneutral plasma physics and provide some references.

The history of research on trapped clouds of unneutralized charges dates back nearly half a century and has roots in atomic physics as well as plasma physics. Penning (1936) invented the basic confinement configuration for use as a vacuum gauge. Dehmelt (1967) pioneered the use of Penning traps for fundamental studies of individual particles, and together with Ramsey and Paul received the 1989 Nobel prize in physics. Gradually the use of Penning traps for research in atomic physics (and chemistry) became widespread. Research on the collective properties of nonneutral plasmas in Penning-trap-like field configurations (magnetrons) dates back to

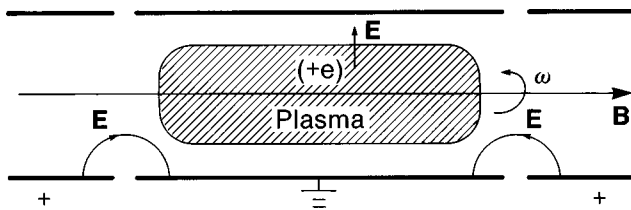


FIG. 1. Schematic diagram of a Malmberg-Penning trap.

efforts in World War II to produce high-power radiation sources for radar. A seminal paper from this period is that by Brillouin (1945). In the late 1960s and early 1970s nonneutral plasma physics experienced a period of rapid development, borrowing techniques and ideas from traditional plasma physics (Davidson, 1974). Research in the atomic physics and plasma physics communities proceeded rather independently until the early 1980s, when collaboration began. The two communities brought different and complementary techniques to the table. The atomic physicists started from rather small plasma samples ( $N \sim 10^2 - 10^4$ ), but brought substantial experience with Penning traps, a tradition of precision measurements, and the powerful techniques of laser cooling and diagnostics. Plasma physicists started with much larger plasmas ( $N \sim 10^{10}$ ) and brought experience with and understanding of collective phenomena and many-body physics. The two communities have learned from each other, borrowed diagnostic techniques and trap designs, exchanged postdocs, and held joint meetings. Much of the work discussed here results from this collaboration.

As general references on nonneutral plasmas, we recommend the two monographs by Davidson (1974, 1990) and the two AIP conference proceedings on Nonneutral Plasma Physics (Roberson and Driscoll, 1988; Fajans and Dubin, 1994). These latter two references focus more explicitly on nonneutral plasmas in traps and include papers from atomic physicists and plasma physicists. A general reference on strongly coupled OCPs is the review article by Ichimaru (1982). A more recent review (Ichimaru, Iyetomi, and Tanaka, 1987) discusses theoretical schemes in the analysis of multiparticle correlations as well as transport calculations in the strongly correlated regime. The proceedings of the recent Nobel Symposium on Trapped Charged Particles and Fundamental Physics (Bergström, Carlberg, and Schuch, 1995) provides a good overview of trap physics from the perspective of atomic physics. Likewise the review article by Brown and Gabrielse (1986) provides an in-depth discussion of the use of Penning traps for confinement of small numbers of charges.

## II. CONFINEMENT AND CONSTANTS OF THE MOTION

### A. Confinement geometry

Figure 1 shows a simple example of a Penning trap (Penning, 1936). A conducting cylinder is divided axially into three sections, with the central section held at

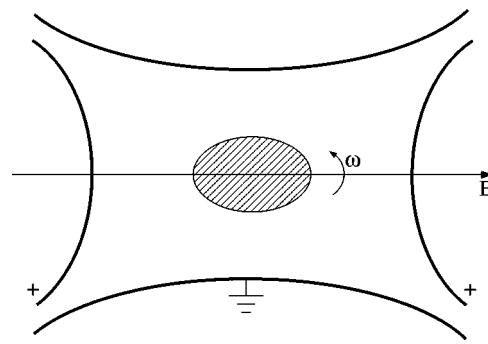


FIG. 2. Penning trap for which the electrodes are hyperbolas of revolution.

ground potential and the two end sections held at positive potential. (Throughout the paper, the figures and discussion refer to positively charged particles, but the case of negative charges is covered by obvious sign changes.) In addition, there is a uniform-axial magnetic field. The plasma resides in the region of the central grounded section, with radial confinement provided by the magnetic field and axial confinement by the electric fields. To understand radial force balance, one must realize that the plasma rotates about the axis of symmetry of the trap. The associated Lorentz force ( $e\mathbf{v} \times \mathbf{B}/c$ ), where  $\mathbf{v}$  is the rotational velocity, is directed radially inward and balances all of the radially outward forces (centrifugal, pressure, and electrostatic). This simple form of the trap (with cylindrical electrodes) is often called a Malmberg-Penning trap, since the late John Malmberg pioneered its use for the confinement of nonneutral plasmas (deGrassie and Malmberg, 1977, 1980). Figure 2 shows a Penning trap in which the cylindrical electrodes are replaced by hyperbolas of revolution. Such traps were developed originally to confine small numbers of charged particles (Dehmelt, 1967; Brown and Gabrielse, 1986), but more recently have been used to confine charge clouds that are large and dense enough to qualify as a plasma. Penning traps of the form shown in these two figures have been used to confine electron plasmas (deGrassie and Malmberg, 1980; Driscoll, Malmberg, and Fine, 1988; Gould and LaPointe, 1991; Hart, 1991; Tan and Gabrielse, 1993; Chu *et al.*, 1993; Tinkle *et al.*, 1994), positive-ion plasmas of one or more species (Brewer *et al.*, 1988; Bollinger, Wineland, and Dubin, 1994), positron plasmas (Surko and Murphy, 1990; Cowan *et al.*, 1993; Greaves *et al.*, 1994; Mohri *et al.*, 1995), and electron-antiproton plasmas (Gabrielse *et al.*, 1989; Holzschneider *et al.*, 1996). We shall develop the theory with traps of this form in mind. To be specific, we shall assume that the trap electrode structure is cylindrically symmetrical, that the potentials on the electrodes are maintained at constant values, and that the magnetic field is uniform and axial and constant in time.

However, it should be noted that this is not the most general trap for which confinement in a state of thermal equilibrium is possible. Confinement requires the plasma to rotate through the magnetic field, and thermal equilibrium requires the trap fields to be stationary in

the rotating frame. If the trap fields are stationary in the laboratory frame, they must have cylindrical symmetry. In relation to our basic model, the magnetic field need not be uniform so long as it has the required cylindrical symmetry. Moreover, the trap fields can be asymmetric and time dependent, so long as they are time independent in some rotating frame. We shall discuss these generalizations in Sec. III.H. The confinement and thermal equilibrium states for these more general configurations can be understood from simple modifications and reinterpretations of the theory developed for our basic model.

## B. Constants of the motion

As a preliminary to a discussion of the thermal equilibrium states, it is necessary to determine the effective constants of the motion for the plasma. These quantities need not be exact constants; it is only necessary that they be nearly constant on the time scale required for interactions to bring the plasma charges into thermal equilibrium with each other. For our theoretical discussion, we introduce an idealized model of the plasma and trap such that the quantities of interest are exact constants.

We consider a plasma of  $N$ -like charges that interact electrostatically in a cylindrically symmetric Penning trap with time-independent voltages applied to the end electrodes and a time-independent and uniform axial magnetic field,  $\mathbf{B} = \hat{z}B$ . The vector potential for this field can be written as  $\mathbf{A} = \hat{\theta}A_\theta(r)$ , where  $A_\theta(r) = Br/2$ . Here,  $(r, \theta, z)$  is a cylindrical coordinate system with the  $z$  axis coincident with the axis of symmetry of the trap. We write the electric potential as

$$\phi(\mathbf{r}) = \phi_T(\mathbf{r}) + \sum_j eG(\mathbf{r}|\mathbf{r}_j), \quad (2.1)$$

where  $\phi_T(\mathbf{r})$  is the trap potential in the absence of a plasma. This potential satisfies Laplace's equation and matches the potential specified on the conducting boundary, that is, on the electrodes. The quantity  $G(\mathbf{r}|\mathbf{r}_j)$  is the Green's function, which vanishes on the conducting boundary, and  $\mathbf{r}_j$  is the position of the  $j$ th charge. The Green's function differs from the Coulomb interaction  $1/|\mathbf{r} - \mathbf{r}_j|$  because of image charges in the conducting boundary.

To a good approximation, the motion of the charges is governed by the Hamiltonian

$$H = \sum_{j=1}^N \left( \frac{p_{r_j}^2}{2m} + \frac{\left[ p_{\theta_j} - \frac{e}{c} A_\theta(r_j) r_j \right]^2}{2mr_j^2} + \frac{p_{z_j}^2}{2m} \right) + \sum_{j=1}^N e\phi_T(\mathbf{r}_j) + \frac{1}{2} \sum_{i,j=1}^N e^2 G(\mathbf{r}_i|\mathbf{r}_j), \quad (2.2)$$

where the prime on the sum denotes that  $j=i$  is excluded, and where the canonical momenta are given by (Goldstein, 1980)

$$p_{r_j} = m\dot{r}_j, \quad p_{\theta_j} = mr_j^2\dot{\theta}_j + \frac{e}{c} A_\theta(r_j)r_j, \quad p_z = m\dot{z}_j. \quad (2.3)$$

The first sum in Eq. (2.2) is the kinetic energy, the second is the electrostatic energy of the charges in the trap potential, and the third is the electrostatic interaction energy of the charges with each other and with their images. Diamagnetic and relativistic effects have been neglected, since velocities are typically small (i.e.,  $|\mathbf{v}_j|/c \ll 1$ ) in the experiments of interest. Also, in the second sum, we have neglected the interaction energy of each charge with its own image; typically this is much smaller than  $e\phi_T(\mathbf{r})$  unless the charge is very near the wall. Note that the interaction of a particular charge with the images of all of the other charges can be large and is retained in the third sum. The constants of the motion follow from the symmetry properties of the Hamiltonian (Landau and Lifshitz, 1976, p. 13), and these properties are not changed by dropping the  $(v/c)^2$  corrections and the interaction of a charge with its own image. These approximations are used only to simplify the notation. In addition, for notational simplicity, we have taken the case of a single-species plasma; the results are easily generalized to a multispecies plasma so long as all of the species have the same sign of charge.

Since the Hamiltonian is invariant under translations in time (i.e.,  $\partial H/\partial t = 0$ ), the Hamiltonian itself is a constant of the motion,

$$H = E. \quad (2.4)$$

We may think of  $H$  as the total particle energy, but should note that  $H$  is not the system energy. Not all of the energy required to assemble the system of charges in the trap is included in  $H$ . The battery that is used to maintain constant voltage on the end electrodes does work against the image charge that flows on and off of these electrodes. In addition, the circuit that keeps the current in the magnetic solenoid constant does work against variations in the plasma magnetic moment (the plasma magnetic moment arises from its rotation). Up to an additive constant, the Hamiltonian is equal to the system energy minus the work done by these external circuits.

The cylindrical symmetry of the apparatus implies that the trap potential is of the form  $\phi_T(\mathbf{r}_j) = \phi_T(r_j, z_j)$  and that the Green's function is of the form  $G(\mathbf{r}_i|\mathbf{r}_j) = G(r_i, z_i, r_j, z_j, \theta_i - \theta_j)$ . Thus the Hamiltonian is invariant under translations in  $\theta$ , i.e.,

$$\sum_{j=1}^N \partial H / \partial \theta_j = 0,$$

and the total canonical angular momentum is conserved:

$$P_\theta \equiv \sum_{j=1}^N p_{\theta_j} = L. \quad (2.5)$$

Of course, for a real plasma in a real trap, the total energy and the total canonical angular momentum are not conserved exactly. The charges slowly radiate away both energy and angular momentum; there are neutrals,

and collisions with the neutrals change the plasma energy and angular momentum; and most importantly there are small field errors and construction errors that break the cylindrical symmetry and apply a small torque on the plasma. However, with care all of these effects can be made sufficiently small that interactions between the particles bring the plasma into thermal equilibrium before the energy and angular momentum change by a significant amount. Thus we proceed with a description of the plasma confinement and thermal equilibrium states using our idealized model.

### C. Confinement theorem

To understand the confinement, it is useful to introduce the Hamiltonian in a frame that rotates with frequency  $-\omega$  (Landau and Lifshitz, 1976, p. 129),

$$H_R = H + \omega P_\theta. \quad (2.6)$$

This quantity is conserved so long as  $H$  and  $P_\theta$  are conserved. Of course, we are free to view the dynamics from any rotating frame that is convenient. It is important to note here that  $-\omega$  is not necessarily the rotation frequency of the plasma. The minus sign is included explicitly so that  $\omega$  can be chosen to be positive (for a plasma of positive charges). When the canonical momenta are replaced with velocity variables, Eq. (2.6) takes the form

$$H_R = \sum_{j=1}^N \frac{m}{2} \mathbf{v}_j^2 + \sum_{j=1}^N e \phi_T(r_j, z_j) + \frac{1}{2} \sum_{i,j=1}^N e^2 G(\mathbf{r}_i | \mathbf{r}_j) + \omega \sum_{j=1}^N \left( m \mathbf{v}_{\theta j} r_j + \frac{e}{c} B r_j^2 / 2 \right), \quad (2.7)$$

where we have used  $(e/c)A_\theta(r)r = eBr^2/2c$ . Carrying out a small amount of algebra yields the result

$$H_R = \sum_{j=1}^N \frac{m}{2} (\mathbf{v}_j + \omega r_j \hat{\theta}_j)^2 + \sum_{j=1}^N e \phi_R(r_j, z_j) + \frac{1}{2} \sum_{i,j=1}^N e^2 G(\mathbf{r}_i | \mathbf{r}_j), \quad (2.8)$$

where

$$e \phi_R(r, z) = e \phi_T(r, z) + m \omega (\Omega_c - \omega) r^2 / 2 \quad (2.9)$$

is the effective trap potential in the rotating frame and  $\Omega_c = eB/mc$  is the cyclotron frequency.

This potential consists of three terms:  $e \phi_T$  is the potential energy due to the voltages maintained on the electrodes,  $-m \omega^2 r^2 / 2$  is the centrifugal potential, and

$$m \omega \Omega_c r^2 / 2 = \int_0^r dr e(\omega r) B / c$$

is the potential induced by rotation through the magnetic field. It is this last term that provides the radial confinement. For a suitable choice of the bias voltage on the end electrodes and for sufficiently large  $\omega(\Omega_c - \omega)$ ,

the equipotential surfaces of  $e \phi_R(r, z)$  are nested surfaces of revolution with the value of  $e \phi_R(r, z)$  increasing outward from the center of the trap. The term  $e \phi_T(r, z)$  increases as  $z$  moves toward either end, where the positively biased end electrodes are located. For sufficiently large  $\omega(\Omega_c - \omega)$ , the term  $m \omega (\Omega_c - \omega) r^2 / 2$  makes  $e \phi_R(r, z)$  an increasing function of  $r$  [even though  $e \phi_T(r, z)$  is decreasing in  $r$ ]. Thus  $e \phi_R(r, z)$  is a potential well that acts to confine the plasma.

A simple confinement theorem can be constructed by noting that the first and third sums in Eq. (2.8) are non-negative.<sup>1</sup> Particles can escape to the wall only by climbing high up in the potential well, that is, by increasing the second sum in Eq. (2.8). This must be accompanied by a decrease in the other two sums, since  $H_R$  is conserved. Physically, the particles can climb up the potential only by using kinetic energy and electrostatic energy of interaction. Because these latter two quantities are non-negative, their initial values set the maximum amount that they can decrease. Suppose that all of the particles are initially inside (bounded by) some equipotential surface  $e \phi_R(r, z) = e \phi_1$  and that the first equipotential where the potential begins to decrease (or intersects the wall) is  $e \phi_R(r, z) = e \phi_2$ . Then only a small fraction of the charges can escape if  $Ne(\phi_2 - \phi_1)$  is much larger than the initial values of the first and third sums in Eq. (2.8).

In applying this theorem, we are free to choose  $\omega$ . However, care must be taken, since  $\omega$  appears both in the effective trap potential and in the kinetic energy (in the rotating frame). In addition,  $\omega$  must lie in the interval  $0 < \omega < \Omega_c$  so that  $\omega(\Omega_c - \omega)$  is positive. Nevertheless, for any initial state of the plasma, the well can be made deep enough to provide confinement for a range of  $\omega$  values, if  $\Omega_c$  and the bias voltage on the end electrodes are sufficiently large.

### D. Constraint on the mean-square radius of the plasma

An alternate confinement theorem focuses on the radial (magnetic) confinement and establishes a constraint on the mean-square radius of the plasma (i.e.,

$$\sum_{j=1}^N r_j^2 \approx \text{const}$$

O'Neil, 1980; Davidson, 1990). Of course, it is the magnetic confinement that one worries about; the axial confinement can be guaranteed simply by choosing the bias voltage on the end electrodes to be sufficiently large.

This theorem illustrates the important role of conservation of angular momentum in guaranteeing radial con-

<sup>1</sup>The non-negative character of the third sum follows from the fact that  $G(\mathbf{r} | \mathbf{r}') > 0$ . A negative value for  $G(\mathbf{r} | \mathbf{r}')$  would imply that  $G(\mathbf{r} | \mathbf{r}')$  reaches a minimum at some point  $r$  inside the confinement region; recall that  $G(\mathbf{r} | \mathbf{r}')$  vanishes on the boundary and is positive near  $\mathbf{r} = \mathbf{r}'$ . Of course, a minimum is not possible since  $\nabla^2 G(\mathbf{r}, \mathbf{r}') = 0$  except at  $\mathbf{r} = \mathbf{r}'$ .

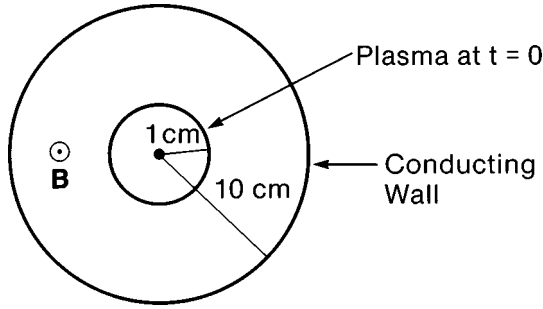


FIG. 3. Schematic diagram used to illustrate the power of the constraint  $\sum_j r_j^2 = \text{const}$ .

finement. In terms of velocity variables, Eq. (2.5) takes the form

$$L = P_\theta = \sum_{j=1}^N m v_{\theta j} r_j + e B r_j^2 / 2c, \quad (2.10)$$

where we have used  $A_\theta(r) = Br/2$ . For a sufficiently large magnetic field, the mechanical part of the angular momentum is small compared to the vector potential part, so Eq. (2.10) reduces to

$$L \approx \sum_{j=1}^N e B r_j^2 / 2c. \quad (2.11)$$

We shall return to this point shortly and bound the neglected terms. Since the plasma contains only a single sign of charge, the charge can be factored out from under the sum along with the other constants, and we obtain a constraint on the mean-square radius of the plasma,

$$\text{const} = L \approx \frac{eB}{2c} \sum_{j=1}^N r_j^2. \quad (2.12)$$

This equation is a very powerful constraint, and it can be illustrated by a simple example. Figure 3 shows the end view of a plasma column that is initially shaped like a cylindrical shell of radius 1 cm [i.e.,  $r_j(t=0) = 1$  cm for  $j=1, \dots, N$ ]. The plasma resides in a long cylindrical trap (see Fig. 1) with the conducting wall at radius  $r = 10$  cm. Taking this situation as the initial condition, what will be the dynamical evolution of the plasma? It turns out that a hollow column is unstable to diocotron modes (Davidson, 1990; Driscoll and Fine, 1990), so these modes grow to large amplitude, nonlinear effects come into play, and a turbulent-like evolution ensues. Interparticle collisions also affect the evolution, particularly the long-time evolution. However, all of this complicated dynamics involves only internal interactions, so

$$L \propto \sum_j r_j^2$$

is conserved. This means that only 1% of the particles can move from  $r_j(0) = 1$  cm out to the wall at  $r = 10$  cm; the other 99% of the particles must remain confined. Of course, on a very long time scale, collisions with neutrals and trap asymmetries produce a slow

change in  $L$ , and the plasma gradually expands. For a neutral plasma, the constraint

$$\sum_j r_j^2 = \text{const}$$

is replaced by

$$\sum_j e_j r_j^2 = \text{const},$$

so an electron and an ion can move to the wall together and still preserve the sum. This is precisely what happens in electron-ion collisional transport as well as in many instabilities. One can see that it is much easier to confine a plasma with a single sign of charge than it is to confine a neutral plasma.

We now return to the derivation and use conservation of energy to place a bound on the neglected terms. Conservation of angular momentum implies that

$$\begin{aligned} & \left| \Omega_c/2 - \omega \right| \left| \sum_{j=1}^N r_j^2(t) - \sum_{j=1}^N r_j^2(0) \right| \\ &= \left| \sum_{j=1}^N r_j(0) \bar{v}_{\theta j}(0) - \sum_{j=1}^N r_j(t) \bar{v}_{\theta j}(t) \right|, \end{aligned} \quad (2.13)$$

where  $\bar{v}_\theta = v_\theta + \omega r$  is the  $\theta$  component of the velocity in a frame that rotates with frequency  $-\omega$ . By using the inequality

$$|\bar{v}_\theta| \leq [\bar{v}_z^2 + \bar{v}_\theta^2 + \bar{v}_r^2]^{1/2} = \bar{v}, \quad (2.14)$$

we obtain the inequality

$$\begin{aligned} & \left| \Omega_c/2 - \omega \right| \left| \sum_{j=1}^N r_j^2(t) - \sum_{j=1}^N r_j^2(0) \right| \\ & \leq \sum_{j=1}^N r_j(0) \bar{v}_j(0) + r_j(t) \bar{v}_j(t). \end{aligned} \quad (2.15)$$

To bound

$$\sum_j r_j \bar{v}_j,$$

we choose the  $\bar{v}$ 's so that

$$\sum_j r_j \bar{v}_j$$

is a maximum for a given value of the kinetic energy

$$K_R = \sum_j m \bar{v}_j^2 / 2,$$

that is, the  $\bar{v}_j$ 's are chosen so that

$$0 = \delta \sum_{j=1}^N r_j \bar{v}_j - \alpha \delta \sum_{j=1}^N \bar{v}_j^2 / 2 = \sum_{j=1}^N (r_j - \alpha \bar{v}_j) \delta \bar{v}_j, \quad (2.16)$$

where  $\delta \bar{v}_j$  is an independent infinitesimal variation and  $\alpha$  is a Lagrange multiplier. Thus we find that  $\bar{v}_j = r_j / \alpha$ , where  $\alpha$  must be chosen so that

$$K_R = (m/\alpha^2) \sum_j r_j^2 / 2.$$

This yields the bound

$$\sum_{j=1}^N r_j \bar{v}_j = \left[ \frac{2K_R}{m} \sum_{j=1}^N r_j^2 \right]^{1/2}. \quad (2.17)$$

Suppose that  $K_R^{\max}$  is the maximum possible value for  $K_R$ . Equations (2.17) and (2.15) then imply the inequality

$$\left| \sum_{j=1}^N r_j^2(t) - \sum_{j=1}^N r_j^2(0) \right| \leq \left[ \frac{8K_R^{\max}}{m(\Omega_c - 2\omega)^2} \right]^{1/2} \left[ \left( \sum_{j=1}^N r_j^2(0) \right)^{1/2} + \left( \sum_{j=1}^N r_j^2(t) \right)^{1/2} \right]. \quad (2.18)$$

By factoring the left-hand side, we obtain

$$|x - 1| \leq \varepsilon, \quad (2.19)$$

where

$$\varepsilon = \left[ \frac{8K_R^{\max}}{m(\Omega_c - 2\omega)^2 \sum_j r_j^2(0)} \right]^{1/2}, \quad x^2 = \sum_j r_j^2(t) / \sum_j r_j^2(0). \quad (2.20)$$

To bound  $K_R^{\max}$ , we use the constancy of

$$H_R = K_R + U + \sum_j e\phi_R(\mathbf{r}_j). \quad (2.21)$$

Here,  $K_R$  and  $U$  represent the first and third sums in Eq. (2.8). As mentioned earlier (see footnote 1),  $U$  is non-negative. For a given bias voltage on the end electrodes,  $\Omega_c$  can be chosen to be large enough that  $\phi_R(\mathbf{r})$  is a potential well even for  $\omega \ll \Omega_c$ . For this theorem there is an advantage in choosing  $\omega$  to be as small as possible, consistent with the condition that  $e\phi_R(\mathbf{r})$  takes its minimum value at  $\mathbf{r}=0$ . If we choose this minimum value to be  $\phi_R(0)=0$ , then the third sum in Eq. (2.21) also is non-negative. Thus we obtain the bounds

$$K_R^{\max} \leq H_R(0) \quad (2.22)$$

and

$$\varepsilon \leq \left[ \frac{8H_R(0)}{m(\Omega_c - 2\omega)^2 \sum_j r_j^2(0)} \right]^{1/2}. \quad (2.23)$$

For a nonneutral plasma, it is typically the case that  $U(0)$  sets the size of  $H_R(0)$ . For a column of density  $n$  and radius  $r(0)$ , a simple estimate yields  $U(0) \sim \pi n e^2 r^2(0) N$ . Thus we find the requirement that  $\varepsilon \sim \omega_p / \Omega_c \ll 1$ , where we have set  $\Omega_c - 2\omega \approx \Omega_c$ .

As a simple numerical example, consider an electron column that is confined in a magnetic field of strength 1 kilogauss and that is of initial radius  $r(0)=1$  cm. For this case,  $m\Omega_c^2 r^2(0)$  is of order  $10^5$  eV, so  $\varepsilon \ll 1$  if  $H_R(0)/N \ll 10^5$  eV. In comparison, for a column of den-

sity  $n \approx 10^7$  cm $^{-3}$  and radius  $r(0)=1$  cm,  $U(0)/N \sim \pi n e^2 r^2(0)$  has the value 5 eV.

### III. MEAN-FIELD DESCRIPTION OF THERMAL EQUILIBRIUM STATES

When the plasma is sufficiently warm that correlations are small (i.e.,  $\Gamma = e^2/akT \ll 1$ ), the thermal equilibrium states may be described with a one-particle (i.e., Boltzmann) distribution.

#### A. Boltzmann distribution

Because the total Hamiltonian and the total canonical angular momentum are both conserved, the Boltzmann distribution takes the form (Davidson and Krall, 1970; Prasad and O'Neil, 1979; Davidson, 1990)

$$f(\mathbf{r}, \mathbf{v}) = \frac{N \exp \left[ -\frac{1}{kT} (h + \omega p_\theta) \right]}{\int d^3\mathbf{r} d^3\mathbf{v} \exp \left[ -\frac{1}{kT} (h + \omega p_\theta) \right]}, \quad (3.1)$$

where

$$h = \frac{mv^2}{2} + e\phi(\mathbf{r}) \quad (3.2)$$

is the one-particle Hamiltonian and

$$p_\theta = m\mathbf{v}_\theta r + \frac{eB}{2c} r^2 \quad (3.3)$$

is the one-particle canonical angular momentum. Here,

$$\phi(\mathbf{r}) = \phi_T(\mathbf{r}) + e \int d^3\mathbf{r}' d^3\mathbf{v}' f(\mathbf{r}', \mathbf{v}') G(\mathbf{r}|\mathbf{r}') \quad (3.4)$$

is the mean-field (or Vlasov) electric potential. Equation (3.4) is the mean-field version of Eq. (2.1). The temperature and rotation frequency ( $T$  and  $\omega$ ) are determined by the values of

$$H = \int d^3\mathbf{r} d^3\mathbf{v} [mv^2/2 + e\phi_T(\mathbf{r})] f(\mathbf{r}, \mathbf{v}) + \frac{1}{2} \int d^3\mathbf{r} d^3\mathbf{v} d^3\mathbf{r}' d^3\mathbf{v}' e^2 G(\mathbf{r}|\mathbf{r}') f(\mathbf{r}, \mathbf{v}) f(\mathbf{r}', \mathbf{v}') \quad (3.5)$$

and

$$P_\theta = \int d^3\mathbf{r} d^3\mathbf{v} \left[ m\mathbf{v}_\theta r + \frac{eBr^2}{2c} \right] f(\mathbf{r}, \mathbf{v}). \quad (3.6)$$

These are the mean-field versions of Eqs. (2.2) and (2.5). Since  $H=E$  and  $P_\theta=L$  are conserved during the evolution to thermal equilibrium,  $T$  and  $\omega$  can be predicted from the initial conditions. As mentioned in the Introduction, this is one of the advantages of being able to use thermal equilibrium statistical mechanics.

It is important to note that  $\omega$  plays a different role in the thermal distribution than in the confinement theorem of Sec. II.C. In the thermal distribution,  $\omega$  is fixed



by the constants of the motion  $H=E$  and  $P_\theta=L$ ; we shall see shortly that  $-\omega$  is the rotation frequency of the plasma. On the other hand, in the confinement theorem,  $-\omega$  is the rotation frequency of the frame from which we view the dynamics; we are free to choose  $\omega$ .

Distribution (3.1) can be derived formally from the Gibbs distribution as an expansion in the small parameter  $1/n\lambda_D^3 = 4\pi\sqrt{3}\Gamma^{3/2} \ll 1$  (Ichimaru, 1992). More simply, it follows from maximization of the entropy

$$S = -k \int d^3\mathbf{r} d^3\mathbf{v} f \ln f, \quad (3.7)$$

subject to fixed values for  $N = \int d^3\mathbf{r} d^3\mathbf{v} f$  and for  $H$  and  $P_\theta$  as defined in Eqs. (3.5) and (3.6). Note that Eqs. (3.5) and (3.7) already have built in the fact that correlations are weak. The variation leads to distribution (3.1) with the mean-field potential given by Eq. (3.4). The parameters  $T$  and  $\omega$  enter as Lagrange multipliers associated with the fixed values of  $H$  and  $P_\theta$ . In distribution (3.1) a third Lagrange multiplier has been eliminated in favor of the constant  $N = \int d^3\mathbf{r} d^3\mathbf{v} f$ .

Substituting Eqs. (3.2) and (3.3) into Eq. (3.1) and carrying out a small amount of algebra yields the distribution

$$f(\mathbf{r}, \mathbf{v}) = n(r, z) \left( \frac{m}{2\pi kT} \right)^{3/2} \exp \left[ -\frac{m}{2kT} (\mathbf{v} + \omega r \hat{\theta})^2 \right], \quad (3.8)$$

where the density is given by

$$n(r, z) = N \frac{\exp \left\{ -\frac{1}{kT} [e\phi_R(r, z) + e\phi_p(r, z)] \right\}}{\int d^3\mathbf{r} \exp \left[ -\frac{1}{kT} (e\phi_R + e\phi_p) \right]}. \quad (3.9)$$

Here,  $\phi_R$  is the effective trap potential in the rotating frame [see Eq. (2.9)], and  $\phi_p$  is the plasma space-charge potential, that is, the second term in Eq. (3.4).

The velocity distribution is Maxwellian in a reference frame that rotates with frequency  $-\omega$ . This implies that the local fluid velocity

$$\mathbf{v} = \frac{\int d^3\mathbf{v} \mathbf{v} f}{\int d^3\mathbf{v} f} = \omega r \hat{\theta} \quad (3.10)$$

is a shear-free, rigid rotation flow. Of course, a thermal equilibrium flow must be shear free. Viscous forces acting on a shear in the flow would produce entropy, and that is impossible for a state of maximum entropy.

To see that the density distribution can correspond to a confined plasma, we recall that  $e\phi_R(r, z)$  is a potential well for a suitable choice of the bias voltage on the end electrodes and of the magnetic-field strength. The plasma simply resides in that potential well. The term  $e\phi_T(r, z)$  [see Eq. (2.9)] forces the distribution to be exponentially small at the ends, where the positively biased electrodes are located, and the term  $m\omega(\Omega_c - \omega)r^2/2$  forces the distribution to be exponentially

small at large  $r$ . Of course, the wall is located beyond the region where the distribution becomes exponentially small.

At this point it is useful to pause for a moment and consider other confinement schemes that can lead to a confined thermal equilibrium identical to Eqs. (3.8) and (3.9). In particular, radio-frequency Paul traps can also confine charged particles for long periods of time. In Paul traps a rapidly oscillating electric field creates a time-averaged force that traps the charges. Provided that the rapid oscillations in the particle position and the velocity caused by the oscillating E field are small and can be neglected, the confinement force is conservative, described by a ponderomotive potential. A thermal equilibrium description of the particle confinement can then be developed, leading back to Eqs. (3.8) and (3.9), with  $\phi_R(\mathbf{r})$  now taking the role of the ponderomotive potential. Usually there is negligible plasma rotation, so  $\omega=0$  in Eq. (3.8) and the velocity distribution (neglecting the rapid oscillations) is a centered Maxwellian. Later we shall describe several experiments involving nonneutral clouds confined in Paul traps (see Sec. IV.E).

It is easy to see that distributions of the form (3.1) are not consistent with confinement of a neutral (or partially neutral) plasma in a Penning trap. When the plasma contains more than one species, there is a distribution for each species, but the distributions must all have the same values of  $T$  and  $\omega$ . Since the sign of the charge enters as a coefficient in the two terms that provide confinement [i.e.,  $e\phi_T(r, z)$  and  $m\omega\Omega_c r^2/2 = e\omega B r^2/2c$ ], confinement of a positively charged species implies nonconfinement of a negatively charged species.

This argument can be extended to the most general form of a thermal equilibrium distribution function (Landau and Lifshitz, 1980, p. 104),

$$f_j = \exp \{ \alpha_j - \beta [h_j + \boldsymbol{\gamma} \cdot \mathbf{p}_j + \boldsymbol{\delta} \cdot (\mathbf{r} \times \mathbf{p}_j)] \}, \quad (3.11)$$

where  $h_j = m_j v_j^2/2 + e_j \phi$  is the one-particle Hamiltonian for a particle of species  $j$  and  $\mathbf{p}_j = m_j \mathbf{v} + (e_j/c) \mathbf{A}(\mathbf{r})$  is the canonical momentum. The Lagrange multipliers  $\beta$ ,  $\boldsymbol{\gamma}$ , and  $\boldsymbol{\delta}$  must have the same values for the electron and ion distributions; the  $\alpha_j$ 's can be different to account for different numbers of electrons and ions (i.e.,  $N_e \neq N_i$ ). Distributions of this form allow for the possibility that the system conserves the number of electrons, the number of ions, the energy, the three components of linear momentum, and the three components of angular momentum. These are the only possible additive constants for a macroscopic system.

Integrating over velocity yields the density distributions

$$n_j = \left( \frac{2\pi}{m_j \beta} \right)^{3/2} \exp \left\{ \alpha_j - \beta \left[ -m_j (\boldsymbol{\gamma} + \boldsymbol{\delta} \times \mathbf{r})^2 \frac{1}{2} + e_j \psi(\mathbf{r}) \right] \right\}, \quad (3.12)$$

where  $\psi(\mathbf{r}) = \phi(\mathbf{r}) + (\boldsymbol{\gamma} + \boldsymbol{\delta} \times \mathbf{r}) \cdot \mathbf{A}(\mathbf{r})/c$ . Thus we obtain

$$[n_e(r)]^z n_i(r) \propto e^{\beta[(Zm_e + m_i)(\boldsymbol{\gamma} + \boldsymbol{\delta} \times \mathbf{r})^2/2]}, \quad (3.13)$$

where  $Z \equiv e_i/|e_e|$ . Confinement would require that  $n_e^Z n_i$  approach zero for large  $|\mathbf{r}|$ , but that is not the case. Thus

a neutral (or partially neutral) plasma cannot be confined by static electric and magnetic fields and also be in a state of thermal equilibrium. That plasmas with a single sign of charge can be so confined is an important property that distinguishes these plasmas from other plasmas.

Finally, it is instructive to look at the thermal equilibrium distribution from the perspective of force balance. Operating on both sides of Eq. (3.9) with  $\partial/\partial r$  yields

$$-nm \frac{v_\theta^2}{r} = -ne \frac{\partial \phi}{\partial r} + ne \frac{v_\theta}{c} B - \frac{\partial p}{\partial r}, \quad (3.14)$$

and operating with  $\partial/\partial z$  yields

$$0 = -ne \frac{\partial \phi}{\partial z} - \frac{\partial p}{\partial z}, \quad (3.15)$$

where  $v_\theta = \omega r$  is the azimuthal fluid velocity,  $\phi = \phi_T + \phi_p$  is the total electric potential,  $p = nkT$  is the pressure, and we have used  $\omega$ ,  $T = \text{const}$ . Equations (3.14) and (3.15) are the fluid dynamic statements of radial and axial force balance for an azimuthally symmetric equilibrium. Of course, we expect that force balance is satisfied by the thermal equilibrium distribution. The more interesting observation is that force balance plus the conditions  $\omega$ ,  $T = \text{const}$  imply the thermal equilibrium density distribution, that is, Eqs. (3.14) and (3.15) can be integrated (for  $\omega$ ,  $T = \text{const}$ ) to obtain density distribution (3.9).

This latter perspective can help us understand the approach to thermal equilibrium. Suppose that initially the plasma is in a stable, azimuthally symmetric equilibrium. If the cyclotron radius is small compared to the plasma radius, as is typically the case, the approach to thermal equilibrium takes place in two stages with well-separated time scales. First, collisions produce a local thermal equilibrium along each field line. The velocity distribution is then Maxwellian and Eq. (3.15) is satisfied along each field line. However, the temperature at this stage typically is not independent of  $r$ . Likewise, the local rotation frequency,  $\omega = v_\theta/r$ , as determined by Eq. (3.14), typically is not independent of  $r$ . On a longer time scale, viscous forces acting on the shear in the rotational flow drive the system toward a state of rigid rotation (i.e.,  $\omega = \text{constant}$ ). Likewise, the radial transport of heat makes the temperature constant. These two conditions plus force balance then imply that the system is in a state of global thermal equilibrium. To finish the story, we note that on an even longer time scale, weak effects that are not included in our idealized model (Sec. II.B) produce a slow change in  $E$  and  $L$ , and, in response, the temperature  $T$  and the rotation frequency  $\omega$  evolve slowly in time.

## B. Experimental observation of thermal-equilibrium states

Thermal equilibrium states (or states close to thermal equilibrium) have been observed in experiments with pure electron plasmas and in experiments with pure ion plasmas. Here, we review the geometry and diagnostic

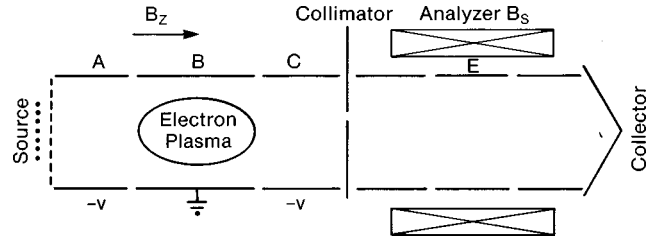


FIG. 4. Schematic diagram of Malmberg-Penning trap used to observe thermal equilibrium states of a pure electron plasma. From Driscoll, Malmberg, and Fine (1988).

techniques for these experiments and present evidence that the plasmas evolved to thermal equilibrium. Further results from the experiments will be discussed as we proceed with the theory.

### 1. Electron plasmas

Experiments with electron plasmas were carried out with an apparatus of the form shown schematically in Fig. 4 (Driscoll, Malmberg, and Fine, 1988). The trapping and confinement region (cylinders A, B, and C) is the same as was shown in Fig. 1, but also shown is a hot filament (the electron source) to the left of cylinder A and a collimator hole, velocity analyzer, and collector assembly to the right of cylinder C. The apparatus was operated in an inject, hold, and dump-and-measure cycle. For injection, cylinder A was briefly grounded so that a column of electrons extended from the hot filament to cylinder C. When cylinder A was returned to negative potential, the flow of electrons from the filament was blocked and a plasma was trapped in the region of cylinder B. After a containment time  $t$ , cylinder C was pulsed to ground potential, and the electrons streamed out along field lines to the collimator, velocity analyzer, and collector. By repeating this cycle for various radial positions of the collimator hole and for various containment times, Driscoll *et al.* were able to determine the plasma density and temperature as a function of  $r$  and  $t$ . The good shot-to-shot reproducibility observed at fixed values of  $r$  and  $t$  implied that the plasmas had good azimuthal symmetry.

Typical parameters for the collection of trapped electrons were a density of  $n \approx 10^7 \text{ cm}^{-3}$ , a temperature of  $kT \approx 1 \text{ eV}$ , and a diameter and length of about 5 cm. The Debye length  $\lambda_D = \sqrt{kT/4\pi ne^2} \approx 0.2 \text{ cm}$  was small compared to the diameter and length, so the collection of electrons was indeed a plasma. The magnetic-field strength was varied from about 50 G to 500 G, so the characteristic cyclotron radius varied from  $r_c = \sqrt{kT/m}/\Omega_c \approx 5 \times 10^{-2} \text{ cm}$  to  $r_c \approx 5 \times 10^{-3} \text{ cm}$ , which is small compared to the plasma radius.

As was discussed above, the approach to thermal equilibrium for a plasma with a small cyclotron radius takes place in two stages with well-separated time scales. On the collisional time scale (about  $10^{-3}$  sec for these plasmas), local thermal equilibrium was established along each field line. On a relatively long time scale (a few seconds for these plasmas), the radial transport process brought the plasma to a state of global thermal

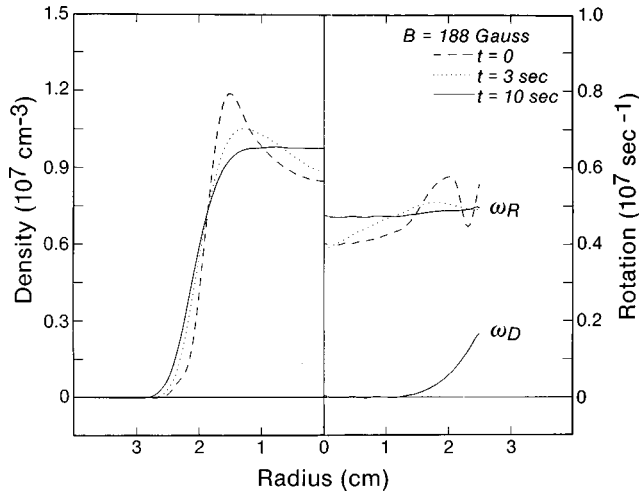


FIG. 5. Experimental density profiles  $n(r,0,t)$  and rotation profiles  $\omega_R(r,0,t)$  at three times ( $t=0,3$  sec,  $10$  sec) showing the evolution to thermal equilibrium. Here  $\omega_D = -(mn\Omega_c r)^{-1} \partial p / \partial r$  is the contribution to rotation from the diamagnetic drift. From Driscoll, Malmberg, and Fine (1988).

equilibrium. It is this latter process that was of interest in the experiments, so the ejection time  $t$  was always chosen to be much larger than the time required to establish local thermal equilibrium.

Thus the assumption of local thermal equilibrium was used in combination with the experimental measurements to determine the plasma state. In particular, the density in each cylindrical shell was assumed to vary in  $z$  according to the Boltzmann factor

$$n(r,z,t) = N(r,t) \frac{\exp[-e\phi(r,z,t)/kT(r,t)]}{\int_{-\infty}^{+\infty} dz \exp[-e\phi(r,z,t)/kT(r,t)]},$$

where the normalization  $N(r,t)$  and the local temperature  $T(r,t)$  were measured directly. The density  $n(r,z,t)$  and the self-consistent potential  $\phi(r,z,t)$  were determined by solving Poisson's equation subject to the known boundary conditions for  $\phi$  specified on the conducting wall. Of course, the Boltzmann factor is a solution to Eq. (3.15). The normalization  $N(r,t)$  was determined by letting the plasma stream out along the field lines and measuring the charge that passed through the collimator hole. In measuring the local temperature  $T(r,t)$ , special care was taken, since a large amount of electrostatic energy was converted to parallel kinetic energy when the plasma disassembled. However, the perpendicular kinetic energy did not change, since the cyclotron period was short compared to the disassembly time, that is,  $\mu = mv_{\perp}^2/2B$  was a good adiabatic invariant. To measure the plasma temperature, the dependence of the electron distribution on perpendicular kinetic energy was determined.

The results were reported for a cut through the plasma at its mid-plane ( $z=0$ ). Figure 5 shows graphs of the density  $n(r,0,t)$  and rotation frequency  $\omega_R(r,0,t) = v_{\theta}(r,0,t)/r$  as a function of  $r$  for three values of  $t$ . The rotation frequency follows from Eq. (3.14) given the val-

ues of  $\partial(nkT)/\partial r$  and  $\partial\phi/\partial r$ . One should note that the graphs labeled  $t=0$  actually refer to a containment time that is long compared to the time to come to local thermal equilibrium, that is, long compared to  $10^{-3}$  sec. The plasma was not in a state of global thermal equilibrium at this time; the radial variation in the rotation frequency shows that the flow had shear. By the time  $t=10$  sec, the shear in the rotational flow had nearly vanished and the density profile had evolved to a form that we shall see is expected for thermal equilibrium. For this particular evolution, the temperature was initially radially uniform at  $0.8$  eV, and it remained uniform throughout the evolution, rising in value to  $1.1$  eV by  $t=10$  sec. For other cases, the temperature typically was nonuniform initially but became uniform during the evolution. In this experiment, local thermal equilibrium was achieved in  $10^{-3}$  sec, global thermal equilibrium in about  $10$  sec, and  $P_{\theta}$  changed substantially (allowing plasma expansion) in about  $10^3$  sec. The three time scales were well separated.

## 2. Ion plasmas

Next we discuss a series of experiments that were carried out with  ${}^9\text{Be}^+$  ion plasmas (Brewer *et al.*, 1988). One of the main advantages of using a plasma that consists of partially ionized atoms is that the atoms have a very large cross section for resonant interaction with light. The cross section for resonant scattering can be 15 orders of magnitude larger than the Thomson scattering cross section for electrons, and even a single atom can be detected. In the experiments, resonant scattering of laser light was used to cool the plasma, to transfer angular momentum to the plasma, and to diagnose the plasma.

The basic idea of Doppler laser cooling is easy to understand (Wineland *et al.*, 1985). A beam of laser light that is tuned to the low-frequency side of some atomic transition is directed through the plasma. Ions with a velocity component that is directed oppositely to the direction of beam propagation (i.e.,  $\mathbf{k} \cdot \mathbf{v} < 0$ ) are Doppler shifted into resonance and absorb photons at a high rate. Here,  $\mathbf{k}$  refers to the wave number of the laser light and  $\mathbf{v}$  to the ion velocity. Conversely, ions with a velocity component in the same direction as the beam propagation (i.e.,  $\mathbf{k} \cdot \mathbf{v} > 0$ ) are Doppler shifted out of resonance and absorb photons at a low rate. When an ion absorbs a photon, the ion suffers the recoil  $\Delta\mathbf{v} = \hbar\mathbf{k}/m$ , where  $2\pi\hbar$  is Planck's constant and  $m$  is the mass of the ion. Subsequently, the ion reemits the photon symmetrically, so that on average the reemission process produces no change in the ion momentum. For a narrow laser beam that passes through (or near) the rotational axis of the plasma, the velocity component  $\mathbf{y} \cdot \mathbf{k}/|\mathbf{k}|$  is associated with the random thermal motion of the ions rather than the coherent rotational motion of the plasma. Thus the net effect of the absorption and reemission process is to cool the plasma. A cooling beam also can be used to exert a torque on the plasma. Suppose that the beam

passes through the plasma in a direction that makes a  $90^\circ$  angle with respect to  $\mathbf{B}$ . If the beam passes directly through the rotational axis, the beam simply cools the plasma, but if the beam is offset slightly to one side of the rotational axis, it cools the plasma and applies a torque on the plasma. When the applied torque and cooling balance the ambient backward torque and heating, a steady state is reached.

In an initial set of experiments, the ions were confined in traps with hyperbolic electrodes of the form shown in Fig. 2. Beams for cooling (and applying a torque) were provided by a frequency-doubled dye laser that produced up to  $50 \mu\text{W}$  of power; it was tuned to the low-frequency side of the transition  $2s^2S_{1/2}(m_J=3/2, m_I=1/2)$  to  $2p^2P_{3/2}(3/2, 3/2)$  of the  ${}^9\text{Be}^+$  ion. A lower-power laser ( $\ll \mu\text{W}$ ), called the probe laser, was used to remove  ${}^9\text{Be}^+$  ions from the  $2s^2S_{1/2}(3/2, 1/2)$  state by resonantly exciting them to the  $2p^2P_{3/2}(3/2, -1/2)$  state, from which they decayed preferentially to a third state. This produced a reduction in the observed scattered light from the cooling beams. The probe beam did not have to overlap with a cooling beam, because the spatial mixing time associated with the rotational and axial motion of the ions was short compared to the lifetime of the depopulation. The size and shape of the plasma was determined by measuring the decrease in scattered light for different positions of the probe beam. The plasma rotation frequency was determined through the Doppler shift by measuring the probe-laser frequency that produced the maximum decrease in scattered light, and the density was determined from the rotation frequency by using Eq. (3.20). The temperature was obtained by determining the Doppler contribution to the frequency broadening of the resonance.

To load the plasma, a vapor of  ${}^9\text{Be}$  atoms was created in the confinement region and then ionized with an electron beam. The initially diffuse and warm cloud of ions was then cooled and increased in density by use of the cooling (and torque) laser. The number of ions trapped ranged from a few to about  $10^4$ . As an example, a particular “large” cloud contained  $N \approx 3 \times 10^4$  ions, at a density of  $n \approx 2.3 \times 10^7 \text{ cm}^{-3}$ , and a perpendicular temperature of  $T_\perp \approx 0.1 \text{ K}$ . Assuming that collisional interactions between the ions maintained an approximate equipartition between the parallel and perpendicular degrees of freedom (i.e.,  $T_\parallel \approx T_\perp$ ), the Debye length was approximately  $\lambda_D \approx 4.5 \times 10^{-4} \text{ cm}$ . This is small compared to the axial and radial dimensions of the cloud ( $2Z_p = 1.6 \times 10^{-3} \text{ cm}$  and  $2R_p = 1.2 \times 10^{-3} \text{ cm}$ ), so the cloud was a plasma.

One signature of global thermal equilibrium is a shear-free rotational flow. The Doppler-shifted center of the depopulation resonance for the probe beam is given by  $\nu' = \nu_0 + \langle \mathbf{k} \cdot \mathbf{v} \rangle / 2\pi$ , where  $\nu_0$  is the frequency of the resonance in the rest frame of the ion and  $\langle \rangle$  denotes an average over the ions along the path of the beam. In the experiments, a narrow probe beam was adjusted to pass through the plasma mid-plane (i.e.,  $z=0$ ) at a distance  $d$  from the axis of rotation. For a shear-free flow (i.e.,  $\mathbf{v} = \hat{\omega} r$ ),  $\mathbf{k} \cdot \mathbf{v} = k\omega r \sin \theta = k\omega d$  at every point along the

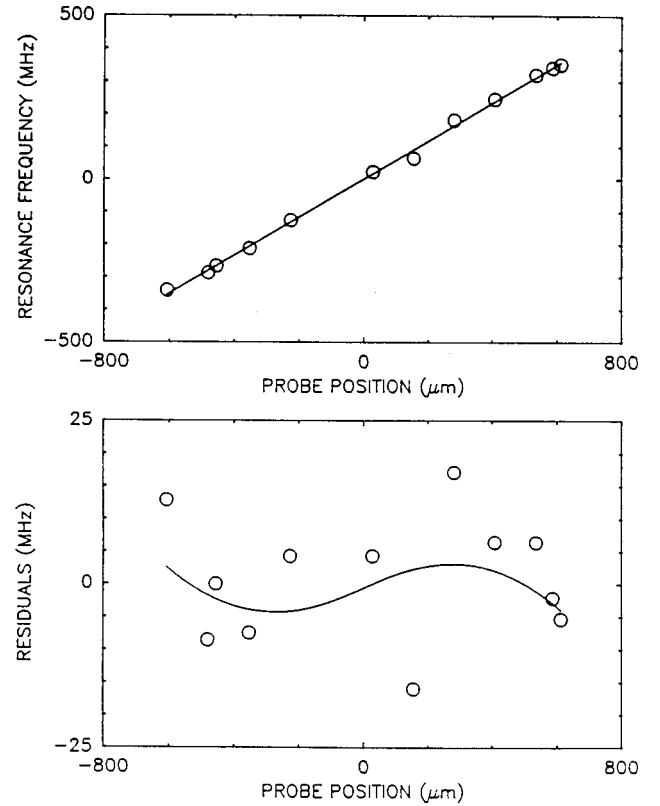


FIG. 6. Doppler shift of resonance frequency vs the probe beam displacement from the axis of rotation for a plasma of  $30\,000 {}^9\text{Be}^+$  ions. The residuals are plotted below along with a fit to the sheared flow  $\omega(r) = \omega(1 + \xi r/r_p)$ , where the least-squares fit is  $\xi = -0.1 \pm 0.1$ . From Brewer *et al.* (1988).

probe beam so  $\nu' - \nu_0 = k\omega d / 2\pi$ . The upper graph in Fig. 6 is a plot of the measured value of  $\nu'_0 - \nu_0$  versus  $d$ , and one can see that the variation with  $d$  is nearly linear. The lower graph is a plot of the residual difference between the resonance frequency data and the best fit to linear variation. The solid curve is a fit to the sheared flow  $\omega(r) = \omega(1 + \xi r/r_d)$ , where  $\xi \approx -0.1 \pm 0.1$ . One might have worried that the ambient torque and the applied laser torque would produce substantial shears in the flow and drive the plasma far away from thermal equilibrium, but this was not the case. Apparently, these torques were small enough that ion-ion interactions (viscous effects) were able to keep the plasma near thermal equilibrium. We shall return later to a discussion of the expected and observed plasma shape.

### C. Self-consistent potential, Debye shielding, and imaginary neutralizing charge

As mentioned in the introduction, we reserve the name plasma for a collection of charges that is large in all of its dimensions compared to the Debye length. A consequence of this definition is that the space-charge potential  $\phi_p$  is not negligible in the thermal equilibrium density distribution [i.e., in Eq. (3.9)]. As a simple example, consider a uniform-density spherical plasma of radius  $R_p$  in free space. One easily finds that

$$\frac{|e\phi_p(R_p) - e\phi_p(0)|}{kT} = \frac{1}{6} \left( \frac{R_p}{\lambda_D} \right)^2 \gg 1. \quad (3.16)$$

Thus it is necessary to solve for  $\phi_p(r, z)$  in order to obtain an explicit expression for  $n(r, z)$ . We must solve Eq. (3.4) or, equivalently, we must solve Poisson's equation,

$$\nabla^2 \phi_p = -4\pi en(r, z), \quad (3.17)$$

subject to the boundary condition that  $\phi_p$  vanish everywhere on the conducting wall. This equation is nonlinear in  $\phi_p$ , since  $\phi_p$  enters the density distribution (3.9) exponentially. We refer to a solution pair  $\phi_p(r, z)$  and  $n(r, z)$  as a self-consistent potential and density. Fortunately, the self-consistent solutions obtained for different  $\phi_R(r, z)$ ,  $T$ , and  $N$  all have the same universal character (Prasad and O'Neil, 1979). The plasma density is nearly constant out to some surface of revolution and there drops to zero on the scale of a Debye length.

We can understand these solutions in simple physical terms. In the rest frame of the plasma, which here is the rotating frame, the plasma charges arrange their positions so that any externally imposed electrostatic field is Debye shielded out (Davidson, 1974; 1990). In the present case,  $\phi_R(r, z)$  is the effective external potential in the rotating frame, so we expect that

$$\phi_p(r, z) + \phi_R(r, z) \approx \text{const} \quad (3.18)$$

inside the plasma. From this equation and Eqs. (2.9) and (3.17), we find that

$$4\pi e^2 n = -\nabla^2 e\phi_p = \nabla^2 e\phi_R = 2m\omega(\Omega_c - \omega). \quad (3.19)$$

Here, we have used  $\nabla^2 \phi_T = 0$ . Thus the density is nearly constant inside the plasma. Furthermore, from this argument it is not surprising that the density drops to zero at the plasma surface on the scale of the Debye length. This variation will be considered in detail in Sec. III.D. Referring again to the experimental results in Fig. 5, one can see that the radial density profile for  $t = 10$  sec is of the expected thermal equilibrium form.

Another way to understand these solutions is to note that the second term in  $e\phi_R(r, z)$  [see Eq. (2.9)] is quadratic in  $r$ . As described in Sec. II.C, this term is the contribution to the potential energy due to rotation. Suppose that the radial confinement were not provided by rotation through a magnetic field, but rather were provided by an imaginary cylinder of uniform negative charge (to confine a plasma of positive charges). Such a cylinder would produce a radial electric field  $E_r = -2\pi en_- r$  and an electric potential  $\phi_- = \pi en_- r^2$ , where  $n_- = \text{const}$  is the density of the imaginary negative charge. If this density were chosen to have the value  $en_- = m\omega(\Omega_c - \omega)/2\pi e$ , the cylinder of negative charge would provide a potential-energy term,  $e\phi_- = m\omega(\Omega_c - \omega)r^2/2$ , that is identical to the second term in  $e\phi_R$ . Thus the thermal equilibrium density distributions for the two systems would be identical. In the Introduction, we promised to demonstrate the equivalence of the thermal equilibrium states for a magnetically confined single-species plasma and a one-component plasma

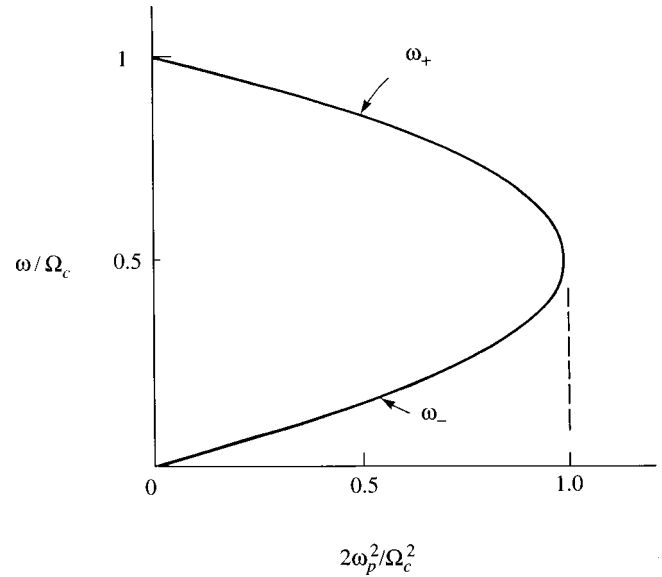


FIG. 7. Plasma rotation frequency as a function of plasma density and magnetic-field strength.

(OCP), and we have here the mean-field version of that demonstration. The equivalence is useful because we know what would happen if we put positive charges into a cylinder of uniform negative charge. Starting at the center of the cylinder, the positive charges would match their density to that of the negative charge, neutralizing the negative charge out to some surface where the supply of positive charges was exhausted. Setting  $n \approx n_-$  and using  $4\pi e^2 n_- = 2m\omega(\Omega_c - \omega)$  immediately reproduces Eq. (3.19).

This equation usually is written as (Davidson, 1990)

$$\omega_p^2 = 2\omega(\Omega_c - \omega), \quad (3.20)$$

where  $\omega_p = (4\pi ne^2/m)^{1/2}$  is the plasma frequency. For given values of the density and magnetic-field strength (or, equivalently, given values of  $\omega_p^2$  and  $\Omega_c$ ), the equation determines two possible rotation frequencies,

$$\omega_{\pm} = \frac{\Omega_c \pm \sqrt{\Omega_c^2 - 2\omega_p^2}}{2}. \quad (3.21)$$

The frequencies are real only if  $2\omega_p^2/\Omega_c^2 \leq 1$  or  $B^2/8\pi \geq mn_- c^2$ . This inequality sets the maximum density that can be confined for a given magnetic-field strength (Brillouin, 1945). In Fig. 7,  $\omega_{\pm}/\Omega_c$  are plotted as a function of  $2\omega_p^2/\Omega_c^2$ ; the solution  $\omega_+$  lies on the upper half of the parabola and the solution  $\omega_-$  on the lower half.

It is important to note that quadratic relation (3.20) is a necessary condition for a solution but not a sufficient condition. Also, the radial confining field  $-\partial(e\phi_R)/\partial r = -\partial e\phi_T/\partial r - m\omega(\Omega_c - \omega)r$  must be negative. Since  $-\partial e\phi_T/\partial r$  is positive,  $\omega(\Omega_c - \omega)$  must be larger than zero. In Sec. III.F, we shall obtain explicit solutions for the case of a quadratic trap potential [see Eq. (3.37)]. For this case,  $-\partial e\phi_T/\partial r$  is given by  $m\omega_z^2 r/2$ , so solutions are possible only for  $\omega_z^2 \leq 2\omega(\Omega_c - \omega)$ . For typical operating conditions  $\omega_z \ll \Omega_c$ , so a thin strip at small  $\omega_p^2 = 2\omega(\Omega_c - \omega)$  is removed from the allowed states in

parabola 7. We shall see in Sec. III.F that at the limit [i.e.,  $\omega_z^2 = 2\omega(\Omega_c - \omega)$ ], the plasma shape becomes a pancake with zero axial extent.

Note that the existence of the two solutions (i.e.,  $\omega_{\pm}$ ) does not contradict our expectations that the total number of particles, total energy, and total canonical angular momentum uniquely determine a thermal equilibrium state. Consider two solutions with the same value for  $\omega_p^2 = 2\omega(\Omega_c - \omega)$ , for  $T$ , and for the total number of particles  $N$ , but with different rotation frequencies  $\omega_+$  and  $\omega_-$  as given by Eq. (3.21). The two solutions have the same density distribution but different velocity distributions. Consequently, the total energy and the total canonical angular momentum are different for the two solutions. In fact, the total canonical angular momentum

$$L = m(\Omega_c/2 - \omega) \int d^3\mathbf{r} n(r, z) r^2 \quad (3.22)$$

differs for the two solutions by a minus sign, since  $(\Omega_c/2 - \omega_+) = -(\Omega_c/2 - \omega_-)$ . In general,  $L$  is positive on the lower half of the parabola where  $\omega < \Omega_c/2$ , is negative on the upper half where  $\omega > \Omega_c/2$ , and vanishes at the Brillouin limit where  $\omega = \Omega_c/2$ . We shall see in Sec. III.F that the rotational state of a pure ion plasma has been varied continuously over all of the allowed states along the parabola by using a laser to continuously vary the total energy and the canonical angular momentum of the plasma.

Further insight into the relation between the two solutions can be obtained by considering the particle dynamics in a frame that rotates with the plasma. In the laboratory frame, the single-particle Hamiltonian is given by

$$h = \frac{p_z^2}{2m} + \frac{p_r^2}{2m} + \frac{(p_\theta - m\Omega_c r^2/2)^2}{2mr^2} + e\phi(r, z). \quad (3.23)$$

A canonical transformation to a frame that rotates with frequency  $-\omega$  yields the Hamiltonian  $h_R = h + \omega p_\theta$ , which can be rewritten as

$$h_R = \frac{p_r^2}{2m} + \frac{p_z^2}{2m} + \frac{[p_\theta - m(\Omega_c - 2\omega)r^2/2]^2}{2mr^2} + [e\phi(r, z) + m\omega(\Omega_c - \omega)r^2/2]. \quad (3.24)$$

The canonical angular momentum  $p_\theta$  is invariant under this canonical transformation. The quantity in square brackets is simply  $(e\phi_R + e\phi_p)$  and so is nearly constant within the plasma. The remaining terms imply cyclotron motion in a uniform magnetic field, but with a cyclotron frequency that is modified from its value in the laboratory frame. The cyclotron frequency in the rotating frame is called the vortex frequency (Davidson, 1990) and is given by  $\Omega_v = \Omega_c - 2\omega$ . Physically, the modification is due to the Coriolis force. For two solutions  $\omega_+$  and  $\omega_-$  as given by Eq. (3.21), the vortex frequencies are equal and opposite—that is, the effective magnetic fields in the two rotating frames are equal and opposite. Other than the reversal in the direction of the field, the particle dynamics (as viewed in the rotating frames) is

the same for the two solutions. We have already noted that the density distributions are the same for the two solutions.

In the rotating frame, the mean velocity vanishes, but individual particles have nonzero velocity because of finite temperature. The cyclotron (or vortex) motion of the particles is characterized by the radius  $r_v = \sqrt{T/m}/\Omega_v$ . This scale length is small compared to the dimensions of the plasma for nearly every state along the parabola. The reason is that  $\lambda_D$  is small compared to the plasma dimensions and  $\sqrt{T/m}/\Omega_c = \lambda_D \omega_p / \Omega_c < \lambda_D$ . However, very near the Brillouin limit (where  $\omega = \Omega_c/2$ ) the vortex frequency vanishes and  $r_v$  becomes infinite. The effective magnetic-field strength in the plasma is zero, and the particles follow straight-line orbits inside the plasma and reflect in the Debye sheath at the plasma edge. Of course, in the sheath the bracket in Hamiltonian (3.24) is not constant.

#### D. Infinitely long column

In this subsection, we obtain the self-consistent potential and density for the simple case of an infinitely long column (O'Neil and Driscoll, 1979; Davidson, 1990). In the next subsection we do the same for a finite-length column of specific dimensions (Prasad and O'Neil, 1979). These solutions corroborate the general character of the self-consistent solutions postulated in the previous subsection, namely, that the plasma density is nearly constant out to some surface of revolution and there drops to zero on the scale of the Debye length.

It is useful to introduce the quantity

$$\begin{aligned} \psi(r, z) = & -\frac{e}{kT} [\phi_R(r, z) + \phi_p(r, z)] \\ & + \frac{e}{kT} [\phi_R(0, 0) + \phi_p(0, 0)]. \end{aligned} \quad (3.25)$$

Density distribution (3.9) then takes the form

$$n(r, z) = n_0 \exp[\psi(r, z)], \quad (3.26)$$

where  $n_0$  is the density at the origin. Poisson's equation can be written as

$$\nabla^2 \psi = \frac{1}{\lambda_D^2} \left[ \exp(\psi) - \frac{2m\omega(\Omega_c - \omega)}{4\pi n_0 e^2} \right], \quad (3.27)$$

where  $\lambda_D^2 = kT/(4\pi n_0 e^2)$  and use has been made of  $\nabla^2 e\phi_R = 2m\omega(\Omega_c - \omega)$ . By introducing the scaled lengths  $\zeta = z/\lambda_D$  and  $\rho = r/\lambda_D$  and defining the parameter

$$\gamma = \frac{2m\omega(\Omega_c - \omega)}{4\pi n_0 e^2} - 1, \quad (3.28)$$

we obtain the convenient form

$$\left( \frac{\partial^2}{\partial \zeta^2} + \frac{1}{\rho} \frac{\partial}{\partial \rho} \rho \frac{\partial}{\partial \rho} \right) \psi = [\exp(\psi) - 1 - \gamma]. \quad (3.29)$$

For an infinitely long column, or for the central region

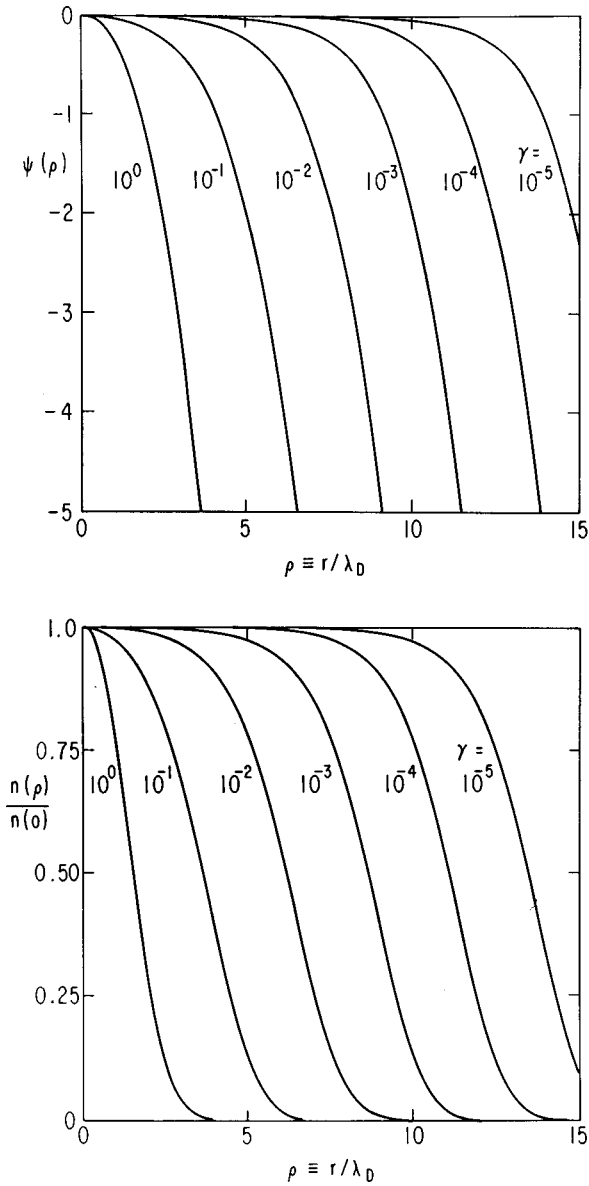


FIG. 8. Self-consistent solutions for  $\psi(\rho)$  and  $n(\rho)/n(0) \equiv \exp[\psi(\rho)]$ , for several values of the parameter  $\gamma$  [see Eq. (3.28)]. From O'Neil and Driscoll (1979).

of a column that is long compared to its radius, we may neglect the  $\zeta$  dependence, so Eq. (3.29) reduces to

$$\frac{1}{\rho} \frac{\partial}{\partial \rho} \rho \frac{\partial \psi}{\partial \rho} = \exp(\psi) - 1 - \gamma. \quad (3.30)$$

The desired solutions  $\psi = \psi(\rho)$  are such that  $\psi(0) = \psi'(0) = 0$ . Note that  $\psi$  is unchanged when  $\phi_p(\rho)$  is shifted by a constant. Consequently, we can always shift  $\phi_p(\rho)$  so that it vanishes on a cylindrical conductor at some large radius.

Figure 8 shows  $\psi(\rho)$  and  $n(\rho)/n_0 = \exp[\psi(\rho)]$  for various values of  $\gamma$ ; these solutions were obtained by numerically integrating Eq. (3.30) out from the origin starting with the conditions  $\psi(0) = \psi'(0) = 0$ . Solutions that imply confinement [i.e.,  $n(\rho) \rightarrow 0$  as  $\rho \rightarrow \infty$ ] are obtained only for  $\gamma > 0$ , and solutions corresponding to a plasma (with small Debye length compared to the width of the

column) are obtained only for  $\gamma \ll 1$ . As we expect, these solutions are such that the density is nearly constant out to the edge of the column and then falls off on the scale of a Debye length. Also note that  $\gamma \ll 1$  implies that Eq. (3.20) is well satisfied.

Some analytic progress can be made in describing these small  $\gamma$  solutions. Interior to the plasma  $|\psi| \ll 1$  so we may use the Taylor expansion  $\exp(\psi) \approx 1 + \psi$  and approximate Eq. (3.30) by the linear equation

$$\frac{1}{\rho} \frac{\partial}{\partial \rho} \rho \frac{\partial \psi}{\partial \rho} - \psi = -\gamma. \quad (3.31)$$

The solution that satisfies the boundary conditions  $\psi(\rho) = \psi'(\rho) = 0$  is given by

$$\psi(\rho) = \gamma[1 - I_0(\rho)], \quad (3.32)$$

where  $I_0(\rho)$  is a Bessel function of imaginary argument. To be specific, let us define the plasma radius  $R_p$  to be the radius where the density drops to  $1/e$  times the central density [i.e.,  $\psi(R_p/\lambda_D) = -1$ ]. Substituting the large  $\rho$  asymptotic expansion  $I_0(\rho) \approx \exp(\rho)/\sqrt{2\pi\rho}$  then yields the relation

$$(2\pi R_p/\lambda_D)^{1/2} \exp[-R_p/\lambda_D] = \gamma. \quad (3.33)$$

For large  $R_p/\lambda_D$ , the falloff in density is a universal function independent of  $\gamma$  except for a shift along the  $\rho$  axis. It is convenient to introduce  $x = \rho - \rho_p$ , where  $\rho_p = R_p/\lambda_D$ . By using  $|x/\rho_p| \ll 1$  and  $\gamma \ll |\psi|$ , we reduce Eq. (3.30) to the form

$$\frac{d^2 \psi}{dx^2} = e^\psi - 1. \quad (3.34)$$

Multiplying by  $d\psi/dx$  and integrating yields

$$\frac{1}{2} \left( \frac{d\psi}{dx} \right)^2 = e^\psi - \psi + A. \quad (3.35)$$

Using the boundary condition  $\psi, d\psi/dx \rightarrow 0$  as  $x \rightarrow -\infty$  allows us to evaluate the constant of integration,  $A = -1$ . A second integral is given by

$$\int_{-1}^{\psi} \frac{d\psi'}{\sqrt{\exp(\psi') - \psi' - 1}} = -\sqrt{2}x, \quad (3.36)$$

where we have used  $\psi(x=0) = -1$ . The final quadrature can be performed numerically, and Fig. 9 shows this solution plotted as a function of  $\rho$ .

### E. Finite-length column

In this subsection, we discuss the self-consistent potentials for a plasma column that is confined in an apparatus of the form shown in Fig. 1 (Prasad and O'Neil, 1979). Suppose that the radius of the cylindrical conductors is  $R$ , that the length of the central conductor is  $L$ , and that the two end conductors are each much longer than  $R$ . Suppose further that the central conductor is grounded and that the two end conductors are held at some positive potential  $V$ . At a distance of a few times  $R$  into the end conductors, the potential has, to good approximation, the constant value  $V$  over the whole



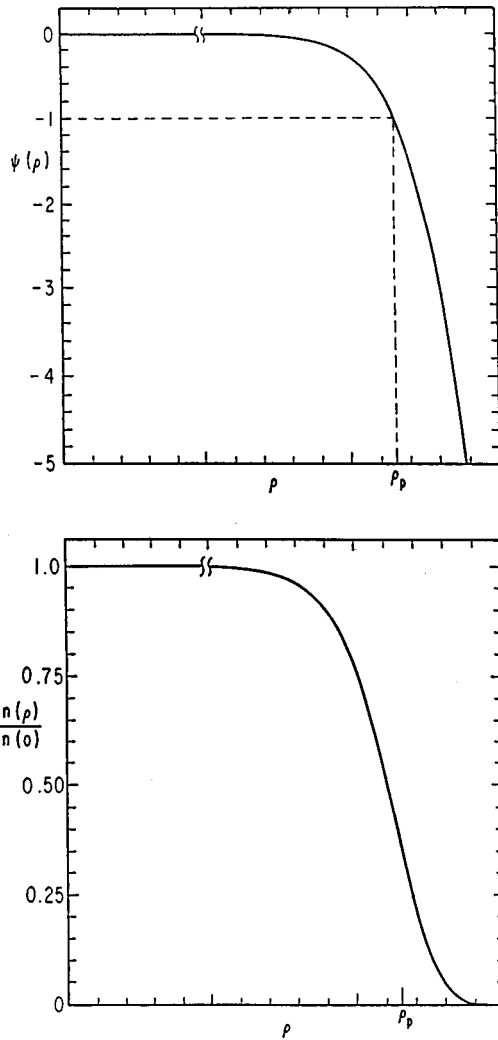


FIG. 9. Self-consistent solutions for  $\psi(\rho)$  and  $n(\rho)/n(0) \equiv \exp[\psi(\rho)]$  in the limit  $\gamma \rightarrow 0$ . From Prasad and O'Neil (1979).

cross section, so one can imagine that the end cylinders are enclosed with conducting end caps.

The scaling that leads to Eq. (3.29) reduces to four the number of parameters on which the solution depends:  $\gamma$ ,  $eV/kT$ ,  $R/\lambda_D$ , and  $L/\lambda_D$ . For small  $\gamma$ , the numerical solutions of Eq. (3.29) exhibit the general features described in Sec. III.B; the density is nearly constant out to a surface of revolution and there falls off on the scale of the Debye length.

The curve  $\psi(\rho, \zeta) = -1$  lies in the surface layer where the density falls off. At any point along this curve, we can introduce a rectangular coordinate system  $(u, v)$ , where the  $u$  axis is tangent to the curve and the  $v$  axis is normal to the curve. For small  $\gamma$ , the radius of curvature of the  $\psi = -1$  curve is typically much larger than unity, that is, much larger than the Debye length in unscaled variables. Consequently, Eq. (3.29) can be approximated by  $\partial^2 \psi / \partial v^2 = \exp(\psi) - 1$ , and the falloff in density (i.e.,  $n(v) = n(0,0) \exp[\psi(v)]$ ) is very nearly of the form shown in Fig. 9. As an example, consider the case  $\gamma = 0.0003$ ,  $eV/kT = 100$ ,  $R/\lambda_D = 16$ , and  $L/\lambda_D = 64$ . Figure 10 shows the  $\psi(\rho, \zeta) = -1$  curve with local coordinate systems attached at the points  $a$ ,  $b$ , and  $c$ . Figure 11

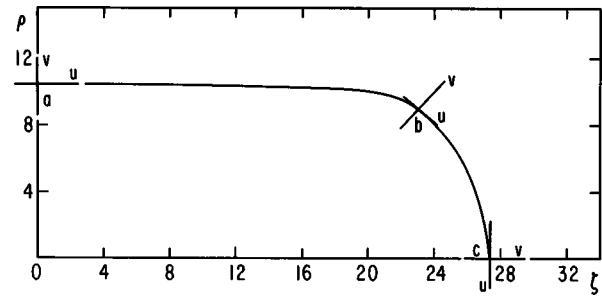


FIG. 10. The curve  $\psi(\rho, \zeta) = -1$  for the case  $\gamma = 0.0003$ ,  $eV/kT = 100$ ,  $\rho_c = 16$ , and  $\zeta_c = 64$ .  $a$ ,  $b$ , and  $c$  are three points where local orthogonal coordinate systems  $(u, v)$  are introduced. From Prasad and O'Neil (1979).

shows a comparison between the numerical result for  $\psi$  plotted as a function of the local variable  $v$  [i.e.,  $\psi(v)$ ] and the solution for  $\psi$  shown in Fig. 9; the solid curve is from Fig. 9, and the circles, triangles, and crosses are numerical values of  $\psi(v)$  along the  $v$  axis in the local coordinate systems at  $a$ ,  $b$ , and  $c$ .

This picture implicitly assumes that the potential applied to end conductors is large enough to provide good confinement. When the applied potential is only slightly larger than the potential at the center of the plasma [i.e.,  $eV - e\phi(0,0) \approx (\text{few})kT$ ], a long finger of plasma can extend into the region of the end cylinder (Peurrung and Fajans, 1990). The transverse dimensions of this finger may not be large compared to the Debye length, even though the overall solution corresponds to small  $\gamma$ .

#### F. Small spheroidal plasmas

For many experiments, the plasma is small compared to the dimensions of the trap and resides in a nearly quadratic potential well. In general, the thermal equilibrium shape of such a plasma is a uniform-density spheroid, that is, an ellipse of revolution (Bollinger and Wineland, 1984; Turner, 1987; Brewer *et al.*, 1988; Bollinger, Wineland, and Dubin, 1994). We assume here that the Debye length is negligibly small compared to the dimensions of the plasma.

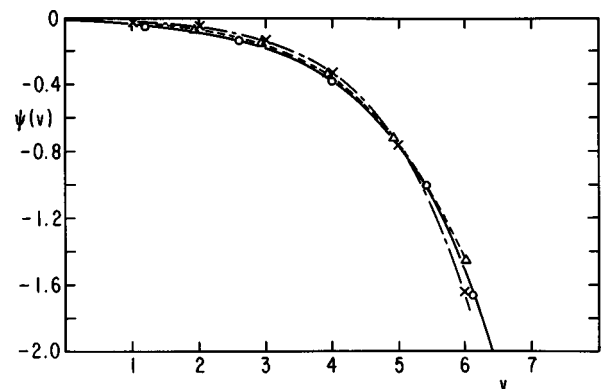


FIG. 11. Comparison of the falloff of  $\psi(v)$  at the points  $a$  (circles),  $b$  (triangles), and  $c$  (crosses) of Fig. 10. The solid curve is  $\psi(\rho)$  from Fig. 9. From Prasad and O'Neil (1979).



Near the center of a trap, one expects (by Taylor expansion) that the trap potential is approximately quadratic:

$$e\phi_T \approx \frac{m\omega_z^2}{2} (z^2 - r^2/2) + C. \quad (3.37)$$

Here,  $\omega_z^2$  and  $C$  are constants, and it is assumed that equal potentials are applied to the two end conductors. The value of  $\omega_z^2$  is proportional to the value of the applied potential; also,  $\omega_z$  can be interpreted as the oscillation frequency of a single particle in small-amplitude motion along the magnetic field (axial motion). The coefficient of  $r^2$  relative to that of  $z^2$  is determined by the requirement  $\nabla^2\phi_T=0$ .

For the case in which only a small number of particles are confined, the simple harmonic axial motion serves as a useful diagnostic and manipulative tool through resonant interaction with an external circuit (Brown and Gabrielse, 1986), so some traps are designed to make the quadratic approximation much better than would in general be expected. For example, Fig. 2 shows a trap for which the conducting electrodes are hyperbolas of revolution. Since the equipotential surfaces for the quadratic potential [i.e.,  $z^2 - r^2/2 = \text{const}$ ] define hyperbolas of revolution, a trap for which the hyperbolas extended to infinity would produce an exactly quadratic potential. In practice, the hyperbolas are truncated, as shown in Fig. 2, so the quadratic form is only an approximation, though it is very good over a substantial region near the center of the trap. If the equation defining the end electrodes is  $z^2 - r^2/2 = z_0^2$ , the equation defining the center ring electrode is  $z^2 - r^2/2 = -r_0^2/2$ , and the potential difference between end and center electrodes is  $V_0$ , the axial oscillation frequency is given by

$$eV_0 = \frac{m\omega_z^2}{2} (z_0^2 + r_0^2/2). \quad (3.38)$$

Even for a trap with cylindrical electrodes, it is possible to achieve a potential that is nearly quadratic over a substantial region (Brown and Gabrielse, 1986). This is accomplished by choosing the lengths of the various cylinders so that the quartic term in the Taylor series vanishes; the cubic and quintic terms vanish by symmetry.

Adding  $m\omega(\Omega_c - \omega)r^2/2$  to  $\phi_T$  yields the effective trap potential in the rotating frame

$$e\phi_R(r, z) = \frac{m\omega_z^2}{2} (z^2 + \beta r^2) + C, \quad (3.39)$$

which is also quadratic. The parameter  $\beta$  is defined as

$$\beta = \frac{\omega(\Omega_c - \omega)}{\omega_z^2} - \frac{1}{2} = \frac{1}{4} \frac{(\Omega_c^2 - \Omega_v^2)}{\omega_z^2} - \frac{1}{2}. \quad (3.40)$$

This parameter determines the symmetry of the effective trap potential and hence the shape of the plasma. For example, when  $\beta=1$  the plasma is spherically symmetric, whereas for  $\beta \gg 1$  the plasma is squeezed into a line along the  $z$  axis, and for  $\beta \rightarrow 0$  the plasma is a flat 2D pancake in the  $x$ - $y$  plane.

As mentioned earlier, not all frequencies in Fig. 7 represent allowed states; it is necessary that the radial confining field,  $-\partial(e\phi_R)/\partial r$ , be negative. In the notation used here, this is the requirement that  $\beta > 0$ , which can be rewritten as  $\omega_z^2 < 2\omega(\Omega_c - \omega)$ . Thus radial confinement in a quadratic trap potential is possible only when the rotation frequency is in the range  $\omega_m < \omega < \Omega_c - \omega_m$ , where  $\omega_m \equiv \Omega_c/2 - [(\Omega_c/2)^2 - \omega_z^2/2]^{1/2}$  is the magnetron frequency (drift frequency) for a single charge alone in the trap (Brown and Gabrielse, 1986). Note that the allowed frequency range shrinks to zero (i.e.,  $\omega_m \rightarrow \Omega_c/2$ ) when  $\omega_z$  approaches  $\Omega_c/\sqrt{2}$ . In this case, the radial electric field of the trap [i.e.,  $-\partial\phi_T/\partial r = (m/e)\omega_z^2 r/2$ ] is so large that radial force balance cannot be achieved; even a single charge cannot be confined.

The condition  $\omega_z^2 < 2\omega(\Omega_c - \omega)$  together with Eq. (3.20) implies a lower limit on the plasma density, that is,  $\omega_z < \omega_p$ . At first this may seem puzzling, but it must be remembered that Eq. (3.20) assumes that the Debye length is small compared to the dimensions of the plasma. We shall see shortly that the plasma assumes the shape of an infinitesimally thin disc as  $\omega_p^2 = 2\omega(\Omega_c - \omega)$  approaches  $\omega_z^2$ . Of course, before the limit is reached, the Debye length ceases to be small compared to the plasma thickness, and at that point there is no longer a requirement that  $\omega_p > \omega_z$  (Paulson and Spencer, 1998).

The quadratic form of  $\phi_R(r, z)$  allows one to determine analytically the shape of the plasma in the limit that the Debye length is small compared to the plasma size (Bollinger and Wineland, 1984; Turner, 1987; Brewer *et al.*, 1988; Bollinger, Wineland, and Dubin, 1994). As discussed earlier, the plasma charges adjust their positions in this limit so that  $e\phi_R + e\phi_p$  is constant inside the plasma. Thus the plasma space-charge potential must be quadratic within the plasma. It is well known that a uniformly charged spheroid (ellipse of revolution) in free space produces an interior potential that is quadratic in  $r$  and  $z$  and an exterior potential that approaches zero at infinity (Landau and Lifshitz, 1960). Here, the plasma dimensions are small compared to the distance to the walls, so the boundary condition that  $\phi_p = 0$  on the conducting walls reduces approximately to the condition that  $\phi_p$  approaches zero at infinity. Thus the bounding surface of the plasma is a spheroid. By writing down the potential due to a uniformly charged spheroid and comparing the coefficients of  $r^2$  and of  $z^2$  to the corresponding coefficients in  $-\phi_R$ , we obtain the relations

$$g(\alpha) = \frac{1}{2\beta + 1}, \quad (3.41)$$

$$\frac{\omega_p^2}{\omega_z^2} = 2\beta + 1, \quad (3.42)$$

where  $\alpha = Z_p/R_p$  is the aspect ratio (shape) of the spheroid,  $2R_p$  is the spheroid diameter, and  $2Z_p$  is the length. Equation (3.42) is equivalent to Eq. (3.20), and the function  $g(\alpha)$  is given by

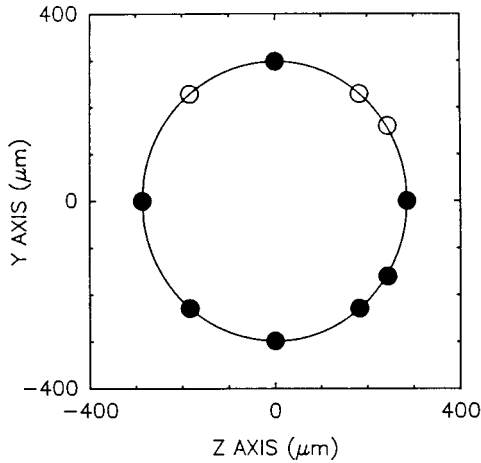


FIG. 12. Comparison of shape of a 5000  ${}^9\text{Be}^+$  ion plasma to an ellipse. The data points indicated by solid circles were measured and those indicated by open circles were inferred by assuming symmetry about the axis of rotation ( $z$  axis). The ellipse was determined from the end points along the  $y$  and  $z$  axis. From Brewer *et al.* (1988).

$$g(\alpha) = Q_1^0(\alpha/\sqrt{\alpha^2-1})/(\alpha^2-1), \quad (3.43)$$

where  $Q_1^0$  is an associated Legendre function of the second kind. The aspect ratio  $\alpha$  is a monotonically increasing function of  $\beta$ , as one would expect on the basis of the physical arguments following Eq. (3.40).

This is a useful place to compare again to experiment. The  ${}^9\text{Be}^+$  plasmas that were discussed in Sec. III.B.2 (Brewer *et al.*, 1988) were small compared to the trap dimensions, and the plasmas resided in a nearly quadratic trap potential. The plasmas were not weakly correlated (i.e.,  $\Gamma \sim 1-10$ ), but we still expect the gross plasma shape to be described by the mean-field analysis given here. Even for strongly correlated plasmas, the mean-field energy typically is much larger than the correlation energy (i.e.,  $e\phi_p \gg e^2/a$ ), so the gross plasma shape and density are substantially determined by a balance of mean-field forces, that is, by requirement (3.18). The correlations simply establish order within that shape.

The shape of the plasma was determined experimentally by measuring the decrease in scattered light for different positions of the probe beam. Figure 12 shows a comparison of measured boundary points and an ellipse that was fitted to the end points along the  $y$  and  $z$  axes. The plasma consisted of 5000  ${}^9\text{Be}^+$  ions at a density of  $4.7 \times 10^7 \text{ cm}^{-3}$ . Figure 13 shows a test of the relationship  $g(Z_p/R_p) = \omega_z^2/2\omega(\Omega_c - \omega)$ , which follows from Eqs. (3.40) and (3.41). The solid curve is a plot of  $g(Z_p/R_p)$ , and the squares, triangles, and circles are measurements taken with different plasma clouds ( $N \sim 2000$  to 40 000  ${}^9\text{Be}^+$  ions) and different trap parameters. The agreement is quite good.

In more recent but as yet unpublished results, Huang, Tan, Bollinger, and Wineland simply imaged the fluorescence from the laser-excited atoms. Figure 14 shows a side-view picture of a small plasma ( $N \approx 8 \times 10^4$   ${}^9\text{Be}^+$  ions) in a quadratic trap potential together with a fit to

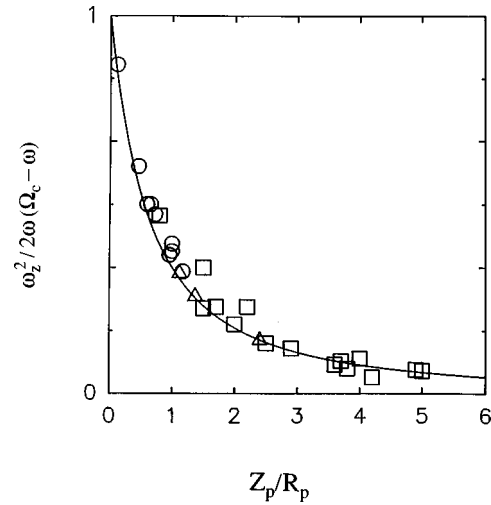


FIG. 13. Experimental test of the expected relationship  $g(Z_p/R_p) = \omega_z^2/2\omega(\Omega_c - \omega)$  [see Eqs. (3.40) and (3.41)]. The solid curve is a plot of  $g(Z_p/R_p)$  and the squares, triangles, and circles are measurements taken with different plasmas ( $N \sim 2000-40\,000$   ${}^9\text{Be}^+$  ions). From Brewer *et al.* (1988).

an ellipse. The aspect ratio as determined from the fitted ellipse is  $\alpha = 1.763$ , which agrees to better than 1% with the aspect ratio  $\alpha = 1.75$  predicted from Eqs. (3.40), (3.41), and (3.42) for the independently determined frequencies  $\omega_z/2\pi = 795 \text{ kHz}$ ,  $\Omega_c/2\pi = 7.608 \text{ MHz}$ , and  $\omega/2\pi = 213.7 \text{ kHz}$ . The ions in this cloud had the microscopic order of a crystal (see Sec. IV), and the rotation frequency was determined by measuring the rotation frequency of a Bragg scattering pattern.

Because a spheroid is a simple analytically tractable shape, the integral expressions for total particle number and total canonical angular momentum and energy in the laboratory frame can be evaluated easily:

$$N = \frac{4}{3} \pi n Z_p R_p^2, \quad (3.44)$$

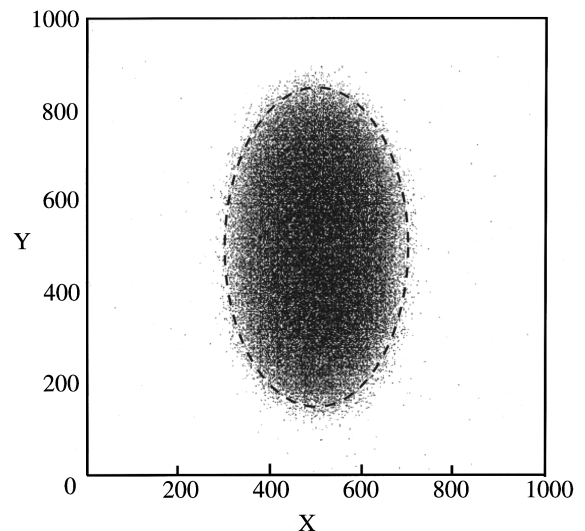


FIG. 14. Side view of  ${}^9\text{Be}^+$  plasma, together with fitted ellipse (the dashed line).

$$L = \frac{1}{5} Nm \Omega_v R_p^2, \quad (3.45)$$

$$E = \frac{1}{10} Nm [2(\omega_p^2 + \omega^2) R_p^2 + 3\omega_z^2 (Z_p^2 - R_p^2)] + NC, \quad (3.46)$$

where  $\Omega_v = \Omega_c - 2\omega$  is the vortex frequency. In the rotating frame the energy  $E_R$  is related to  $E$  and  $L$  via Eq. (2.6):

$$E_R = \frac{3}{10} Nm \omega_z^2 [2\beta R_p^2 + Z_p^2] + NC. \quad (3.47)$$

There are no temperature corrections, since this whole discussion assumes that the Debye length (and temperature) are negligibly small.

Equations (3.44) and (3.45), together with Eqs. (3.41) and (3.42), determine the plasma state ( $n$ ,  $Z_p$ ,  $R_p$ , and  $\omega$ ) in terms of the trap parameters  $\omega_z$  and  $\Omega_c$  and the constants of the motion  $N$  and  $L$ . Equation (3.46) is not needed to determine the plasma state; for a given state this equation determines the value of  $E$  such that the temperature is zero. To simplify the algebra we scale frequencies by  $\omega_z$ :  $\hat{\Omega}_v = \Omega_v / \omega_z$ ,  $\hat{\omega} = \omega / \omega_z$ , and  $\hat{\Omega}_c = \Omega_c / \omega_z$ , and we introduce a scale length  $a_0 \equiv (e^2 / m \omega_z^2)^{1/3}$ . This scale length is equal to the Wigner-Seitz radius  $a$  when the plasma is spherically symmetric. Then Eqs. (3.44) and (3.45) become

$$\hat{R}_p^3 = \left( \frac{R_p}{a_0} \right)^3 = \frac{3}{2\beta + 1} \frac{N}{\alpha(\beta)}, \quad (3.48)$$

$$\hat{L} \equiv \frac{L}{m N a_0^2 \omega_z} = \frac{1}{5} \left( \frac{R_p}{a_0} \right)^2 \hat{\Omega}_v, \quad (3.49)$$

where  $\alpha(\beta)$  is given by Eq. (3.41).

Now,  $\beta$  is a symmetric quadratic function of  $\hat{\Omega}_v$  [see Eq. (3.40)], taking on its maximum value,  $\beta_B = (1/4)\hat{\Omega}_c^2 - 1/2$ , at the Brillouin limit where  $\hat{\Omega}_v = 0$ . Thus Eq. (3.48) implies that the scaled plasma radius  $\hat{R}_p$  is also symmetric in  $\hat{\Omega}_v$ , taking on its minimum value  $\hat{R}_B$  at the Brillouin limit (recall that the aspect ratio  $\alpha$  is a monotonically increasing function of  $\beta$ ). Equation (3.49) then implies that  $L$  is an antisymmetric and monotonically increasing function of  $\hat{\Omega}_v$ , taking on positive values in the lower half of the parabola of Fig. 7 and negative values in the upper half. The inverse of this relation therefore exists and yields the required relation between  $\hat{\Omega}_v$  and the parameters  $N$ ,  $L$ ,  $\omega_z$ , and  $\Omega_c$ .  $\hat{\Omega}_v = \hat{\Omega}_v(\hat{L}, \hat{\Omega}_c)$ , or alternatively  $\hat{\omega} = \hat{\omega}(\hat{L}, \hat{\Omega}_c)$ . This value for  $\hat{\omega}$  can then be employed to determine  $R_p/a_0$ ,  $Z_p/a_0$ , and  $n$  using Eqs. (3.40), (3.41), (3.42), and (3.48).

This analysis is relevant to a series of experiments in which a small plasma of  ${}^9\text{Be}^+$  ions in a quadratic trap potential was made to evolve through a sequence of thermal equilibrium states by the application of laser cooling and laser torque beams (Bollinger *et al.*, 1995). The cooling beam passed through the rotational axis of the plasma and was tuned 10–50 MHz below the reso-

nance frequency of a  ${}^9\text{Be}^+$  ion at rest. The torque beam was displaced substantially off the rotational axis so that it could act with a large lever arm and exert a large torque, which tended to increase  $\omega$ . The frequency of the torque beam,  $\omega_T/2\pi$ , was adjusted from 0 to 1500 MHz above  $\omega_0/2\pi$  to compensate for the Doppler shift associated with the rotational motion. To measure the plasma rotation frequency accurately, microwaves were used to drive the electron spin-flip transition  $(+3/2, +1/2) \rightarrow (+3/2, -1/2)$  of the  ${}^9\text{Be}^+$  ground state. A decrease in fluorescence was observed when the microwave frequency  $\omega_s$  or the motional sideband frequency  $\omega_s \pm \omega$  fell within the resonance width of the spin-flip transition. The sidebands enter because the rotating ions see the microwave field as modulated at the rotation frequency. By using this technique, the rotation frequency was determined to an accuracy of a few kHz.

By use of the cooling and torque lasers to control the total energy and canonical angular momentum of the plasma, the plasma rotation frequency was varied continuously over the full range of allowed frequencies,  $\omega = \omega_m$  to  $\omega = \Omega_c - \omega_m$ . The torque laser changed the angular momentum of the plasma and also did work on the plasma, since the torque was applied to a rotating plasma. As the plasma evolved, this work appeared as a change in the electrostatic energy, kinetic energy of rotation, and heat, but the cooling laser was able to remove the heat fast enough that the temperature (and Debye length) remained small. Thus the conditions of the experiment match the assumptions used in our theoretical discussion.

From that discussion we can predict the plasma evolution as a function of  $L$ . The plasma starts off in a state with large and positive  $L$  and, correspondingly, with small rotation frequency, density, and aspect ratio (i.e.,  $\omega \approx \omega_m$ ,  $\omega_p \approx \omega_z$ , and  $\alpha \approx 0$ ). As  $L$  is decreased, the rotation frequency, density, and aspect ratio all increase. When  $L$  passes through zero, the rotation frequency is  $\omega = \Omega_c/2$  and the density and aspect ratio reach their maximum values [ $\omega_p = \Omega_c/\sqrt{2}$  and  $\alpha = g^{-1}(2\omega_z^2/\Omega_c^2)$ ]. As  $L$  becomes progressively more negative, the frequency continues to increase, but the density and aspect ratio decrease. For large and negative  $L$ , the frequency approaches the upper limit  $\Omega_c - \omega_m$  and the density and aspect ratio again approach their minimum values ( $\omega_p = \omega_z$  and  $\alpha \approx 0$ ).

As a specific check on the theory, Fig. 15, taken from Bollinger *et al.* (1995), shows a plot of  $R_p/R_B$  versus  $\omega/\Omega_c = [1 - \hat{\Omega}_v/\hat{\Omega}_c]/2$ , as given by Eq. (3.48) for the case  $\hat{\Omega}_c = 6.62$ . The points are measurements of  $R_p/R_B$  versus  $\omega/\Omega_c$ , and one can see that the agreement with theory is quite good.

It is interesting to note that a continuously negative torque makes the plasma contract radially for  $\omega < \Omega_c/2$  and expand radially for  $\omega > \Omega_c/2$ . Intuitively, we can think of the radial transport as a radial drift that is produced by an azimuthal force. The sign of the azimuthal force remains constant, but the direction of the drift reverses at  $\omega = \Omega_c/2$  because the direction of the effective

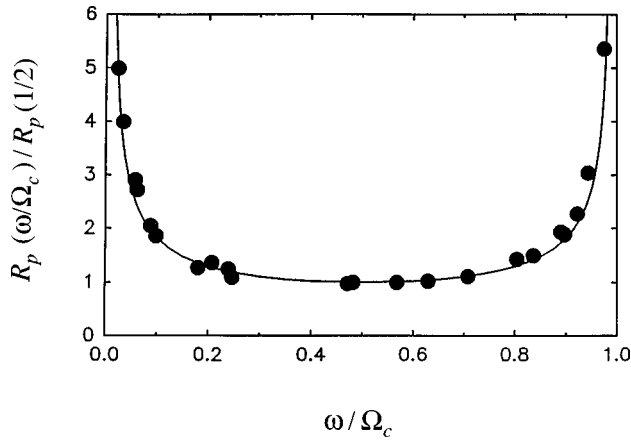


FIG. 15. Radius of a  $2000\text{ }^9\text{Be}^+$  ion plasma as a function of rotation frequency. The radius is scaled to the radius at the Brillouin limit and the rotation frequency to the cyclotron frequency. The solid curve is the theoretical prediction with no adjustable parameters. From Bollinger *et al.* (1995).

magnetic field (in the rotating frame of the plasma) reverses at  $\omega = \Omega_c/2$ . Recall that the effective cyclotron frequency in the rotating frame of the plasma is the vortex frequency  $\Omega_v = \Omega_c - 2\omega$ .

### G. Centrifugal separation

A plasma with a single sign of charge need not be a single-species plasma. For a many-species plasma, the thermal equilibrium density distribution for species  $j$  can be written as

$$n_j(r, z) = n_{j0} \exp[\psi_j(r, z)], \quad (3.50)$$

where

$$\psi_j(r, z) = \frac{-e_j}{kT} \left[ \phi(r, z) - \phi(0, 0) + \frac{\omega B r^2}{2c} - \frac{m_j}{e_j} \frac{\omega^2 r^2}{2} \right]. \quad (3.51)$$

In general, the density distribution for species  $j$  differs from that for species  $i$  if  $e_i \neq e_j$  or if  $m_j/e_j \neq m_i/e_i$ . We refer to the difference produced by  $e_i \neq e_j$  as charge difference separation and that produced by  $m_j/e_j \neq m_i/e_i$  as centrifugal separation.

To explore the distinction between these two effects, it is useful to consider the simple case in which species  $j=1$  is dominant and forms a plasma that is many Debye lengths across, and species  $j=2$  is a trace admixture that makes a negligible contribution to the electric potential  $\phi(r, z)$ . From Eq. (3.51) we obtain

$$\psi_2 = \frac{e_2}{e_1} \psi_1 + \frac{e_2}{kT} \left( \frac{m_2}{e_2} - \frac{m_1}{e_1} \right) \frac{\omega^2 r^2}{2}. \quad (3.52)$$

Under the conditions postulated,  $|\psi_1(r, z)|$  is exponentially small throughout the plasma interior and rises to order unity in a thin (Debye-scale) shell at the surface. Charge difference separation, which is due to the first term in Eq. (3.52), can be significant only in this thin shell and plays no role in the limit of zero Debye length. In contrast, centrifugal separation, which is due to the

second term in Eq. (3.52), can be significant throughout the plasma and becomes particularly important in the limit of small temperature (small Debye length).

The transport mechanism that brings about the separation is easy to understand. Because of the centrifugal force, two ions that are at the same radial position but have different charge-to-mass ratios rotate about the plasma axis at different rates. The collisional drag between two species gives rise to a radial drift of one species outward and the other inward. Because the Coulomb interaction is long range, we expect that the drag can be exerted even over a small gap between the species, producing complete separation.

In what follows, we go to the limit of zero Debye length, so the charge-difference separation plays no role, and, as we shall see, the centrifugal separation is complete. The simple case of an infinitely long column can be treated analytically (O'Neil, 1981). To be specific, we choose  $m_{j+1}/e_{j+1} > m_j/e_j$ . Species  $j$  then forms a ring that extends from  $r=a_j$  to  $r=b_j$ , where  $b_j < a_{j+1}$ . Of course, the innermost species forms a central column (i.e.,  $a_1=0$ ). In the limit of zero Debye length, it is necessary that

$$\phi(r) + \frac{\omega B r^2}{2c} - \frac{m_j}{e_j} \frac{\omega^2 r^2}{2} \approx \text{const} \quad (3.53)$$

inside the ring occupied by species  $j$  (i.e., for  $a_j < r < b_j$ ). In this region, only species  $j$  makes a significant contribution to the charge density, so we can set

$$\nabla^2 \phi = -4\pi e_j n_j(r). \quad (3.54)$$

Operating on Eq. (3.53) with  $\nabla^2$  and using Poisson's equation then implies that the density of species  $j$  is nearly constant within the ring

$$n_j(r) \approx n_j = \frac{2m_j\omega(\Omega_j - \omega)}{4\pi e_j^2}. \quad (3.55)$$

For finite but small temperatures, we would find that the rise in density near  $r=a_j$  and the drop in density near  $r=b_j$  occurs on the scale of a few Debye lengths  $\lambda_{D,j} = (kT/4\pi e_j^2 n_j)^{1/2}$ . Outside the ring—that is, well beyond the Debye-sheath regions at the edges—the density of species  $j$  would be exponentially small. Thus the criterion for complete separation is simply that the Debye lengths for two neighboring species be small compared to the gap between the species (i.e.,  $\lambda_{D,j}, \lambda_{D,j+1} \ll a_{j+1} - b_j$ ). Indeed this is the criterion for the validity of this treatment.

Over most of a gap, the potential satisfies Laplace's equation, so it follows that

$$a_{j+1} \left. \frac{d\phi}{dr} \right|_{a_{j+1}} = b_j \left. \frac{d\phi}{dr} \right|_{b_j}. \quad (3.56)$$

Operating on Eq. (3.53) with  $r d/dr$  and evaluating the result at  $r=a_{j+1}$  and at  $r=b_j$  yields two equations, which when combined with Eq. (3.56) yield a relation that determines the width of the gap,

$$a_{j+1}^2 - b_j^2 = \frac{e_{j+1}(m_{j+1}/e_{j+1} - m_j/e_j)\omega^2 b_j^2}{m_{j+1}\omega(\Omega_{j+1} - \omega)}. \quad (3.57)$$

If there are  $M$  species ( $j=1, \dots, M$ ), then  $3M+1$  relations are necessary to determine all of the parameters  $a_j$ ,  $b_j$ ,  $n_j$ , and  $\omega$ . These are the  $M$  relations given by Eq. (3.55), the  $M-1$  relations given by Eq. (3.57) plus the condition  $a_1=0$ , the  $M$  relations that specify the number of particles per unit length for each of the species

$$\frac{N_j}{L} = n_j \pi (b_j^2 - a_j^2), \quad (3.58)$$

and the relation that specifies the total canonical angular momentum per unit length,

$$\frac{P_\theta}{L} = \sum_j m_j (-\omega + \Omega_c/2) n_j \pi (b_j^4 - a_j^4)/4. \quad (3.59)$$

Centrifugal separation has been observed experimentally (Larson *et al.*, 1986; Imajo *et al.*, 1997). The experiments by Larson *et al.* were carried out with a plasma of  $\text{Be}^+$  and  $\text{Hg}^+$  ions that were confined in a Penning trap with a parabolic potential. Figure 16(a) shows the measured shape of a small  $\text{Be}^+$  plasma before and after the addition of  $\text{Hg}^+$  ions, and Fig. 16(b) shows the same thing for a larger plasma. Figure 16(c) shows the results of a numerical calculation of the plasma shape assuming zero Debye length and numbers of  $\text{Be}^+$  and  $\text{Hg}^+$  ions that correspond to the experiment of Fig. 16(a). The theory predicts complete separation, but this could not be checked experimentally because of the orientation of the probe laser. A later experiment (Wineland, Weimer, and Bollinger, 1993) did observe complete centrifugal separation of the  $\text{Be}^+$ - $\text{Mg}^+$  plasma. The experiments of Imajo *et al.* observed complete separation in a plasma of  $\text{Be}^+$  and  $\text{Cd}^+$  ions.

## H. Generalization of the confinement geometry

Thus far we have assumed that the trap and trap fields are time independent and cylindrically symmetrical and that the magnetic field is uniform and axial. However, these are not the most general assumptions that are consistent with confinement in a state of thermal equilibrium and with the confinement theorem of Sec. II.C.

### 1. Inhomogeneous but cylindrically symmetric magnetic field

An obvious generalization is that the magnetic field need not be homogeneous so long as it is cylindrically symmetrical. To include this generalization, we need only set  $A_\theta = A_\theta(r, z)$  in the previous results. By using  $\oint \mathbf{A} \cdot d\mathbf{l} = \iint \mathbf{B} \cdot d\mathbf{S}$ , we obtain

$$2\pi r A_\theta(r, z) = \int_0^r 2\pi r' dr' B_z(r', z) = \Phi(r, z), \quad (3.60)$$

where  $\Phi(r, z)$  is the magnetic flux through a circle of radius  $r$  at axial location  $z$ . In the effective trap potential in the rotating frame [see Eq. (2.9)], we must replace  $m\omega\Omega_c r^2/2 = (e\omega/c)A_\theta(r)r$  by  $(e\omega/2\pi c)\Phi(r, z)$ . The result is

$$e\phi_R(r, z) = e\phi_T(r, z) + \frac{e\omega}{2\pi c} \Phi(r, z) - \frac{m\omega^2 r^2}{2}. \quad (3.61)$$

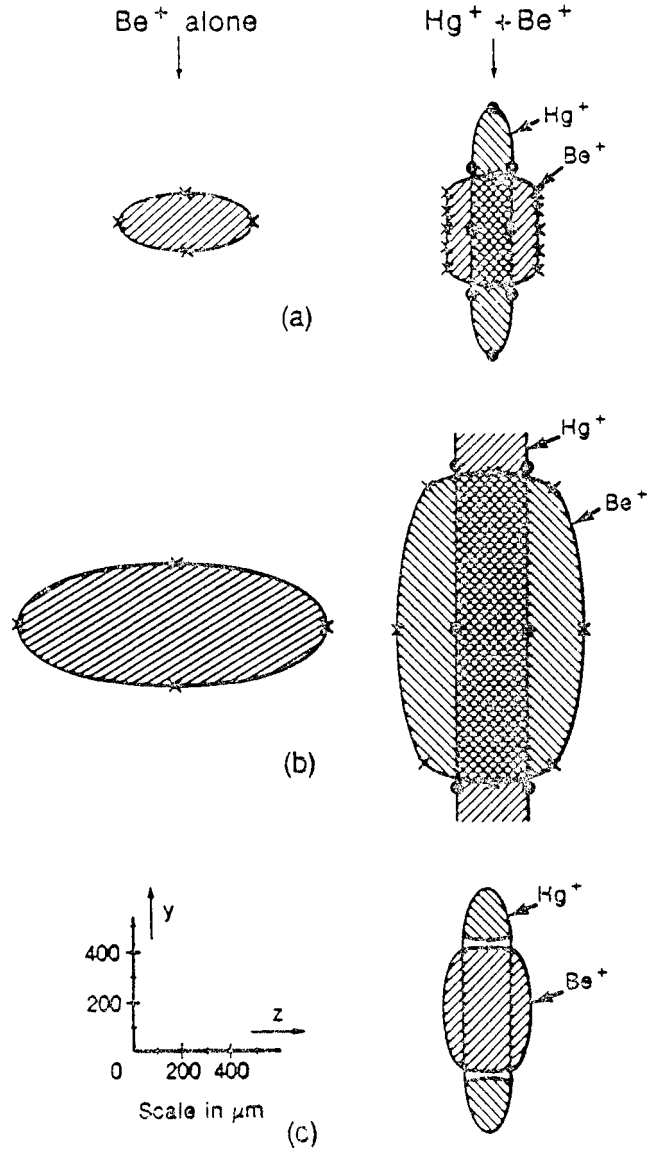


FIG. 16. Experimental observation of centrifugal separation for a  $\text{Be}^+$  and  $\text{Hg}^+$  ion plasma: (a) the measured shape of an 800  $\text{Be}^+$  ion plasma with and without the addition of  $\text{Hg}^+$  ions; (b) the same measurements for a 12 000  $\text{Be}^+$  ion plasma and a  $\text{Hg}^+$  plasma that extends beyond the visibility aperture; (c) the theoretically predicted shapes for conditions in (a). From Larson *et al.* (1986).

This generalized trap potential can be used in the confinement theorem of Sec. II.C and in the thermal equilibrium distribution [Eq. (3.9)].

If the Debye length is small, we again expect the plasma charges to adjust their positions so that Eq. (3.18) is satisfied within the plasma. From this equation and Eqs. (3.17) and (3.61), we obtain

$$4\pi e^2 n(r, z) = -\nabla^2 e\phi_p = \nabla^2 e\phi_R = -2m\omega^2 + \frac{e\omega}{2\pi c} \nabla^2 \Phi, \quad (3.62)$$

where we have used  $\nabla^2 \phi_T = 0$ . Equation (3.62) is the generalization of Eq. (3.19). By using the relations

$$\begin{aligned}\frac{\partial \Phi}{\partial r} &= 2\pi r B_z(r, z), & \frac{\partial \Phi}{\partial z} &= -2\pi r B_r(r, z) \\ 0 &= (\nabla \times \mathbf{B})_\theta = \frac{\partial B_r}{\partial z} - \frac{\partial B_z}{\partial r},\end{aligned}\quad (3.63)$$

we find that

$$\nabla^2 \Phi = 4\pi B_z(r, z). \quad (3.64)$$

Thus Eq. (3.62) reduces to (Turner, 1991)

$$\omega_p^2(r, z) = -2\omega^2 + \frac{2\omega e}{mc} B_z(r, z), \quad (3.65)$$

which is the same as Eq. (3.20) except that  $B_z(r, z)$  has replaced  $B$ . Of course, the density (and  $\omega_p^2$ ) here are functions of  $(r, z)$ . The right-hand side of Eq. (3.65) can be written as  $\omega_{p-}^2(r, z) = 4\pi e^2 n_-(r, z)/m$ , where  $n_-(r, z)$  is the density of the imaginary neutralizing charge, and Eq. (3.65) can then be interpreted as the small Debye-length requirement of charge neutrality [i.e.,  $n(r, z) = n_-(r, z)$ ].

An interesting conclusion can be drawn from Eq. (3.65) concerning the possibility of traps with closed field lines (e.g., toroidal traps). It is not possible to have a region of positive  $\omega_{p-}^2(r, z)$  where  $B_z > 0$  and another region of positive  $\omega_{p-}^2(r, z)$  where  $B_z < 0$ . Therefore there cannot be a closed field line that lies completely in the region of positive  $\omega_{p-}^2(r, z)$ . In Sec. VI, we shall briefly discuss work in which the requirement that the plasma be in thermal equilibrium is replaced by the less restrictive requirement that the plasma be stable. It is observed that stable equilibria are possible for a toroidal magnetic configuration.

When finite temperature effects are included, the problem becomes more complicated. The plasma potential is no longer constant along the magnetic-field lines, and certain populations of particles are trapped in both the low- and high-field regions (Fajans *et al.*, 1996).

## 2. Rotating wall

The essential requirement of the confinement theorem of Sec. II.C. is that there exist a rotating frame where the Hamiltonian  $H_R$  is a constant of the motion. In Sec. II.C, we assumed that the trap and trap fields were time independent and cylindrically symmetrical. We argued that  $H$  and  $P_\theta$  were conserved separately and that, therefore,  $H_R = H + \omega P_\theta$  was conserved. However, this is a special case.  $H_R$  can be conserved even if  $H$  and  $P_\theta$  are not conserved. To be specific,  $H_R$  is conserved if and only if  $H_R$  does not depend explicitly on time (i.e.,  $dH_R/dt = \partial H_R/\partial t = 0$ ). Of course, when checking the time dependence, we must express  $H_R$  in terms of the angle variables for the rotating frame (i.e.,  $\bar{\theta}_j = \theta_j + \omega t$ ).

Likewise, the Boltzmann distribution (3.1) does not require that  $H$  and  $P_\theta$  be separately conserved. It is sufficient that there exist a rotating frame ( $-\omega$ ) in which  $H_R$  is conserved. In this case,  $\omega$  is no longer a free parameter to be determined by Eqs. (3.5) and (3.6). The temperature  $T$  is the only free parameter, and it is de-

termined by the value of  $H_R$ . Of course, Eqs. (3.5) and (3.6) can be combined to give the mean-field expression for  $H_R = H + \omega P_\theta$ .

As an example, suppose that a trap of the form shown in Fig. 1 is modified by azimuthally dividing one of the cylinders into many sections. By applying properly phased and temporally varying potentials to each sector, one can produce a trap potential of the form  $\phi_T = \phi_T(r, \theta + \omega t, z)$ . The aliasing fields are small in the region of the plasma if the sectors are sufficiently small and numerous and if the plasma is sufficiently far from the walls. This is the type of trap potential that would be produced by rotating an asymmetric electrode structure, so we say that the trap has a “rotating wall.”

Since  $\phi_T(r, \theta + \omega t, z)$  depends explicitly on  $t$  and  $\theta$ , neither  $H$  nor  $P_\theta$  are conserved. On the other hand,  $\phi_T$  is independent of time when expressed in terms of the angle variable for the rotating frame (i.e.,  $\bar{\theta} = \theta + \omega t$ ), so  $H_R$  does not depend explicitly on time and is conserved. Thus the confinement theorem and the thermal equilibrium results apply, except that  $\omega$  must be interpreted as a trap parameter. For example, Eq. (3.20) uniquely determines the density of the plasma in terms of the two trap parameters  $\omega$  and  $\Omega_c$ . (For simplicity, we assume here that the magnetic field is uniform.) The plasma density is uniform out to some surface, but that surface is not a surface of revolution.

This surface of revolution can be evaluated explicitly when the plasma is small in size compared to the size of the electrodes. In this case the trap potential can be approximated by a harmonic form obtained through Taylor expansion about the saddle point at the center of the trap potential. Note that this point may be shifted from the geometrical center of the trap electrodes if the rotating-wall field has a dipole component. However, when image charges are neglected this merely shifts the plasma center of mass, provided that the plasma is single species. [If the plasma consists of several species, a dipole-field rotating wall can cause centrifugal separation and nontrivial changes in the plasma shape (Huang *et al.*, 1998a).] Here we consider the shape change in a single-species plasma due to quadrupole components of the rotating-wall potential. In the rotating frame where the rotating-wall potential is stationary, the potential takes the form

$$e\phi_T = \frac{1}{2} m \omega_z^2 \left\{ z'^2 - \frac{1}{2} [(1-2\delta)x'^2 + (1+2\delta)y'^2] \right\}, \quad (3.66)$$

where  $\delta$  is a measure of the  $x'-y'$  anisotropy of the potential, and where  $(x', y', z')$  are coordinates chosen so that there are no cross terms in  $\phi_T$ . These coordinates are rotated by some angles  $\theta$  and  $\psi$  with respect to the frame of reference that is aligned with the magnetic-field direction  $\hat{z}$  (see Fig. 17). Note that the Laplacian of  $\phi_T$  is zero.

To this trap potential we add the corrections due to rotation,  $m\omega(\Omega_c - \omega)(x^2 + y^2)/2$ , to obtain the effective trap potential in the rotating frame,  $\phi_R$ ,

$$e\phi_R = \frac{1}{2} m \omega_z^2 \mathbf{x}' \cdot \boldsymbol{\epsilon}_R \cdot \mathbf{x}', \quad (3.67)$$

where  $\boldsymbol{\epsilon}_R$  is the symmetric matrix

$$\epsilon_R = \begin{pmatrix} -\frac{1}{2} + \delta + (\beta + \frac{1}{2})(1 - \sin^2 \theta \sin^2 \psi) & \frac{-(\beta + \frac{1}{2})\sin^2 \theta \sin 2\psi}{2} & \frac{-(\beta + \frac{1}{2})\sin 2\theta \sin \psi}{2} \\ & -\frac{1}{2} - \delta + (\beta + \frac{1}{2})(1 - \sin^2 \theta \cos^2 \psi) & \frac{-(\beta + \frac{1}{2})\sin 2\theta \cos \psi}{2} \\ & & 1 + (\beta + \frac{1}{2})\sin^2 \theta \end{pmatrix}, \quad (3.68)$$

and where  $\beta$  is the trap parameter, given by Eq. (3.40).

This potential can be converted to normal form by performing another rotation to new coordinates  $(x'', y'', z'')$  that diagonalize  $\epsilon_R$ :

$$e\phi_R = \frac{1}{2} m \omega_z^2 (ax''^2 + by''^2 + cz''^2), \quad (3.69)$$

where  $a$ ,  $b$ , and  $c$  are the eigenvalues of  $\epsilon_R$  and are functions of  $\beta$ ,  $\delta$ ,  $\theta$ , and  $\psi$ .

In general  $a$ ,  $b$ , and  $c$  are the solutions to a cubic polynomial. When  $\theta$  and  $\psi$  equal zero no rotation is necessary and  $a$ ,  $b$ , and  $c$  take on the values

$$a = \beta + \delta, \quad (3.70a)$$

$$b = \beta - \delta, \quad (3.70b)$$

$$c = 1. \quad (3.70c)$$

When  $\psi = 0$  but  $\theta \neq 0$  (i.e., a tilt about the  $x$  axis),

$$a = \beta + \delta, \quad (3.71a)$$

$$b = \frac{\beta - \delta + 1 + S \sqrt{(\beta - \delta - 1)^2 + (2\beta + 1)(3 + 2\delta)\sin^2 \theta}}{2}, \quad (3.71b)$$

$$c = \frac{\beta - \delta + 1 - S \sqrt{(\beta - \delta - 1)^2 + (2\beta + 1)(3 + 2\delta)\sin^2 \theta}}{2}, \quad (3.71c)$$

where  $S$  equals  $\pm 1$ ; which sign one chooses is arbitrary depending on which axis one wishes to label  $y''$  and which one wishes to label  $z''$ . For example, for small  $\theta$ , there is a near zero in the square root at  $\beta - \delta - 1 = 0$ , and in order to have  $b$  and  $c$  approach their  $\theta = 0$  values  $\beta - \delta$  and 1, respectively, one must choose  $S$  such that

$$S = \begin{cases} 1, & \delta \leq \beta - 1, \\ -1, & \delta \geq \beta - 1. \end{cases} \quad (3.72)$$

The results for  $a$ ,  $b$ , and  $c$  are shown in Fig. 18 as a function of  $\delta$  for a particular value of  $\beta$  and for  $\theta = 0^\circ$  and  $10^\circ$ . The choice of  $S$  in Eq. (3.72) allows  $b$  and  $c$  to

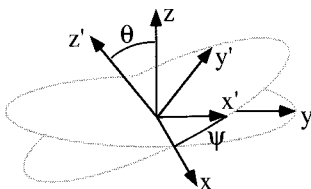


FIG. 17. Frame of reference  $(x', y', z')$  in which the harmonic rotating-wall trap field takes the form of Eq. (3.66).

approach their  $\theta = 0$  limits for all values of  $\beta$  and  $\delta$ ; however, this choice creates a discontinuity in  $b$  and  $c$  at  $\delta = \beta - 1$ . Physically, this discontinuity is merely an interchange of the  $y''$  and  $z''$  axes, which can be carried out by a  $90^\circ$  rotation around the  $x'$  axis; note that  $\theta \rightarrow \theta + \pi/2$  does not change the matrix coefficients in Eq. (3.68).

It is not difficult to show that the arguments of the square roots in Eqs. (3.71b) and (3.71c) are always non-negative, so that  $a$ ,  $b$ , and  $c$  are always real. However, for arbitrary values of  $\beta$ ,  $\delta$ , and  $\theta$ ,  $a$ ,  $b$ , and  $c$  need not be positive, as can be seen in Fig. 18. Nevertheless, they are required to be positive in order to confine the plasma, and this leads to limits on the possible values of  $\beta$ ,  $\delta$ , and  $\theta$ .

For example, for  $\theta = 0$ , Eqs. (3.70) imply  $\beta > |\delta|$  is required for confinement. When  $\theta \neq 0$  Eqs. (3.71) imply that

$$\beta > |\delta| \quad (3.73)$$

and

$$\frac{4\beta - 3(2\beta + 1)\sin^2 \theta}{2 + (2\beta + 1)\sin^2 \theta} > 2\delta \quad (3.74)$$

are required to confine the plasma. These bounds in the  $\beta - \delta$  plane are plotted in Fig. 19 for different  $\theta$  values. They are generalizations of the requirement that  $\beta > 0$  for an axisymmetric-aligned trap potential.

The shape of a zero-temperature mean-field plasma follows from the quadratic form of Eq. (3.69). In potential theory it is well known that the potential inside a uniform ellipsoid of density  $n_-$  with principal axes  $(a_1, a_2, a_3)$  aligned along the  $x''$ ,  $y''$ , and  $z''$  axes, respectively, takes the form

$$\phi_p(\mathbf{x}'') = -\frac{1}{4} \frac{m}{e} \omega_p^2 (A_1 x''^2 + A_2 y''^2 + A_3 z''^2) + C, \quad (3.75)$$

where  $C$  is a constant and where  $A_1$ ,  $A_2$ , and  $A_3$  are dimensionless functions of the ratios of the principal axes  $a_3/a_1, a_2/a_1$  that can be written in terms of elliptic integrals (Binney and Tremaine, 1987):

$$A_1(a_2/a_1, a_3/a_1) = 2 \frac{a_2 a_3}{a_1^2} \frac{F(\theta, k) - E(\theta, k)}{k^2 \sin^3 \theta}, \quad (3.76a)$$

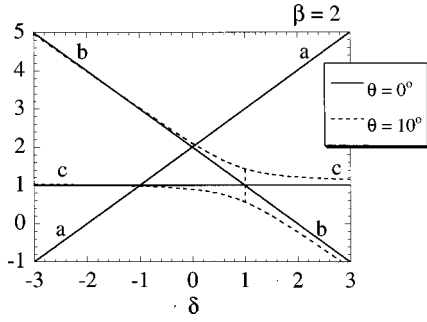


FIG. 18. Coefficients  $a$ ,  $b$ , and  $c$  entering into the effective confinement potential of a harmonic rotating wall for  $\beta=2$  as a function of the anisotropy parameter  $\delta$ , for  $\psi=0^\circ$ ,  $\theta=0^\circ$  (solid line), and  $10^\circ$  (dotted line).

$$A_2(a_2/a_1, a_3/a_1)$$

$$= 2 \frac{a_2 a_3}{a_1^2} \frac{E(\theta, k) - k'^2 F(\theta, k) - (a_3/a_2) k^2 \sin \theta}{k^2 k'^2 \sin^3 \theta}, \quad (3.76b)$$

$$A_3(a_2/a_1, a_3/a_1) = 2 \frac{a_2 a_3}{a_1^2} \frac{(a_2/a_3) \sin \theta - E(\theta, k)}{k'^2 \sin^3 \theta}, \quad (3.76c)$$

where  $k = \sqrt{(a_1^2 - a_2^2)/(a_1^2 - a_3^2)}$ ,  $k'^2 = 1 - k^2$ , and  $\theta = \cos^{-1}(a_3/a_1)$ , and  $F(\theta, k)$  and  $E(\theta, k)$  are elliptic integrals of the first and second kind, respectively. The notation used for the elliptic integrals is that of Gradshteyn and Ryzhik (1980); for example,

$$E(\theta, k) = \int_0^\theta d\alpha \sqrt{1 - k^2 \sin^2 \alpha}.$$

The functions defined in Eqs. (3.76) satisfy  $A_1 + A_2 + A_3 = 2$ , so that  $\nabla^2 \phi_p = -4\pi e n_-$ . The requirement that the total potential  $\phi_p + \phi_R$  be constant inside the plasma then implies that  $n_- = m\omega(\Omega_c - \omega)/2\pi e^2$ , the same requirement on the density as for axisymmetric traps without rotating walls. Here, we have used Eqs. (3.67) and (3.68) to find  $\nabla^2 e \phi_R = m\omega_z^2 \text{Tr}(\epsilon_R)$  which is invariant under rotations.

Furthermore, force balance in the  $x''$ ,  $y''$ , and  $z''$  directions leads to

$$\frac{\omega_p^2}{2} A_1 = \omega_z^2 a, \quad (3.77a)$$

$$\frac{\omega_p^2}{2} A_2 = \omega_z^2 b, \quad (3.77b)$$

$$\frac{\omega_p^2}{2} A_3 = \omega_z^2 c. \quad (3.77c)$$

Any two of these equations can be employed to determine  $a_3/a_1$  and  $a_2/a_1$ , and these two aspect ratios specify the plasma shape.

As a specific example, we take the case in which  $\theta = \psi = 0$  and in which the plasma is very long,  $\omega_z \rightarrow 0$ , but  $\omega_z^2 \delta$  is finite so that there remains a finite asymmetric  $x-y$  trap potential. The plasma then becomes a cylinder with an elliptical cross section and shape determined by

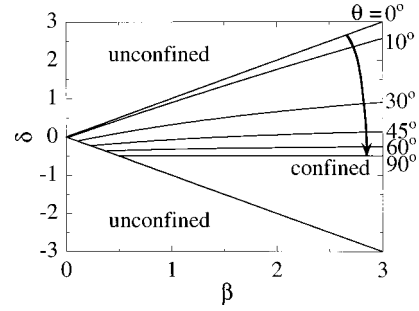


FIG. 19. Limits on the trap parameter  $\beta$  and the anisotropy parameter  $\delta$  for confinement within a harmonic rotating wall,  $\psi=0^\circ$ .

Eqs. (3.77) and (3.70). In this limit  $A_1$ ,  $A_2$ , and  $A_3$  simplify to

$$A_1 = \frac{2a_2}{a_1 + a_2}, \quad A_2 = \frac{2a_1}{a_1 + a_2}, \quad A_3 = 0. \quad (3.78)$$

The elliptical-cylinder aspect ratio is then provided by the simple result

$$\frac{a_1}{a_2} = \frac{\beta - \delta}{\beta + \delta}, \quad (3.79)$$

where we have used Eqs. (3.70a) and (3.70b) and have divided Eq. (3.77a) by Eq. (3.77b).

Another analytically tractable limit is the case in which the trap fields are chosen so that the plasma forms an elliptical disc; for example,  $a_3 \rightarrow 0$ , with  $a_1$  and  $a_2$  finite. In this case  $\theta \rightarrow \pi/2$ ,  $k \rightarrow \sqrt{1 - a_2^2/a_1^2}$ ,  $k' \rightarrow a_2/a_1$ , and Eq. (3.76c) implies  $A_3 \rightarrow 2$ . Then, by Eq. (3.77c),  $\omega_p^2 \rightarrow \omega_z^2 c$ , and Eqs. (3.76a) and (3.76b) imply that  $A_1$  and  $A_2$  are of order  $a_3$ :

$$\lim_{a_3 \rightarrow 0} \frac{A_1}{a_3} = \frac{2a_2}{a_1^2} \frac{K - E}{1 - a_2^2/a_1^2}, \quad (3.80a)$$

$$\lim_{a_3 \rightarrow 0} \frac{A_2}{a_3} = \frac{2}{a_2} \frac{E - (a_2^2/a_1^2)K}{1 - a_2^2/a_1^2}, \quad (3.80b)$$

where  $K = K(\sqrt{1 - a_2^2/a_1^2})$  and  $E = E(\sqrt{1 - a_2^2/a_1^2})$  are complete elliptic functions of the first and second kinds (Gradshteyn and Ryzhik, 1980).

The elliptic disc's shape is found by taking the ratio of Eqs. (3.77a) and (3.77b),

$$\frac{a_2^2}{a_1^2} \frac{K - E}{E - a_2^2 K/a_1^2} = \frac{a}{b}, \quad (3.81)$$

which can be solved numerically for the aspect ratio  $a_2/a_1$ .

Any real trap has unavoidable field asymmetries (field errors) that are stationary in the laboratory frame, and these asymmetries exert a drag on the rotating plasma. In equilibrium this backward torque must be balanced by a forward torque due to the rotating asymmetry. If the plasma is a fluid, such a torque can develop only if there is some slippage between the rotational flow of the fluid and the rotating asymmetry. In other words, only when the asymmetry rotates faster than the fluid can it



create a viscous torque that tends to increase the fluid rotation. On the other hand, if the plasma is a crystal that can support shear stress, there need not be such slippage. Instead, the deformation of the crystal caused by the rotating asymmetry can create a static shear stress in the rotating frame that torques on the crystal, even without slippage. Furthermore, the field errors, which are stationary in the laboratory frame, are time dependent in the rotating frame. This explicit time dependence means that  $dH_R/dt = \partial H_R/\partial t$  has a small nonzero value. If the heating rate is slow compared to the time to come into thermal equilibrium, the thermal equilibrium description is still valid, but the temperature  $T$  slowly increases. To have a steady state, the plasma also must be cooled.

If the slippage between the rotating-field asymmetry and the rotational flow of the plasma is substantial, the plasma is not even close to being in thermal equilibrium in the frame of the rotating asymmetry. In this case, it is more useful to think of the rotating asymmetry as simply a means of applying a torque on the plasma, much as the laser beam applies a torque. We assume that the plasma is in some cylindrically symmetrical thermal equilibrium state, but that  $T$  and  $\omega$  evolve slowly as a result of slow changes in the plasma energy  $E$  and angular momentum  $L$ . The rotating asymmetry and any stationary asymmetry are assumed to be weak, and the time for Coulomb collisions to bring the plasma into a state of thermal equilibrium is assumed to be short compared to the time for significant changes in  $E$  and  $L$ . A steady state is reached when there is a balance such that the net torque and the net energy input are zero (i.e.,  $E = L = 0$ ). In Sec. V, we develop a thermodynamic approach to transport and discuss such issues as the frequency and temperature stability near a steady state.

In experiments with pure electron plasmas (Pollock and Anderegg, 1994), a rotating-wall configuration (with eight sectors) confined the electrons for arbitrarily long times in a steady state. In this case, the cooling was due to cyclotron radiation. In addition, a rotating wall configuration (again with eight sectors) achieved arbitrarily long steady-state confinement of a pure ion plasma (Huang *et al.*, 1997). In this case, the cooling was due to collisions with neutrals. In these experiments the plasma was not in thermal equilibrium in the rotating frame of the wall. The wall could develop sufficient torque to balance the ambient torques only if there was substantial slippage between the wall and plasma.

In more recent experiments (Huang *et al.*, 1996) with strongly correlated  $\text{Be}^+$  ion plasmas (pure ion crystals), there was zero slip between the rotating plasma and the rotating wall, so the analysis presented here presumably applies. In these experiments, the crystal structure was monitored by Bragg scattering, and the rotation rate of the crystal was determined precisely by measuring the rotation rate of the scattering pattern. For long periods, the crystal and rotating wall were locked in phase, rotating together. The rotating-field asymmetry was quadratic, as is assumed in the present analysis, but the field

amplitudes were so small that distortion of the plasma from cylindrical symmetry could not be measured.

#### IV. STRONG CORRELATION

In this section, we consider nonneutral plasmas for which the coupling parameter  $\Gamma = e^2/akT$  is large. The plasma charges are then strongly correlated, and liquid and crystalline states are predicted and observed. We shall see that the structure of the ordered state can depend on plasma size and shape as well as on the value of  $\Gamma$ . Three size regimes in which the plasmas have qualitatively different properties are, in order of decreasing size, *large plasmas*, *mesoscopic plasmas*, and *Coulomb clusters*. We shall discuss these three regimes separately.

While the physics of strong correlation presents us with several new effects, it is fortunate that the main conclusions of the last section concerning the overall shape and size of the plasma remain valid for both mesoscopic and large plasmas and can be a reasonable first approximation even for Coulomb clusters. Even for strong correlation, the characteristic mean-field potential  $e\phi$  is large compared to  $e^2/a$  when  $N \gg 1$ . Thus the gross plasma shape is still determined by a balance of mean-field forces, so the shape as discussed in the previous section remains almost unchanged. The influence of correlations is to establish order within that gross shape.

##### A. Microcanonical and canonical ensembles

Of course, strongly correlated plasmas cannot be described by the Boltzmann distribution (a one-particle distribution). Rather, an  $N$ -particle distribution must be used. As discussed in Sec. II, an isolated plasma of  $N$  interacting charges in a cylindrically symmetrical trap with time-independent fields admits two constants of the motion: the Hamiltonian  $H(\mathbf{r}_1, \mathbf{v}_1, \dots, \mathbf{r}_N, \mathbf{v}_N)$  and the canonical angular momentum  $P_\theta(\mathbf{r}_1, \mathbf{v}_1, \dots, \mathbf{r}_N, \mathbf{v}_N)$ . The microcanonical ensemble for such a plasma is characterized by the distribution (Landau and Lifshitz, 1980, p. 12)

$$f_{\text{m.c.}}(\mathbf{r}_1, \mathbf{v}_1, \dots, \mathbf{r}_N, \mathbf{v}_N) = A \delta[H - E] \delta[P_\theta - L], \quad (4.1)$$

where  $A$  is a constant that is chosen to normalize the phase-space integral of the distribution to unity and  $E$  and  $L$  are the fixed values of  $H$  and  $P_\theta$ . According to the ergodic hypothesis, this distribution describes the thermal equilibrium state of the plasma. The average of any function  $G(\mathbf{r}_1, \mathbf{v}_1, \dots, \mathbf{r}_N, \mathbf{v}_N)$  taken over the microcanonical distribution is equal to the long-time average of the function taken along the system trajectory in the  $6N$ -dimensional phase space.

On the other hand, the distribution for a canonical ensemble (the Gibbs distribution) is given by (Landau and Lifshitz, 1980, p. 106)

$$f_c(\mathbf{r}_1, \mathbf{v}_1, \dots, \mathbf{r}_N, \mathbf{v}_N) = C \exp[-(H + \omega P_\theta)/kT], \quad (4.2)$$

where  $C$  is a factor used to normalize the integral of  $f_c$  to unity. This constant is related to the canonical partition function  $Z_c$  through

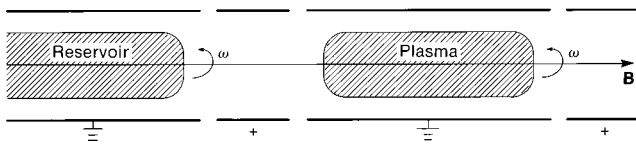


FIG. 20. Plasma in thermal contact with heat and angular momentum reservoir.

$$C^{-1} = Z_c N! \left( \frac{h}{m} \right)^{3N} = \int_{-\infty}^{+\infty} d^3 \mathbf{r}_1 \dots d^3 \mathbf{v}_N \exp[-(H + \omega P_\theta)/kT], \quad (4.3)$$

where  $h$  is Planck's constant. The Gibbs distribution is similar to the Boltzmann distribution [Eq. (3.1)] in that both represent a system with fixed values of the temperature  $T$  and rotation frequency  $-\omega$ . However, the full  $N$ -particle Hamiltonian and angular momentum enter the Gibbs distribution, whereas the mean-field single-particle energy and angular momentum enter the Boltzmann distribution, so correlations between particles are kept in the Gibbs distribution and are omitted in the Boltzmann distribution. The Gibbs distribution describes a plasma that is in thermal contact with an energy and angular momentum reservoir. For example, Fig. 20 shows a trapped plasma that is in thermal contact with an infinitely long column (the reservoir) that is characterized by temperature  $T$  and rotation frequency  $-\omega$ . Thermal fluctuations produce a transfer of energy and angular momentum back and forth between the reservoir and plasma.

For a sufficiently large plasma (i.e.,  $N \gg 1$ ), the fluctuations in plasma energy and angular momentum are small compared to the mean energy and angular momentum and have only a small influence on the plasma state. Thus, for most physical quantities, an average over the microcanonical distribution can be replaced by an average over the Gibbs distribution (Reif, 1965). In establishing the correspondence between the two distributions, one chooses  $T$  and  $\omega$  so that  $E = \langle H \rangle$  and  $L = \langle P_\theta \rangle$ , where the averages are over the Gibbs distribution. This well-known equivalence between the two distributions is useful because the Gibbs distribution offers advantages analytically; for example,  $H$  and  $P_\theta$  enter the Gibbs distribution only through the combination  $H_R = H + \omega P_\theta$ . However, we should note that the equivalence does not extend to averages of certain fluctuations; for example,  $\langle (H - E)^2 \rangle$  is identically zero for the microcanonical distribution and is small [i.e.,  $\langle (H - E)^2/E^2 \rangle \sim 1/N$ ] but nonzero for the Gibbs distribution. We shall discuss fluctuations separately in Sec. V.E.

#### 1. Mesoscopic plasmas, large plasmas, and Coulomb clusters

Later in this section we shall numerically evaluate averages according to both the microcanonical and the Gibbs distributions. For  $N \gtrsim 100$ , we will find no noticeable difference in average quantities such as the local

density when evaluated using the two distributions. Thus we take  $N \gtrsim 100$  to be a loose criterion for the applicability of the Gibbs distribution.

Although a plasma with  $N \sim 100$  is large enough that the Gibbs distribution is applicable, such a plasma is not large enough to be considered infinite and homogeneous. In fact, it has been found that surface effects can strongly influence the correlation properties of a crystallized plasma even when  $N > 10^4$  (Rahman and Schiffer, 1986; Dubin and O'Neil, 1988; Gilbert, Bollinger, and Wineland, 1988; Dubin, 1989; Schiffer, 1995). Plasmas that are sufficiently small that correlations are strongly influenced by plasma shape and size, but that are sufficiently large ( $N \gtrsim 100$ ) that the Gibbs distribution is applicable, are referred to here as mesoscopic.

On the other hand if the plasma is large enough, surface effects can be neglected in the plasma interior. The microscopic structure in the interior is the same as for an infinite homogeneous plasma. In Sec. IV.D we estimate that bulk crystalline properties do not begin to dominate over surface properties until the plasma's minimum dimension is approximately 60 interparticle spacings [ $(N \gtrsim 10^5)$  for a spherical plasma (Dubin, 1989)]. However, when the plasma is not too strongly correlated, i.e.,  $\Gamma \lesssim 10$ , the plasma size required to neglect surface effects drops appreciably, to  $N \gtrsim 10^3$  for a spherical cloud. This is because the correlation length of the fluid phase is only on the order of one or two interparticle spacings, and the effect of the surface penetrates into the interior only over this distance. We refer to plasmas for which surface effects are negligible as large plasmas.

Finally, when  $N$  is very small,  $N \lesssim 10$ , the Gibbs and microcanonical distributions are no longer equivalent. This is the regime of Coulomb clusters. When cooled to low temperatures such clusters have been observed to form simple geometric configurations whose structures vary with particle number and external fields (Wineland *et al.*, 1987; Deidrich *et al.*, 1987). Predictions for the structures of Coulomb clusters can be made by minimizing the energy of the system subject to the constraints of either constant rotation frequency (canonical ensemble) or constant angular momentum (microcanonical ensemble). Catalogs of such structures have been compiled (Rafac *et al.*, 1991) and compared to experiment (Deidrich *et al.*, 1987; Wineland *et al.*, 1987; Itano, Bergquist, and Wineland, 1989).

#### 2. Spatial and reduced distribution functions

For the case of a trap with a uniform axial magnetic field, the combination  $H_R = H + \omega P_\theta$  is written out in Eq. (2.8). The velocity dependence and spatial dependence of the Gibbs distribution can be separated:

$$f_c(\mathbf{r}_1, \mathbf{v}_1 \dots \mathbf{r}_N, \mathbf{v}_N) = (2\pi kT/m)^{-3N/2} \times \exp \left[ - \sum_{i=1}^N \frac{1}{2} m(\mathbf{v}_i + \omega \mathbf{r}_i \hat{\theta}_i)^2 / kT \right] \times f_c^{(s)}(\mathbf{r}_1, \dots, \mathbf{r}_N). \quad (4.4)$$

The spatial part of the Gibbs distribution is

$$f_c^{(s)}(\mathbf{r}_1 \dots \mathbf{r}_N) = \bar{C} \exp \left[ - \sum_{j=1}^N \left\{ \frac{1}{2} \sum_{i \neq j} e^2 G(\mathbf{r}_i | \mathbf{r}_j) + e \phi_R(r_j, z_j) \right\} / kT \right], \quad (4.5)$$

where  $\bar{C}$  is a constant normalizing  $f_c^{(s)}$  to unity. The velocity dependence in Eq. (4.4) is a product of Maxwellians as viewed in a frame that rotates with frequency  $-\omega$ . The spatial dependence corresponds to a set of interacting charges that resides in (is confined by) the external potential  $\phi_R(r, z)$ .

It is useful to introduce the reduced spatial distribution functions

$$\rho^{(M)}(\mathbf{r}_1, \dots, \mathbf{r}_M) = \int d^3\mathbf{r}_{M+1} \dots d^3\mathbf{r}_N f_c^{(s)}(\mathbf{r}_1, \dots, \mathbf{r}_N). \quad (4.6)$$

For example, the plasma density  $n(\mathbf{x})$  is related to the first reduced distribution  $\rho^{(1)}(\mathbf{x})$  through

$$n(\mathbf{r}) = N \rho^{(1)}(\mathbf{r}). \quad (4.7)$$

The correlation function  $g(\mathbf{r}_1, \mathbf{r}_2)$ , which describes two-body spatial correlations, is defined in terms of  $\rho^{(2)}$  through

$$\rho^{(2)}(\mathbf{r}_1, \mathbf{r}_2) = \rho^{(1)}(\mathbf{r}_1) \rho^{(1)}(\mathbf{r}_2) [1 + g(\mathbf{r}_1, \mathbf{r}_2)]. \quad (4.8)$$

The correlation function measures the extra probability, beyond what would be expected of a completely random distribution, of finding particles at  $\mathbf{r}_1$  and  $\mathbf{r}_2$ . Because the Coulomb interaction is a binary interaction, all of the thermodynamic functions can be evaluated from knowledge of  $n(\mathbf{r})$  and  $g(\mathbf{r}_1, \mathbf{r}_2)$  (and  $T$ ). In Secs. IV.B–IV.D we shall consider the behavior of both these functions in mesoscopic and large plasmas. Coulomb clusters are sufficiently small that other techniques for examining correlations, such as directly viewing the particle positions, can be more instructive. Clusters will be discussed in Sec. IV.E.

### 3. Relation to a one-component plasma

Much of the remaining discussion in this section follows from a useful analogy between a trapped nonneutral plasma and a one-component plasma (OCP). As described in the introduction, an OCP is a system of point charges that is embedded in a uniform neutralizing background charge. In Sec. III.C, we established an equivalence between the mean-field, thermal equilibrium, spatial structure of a magnetically confined plasma and an OCP. Here, we establish the same equivalence using the Gibbs distribution, so the equivalence includes all spatial correlation properties (Malmberg and O'Neil, 1977) (but does not include time-dependent correlations such as two-time correlation functions). Following the discussion in Sec. III.C, we note that the second term on the right-hand side of Eq. (2.9) can be interpreted as the potential due to an imaginary cylinder of negative charge [i.e.,  $e\phi_- = \pi en_- r^2$ , where  $n_- = m\omega(\Omega_c - \omega)/2\pi e^2$ ]. Thus the Gibbs distribution for a single-

species plasma in a Penning trap differs only by rotation from that for the same plasma confined by a cylinder of neutralizing charge and externally applied electrode potentials. In regard to the thermal equilibrium properties, the Penning trap plasma provides a laboratory realization of an OCP. This equivalence is particularly useful for large trapped plasmas, since infinite homogeneous OCP's have been the subject of much theoretical study, and we can borrow results from these studies to obtain a theoretical description of correlation effects in large trapped plasmas.

### 4. Infinite homogeneous one-component plasma and the coupling parameter $\Gamma$

An infinite homogeneous classical OCP that is in a state of thermal equilibrium is characterized by the density  $n = n_-$ , the charge  $e$  and mass  $m$  of the particles, and the energy  $kT$ . The only dimensionless parameter that can be constructed from these quantities is the coupling parameter,  $\Gamma = e^2/akT$ , where  $a = (3/4\pi n)^{1/3}$  is the Wigner-Seitz radius. Thus, when lengths are scaled by  $a$ , the correlation function must take the form  $g = g(\mathbf{r}_1/a, \mathbf{r}_2/a; \Gamma)$ ; that is, time-independent correlation phenomena can be parametrized by the single number  $\Gamma$ . For example, a plasma with density  $n_1$  and temperature  $T_1$  is equivalent to a plasma with a different density  $n_2$  provided that  $T_2 = (n_2/n_1)^{1/3} T_1$ , since  $\Gamma$  is identical for the two systems. This ability to vary the density and temperature without changing the correlation properties follows from the lack of any intrinsic spatial scale in the interparticle potential  $|\mathbf{r}_i - \mathbf{r}_j|^{-1}$ . (The Coulomb potential is a particular case of a more general class of scale-free inverse-power potentials of the form  $|\mathbf{r}_i - \mathbf{r}_j|^{-n}$ , all of which have the property that their correlations depend only on a single parameter.)

The coupling parameter  $\Gamma$  is simply the ratio of the interaction energy between neighboring charges  $e^2/a$  to the kinetic energy per degree of freedom  $kT$ . Correlations are weak when  $\Gamma \ll 1$  and are strong when  $\Gamma \gg 1$ . The regime  $\Gamma \ll 1$  is typical for neutral plasmas and indeed most nonneutral plasma experiments are also carried out in this regime. One can get an idea of the sort of densities and temperatures required to enter the strongly correlated regime  $\Gamma > 1$  by writing  $\Gamma$  in physical units:

$$\Gamma = 2.69 Z^2 \left( \frac{n}{10^9 \text{ cm}^{-3}} \right)^{1/3} \left( \frac{T}{\text{K}} \right)^{-1}, \quad (4.9)$$

where  $Z$  is the number of elementary charges on each particle. For a low- $Z$  plasma, with temperatures on the order of  $10 \text{ eV} = 1.1 \times 10^5 \text{ K}$ , rather large densities on the order of  $10^{23} \text{ cm}^{-3}$  are required for  $\Gamma \sim 1$ ; such parameters are not impossible to achieve for very short times in experiments using shock tubes (Chace and Moore, 1959; Ivanov *et al.*, 1976; DeSilva and Kunze, 1993) or solids heated and compressed by lasers (Brueckner and Jorna, 1974; Craxton, McCrory, and Soares, 1986), for example. In astrophysical contexts, such as the interior of a white or brown dwarf star, densities are sufficiently

large, of order  $10^{31} \text{ cm}^{-3}$ , that the strongly correlated regime is accessible even when temperatures are on the order of  $10^7 \text{ K}$  (Schatzman, 1958). In experiments with nonneutral plasmas, strong correlation has been achieved by reducing the temperature to the cryogenic regime. With pure electron plasmas, temperatures on the order of  $4 \text{ K}$  are obtained by cooling the vacuum chamber and electrode structure with a liquid-helium bath; the electrons come to temperature equilibrium with the walls through cyclotron radiation. At densities on the order of  $10^{10} \text{ cm}^{-3}$  correlation parameters of order unity have been achieved (Malmberg *et al.*, 1988). In other cryogenic experiments, electrons have been trapped in a 2D layer directly on the surface of liquid helium, forming a 2D strongly correlated plasma (Cole, 1974). In experiments involving pure ion plasmas, the technique of laser cooling (see Sec. III.B.2) has been applied in order to lower temperatures to the milliKelvin range. At typical densities of order  $10^9 \text{ cm}^{-3}$ , correlation parameters of several hundred have been achieved (Bollinger and Wineland, 1984; Bollinger, Wineland, and Dubin, 1994).

Another route to strong correlation takes advantage of the  $Z^2$  dependence in  $\Gamma$ . Indeed, in what we believe to be the first experiment on strongly correlated trapped charges (Weurker, Shelton, and Langmuir, 1959), several dust grains were charged to  $Z \sim 10^4$  or more and were suspended in the fields of a Paul trap in crystalline configurations reminiscent of the Coulomb clusters to be discussed in Sec. IV.E. For such large  $Z$  values,  $\Gamma \gg 1$  was achieved even though the “temperature” of the grains was rather large. (However the number of trapped dust grains was only on the order of 10 to 20.) In heavy-ion storage rings many highly stripped ions can be trapped, and it has been theorized that strongly correlated nonneutral plasmas could be produced (Rahman and Schiffer, 1986). However, in the present experiments densities and temperatures are not sufficient to achieve strong correlation.

It is instructive to display the correlation criterion in a density and temperature “phase diagram” (Malmberg and O’Neil, 1977). In Fig. 21, the ordinate is  $\log_{10} T$ , where  $T$  is measured in degrees Kelvin. The abscissa along the bottom of the figure is  $\log_{10} n$ , where  $n$  is measured in particles per cubic centimeter. The abscissa along the top of the figure is the  $\log_{10} B$ , where  $B$  is measured in Gauss and is related to  $n$  through the Brillouin limit for an electron plasma (i.e.,  $\omega_p = \Omega_c / \sqrt{2}$ ). In other words, the value of  $B$  that appears above a particular  $n$  is the lowest value of  $B$  for which an electron plasma of that density can be confined. For an ion plasma, the value of  $B$  must be increased by the square root of the mass ratio  $\sqrt{m_i/m_e}$ . As a rough indication of the current technical limit on steady large-scale magnetic fields, a vertical dotted line is drawn at  $B = 100 \text{ kG}$ , which corresponds to a maximum electron density of  $n = 5 \times 10^{14} \text{ cm}^{-3}$ . For comparison the maximum density of a  $\text{Be}^+$  ion plasma is displayed as the dashed line at the density  $n = 3 \times 10^{10} \text{ cm}^{-3}$ . The onset of the fluid state is indicated by the diagonal line at  $\Gamma = 2$

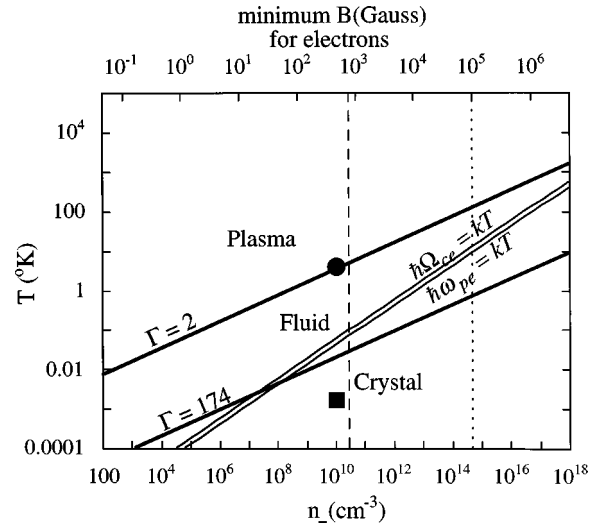


FIG. 21. Phase diagram of the one-component plasma: temperature  $T$  vs density  $n$ . Also shown on upper  $x$  axis is the minimum magnetic field required to produce the corresponding density,  $B = \sqrt{8\pi mn} c^2$  [see Eq. (3.21)].

and of the crystalline state by the diagonal line at  $\Gamma = 174$ . The phase diagram shows that a crystalline OCP is accessible for  $\text{Be}^+$  plasmas that are laser cooled to  $1\text{--}10 \text{ mK}$  and that a fluid OCP is accessible for electron plasmas that are cooled to about  $4 \text{ K}$ . The dot and square show temperatures and densities that have been reached in experiments with reasonably large electron and ion plasmas, respectively (Malmberg *et al.*, 1988; Bollinger, Wineland, and Dubin, 1994).

In electron experiments quantum effects can also play a role at low temperatures. For example, the electron cyclotron motion becomes quantized when  $kT \lesssim \hbar\Omega_c$ . This criterion is displayed in the figure for the magnetic fields given by the upper abscissa, and it is clear that at  $4 \text{ K}$  the cyclotron motion cannot be treated classically at typical magnetic fields of order  $40 \text{ kG}$ . However, it has been shown that quantization of the cyclotron motion has no effect on the spatial correlation properties, including the freezing transition, provided that the other degrees of freedom remain classical (Dubin and O’Neil, 1986a). This can be understood from a physical picture of a system of charges with quantized gyromotion. The cyclotron radius  $v_\perp / \Omega_c$  is replaced by the quantum cyclotron radius  $\sqrt{\hbar/m\Omega_c}$ . Each charge can then be thought of as a guiding center for which the perpendicular kinetic energy associated with the Larmor motion is quantized; however, the guiding centers still interact via what is essentially the classical Coulomb interaction, so the spatial correlations between these guiding centers are unaffected by the magnetic field, provided that the quantum Larmor radius is small compared to an average interparticle spacing. On the other hand, functions such as the specific heat which depend on the mean perpendicular kinetic energy are greatly affected by the quantization of the cyclotron motion. Nevertheless, that portion of the specific heat that depends on correlations is given by the classical formula.

At even lower temperatures for which  $\hbar\omega_p \gtrsim kT$  the phonons in the solid phase become quantized and the motions of the particles in the fluid phase must also be described in quantum-mechanical terms. The freezing transition is affected by the quantization of the plasma oscillations. While the Wigner-Kirkwood expansion (Hansen and Vieillefosse, 1975; Landau and Lifshitz, 1980, p. 98) works to provide quantum corrections when  $\hbar\omega_p \ll kT$ , only recently have accurate theory results been obtained for the size of the effect when  $\hbar\omega_p \gtrsim kT$ . Estimates based on the Lindemann melting criterion, including the zero-point oscillations of the phonons, indicate a small decrease in the temperature required for melting (Mochkovitch and Hansen, 1979). More detailed quantum Monte Carlo simulations of the solid and liquid free energies substantially verify this effect (Iida and Ichimaru, 1995). Experiments on pure-electron quantum liquids and crystals could provide useful empirical data for the freezing transition in this nondegenerate quantum regime. Such data would be of great interest to the astrophysics community since the interior of white dwarf stars can fall into this regime (Chabrier, Ashcroft, and DeWitt, 1992).

Finally, if the plasma density is large enough so that  $\hbar\omega_p \gtrsim e^2/a$ , the zero-point energy of the phonon oscillations is, by itself, sufficiently large to melt the lattice; this is called Wigner melting (Wigner, 1934). In addition, spin-spin correlations caused by exchange effects can cause ferromagnetic transitions in OCP's with Fermi statistics (Ceperley and Alder, 1980). However, the densities needed to enter this regime are much larger than can be attained in present nonneutral plasma experiments: for electrons  $n \gtrsim 10^{22} \text{ cm}^{-3}$  is required.

## B. Numerical experiments on mesoscopic plasmas

In the early experiments with strongly coupled  $\text{Be}^+$  plasmas (Bollinger and Wineland, 1984; Gilbert, Bollinger, and Wineland, 1988), the number of particles was typically in the range  $10^2 < N < 10^4$ . Such plasmas were mesoscopic in scale—large enough to admit a Gibbs description but small enough that surface effects were important. In this section we explore the thermal equilibrium states of such plasmas numerically.

In accord with the experiments, the trap potential is taken to be harmonic; see Eq. (3.37). As noted in Eq. (3.39), the trap potential in the rotating frame,  $\phi_R$ , is then also harmonic. Since the plasmas are small compared to the distance to the walls,  $G(\mathbf{r}_1|\mathbf{r}_2)$  can be set equal to  $|\mathbf{r}_1 - \mathbf{r}_2|^{-1}$ . When distances are scaled by the Wigner-Seitz radius  $a$ , the spatial part of the Gibbs distribution takes the form

$$f_c^{(s)}(\mathbf{r}_1, \dots, \mathbf{r}_N) = \bar{C} \exp \left[ -\Gamma \sum_{j=1}^N \left\{ \sum_{i>j} |\bar{\mathbf{r}}_i - \bar{\mathbf{r}}_j|^{-1} + \frac{3}{4\beta+2} (\bar{z}_j^2 + \beta \bar{r}_j^2) \right\} \right], \quad (4.10)$$

where  $\beta$  is defined in Eq. (3.40). Thus the spatial struc-

ture of the plasma is completely determined by the values of  $N$ ,  $\Gamma$ , and  $\beta$ . The trap parameter  $\beta$  determines the gross shape of the plasma,  $N$  determines the size, and, for a mesoscopic plasma,  $\Gamma$ ,  $N$ , and  $\beta$  determine correlation structure. For example, the plasma is crystallized when  $\Gamma = \infty$ , but the structure of the crystal depends on both  $\beta$  and  $N$  in the mesoscopic range.

Several authors have performed simulations of plasmas in such harmonic traps using different numerical techniques (Rahman and Schiffer, 1986; Totsuji, 1987; Dubin and O'Neil, 1988; Hasse and Avilov, 1991; Tsuruta and Ichimaru, 1993). The Monte Carlo method directly evaluates average quantities in the canonical ensemble. One considers a sequence of random steps of each particle in configuration space and conditions acceptance or rejection of a given step by the change in the probability of the  $N$ -particle state, that is, the change in the value of the configurational portion of the Gibbs distribution,  $f_c^{(s)}$ . When  $f_c^{(s)\text{new}}/f_c^{(s)\text{old}} > 1$ , the step is accepted, but if  $f_c^{(s)\text{new}}/f_c^{(s)\text{old}} < 1$ , the step is accepted only with probability  $f_c^{(s)\text{new}}/f_c^{(s)\text{old}}$ ; otherwise the particle is replaced in its old position. Averages are taken over the sequence of configurations generated in this way, and for a sufficiently long sequence the average approaches an average taken with respect to  $f_c^{(s)}$ . Only static properties of the system can be studied with this technique.

Another numerical approach evaluates a time average over the phase-space trajectory of the  $N$ -particle system, generated via a molecular dynamics simulation. In molecular dynamics the equations of motion of  $N$  interacting charges are integrated forward in time numerically for a time long enough that the particles come to thermal equilibrium with each other. Since energy and angular momentum are conserved to within the numerical accuracy of the simulation, a time average of any phase function is expected to be equal to an average over the microcanonical distribution, which for large  $N$  is in turn expected to give the same results as the average over the Gibbs distribution. Indeed, differences between averages evaluated by the two methods were negligible for  $N \gtrsim 100$  (Dubin and O'Neil, 1988).

Furthermore, there is latitude in the choice of dynamics employed in the molecular dynamics simulation provided that  $N$  is large enough for the Gibbs distribution to apply and that one is interested only in static thermal equilibrium properties. The spatial part of the Gibbs distribution simply describes a collection of interacting charges that reside in the potential  $\phi_R(r, z)$ . Any dynamics that yield this effective trap potential must predict the same thermal equilibrium spatial structure for the plasma. We have already seen one example of this latitude in the equivalence between the (magnetically confined) Penning trap plasma and an (electrostatically confined) one-component plasma. Some authors neglect the magnetic field entirely and perform molecular dynamics simulations of  $N$  charges in an effective potential well  $\phi_R$  [such simulations apply dynamically to charges in a Paul trap, neglecting the micromotion caused by the rf field (Rahman and Schiffer, 1986; Hasse and Avilov, 1991)]. While the dynamics of the particle trajectories

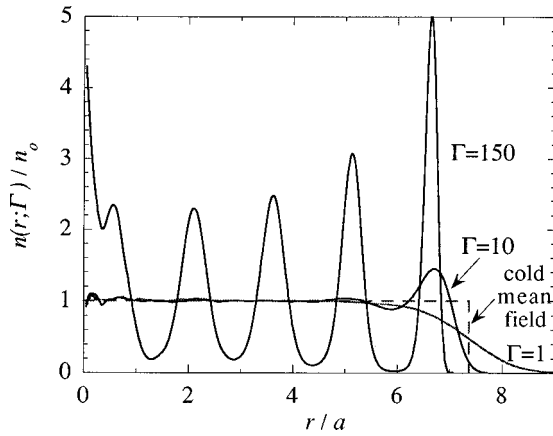


FIG. 22. Equilibrium density as a function of spherical radius  $r$  in a spherically symmetric ( $\alpha=\beta=1$ ) nonneutral plasma of  $N=400$  charges, for  $\Gamma=1, 10$ , and  $150$ . The density is normalized to the cold mean-field value  $n_-$ . Dashed line is the cold mean-field theory. From Dubin (1996).

are quite different from those of charges in a Penning trap, long time averages of any phase function  $G(\mathbf{r}_1, \dots, \mathbf{r}_N)$  are guaranteed to be identical to the results of molecular dynamics simulations that include the magnetic field. Other authors have integrated the equations of motion, including the Lorentz force of the applied magnetic field (Totsuji, 1987). One can also employ guiding-center dynamics in molecular dynamics simulations, which assumes that  $B$  is large, as is often the case in the experiments (Dubin and O'Neil, 1988). The effective potential  $\phi_R(r, z)$  is the same for guiding-center dynamics as for the actual dynamics except for a rescaling of the magnetic-field strength [i.e.,  $m\omega(\Omega_c - \omega) \rightarrow m\omega\Omega_c'$ ] because guiding-center dynamics neglects the centrifugal force. The advantage of using guiding-center dynamics is that the rapid cyclotron motion is averaged out and need not be followed numerically.

Using these numerical techniques, several authors have considered the effect of correlations on the density  $n(\mathbf{r})$  of particles in a harmonic trap. In the Monte Carlo method  $n(\mathbf{r})$  is obtained from a reduced distribution function using Eq. (4.7), whereas in molecular dynamics  $n(\mathbf{r})$  is evaluated through the time average of the Klimontovich density:

$$n(\mathbf{r}) = \frac{1}{T} \int_0^T dt \sum_{j=1}^N \delta[\mathbf{r} - \mathbf{r}_j(t)]. \quad (4.11)$$

In practice the procedure for obtaining  $n(\mathbf{r})$  is identical in both cases. The trap volume is cut into a grid of small subvolumes. For each generated configuration in Monte Carlo, or time step in molecular dynamics, the density is measured by counting the number of charges that fall within each subvolume; an average over many configurations (Monte Carlo) or long times (molecular dynamics) is then performed to reduce statistical noise.

Figure 22 shows the results of a Monte Carlo calculation for a range of  $\Gamma$  values from 1 to 150 for a cloud of 400 charges (Dubin, 1996). The rotation frequency  $\omega$

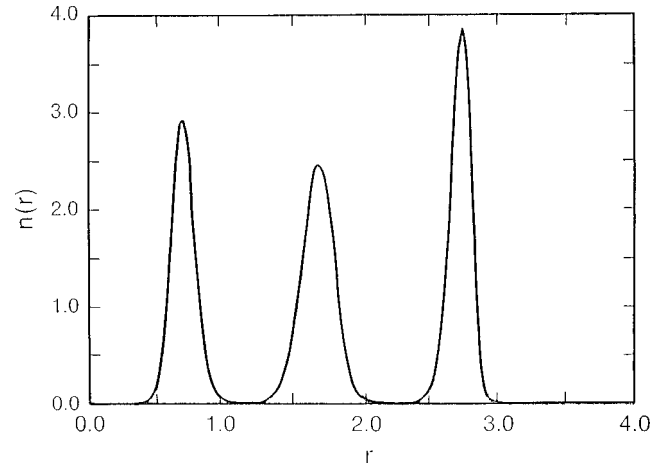


FIG. 23. Density as a function of spherical radius for  $N=100, \Gamma=140, \alpha=\beta=1$ . Position is in units of  $(3e^2/m\omega_z^2)^{1/3}$ , density is in units of  $(3e^2/m\omega_z^2)^{-1}$ . From Dubin and O'Neil (1988).

was chosen so that the effective trap potential  $\phi_R$  was spherically symmetric ( $\beta=1$ ). The average density  $n(r)$  was plotted as a function of spherical radius  $r$ . For  $\Gamma=1$  the density fell smoothly to zero in a manner qualitatively similar to the limit of weak correlation (see Fig. 9). As  $\Gamma$  increased, the plasma edge steepened, approaching the Heaviside step-function density of cold mean-field theory, shown in the figure as the dotted line. However, the density also began to exhibit oscillations near the plasma edge. These oscillations are evidence of local order—the damping length of the oscillations is a measure of the correlation length—and are a precursor to the formation of lattice planes. Such behavior has been seen in a similar system at moderate values of  $\Gamma$ , the one-component plasma with an edge (see, for example, Ichimaru, Iyetomi, and Tanaka, 1987, and references therein). Oscillatory density profiles are also expected to occur at the interface of simple liquids in contact with a wall (Hansen and McDonald, 1986).

As  $\Gamma$  increases further, the oscillations increase in magnitude until the density between the peaks approaches zero and the ion cloud separates into concentric shells. For  $N=100$  and  $\beta=1$  this occurs at  $\Gamma \sim 140$  [see Fig. 23 (Dubin and O'Neil, 1988)]. For larger clouds the  $\Gamma$  value required to separate the cloud into shells increases and a few interstitial charges sometimes appear to be caught between the shells, although there has been no systematic study of this phenomenon. The distance between shells is on the order of a Wigner-Seitz radius  $a$ , as one would expect. The distance between ions within a shell is also of order  $a$ . Thus the number of ions per shell roughly scales as the surface area of the shell, the number of shells roughly scales as  $N^{1/3}$ , and the average density equals  $n_-$ .

Shell structure is also observed when  $\beta$  is not equal to unity. For  $\beta \neq 1$  the overall shape of the cloud is very close to the spheroid of cold mean-field theory (see Fig. 24), but the cloud consists of concentric nested shells. The number of particles per unit area is approximately

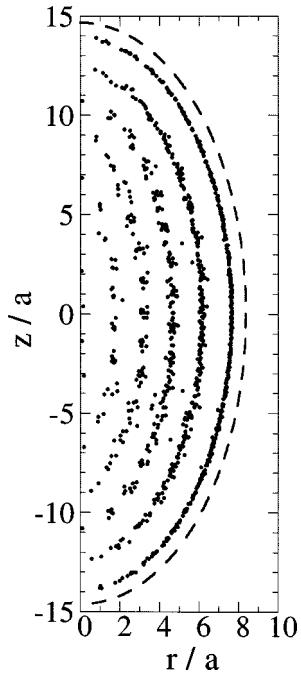


FIG. 24. Particle positions as a function of cylindrical radius  $r$  and axial position  $z$  in a crystallized ( $T=0$ ) plasma of  $N=1028$  charges,  $\beta=2.0$ . Dashed curve is the plasma edge in cold mean-field theory.

the same on each shell, and the distance between shells is also constant, of order the Wigner-Seitz radius  $a$ . This implies that the inner shells are typically not spheroids (ellipses of revolution), since the figure obtained by drawing a curve where each point on the curve is equidistant from an ellipse is not itself an ellipse. Instead, the inner shells are spheroidlike surfaces of revolution (Schiffer, 1995). The reason for this behavior will be discussed in Sec. IV.D.2. For  $\beta \rightarrow \infty$  (i.e.,  $\omega_z \rightarrow 0$ ) the plasma becomes cylindrical, and concentric cylindrical shells are observed to form (Rahman and Schiffer, 1986). When  $\beta \rightarrow 0$  (i.e.,  $\omega_z \rightarrow \infty$ ) the charges are compressed into a 2D system in the  $x$ - $y$  plane, and the system forms a distorted 2D hexagonal lattice rather than shells (Rafac *et al.*, 1991; Bedanov and Peeters, 1994). The 2D structure is similar to the bounded vortex lattices observed in superfluid helium, since such vortices also interact via a repulsive Coulomb potential, albeit of logarithmic rather than  $1/r$  form (Campbell and Ziff, 1979).

Concentric shell structures have been observed in experiments with  $\text{Be}^+$  ion plasmas that have been laser cooled into the strongly coupled regime (Gilbert, Bollinger, and Wineland, 1988). Figure 25 shows a schematic diagram of the apparatus used in these experiments. Three laser beams (perpendicular cooling beam, diagonal cooling beam, and probe beam) intersected the plasma cloud, exciting atoms in the various shells, and the resulting fluorescence was focused onto a photon-counting imaging tube located at one end of the cylindrical electrode assembly. The probe beam could be translated along the  $z$  axis in order to observe how the radii of the shells varied with  $z$ .

Figure 26 shows three images of shell structure to-

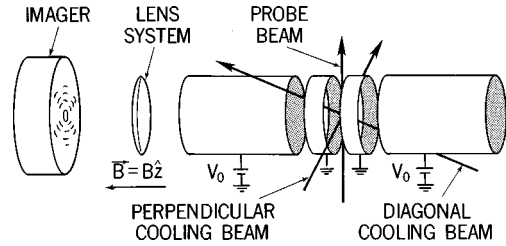


FIG. 25. Schematic diagram of apparatus used to image shell structure of strongly correlated  $\text{Be}^+$  ion plasmas (Gilbert, Bollinger, and Wineland, 1988). Three laser beams excite atoms in the various shells, and the resulting fluorescence is focused onto a photon-counting imaging tube.

gether with a length scale. Figure 26(a) shows a single shell for a small rather elongated cloud ( $N \approx 20, \alpha \approx 6.5$ ), Figure 26(b) shows sixteen shells (probe-beam fluorescence only) for a much larger, nearly spherical cloud ( $N \approx 15\,000, \alpha \approx 0.8$ ), and Fig. 26(c) shows eleven shells plus a central column for the same cloud under different trap parameters (and therefore different aspect ratio,  $\alpha \approx 2.4$ ). In this latter image, fluorescence from all three lasers is shown. The number of shells and the spacing between the shells is in qualitative agreement with the results of the computer simulations.

While in many cases the shells were spheroidlike, as expected from theory, in some cases the shells were open cylinders whose lengths varied so that the cylinders fit within an overall spheroidal shape. Figure 26(c) is an example of such cylindrical structure: it is apparent that the shells cut by the diagonal beam have the same cylindrical radius as those cut by the transverse probe and cooling beams, although the diagonal beam cuts these shells at different values of  $z$ . It has been suggested that shear between the shells (induced perhaps by laser

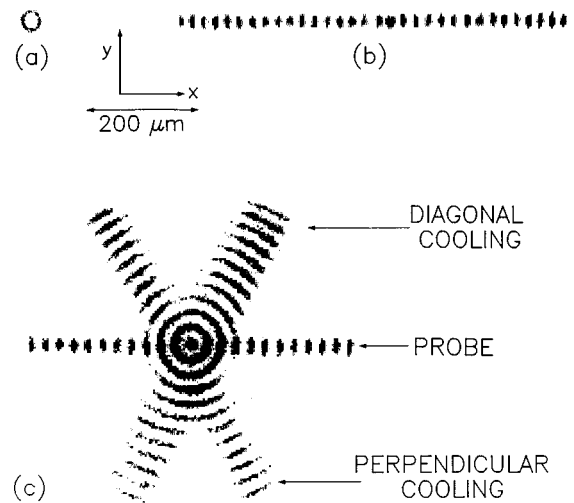


FIG. 26. Experimental images of shell structures: (a) A single shell in a cloud containing approximately 20 ions. (b) Sixteen shells in a cloud containing about 15 000 ions with  $\alpha \approx 0.8$ ; (c) Eleven shells plus a central column in the same cloud as (b) with  $\alpha \approx 2.4$ . This image shows ion fluorescence from all three laser beams. From Gilbert, Bollinger, and Wineland (1988).

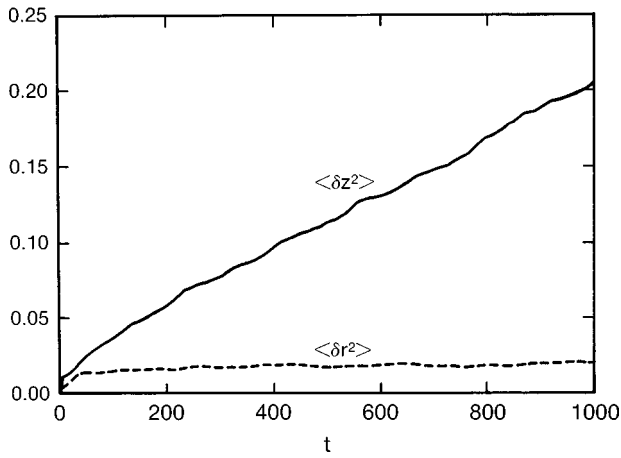


FIG. 27. Mean-square change in position versus time for the plasma shown in Fig. 23 and for  $\Omega_c/\omega_z=10$ . Taken from Dubin and O'Neil (1988). Position is measured in units of  $(3e^2/m\omega_z^2)^{1/3}$ , time is in units of  $\omega_z^{-1}$ .

torques) may account for this discrepancy between the experiments and theory based on thermal equilibrium. However, no definite explanation of this effect has been found as yet.

In the simulations the ions appear to be well confined within the shells—ions rarely hop from one shell to another. This observation can be quantified by measuring the mean-square change in the radial position of the ions in molecular dynamics simulations when the cloud is spherical (Dubin and O'Neil, 1988):

$$\langle [\delta r(t)]^2 \rangle = \frac{1}{MN} \sum_{i=1}^N \sum_{j=1}^M [r_i(t_j+t) - r_i(t_j)]^2, \quad (4.12)$$

where  $t_j - t_{j-1}$  is a constant time offset and  $t < t_j - t_{j-1}$ . For the  $N=100$ ,  $\Gamma=140$ , and  $\beta=1$  case of Fig. 23, one observes that  $\langle [\delta r(t)]^2 \rangle$  is almost constant. On the other hand, ions do diffuse within the shells. This can be seen by examining the mean-square change in  $z$  position,  $\langle [\delta z(t)]^2 \rangle$ , defined in an analogous manner to Eq. (4.12). This function increases linearly with time provided that  $\langle [\delta z(t)]^2 \rangle$  is small compared to the radius of the cloud (see Fig. 27), so we may obtain an average diffusion coefficient in the  $z$  direction through the definition  $\langle \delta z^2(t) \rangle = 2D_{zz}t$ . As  $\Gamma$  increases,  $D_{zz}$  is observed to decrease (see Fig. 28), but it remains nonzero even at rather large  $\Gamma$  values, showing no abrupt transition to a crystallized state. Thus the system behaves like a fluid within each shell, but can be characterized as a solid in the direction perpendicular to the shells, since charges are localized within a given shell. Similar behavior is observed in smectic liquid crystals.

For very large values of  $\Gamma$  the particle diffusion within the shells ceases and the charges in each shell are confined to a distorted 2D hexagonal lattice. In addition, there can be a few “interstitial” charges caught between shells. The hexagonal symmetry is immediately apparent when one views one of the shells in the rotating frame. Figure 29 shows a projection of one-half of the outer shell for an  $N=256$  spherical plasma (O'Neil, 1988).

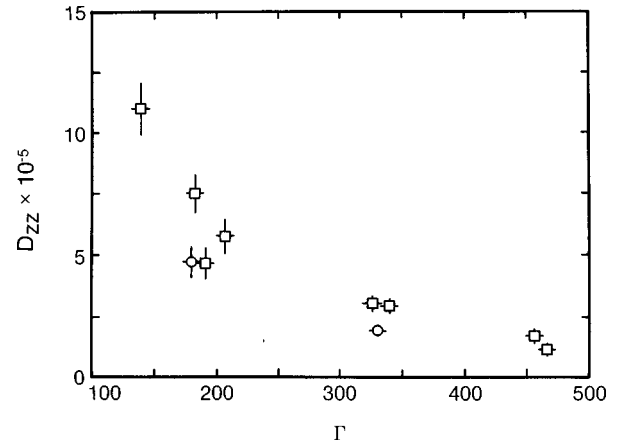


FIG. 28. Average single-particle diffusion in  $z$  direction as a function of  $\Gamma$  in spherical plasmas. Squares  $N=100$ ; circles  $N=256$ ;  $\Omega_c/\omega_z=10$ . Position is measured in units of  $(3e^2/m\omega_z^2)^{1/3}$ , time is in units of  $\omega_z^{-1}$ . From Dubin and O'Neil (1988).

While most charges have six nearest neighbors in a hexagonal arrangement, twelve pentagonal defects also occur. There is always an ion at the center of the pentagon, although in some cases this charge is an interstitial. This state is a local equilibrium that can be loosely thought of as the  $\Gamma=\infty$  or  $T=0$  limit. However, there are many other local minima in the potential energy of the system. Many simulations have been run in which clouds have been cooled to large  $\Gamma$  values starting with different initial conditions, and, while the final state can vary slightly from case to case, the overall hexagonal structure within the shells is preserved.

An example of a larger system is also displayed in Figs. 30 and 31. In Fig. 30 the equilibrium positions of  $N=4096$  charges cooled to a local minimum-energy

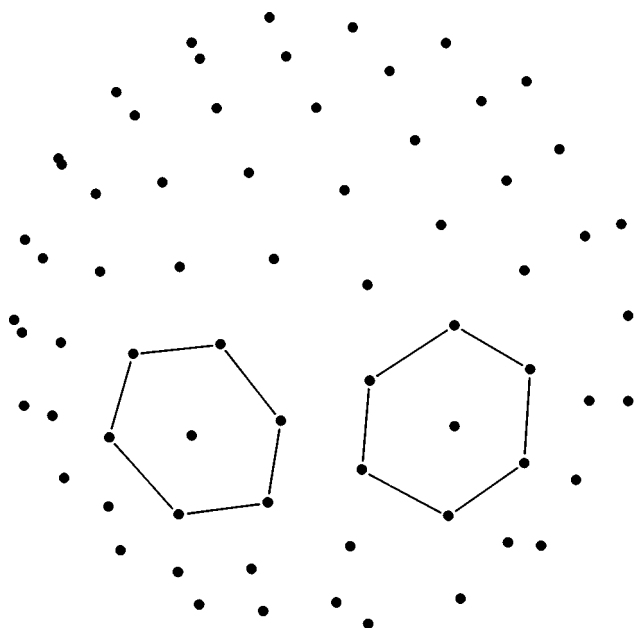


FIG. 29. Half of the outer shell of a spherical cloud of  $N=256$  charges, projected onto the  $x-y$  plane (O'Neil, 1988).



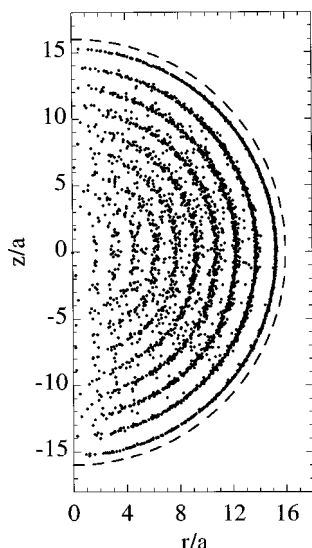


FIG. 30. Particle positions as a function of cylindrical radius  $r$  and axial position  $z$  in a crystallized plasma of  $N=4096$  charges,  $\alpha=\beta=1$ . Cold mean-field theory for the plasma edge follows the dashed curve.

state with spherical symmetry are displayed as a function of cylindrical radius  $r$  and  $z$ . As can be observed here, it is typically the case that the outer shell is the best defined while the inner shells become progressively less well defined and more interstitials appear. In some cases, however, the shells nearest the center of the plasma are also quite well defined, as though the particles in the center, far from the boundaries, preserved some information concerning the overall spherical symmetry of the plasma (see, for example, Fig. 22).

The hexagonal structure in the outer shell of the large plasma is immediately apparent when a projection of half the shell is performed, as in Fig. 31. Here we have also determined the number of nearest neighbors for each particle in the shell using Wigner-Seitz construc-

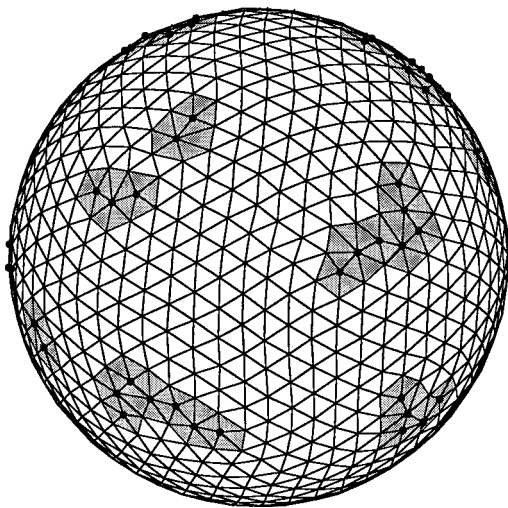


FIG. 31. Half of the outer shell of the  $N=4096$  cloud of Fig. 30. Wigner-Seitz construction employed to connect nearest neighbors. Regions of dislocations are shaded.

tion, and have connected the nearest neighbors. Several defects in the structure are apparent; such defects must occur in any lattice on a closed surface except for a few special cases such as the Platonic solids. However, the defects do appear to group together into areas surrounded by relatively large regions of good hexagonal order. Whether there is a preferred arrangement for the defects on the surface is an outstanding question.

The number of defects have been studied carefully for  $N \leq 10^3$  (Tsuruta and Ichimaru, 1993). The defects are constrained by the geometry of the convex shell in which they lie. Euler's theorem (Britannica Online, 1998) states that for any convex polytope the number of vertices  $V$ , the number of edges  $E$ , and the number of faces  $F$  satisfy  $V + F = E + 2$ . If we define  $N(x)$  to be the number of particles in the shell with  $x$  nearest neighbors, a straightforward application of this theorem yields

$$\sum_x (6-x)N(x) = 12. \quad (4.13)$$

If only  $N(5)$  and  $N(6)$  are nonzero, then Eq. (4.13) implies that  $N(5)=12$ . This result is consistent with the defect structure for many cases. However, as one can see in Fig. 31, other types of defects also occur:  $N(5)$  and  $N(7)$  are nonzero, and particles with eight nearest neighbors sometimes occur as well. However, Eq. (4.13) must be satisfied. For example, in the  $N=4096$  case shown in Fig. 31, the number of particles in the outer shell is 1040, and  $N(5)=49$ ,  $N(7)=35$ ,  $N(8)=1$ ; these numbers satisfy Eq. (4.13).

Of course the number of defects quoted above are only approximate, particularly for the larger clouds. There are many local minimum-energy states with differing numbers of defects. Since these defects distort the surrounding lattice they cost energy, and so the minimum-energy state is expected to have a small number of defects. By carefully cooling and reheating the cloud several times one can anneal the cloud and come close to the absolute minimum-energy state; however, for large  $N$ , constraints on computer time do not allow one to be sure of finding the absolute minimum. For example, for the  $N=256$  case displayed in Fig. 29,  $N(5)=12$  and there are no other types of defects in the outer shell. In the simulations performed by Tsuruta and Ichimaru (1993) the system was cooled to a slightly different minimum-energy state, with  $N(5)=16$  and  $N(7)=4$ . Nevertheless, the overall trends displayed in Fig. 32 of increasing numbers of defects but a smaller percentage of defects with increasing shell size do appear to occur even when considerable effort is employed to find the minimum-energy states.

The value of  $\Gamma$  required to crystallize the charges within the shells appears to vary sensitively with  $N$  and  $\beta$ . This has not been studied carefully because the melting temperature also appears to vary sensitively with the particular local minimum configuration in which the system is initially trapped. Nevertheless, it may be useful to discuss a few particular cases. For  $\beta=1$  and  $N=100$  the charges continue to diffuse even for  $\Gamma$  values of 800–1000, whereas for the  $\beta=1$ ,  $N=256$  case diffusion ceases

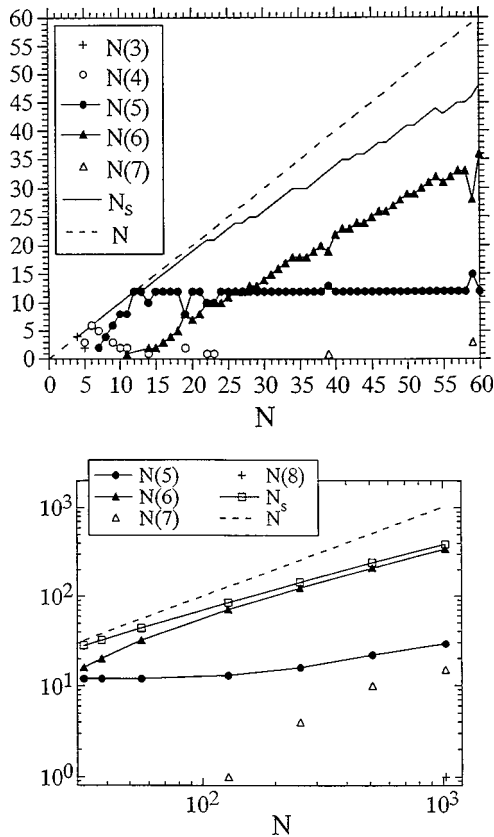


FIG. 32. Number of particles  $N(x)$  with  $x$  nearest neighbors in the outer shell of a spherical crystallized plasma with  $N$  particles; (a)  $4 \leq N \leq 60$ ; (b)  $32 \leq N \leq 1024$ . From Tsuruta and Ichimaru (1993).

at  $\Gamma \sim 380$  for the local minimum whose outer shell is depicted in Fig. 29. These  $\Gamma$  values are considerably larger than the critical value  $\Gamma \approx 174$  for a fluid-bcc transition in an infinite homogeneous system. Furthermore, the observed shell structure is incompatible with bcc symmetry.

The differences between bcc symmetry and the shell structure are apparent in the probability function  $c(r)$  (Rahman and Schiffer, 1986; Dubin and O'Neil, 1988). This function provides the probability density of finding two charges at a distance  $r$  from each other, averaged over some given set of particles. For an infinite homogeneous system,  $c(r) = 1 + g(r)$ , where  $g(r)$  is the angle-averaged correlation function.  $c(r)$  is related to the coordination number  $N(r)$  by the equation

$$N(r) = n_- \int_0^r c(r) 4\pi r^2 dr. \quad (4.14)$$

The coordination number is the average number of particles within a distance  $r$  of any given charge in the set. This function can be used to determine the average number of nearest neighbors around each charge.

Figure 33(a) shows  $c(r)$  for the interior of the crystalline cloud of  $N = 4096$  charges shown in Figs. 30 and 31, counting only particles with positions  $r_i \leq 10a$  in order to avoid surface effects (the particles in the outer shell have fewer nearest neighbors than those in the interior

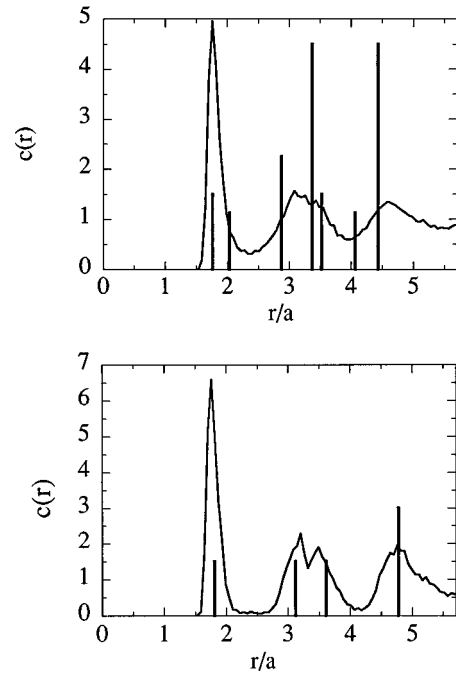


FIG. 33. Spatial correlation in a mesoscopic plasma: (a) Two-particle probability function  $c(r)$  within the cloud of  $N = 4096$  charges shown in Figs. 30 and 31; (b) Same as (a) but only counting charges within the outer shell.

of the cloud). Also shown for comparison is  $c(r)$  for a bcc lattice of the same density. As can be seen from Fig. 34(a), which plots  $c(r)$  versus the coordination number  $N(r)$ , the first peak in  $c(r)$  contains about 14 charges, which equals the number of first and second nearest neighbors of the bcc lattice. However, there is no other resemblance between the correlation function of the bcc lattice and that of the cloud. The decaying oscillations observed in  $c(r)$  are reminiscent of the fluid phase and are not substantially modified by increasing  $N$  up to values as high as 20 000 [the largest number that has been simulated so far (Schiffer, 1995, p. 191)]. From such a correlation function one might conclude that the charges are in a disordered or glassy state.

However, if one considers the correlations between charges only within a given shell, the order apparent in Fig. 29 or 31 reemerges. Figure 33(b) displays  $c(r)$  counting only the charges within the outer shell of the same cloud of  $N = 4096$  charges as in Fig. 33(a). Also shown is  $c(r)$  for a 2D hexagonal lattice. The 2D hexagonal lattice is apparent in both the position of the peaks and the number of nearest neighbors within the shell. The number of nearest neighbors can be determined by evaluating the 2D coordination number

$$N_{2D}(r) = \sigma \int_0^r c(r) 2\pi r dr, \quad (4.15)$$

where  $\sigma$  is the average number of particles per unit area in the shell. The probability function is plotted versus  $N_{2D}(r)$  in Fig. 34(b), showing that there are six nearest neighbors in the first peak of  $c(r)$  and twelve particles in the next two peaks, as expected for a 2D hexagonal lattice.

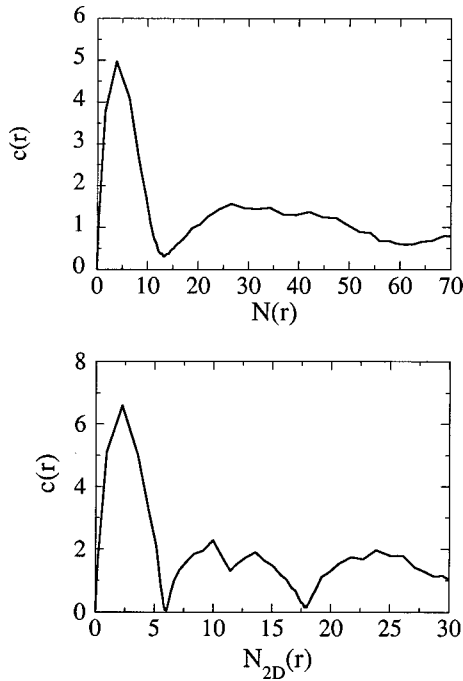


FIG. 34. Determination of nearest neighbors: (a)  $c(r)$  of Fig. 33(a) plotted vs coordination number  $N(r)$ ; (b) Same as (a) but only counting charges within the outer shell.

Apparently, the concurrence of good two-dimensional order within a shell along with low three-dimensional order is caused by a lack of spatial correlation between charges in neighboring shells. The number of charges per unit area is nearly the same in each shell. The 2D lattices in neighboring shells then go “out of phase” with each other as one moves from point to point along the shell, since an equal interparticle spacing will subtend a different angle in different shells.

The lack of spatial correlation between shells explains the 2D hexagonal structure observed in the simulations. It is well known that the preferred lattice structure of a 2D one-component plasma of charges confined in a plane is 2D hexagonal (Cole, 1974). In the shell-structure phase each shell can be thought of as a 2D one-component plasma, distorted into a closed surface and substantially uncorrelated with the other shells; hence the 2D hexagonal lattice. Indeed, this picture of the system forms the basis of a useful model of the shell-structure phase that we consider in Sec. IV.D.

### C. Large plasmas

We say that a plasma is large when the influence of the surface is limited to a surface layer that is thin by comparison to the plasma dimensions. Rather than the shell structure observed in mesoscopic plasmas, large plasmas have interior correlation properties that are the same as those for an infinite homogeneous one-component plasma. Therefore we first review the thermal equilibrium properties of the infinite homogeneous OCP.

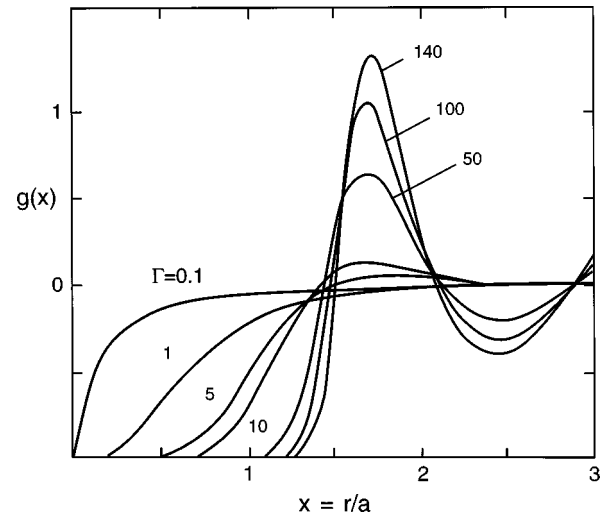


FIG. 35. The two-particle correlation function  $g(r)$  for a one-component plasma at various values of the correlation parameter  $\Gamma$ . From Ichimaru (1982).

#### 1. The correlation function of the one-component plasma

In an infinite homogeneous plasma the correlation function  $g(\mathbf{r}_1, \mathbf{r}_2)$ , defined by Eq. (4.8), is a function only of  $\mathbf{r}_1 - \mathbf{r}_2$ . In a weakly correlated OCP an expansion of the second equation in the equilibrium Bogoliubov-Born-Green-Kirkwood-Yvon (BBGKY) hierarchy in the small parameter  $\Gamma$  yields the well-known expression for  $g(\mathbf{r})$  (Montgomery and Tidman, 1964; Ichimaru, 1973):

$$g(\mathbf{r}) = \frac{-e^2}{kT} \frac{e^{-r/\lambda_D}}{r}. \quad (4.16)$$

Thus the correlation length in a weakly correlated plasma is the Debye length  $\lambda_D$ : particles separated by a distance larger than  $\lambda_D$  are screened from one another and so are uncorrelated. However, when  $\Gamma \geq 1$  this expression is no longer valid. The Debye length becomes less than an interparticle spacing and is no longer physically meaningful. In the strongly correlated regime,  $g(\mathbf{r})$  has been evaluated using large-scale Monte Carlo simulations of the homogeneous OCP in periodic boundary conditions (Hansen, 1973; Slattery, Doolen, and DeWitt, 1980; Stringfellow, DeWitt, and Slattery, 1990), as well as through analytic approximations such as the hypernetted-chain approximation (Ichimaru, Iyetomi, and Tanaka, 1987, and references therein). Simulation results for  $g(\mathbf{r})$  are displayed in Fig. 35 for different values of  $\Gamma$ . It is apparent that when  $\Gamma > 1$  the length scale over which  $g$  approaches zero (the correlation length) is of order  $a$  rather than  $\lambda_D$ . Furthermore, as  $\Gamma$  increases beyond about 2, oscillations begin to appear in  $g(\mathbf{r})$ . These oscillations signify the onset of local ordering—a characteristic of a fluid. However, there is apparently no discontinuous vapor-liquid phase transition; rather, the system behaves like a fluid beyond the critical point. This observation is consistent with the hypothesis that a vapor-liquid phase transition requires an attractive component to the interaction between particles (Alder and Wainwright, 1957).

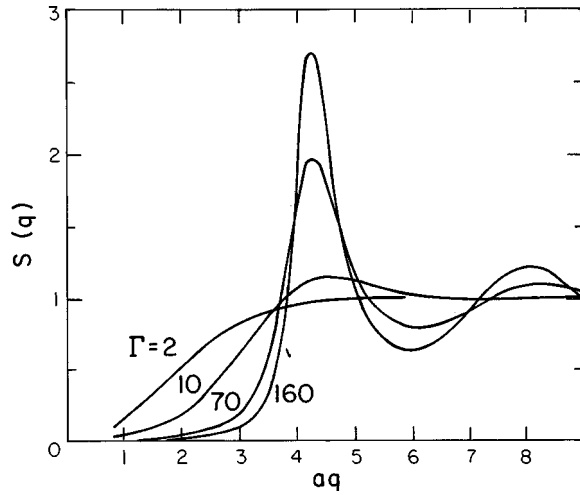


FIG. 36. The static structure factor  $S(k)$  for a one-component plasma at various values of  $\Gamma$ . From Ichimaru (1982).

As  $\Gamma$  increases further, the oscillations in  $g(\mathbf{r})$  become more pronounced and the correlation length increases. Finally, at  $\Gamma \sim 174$  a first-order phase transition to a bcc crystalline phase with long-range order is predicted to occur. This prediction is based on a comparison of the Helmholtz free energy of the fluid phase to that of the crystalline phase and is considered in more detail in the next subsection. For a perfect bcc lattice,  $g(\mathbf{r})$  is anisotropic. At  $T=0$  it consists of an infinite sum of delta functions at the bcc lattice sites,

$$g(\mathbf{r}) = n^{-1} \sum'_{\mathbf{p}} \delta(\mathbf{r} - \mathbf{p}) - 1, \quad (4.17)$$

where the set of lattice points is  $\mathbf{p}/a = (3/8\pi)^{1/3} [\hat{x}(l-m+n) + \hat{y}(l+m-n) + \hat{z}(-l+m+n)]$  for integers  $l$ ,  $m$ , and  $n$ ; the prime on the sum indicates that the point  $\mathbf{p} = 0$  is not included.

The Fourier transform of  $g(\mathbf{r})$  is also of interest:

$$S(\mathbf{k}) = 1 + n \int d^3r e^{-i\mathbf{k} \cdot \mathbf{r}} (g(\mathbf{r}) + 1). \quad (4.18)$$

This function, called the static structure factor, can be directly measured in Bragg scattering experiments. In the fluid phase,  $S$  is a function only of the magnitude of  $\mathbf{k}$  and, like  $g(\mathbf{r})$ , displays decaying oscillations (see Fig. 36). However, in the solid phase  $S(\mathbf{k})$  becomes anisotropic and is sharply peaked around particular  $\mathbf{k}$  values corresponding to the lattice reciprocal to  $\{\mathbf{p}\}$ . At zero temperature, Eq. (4.17) can be used in Eq. (4.18) to obtain

$$S(\mathbf{k}) = N \sum_{\mathbf{g}} \Delta(\mathbf{g} - \mathbf{k}), \quad (4.19)$$

where  $\Delta(\mathbf{x})$  is a Kronecker delta function and the set  $\{\mathbf{g}\}$  is the set of lattice points reciprocal to the set  $\{\mathbf{p}\}$ . For example, when  $\{\mathbf{p}\}$  is a bcc lattice  $\{\mathbf{g}\}$  is fcc, and vice versa (Kittel, 1976). Thus measurement of  $S(\mathbf{k})$  provides direct evidence of spatial correlations.

Recently, Bragg scattering experiments that probe  $S(\mathbf{k})$  were performed (Tan, Bollinger, Jelenkovic, and

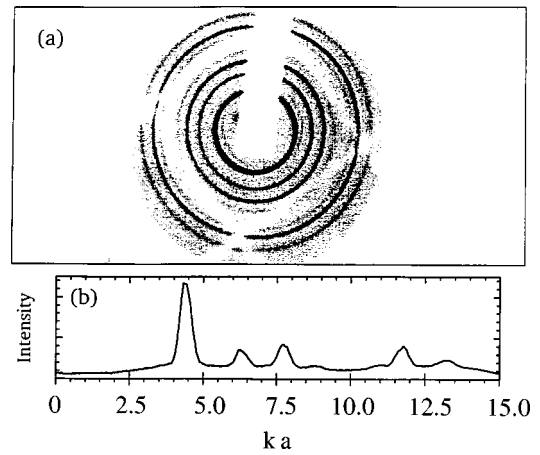


FIG. 37. Evidence of long-range order: (a) Observed Bragg scattering pattern from  $N = 2.7 \times 10^5$  ions. The pattern is partially blocked by the shadow from various trap components. (b) Intensity vs scattered wave number  $k$  normalized to the Wigner-Seitz radius  $a$ . From Tan *et al.* (1995a, 1995b) and Itano *et al.* (1998).

Wineland, 1995a; Tan *et al.*, 1995b, p. 387; Itano, Bollinger, Tan, Jelenkovic, Huang, and Wineland, 1998). In these experiments a laser beam was directed along the  $z$  axis of the trap. A small amount of this light was scattered by the ions and it was this signal, picked up with a photo cathode positioned as in Fig. 25, that was used to reconstruct  $S(k)$ . This was difficult since the laser operated in the UV at 313 nm and the ions were spaced by microns, so the scattering angle was quite small. Nevertheless, by using polarized light and by careful positioning of a beam dump for the unscattered beam, Tan *et al.*, were able to observe Bragg rings in the scattered light. An image of the rings is shown in Fig. 37(a) for a cloud with  $2 \times 10^5$   $\text{Be}^+$  ions. The pattern is partially blocked by the beam dump and by a wire mesh; nevertheless, several rings can be observed which are evidence of long-range order. The angle  $\theta$  subtended by a Bragg ring is inversely proportional to  $a$ , a fact which was verified by changing the plasma density using laser torque. Figure 37(b) is a differential scattering cross section (i.e., scattered light intensity versus scattered wave number  $k$ ) generated from Fig. 37(a) by averaging the photon counts azimuthally about the  $z$  axis. The scattered wave number  $k$  is determined from the scattering angle  $\theta$  observed in Fig. 37(a) via the Bragg relation  $k = 2q \sin(\theta/2) \approx q\theta$ , where  $q$  is the wave number of the incident light. Thus each Bragg peak in Fig. 37(b) corresponds to a ring in Fig. 37(a).

Several such patterns were created by heating and re-cooling the cloud. Figure 38(a) shows a histogram of the number of observed Bragg peaks as a function of their position  $ka$ . Here  $a$  is measured from the density of the plasma, known to about 5% accuracy from the rotation frequency. The positions of the peaks are consistent with bcc order. Even better agreement is obtained by allowing  $a$  to be a fitting parameter, as shown in Fig. 38(b). A histogram was employed in Fig. 38 because in any one ring pattern, only a few of the many possible bcc Bragg peaks were observed [see Fig. 37(b)]. When the plasma

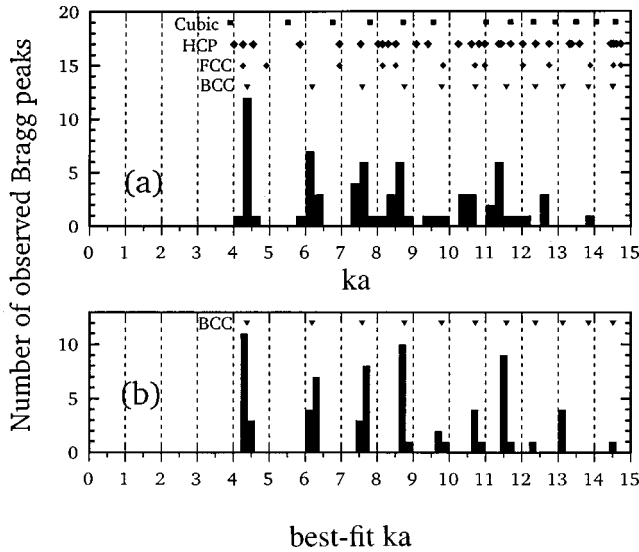


FIG. 38. (a) Histogram counts the number of observed peaks (not intensity) from various diffraction patterns of the same cloud ( $N = 2.7 \times 10^5$  ions), with no adjustable parameters; (b) Same as (a), but allowing  $a$  to be determined as a fitting parameter; now even large  $k$  peaks fit the bcc lattice pattern. Ticks indicate positions of Bragg peaks for various lattice types. From Tan *et al.* (1995a, 1995b), and Itano *et al.* (1998).

was heated and recooled different ring positions would emerge. The reason for this behavior became apparent after a second more sophisticated experiment, in which the Laue pattern was directly observed using a stroboscopic technique that removed the effect of plasma rotation (Tan *et al.*, 1995b; Itano *et al.*, 1998). The Bragg scattering pattern from a single stationary crystal consists of dots (the Laue pattern). The pattern of dots depends on the orientation of the crystal with respect to the incident beam. In the experiments the crystal rotated, so the dots became rings. However, at any given point in a ring, the light intensity was modulated at some multiple of the rotation frequency. This modulation was observed and used to determine the rotation frequency to high accuracy. The photon fluorescence detector used to image the Bragg pattern was strobed at this frequency, resulting in an image of the Laue dots. The observed Laue patterns were often consistent with a single bcc crystal oriented with a fourfold symmetry axis [the (100) plane] along the laser [Fig. 39(a)]. Although a square pattern is also consistent with an fcc (100) plane oriented along the laser, the absolute magnitude of the scattering angles was consistent only with bcc order. Other orientations also occurred. In Fig. 39(b), a sixfold symmetry pattern consistent with the bcc (111) plane oriented parallel to the beam is shown, and in Fig. 39(c), a pattern consistent with the orientation of the bcc (1,1,-5) plane along the laser is shown. Apparently in each case displayed here the pattern was created by a single bcc crystal rather than several randomly oriented bcc crystallites, which would have produced rings at every allowed Bragg angle rather than a single Laue pattern. These data are the first direct evidence of crystallization in an effectively infinite homogeneous OCP.

## 2. Correlation energy

The thermodynamic expression for the energy of an infinite OCP is given by (Brush, Sahlin, and Teller, 1966)

$$U = \frac{3}{2} NkT + U_{\text{corr}}, \quad (4.20)$$

where the first term is the average kinetic energy and the second term is the average potential energy due to Coulomb interactions:

$$\frac{U_{\text{corr}}}{NkT}(\Gamma) = \frac{e^2 n_-}{2kT} \int d^3\mathbf{r} \frac{g(\mathbf{r})}{r}. \quad (4.21)$$

Because there is a neutralizing background charge the potential energy would be zero except for correlations. Therefore the average potential energy is often referred to as the correlation energy; it is also often referred to as the excess internal energy.

This quantity has been carefully studied through both analytic approximations and large-scale numerical simulations. For nearly uncorrelated plasmas, the classic analytic expansion techniques for neutral gases such as the virial expansion do not work because of the long-range nature of the Coulomb interaction. However, for  $\Gamma \ll 1$  one can employ Eq. (4.16) in Eq. (4.21) to obtain the Debye-Huckel approximation to the correlation energy (Landau and Lifshitz, 1980, p. 242),

$$\frac{U_{\text{corr}}}{NkT} = -\frac{2\pi e^4 n_-}{(kT)^2} \int_0^\infty dr e^{-r/\lambda_D} = -\frac{\sqrt{3}}{2} \Gamma^{3/2}. \quad (4.22)$$

Although the interparticle potential is repulsive, the correlation energy is negative because of the uniform neutralizing background. Around a given charge a correlation hole develops in which it is unlikely to find other particles due to the repulsion between like charges. This correlation hole has an opposite neutralizing charge associated with it because of the neutralizing background, and the hole and the charge at its center have a negative potential energy.

The idea of a correlation hole can be used to estimate the correlation energy of the OCP for larger values of  $\Gamma$  (Ichimaru, 1982). Consider the situation depicted in Fig. 40. For large  $\Gamma$  the charges repel one another and are roughly equally spaced at a distance of order  $a$ . We then dissociate the infinite homogeneous OCP into a collection of  $N$  charges together with a spherical piece of the uniform background of radius  $a$  and equal but opposite charge. Since the spheres do not overlap, and since the total charge within each sphere is zero, there is no interaction between the spheres and the potential energy is just the sum of the potential energy of each sphere. A straightforward electrostatics calculation provides us with this energy:

$$\frac{U_{\text{corr}}^{\text{sphere}}}{NkT} = -\frac{9}{10} \Gamma. \quad (4.23)$$

The correlation energy has been evaluated numerically by a number of authors over several decades in a



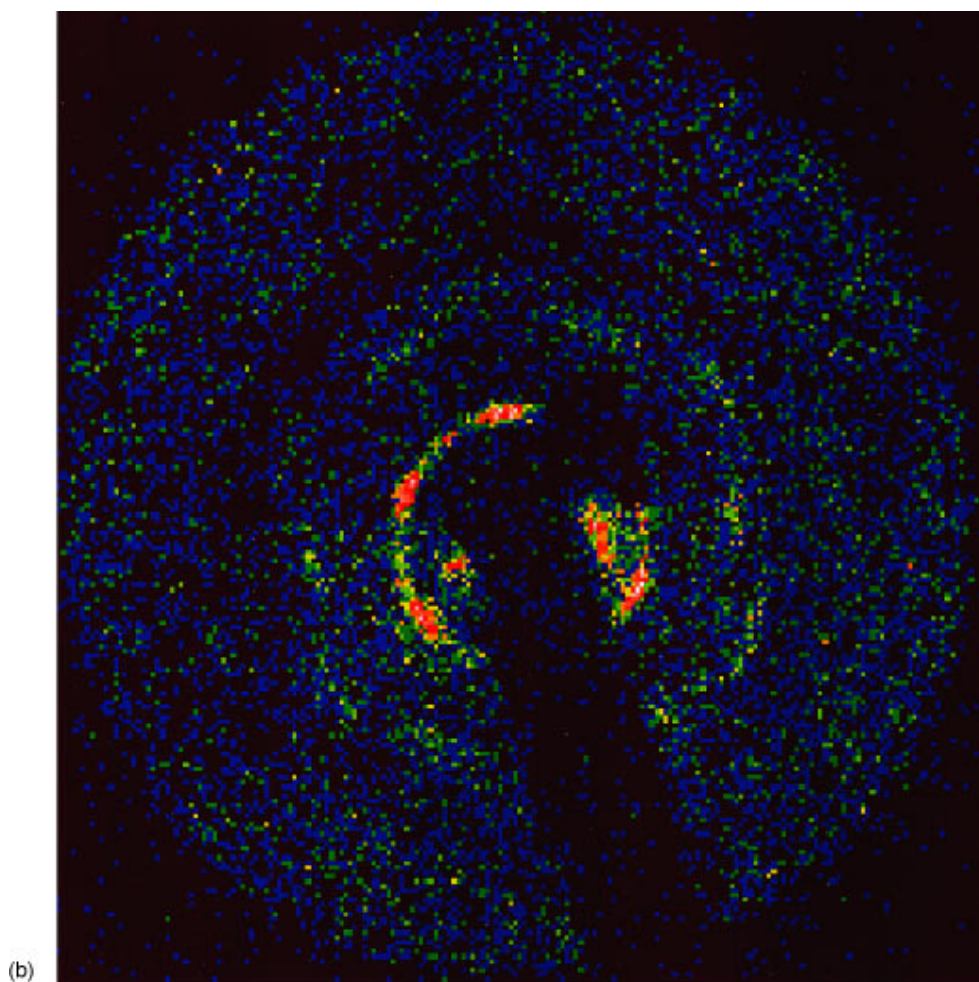
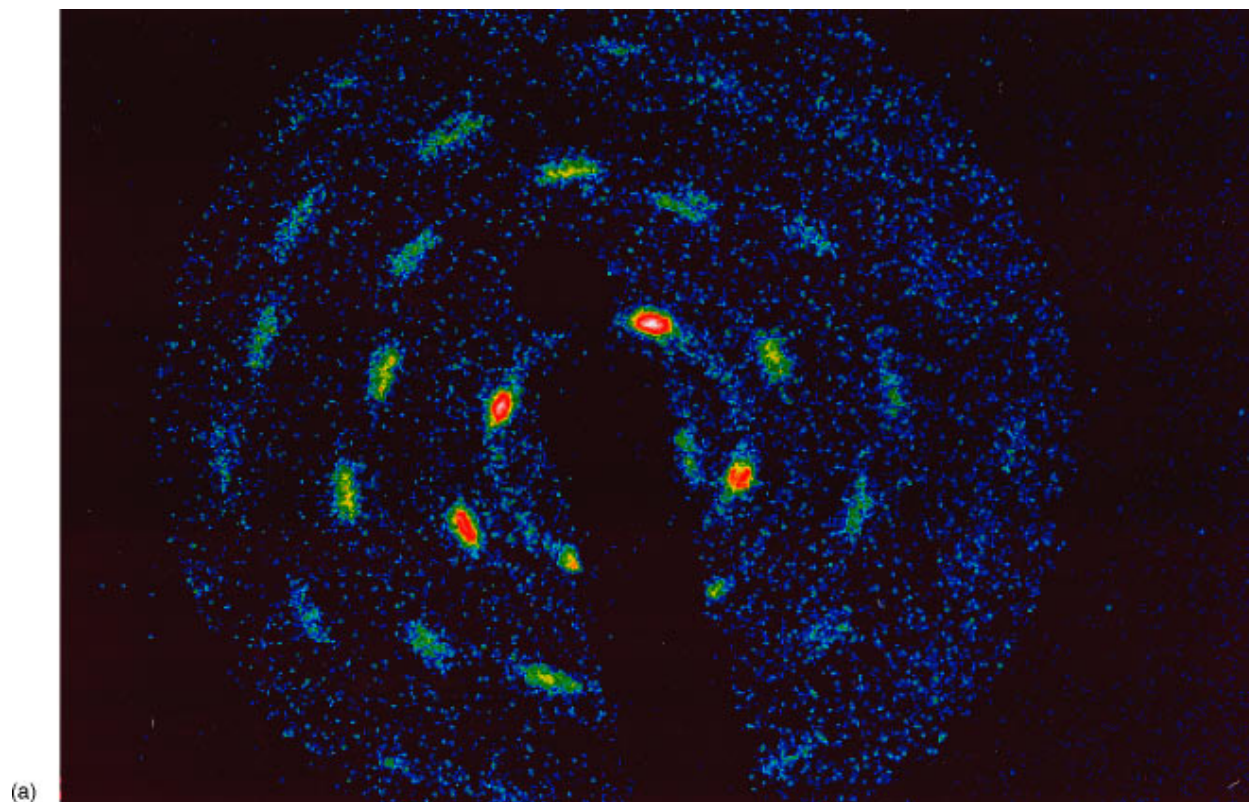


FIG. 39. (Color) Images of Laue patterns created by Bragg scattering off of different clouds, made by gating the photocathode at the rotation frequency. From Tan *et al.* (1995a, 1995b), and Itano *et al.* (1998).



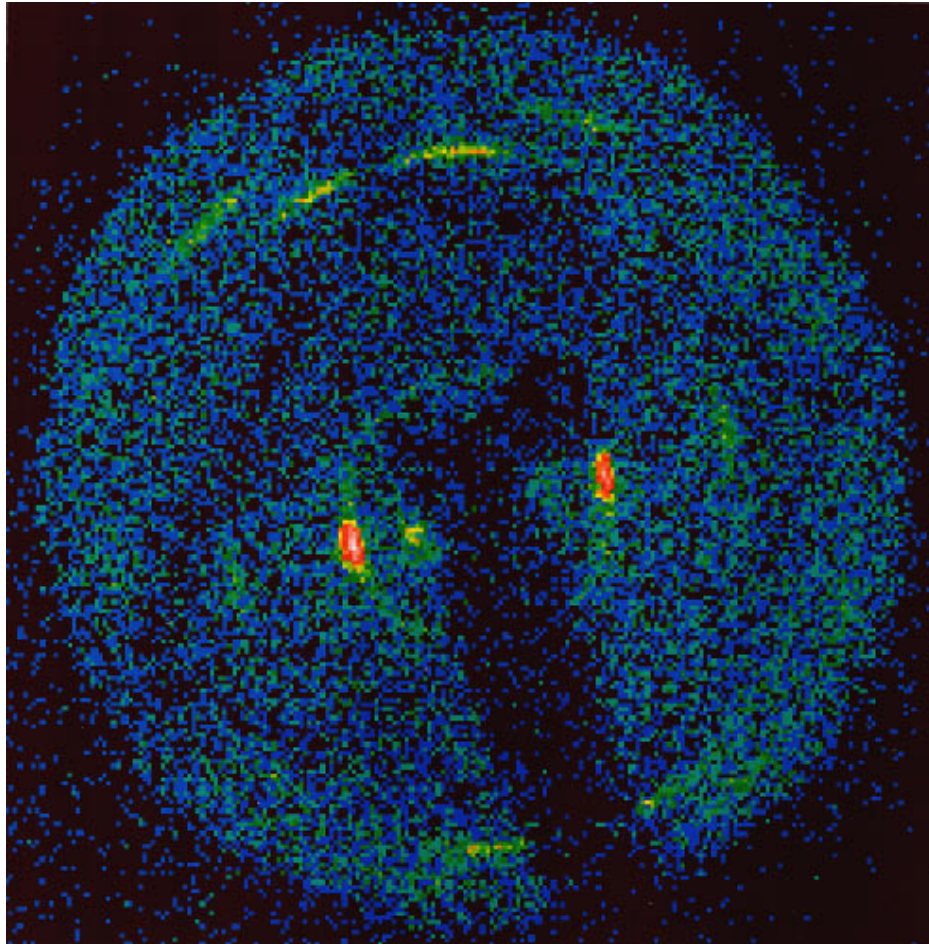


FIG. 39. (Continued).

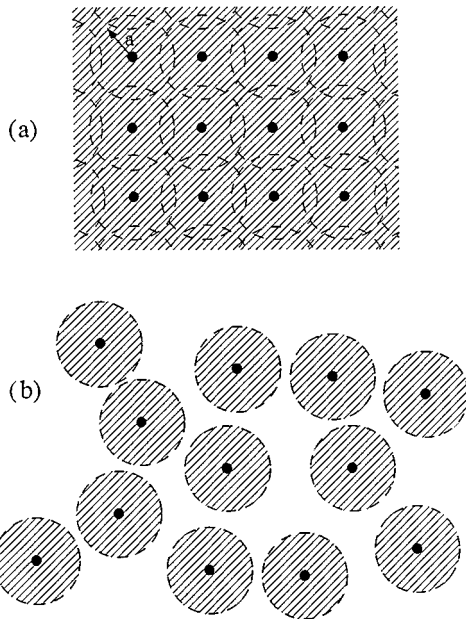


FIG. 40. Dissociation of an infinite one-component plasma into ion spheres.

series of increasingly accurate Monte Carlo simulations, as faster and faster computers became available. The latest work provides separate results for  $U_{\text{corr}}$  in the fluid and solid phases. In the fluid phase the Monte Carlo data are well described for  $\Gamma \geq 1$  by the semiempirical fitting function

$$\frac{U_{\text{corr}}^{\text{fluid}}}{NkT} = a\Gamma + b\Gamma^{1/3} + c, \quad (4.24)$$

where  $a = -0.90$ ,  $b = 0.590673$ ,  $c = -0.26569$  (Stringfellow, DeWitt, and Slattery, 1990). Note that at large  $\Gamma$  values, Eq. (4.24) implies that  $U_{\text{corr}}$  is close to the ion-sphere model, Eq. (4.23).

Turning to the solid phase, for which  $\Gamma \gg 1$ , we use an expansion of  $U_{\text{corr}}$  in powers of  $(1/\Gamma)$ :

$$\frac{U_{\text{corr}}^{\text{solid}}}{NkT} = A_{-1}\Gamma + A_0 + \frac{A_1}{\Gamma} + \frac{A_2}{\Gamma^2} + \cdots. \quad (4.25)$$

TABLE I. Expansion coefficients in the free energy of the solid phase for various lattices.

	$A_{-1}$	$A_0$	$\langle \ln(\omega_p/\omega_n) \rangle$	$A_1$	$A_2$	$A_3$
bcc	-0.895929	1.5	2.4939	10.84	352.8	$1.794 \times 10^5$
fcc	-0.895874	1.5	2.4537	12.35	-36.46	$3.051 \times 10^5$
hcp	-0.895838	1.5	2.4481	←	unknown	→

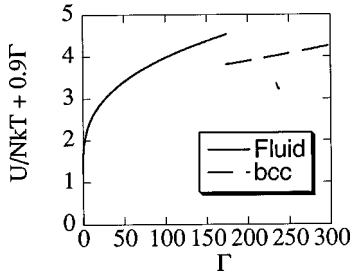


FIG. 41. Internal energy  $U$  vs correlation parameter  $\Gamma$  for an infinite classical one-component plasma for both fluid and solid phases: (dashed line, bcc; solid line, fluid). The ion-sphere energy  $-0.9\Gamma$  is subtracted in order to more easily observe the variation of  $U$  with  $\Gamma$ .

The constants  $A_{-1}$  and  $A_0$  follow from harmonic lattice theory:  $A_0 = 3/2$  is the thermal correction associated with an ideal gas of phonons, while  $A_{-1}$  is half the Madelung energy of the static lattice. Values of  $A_{-1}$  are listed for several lattices in Table I; note that they are all close to the ion-sphere model. The bcc and fcc constants differ only by one part in  $10^{-4}$ , so the bcc lattice is only slightly more stable than the fcc lattice at large  $\Gamma$  values. This is an important property of the OCP to which we shall return in Sec. IV.D.4 when we consider surface effects on the lattice structure.

The higher-order constants  $A_1$ ,  $A_2$ , etc., represent the corrections to the harmonic lattice approximation when phonon-phonon collisions are taken into account. For many years it was thought that  $A_1$  was identically zero. However, more recently  $A_1$  has been evaluated analytically for fcc and bcc lattices; the values are displayed in Table I (Nagara, Nagata, and Nakamura, 1987; Dubin, 1990). Exact values for the higher coefficients are not known, but the numerical Monte Carlo data for the solid phase  $U_{\text{corr}}^{\text{solid}}$  are well fitted by keeping  $A_2$  and  $A_3$  and dropping higher terms (Dubin, 1990):

$$\frac{U_{\text{corr}}^{\text{solid}}}{NkT} = A_{-1}\Gamma + A_0 + \frac{A_1}{\Gamma} + \frac{A_2}{\Gamma^2} + \frac{A_3}{\Gamma^3}. \quad (4.26)$$

The values of  $A_2$  and  $A_3$  used in the fits to the Monte Carlo data are displayed in Table I.

The results for  $U$  in the fluid and solid phases are shown in Fig. 41. We can use these results to show that there is a first-order fluid-solid phase transition that liberates energy when the fluid freezes.

### 3. Free energy, the freezing transition, and correlation pressure

In order to determine the location of the phase transition, one compares the Helmholtz free energy of the fluid phase to that of the solid phase. The Helmholtz free energy rather than the Gibbs free energy is used because the density of the system is fixed by the uniform background density  $n_-$ .

The Helmholtz free energy  $F$  of the OCP is related to the internal energy  $U$  [see Eq. (5.2)] through

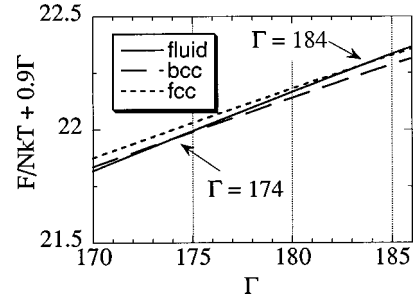


FIG. 42. Free energies of the solid and fluid phases for an infinite classical one-component plasma. The ion-sphere energy  $-0.9\Gamma$  is subtracted from  $F/NkT$  so that the crossing of the curves can be more easily seen.

$$U = -T^2 \left. \frac{\partial(F/T)}{\partial T} \right)_{V,N}. \quad (4.27)$$

By integrating this equation one can find  $F$  in terms of an integral over  $U$ :

$$\frac{F(T)}{T} = - \int_{T_0}^T \frac{U(T')}{T'^2} dT' + \frac{F(T_0)}{T_0}, \quad (4.28)$$

where  $T_0$  is a reference temperature where  $F$  is known. To evaluate the fluid-phase free energy, one takes  $T_0$  very large ( $\Gamma_0 \rightarrow 0$ ) so that the reference system is a weakly correlated OCP for which

$$F(T_0) = NkT_0 [\ln[n_- \lambda_d^3] - 1], \quad (4.29)$$

where  $\lambda_d(T_0) = (h^2/2\pi m k T_0)^{1/2}$  is the thermal deBroglie wavelength. The integral in Eq. (4.28) can be carried out for the fit to the fluid energy of Eq. (4.24), and one obtains, for  $\Gamma > 1$ ,

$$F^{\text{fluid}} NkT(T) = a\Gamma + 3b\Gamma^{1/3} + (3+c)\ln \Gamma - [a + 3b + 1.1516] + \frac{3}{2} \ln \left[ \frac{2\hbar^2 k T}{me^4} \right]. \quad (4.30)$$

The constant 1.1516 arises from numerical integration of Monte Carlo data for  $U$  from  $0 \leq \Gamma \leq 1$  (Slattery, Doolen, and DeWitt, 1982). Note that  $T_0$  in Eq. (4.29) is replaced by  $T$  in the last term of Eq. (4.30) because  $U \rightarrow 3NkT/2$  in the  $\Gamma \rightarrow 0$  limit.

For the free energy of the crystalline phase one uses Eq. (4.26) for  $U$ , taking the reference temperature to be small so that  $F(T_0)$  is now given by the results of harmonic lattice theory:

$$\frac{F_{\text{harmonic}}(T)}{NkT} = A_{-1}\Gamma + 3 \ln \left( \frac{\hbar \omega_p}{kT} \right) - \frac{1}{N} \sum' \ln \left( \frac{\omega_p}{\omega_n} \right), \quad (4.31)$$

where this form assumes  $\hbar \omega_p \ll kT$ . The sum in the last term runs over the frequencies  $\omega_n$  of the  $3N$  independent phonon modes of the lattice, neglecting zero-frequency modes. This term, referred to as the phonon entropy by some authors, becomes an average over the first Brillouin zone as  $N \rightarrow \infty$ , denoted as  $\langle \ln(\omega_p/\omega_n) \rangle$ . This average has been evaluated for various



lattice types, and the values are displayed in Table I. The solid free energy is equal to

$$\frac{F_{\text{solid}}(T)}{NkT} = \frac{F_{\text{harmonic}}(T)}{NkT} - \frac{A_1}{\Gamma} - \frac{A_2}{2\Gamma^2} - \frac{A_3}{3\Gamma^3}. \quad (4.32)$$

The solid and fluid free energies are then compared to determine where they are equal. Note that Planck's constant enters in the same way for both the fluid and the solid free energies and cancels out of the difference, so the free-energy difference depends only on  $\Gamma$ . The solid and fluid free energies are displayed in Fig. 42. The bcc solid free energy is lower than the fluid free energy for  $\Gamma > 174$ . The value  $\Gamma = 172$  that is usually quoted for the freezing transition (Nagara, Nagata, and Nakamura, 1987; Dubin, 1990) was obtained using the solid free energy of Eq. (4.32), but the form used for  $F_{\text{fluid}}$  was given by a slightly less accurate expression than Eq. (4.30) (Slattery, Doolen, and DeWitt, 1982), which was the best available at the time. On the other hand, other authors have recently obtained the value  $\Gamma = 173$  using molecular dynamics simulations and fitting functions of comparable accuracy to Eqs. (4.24) and (4.26) (Farouki and Hamaguchi, 1993). Clearly, the exact  $\Gamma$  value at the phase transition is very sensitive to slight changes in the fluid and solid free energies, because the fluid and solid free-energy curves are nearly parallel near the intersection (Stringfellow, DeWitt, and Slattery, 1990).

At the phase transition there is a latent heat that follows from the energy and entropy difference of the solid and fluid phases and is given by the jump in internal energy shown in Fig. 41:

$$\frac{\text{latent heat}}{NkT} = \frac{\Delta U}{NkT} = 0.72. \quad (4.33)$$

However, for an infinite OCP there is no volume change at this first-order transition, since the density is set by the uniform background.

The free energy for an fcc solid is also shown in Fig. 42. Note that the fcc free energy is only slightly larger than the bcc free energy. Only small changes in the free energies would be necessary to make the fcc lattice more stable than the bcc lattice. The fcc lattice becomes more stable than the fluid phase at  $\Gamma \approx 184$ . In Sec. IV.D we shall find that the addition of surface effects due to finite size can cause a structural phase transition from bcc to fcc.

Derivatives of the free energy yield other thermodynamic functions. One such function, the pressure  $p$ , will be of use in later sections. The pressure is defined as

$$p = - \left( \frac{\partial F}{\partial V} \right)_{T,N}. \quad (4.34)$$

This derivative can be evaluated explicitly by noting that  $U/NkT$  is a function only of  $\Gamma$ . Taking a derivative of Eq. (4.28) with respect to  $V$ , and taking  $T_0$  large so that  $F(T_0)$  is given by Eq. (4.29), yields the result

$$p = n_- kT \left( 1 + \frac{1}{3} \frac{U_{\text{corr}}}{NkT}(\Gamma) \right). \quad (4.35)$$

When  $\Gamma$  is small the pressure is given by that of an ideal gas,  $p = n_- kT$ . However, in the strongly correlated regime the pressure is dominated by the potential energy of the interacting charges and  $p \approx -0.3n_- e^2/a$ , where we have employed Eq. (4.23). The fact that both the pressure and the derivative  $-\partial p/\partial V$  are negative does not imply that the OCP is unstable; the uniform neutralizing background charge provides a stabilizing force.

Equation (4.35) together with Eq. (4.33) implies that the thermal pressure of the fluid phase differs from that of the solid phase at the phase transition. In ordinary fluids this is impossible, since phase equilibrium requires that the pressures be identical. In the infinite OCP the phases can be in equilibrium with different thermal pressures because the uniform neutralizing background makes up the pressure difference.

#### 4. Thermodynamic functions for a large trapped plasma

In Sec. V, we shall discuss the thermodynamics of trapped plasmas systematically. Here, we preempt a portion of that discussion and relate the thermodynamic functions for a large trapped plasma to those for an OCP. As mentioned earlier, a plasma is said to be large when the influence of the plasma surface is limited to a thin surface layer. For the fluid phase, the thickness of this surface layer is about a correlation length. For a crystal, the thickness of the layer can be less than the bulk correlation length because of dislocations near the surface. The scale of the thickness is set by  $\lambda_D$  for weak correlation and by  $a$  for strong correlation. In general, we shall denote the thickness by  $\lambda$  and assume that  $\lambda$  is small compared to all three plasma dimensions. In the limit where the volume of the surface layer is negligibly small compared to the volume of the plasma as a whole, we shall see that the free energy of the trapped plasma (as viewed in the rotating frame) is simply related to the OCP free energy discussed in the last section.

The plasma energy in the rotating frame is given by

$$E_R = \langle H_R \rangle = \frac{3}{2} NkT + \int d^3\mathbf{r}_1 \dots d^3\mathbf{r}_N \times \left[ \left( \frac{1}{2} \sum_{i \neq j} e^2 G(\mathbf{r}_i | \mathbf{r}_j) + \sum_i e \phi_R(\mathbf{r}_i) \right) \right] f_c^{(s)}(\mathbf{r}_1, \dots, \mathbf{r}_N), \quad (4.36)$$

where use has been made of Eqs. (2.8) and (4.4). The averages can be written in terms of the reduced distribution functions:

$$E_R = \frac{3}{2} NkT + \int d^3\mathbf{r}_1 e \phi_R(\mathbf{r}_1) n(\mathbf{r}_1) + \frac{N(N-1)}{2} \int d^3\mathbf{r}_1 d^3\mathbf{r}_2 e^2 G(\mathbf{r}_1 | \mathbf{r}_2) \rho^{(2)}(\mathbf{r}_1; \mathbf{r}_2). \quad (4.37)$$

Writing  $\rho^{(2)}$  in terms of the correlation function  $g(\mathbf{r}_1, \mathbf{r}_2)$  then yields the result

$$\begin{aligned}
E_R = & \frac{3}{2} NkT + \int d^3\mathbf{r}_1 n(\mathbf{r}_1) \left[ e\phi_R(\mathbf{r}_1) \right. \\
& + \frac{1}{2} \int d^3\mathbf{r}_2 e^2 G(\mathbf{r}_1|\mathbf{r}_2) n(\mathbf{r}_2) \left. \right] \\
& + \frac{1}{2} \int d^3\mathbf{r}_1 d^3\mathbf{r}_2 n(\mathbf{r}_1) n(\mathbf{r}_2) g(\mathbf{r}_1, \mathbf{r}_2) e^2 G(\mathbf{r}_1|\mathbf{r}_2),
\end{aligned} \quad (4.38)$$

where  $N-1$  has been approximated by  $N$ .

For a large plasma, the second of the three terms in this expression for  $E_R$  is much larger than the other two. It is useful to compare this term to the energy of a zero-temperature mean-field plasma,

$$\begin{aligned}
E_R^{(0)} = & e \int d^3\mathbf{r} \phi_R(\mathbf{r}) n^{(0)}(\mathbf{r}) \\
& + \frac{e^2}{2} \int d^3\mathbf{r}_1 d^3\mathbf{r}_2 n^{(0)}(\mathbf{r}_1) n^{(0)}(\mathbf{r}_2) G(\mathbf{r}_1|\mathbf{r}_2),
\end{aligned} \quad (4.39)$$

where  $n^{(0)}(\mathbf{r})$  is equal to  $n_-$  out to the surface of the cold mean-field plasma and is zero beyond. The surface is a sharp boundary because  $\lambda_D=0$  for  $T=0$ . The cold mean-field plasma has the same number of particles, the same rotation frequency, and the same trap parameters as the actual plasma. The reader may recall that  $E_R^{(0)}$  was evaluated in Eq. (3.47) for the case of a spheroidal plasma. The density difference  $\Delta n(\mathbf{r}) \equiv n(\mathbf{r}) - n^{(0)}(\mathbf{r})$  is nonzero only within a distance  $\lambda$  of the surface; both  $n(\mathbf{r})$  and  $n^{(0)}(\mathbf{r})$  must equal  $n_-$  in the plasma interior. Spatial oscillation (or simply spatial variation) of  $n(\mathbf{r})$  is possible only within the surface layer, because knowledge of the surface position is necessary to define the phase of the oscillation. Thus, for a large plasma,  $E_R^{(0)}$  is close in value to the second term in the expression for  $E_R$  in Eq. (4.38).

Formally, we shall show that the difference is negligible in the limit where the volume of the surface layer is negligible compared to the volume of the plasma as a whole. To this end, consider the difference

$$\begin{aligned}
E_R - E_R^{(0)} = & \frac{3}{2} NkT + \int d^3\mathbf{r}_1 \Delta n(\mathbf{r}_1) \left[ e\phi_R(\mathbf{r}_1) \right. \\
& + \int d^3\mathbf{r}_2 e^2 G(\mathbf{r}_1|\mathbf{r}_2) n^{(0)}(\mathbf{r}_2) \left. \right] \\
& + \frac{1}{2} \int d^3\mathbf{r}_1 d^3\mathbf{r}_2 e^2 G(\mathbf{r}_1|\mathbf{r}_2) \Delta n(\mathbf{r}_1) \Delta n(\mathbf{r}_2) \\
& + \frac{1}{2} \int d^3\mathbf{r}_1 d^3\mathbf{r}_2 n(\mathbf{r}_1) n(\mathbf{r}_2) g(\mathbf{r}_1, \mathbf{r}_2) e^2 G(\mathbf{r}_1|\mathbf{r}_2).
\end{aligned} \quad (4.40)$$

The second term can be rewritten as

$$\int d^3\mathbf{r}_1 e \Delta n(\mathbf{r}_1) [\phi_R(\mathbf{r}_1) + \phi_p^{(0)}(\mathbf{r}_1)],$$

where  $\phi_p^{(0)}(\mathbf{r}_1)$  is the space-charge potential for the cold mean-field plasma. According to Eq. (3.18),  $\phi_R(\mathbf{r})$

+  $\phi^{(0)}(\mathbf{r})$  is a constant, say  $C$ , inside the cold mean-field plasma. Also, because the cold mean-field plasma and the plasma have the same number of charges,  $\int d^3\mathbf{r} \Delta n(\mathbf{r})$  is zero. Thus the second term in Eq. (4.40) can be rewritten as

$$\int_{\text{outside}} d^3\mathbf{r}_1 e n(\mathbf{r}_1) [\phi_R(\mathbf{r}_1) + \phi_p^{(0)}(\mathbf{r}_1) - C], \quad (4.41)$$

where the integral is over the volume outside the cold mean-field plasma. The density  $n(\mathbf{r}_1)$  is nonzero only out to a distance  $\lambda$  beyond the surface of the cold mean-field plasma. Near the surface,  $\phi_R(\mathbf{r}) + \phi_p^{(0)}(\mathbf{r})$  differs from  $C$  by only a small amount

$$\phi_R(\mathbf{r}) + \phi_p^{(0)}(\mathbf{r}) \approx \frac{x^2}{2} (\hat{n} \cdot \nabla)^2 [\phi_R(\mathbf{r}) + \phi_p^{(0)}(\mathbf{r})],$$

where  $\hat{n}$  is the normal to the surface,  $x$  is the distance from the surface, and the derivatives are evaluated just outside the surface. First-order terms in  $x$  vanish since  $\nabla(\phi_R + \phi_p^{(0)})$  is zero inside and continuous at the surface. Thus integral (4.41) is of order  $A\lambda^3 e n_- (\hat{n} \cdot \nabla)^2 [\phi_R + \phi_p^{(0)}] \sim A\lambda n_- e^2 n_- \lambda^2$ , where  $A$  is the surface area of the plasma. By setting  $A\lambda n_- = N\Delta V/V$ , where  $\Delta V$  is the volume of the correlation-length-thick surface shell and  $V$  is the volume of the plasma as a whole, and by noting that  $\lambda$  is of order  $\lambda_D$  or  $a$ , we obtain the estimates  $N(\Delta V/V)kT$  or  $N(\Delta V/V)e^2/a$ . The first term in Eq. (4.40) is of order  $NkT$  and the last of order  $Ne^2/a$ , so the second term is negligible in the limit  $\Delta V/V \rightarrow 0$ .

Similarly, the third term in Eq. (4.40), for which the integrand is nonzero only when both  $\mathbf{r}_1$  and  $\mathbf{r}_2$  are within a length  $\lambda$  of the surface, is another surface contribution. One can see this by writing this term as

$$\begin{aligned}
& \frac{1}{2} \int d^3\mathbf{r}_1 d^3\mathbf{r}_2 e^2 G(\mathbf{r}_1|\mathbf{r}_2) \Delta n(\mathbf{r}_1) \Delta n(\mathbf{r}_2) \\
& = \frac{e}{2} \int d^3\mathbf{r}_2 \Delta \phi_p(\mathbf{r}_2) \Delta n(\mathbf{r}_2),
\end{aligned}$$

where  $\Delta \phi_p(\mathbf{r}_2)$  is the potential difference caused by  $\Delta n(\mathbf{r}_1)$ . Writing  $d^3\mathbf{r}_2$  as  $d^2\mathbf{r} dx$  where  $d^2\mathbf{r}$  is an area element of the surface and  $x$  is a coordinate normal to the surface, we integrate by parts, neglecting surface curvature, to obtain

$$-\frac{e}{2} \int d^2\mathbf{r} \int dx \frac{\partial \Delta \phi_p}{\partial x} \int_{-\infty}^x dx' \Delta n(x').$$

Since  $\partial \Delta \phi_p / \partial x \rightarrow 0$  as  $x \rightarrow \pm \infty$ , we replace  $\partial \Delta \phi_p / \partial x$  by its maximum magnitude,  $4\pi e n_- \lambda$  (this follows from the Poisson equation  $\partial^2 \Delta \phi / \partial x^2 \approx -4\pi e \Delta n$ ). Since

$$\int_{-\infty}^{\infty} dx \Delta n(x) = 0,$$

we estimate

$$\int_{-\infty}^{\infty} dx \int_{-\infty}^x dx' \Delta n(x')$$

to be of order  $n_- \lambda^2$ . Then the magnitude of the third term in Eq. (4.40) is of order  $A 2\pi e^2 n_- \lambda n_- \lambda^2$ , which is the same estimate that was obtained for the second term. Thus the third term also is negligible in the limit  $\Delta V/V \rightarrow 0$ .

In this limit, we can also neglect contributions to the integral in the fourth term for  $\mathbf{r}_1$  and  $\mathbf{r}_2$  values within the surface layer. In the plasma interior, we may set  $n(\mathbf{r}) = n_-$ ,  $g(\mathbf{r}_1, \mathbf{r}_2) = g(\mathbf{r}_1 - \mathbf{r}_2)$ , and  $G(\mathbf{r}_1 | \mathbf{r}_2) = |\mathbf{r}_1 - \mathbf{r}_2|^{-1}$ ; so Eq. (4.40) reduces to the result

$$E_R - E_R^{(0)} = U, \quad (4.42)$$

where  $U$  is the internal energy of an OCP as given in Eq. (4.20). Again we note that the mean-field electrostatic energy dominates the energy of a large trapped plasma, that is,  $E_R^{(0)}$  is much larger than  $U$ . In an OCP this mean-field energy does not appear because there really is a uniform neutralizing background charge present, and the self-energy of this background, which is not included in Eq. (4.42), just cancels  $E_R^{(0)}$ . Equation (4.42) was previously recognized to hold for the special cases of large plasmas in slab geometry (Dubin, 1989) and spherical geometry (Hasse and Avilov, 1991).

A word of caution should be added concerning the neglected surface contributions. In the limit  $\Delta V/V \rightarrow 0$  these terms clearly are negligible, but for any real trapped plasma  $\Delta V/V$  is finite. In practice, there remains the question of just how small  $\Delta V/V$  must be for the surface terms to be negligible. The answer to this question is nontrivial and depends on the correlation state of the bulk plasma. For example, the bulk correlation energies for bcc and fcc crystals are the same to within four significant figures [e.g.,  $|U_{\text{bcc}} - U_{\text{fcc}}| = (5.6 \times 10^{-5}) Ne^2/a$  at  $T=0$ ]. For the surface energy [i.e.,  $(\Delta V/V) Ne^2/a$ ] to be negligible compared to the difference between the bulk energies for the two crystal structures, it is necessary that  $\Delta V/V$  be quite small. In Sec. V.D.4 this question is discussed in detail, and it is argued that the plasma must be about 60 lattice planes across for surface terms to be negligible. For the fluid phase, the condition is not so restrictive.

Equation (4.42) can be used to obtain the Helmholtz free energy  $F_R$  of a large plasma as seen in the rotating frame. The free energy is related to the energy through  $\partial(F_R/T)/\partial T = -E_R/T^2$  [see Eq. (5.2)]. Integrating this equation with respect to  $T$ , and substituting for  $E_R$  via Eq. (4.42), we observe that the integral involving  $E_R^{(0)}$  yields  $E_R^{(0)}/T$  because  $E_R^{(0)}$  is independent of  $T$ , and the integral involving  $U$  yields  $F/T$  where  $F$  is the Helmholtz free energy of an OCP [see Eq. (4.28)]. Thus we are led to

$$F_R = E_R^{(0)} + F. \quad (4.43)$$

This relation also follows from a physical argument: for a large plasma, where the volume of the thin surface shell is negligible, the entropy is determined by the bulk plasma. However, the particle distribution function for the bulk is the same as for an infinite OCP, so the plasma entropy is the same as the OCP entropy. This

observation, together with the relations  $F_R = E_R - TS$  and  $F = U - TS$  lead to Eq. (4.43).

In Sec. V, we shall write other thermodynamic functions as derivatives of  $F_R$ . In general,  $F_R$  depends on  $T$ ,  $\omega$ ,  $N$ ,  $B$ , and  $\{V_{jj}\}$ , where the  $\{V_{jj}\}$  are voltages on the electrodes. Here, we note some consequences of the separation  $F_R = E_R^{(0)} + F$  and of the distinct properties of  $E_R^{(0)}$  and  $F$ . As mentioned earlier,  $E_R^{(0)}$  is much larger than  $F$ . Also,  $E_R^{(0)}$  increases with  $N$  faster than the first power, that is,  $E_R^{(0)}$  is nonextensive in the limit  $N \rightarrow \infty$ ; whereas,  $F$  is proportional to  $N$  and so is extensive. Thus the nonextensive dependence enters only through  $E_R^{(0)}$ , and this dependence is particularly simple because  $E_R^{(0)}$  does not depend on temperature (or on the state of correlation).  $E_R^{(0)}$  is completely determined by  $n_-$  [or, equivalently, by  $\omega(\Omega_c - \omega)$ ] and the shape and size of the cold mean-field plasma. The shape is determined by some combination of  $\omega$ ,  $N$ ,  $B$ , and  $\{V_{jj}\}$ . In contrast,  $F/N$  depends on  $n_-$  and  $T$  (and through these on the correlation state), but does not depend on plasma shape or size.

As simple examples, consider the relations [see Eq. (5.9)]

$$L = \frac{\partial F_R}{\partial \omega} \bigg|_{T, N, B, \{V_{jj}\}}, \quad (4.44)$$

$$S = - \frac{\partial F_R}{\partial T} \bigg|_{\omega, N, B, \{V_{jj}\}}, \quad (4.45)$$

where  $L$  is the mean angular momentum. Since  $E_R^{(0)}$  is much larger than  $F$ , Eq. (4.44) can be written to a good approximation as  $L \approx \partial E_R^{(0)} / \partial \omega |_{T, N, B, \{V_{jj}\}}$ . Thus  $L$  is nonextensive and is largely independent of  $T$  (and the correlation state of the plasma). In the next section we shall obtain an explicit expression for the small temperature-dependent correction. On the other hand, since  $E_R^{(0)}$  is independent of  $T$ , Eq. (4.45) reduces, as expected, to the entropy for an OCP,  $S = -\partial F / \partial T |_{n_-, N}$ . Since  $F$  is extensive,  $S$  is extensive. Thus  $s \equiv S/N$  is intensive and depends only on  $n_-$  and  $T$  (Dubin and O'Neil, 1986a, 1986b).

A differential  $Tds$  relation for a large plasma can be written as

$$Tds = T \frac{\partial s}{\partial T} \bigg|_{n_-} dT + T \frac{\partial s}{\partial n_-} \bigg|_T dn_-, \quad (4.46)$$

where the coefficients are related to well-known thermodynamic functions for an OCP. For example, the first coefficient can be written as

$$T \frac{\partial s}{\partial T} \bigg|_{n_-} = \frac{T}{N} \frac{\partial S}{\partial T} \bigg|_{n_-} = \frac{1}{N} c_{n_-}, \quad (4.47)$$

where  $c_{n_-}$  is the specific heat at constant density. By using  $S = -\partial F / \partial T |_{n_-, N}$  and the relation

$$U_{\text{corr}} = -T^2 \partial[(F - F_{\text{ideal}})/T] / \partial T |_{n_-, N}$$

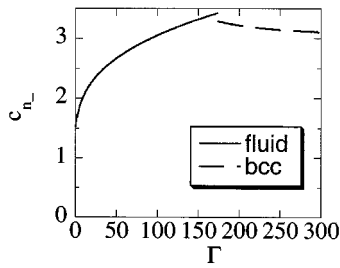


FIG. 43. Specific heat at constant density,  $c_{n-}(\Gamma)$ , for an infinite classical one-component plasma.

we obtain

$$\frac{c_{n-}}{Nk} = \frac{3}{2} - \Gamma^2 \frac{\partial}{\partial \Gamma} \left[ \frac{U_{\text{corr}}}{NkT}(\Gamma)/\Gamma \right]. \quad (4.48)$$

As shown in Fig. 43, the specific heat displays large deviations from the ideal-gas value of  $3/2$ , approaching the classical harmonic lattice value of  $3$  in the strongly correlated limit.

The second coefficient can be written as

$$T \left. \frac{\partial s}{\partial n_-} \right|_T = - \frac{TV}{n_-} \left. \frac{\partial s}{\partial V} \right|_{T,N} = \frac{TV}{n_-} \left. \frac{\partial^2(F/N)}{\partial V \partial T} \right|_{T,N},$$

where  $V = N/n_-$  is the plasma volume. By using Eq. (4.34), we obtain

$$T \left. \frac{\partial s}{\partial n_-} \right|_T = - \frac{T}{n_-^2} \left. \frac{\partial p}{\partial T} \right|_{n_-}, \quad (4.49)$$

where  $p = p(n_-, T)$  is the OCP pressure given in Eq. (4.35).

Thus Eq. (4.46) reduces to

$$Tds = \frac{1}{N} c_{n-} dT + T \left. \frac{\partial p}{\partial T} \right|_{n_-} d\left(\frac{1}{n_-}\right), \quad (4.50)$$

which is well known from the thermodynamics of homogeneous fluids (Zemansky, 1968). It is instructive to compare this form for  $Tds$  to that in Eq. (5.10), which is the analogous result for a general (possibly mesoscopic) trapped plasma. The general form includes differentials of  $E$ ,  $L$ ,  $N$ ,  $B$ , and  $\{V_j\}$ , but these quantities enter Eq. (4.50) only through their effect on  $T$  and  $n_-$ . Clearly, the separation  $F_R = E_R^{(0)} + F$  has a powerful simplifying effect.

As a simple application of Eq. (4.50), let us consider an adiabatic change of state

$$Tds = 0 = \frac{c_{n-} dT}{N} - \frac{T}{n_-^2} \frac{\partial p}{\partial T} dn_-. \quad (4.51)$$

In an uncorrelated plasma,  $p = n_- kT$  and  $c_{n-} = c_{\text{ideal}}$ , where  $c_{\text{ideal}} = 3Nk/2$  for classical point charges. We then find the usual adiabatic relation between  $T$  and  $n_-$  for an ideal gas:

$$\frac{\partial \ln T}{\partial \ln n_-} \bigg|_s = \frac{Nk}{c_{\text{ideal}}}. \quad (4.52)$$

However, in a strongly correlated plasma the relation is modified, since both  $p$  and  $c_{n-}$  depend on  $\Gamma$ ; see Eqs. (4.48) and (4.35). As discussed in Sec. IV.C.3, for  $\Gamma \gtrsim 3$  the pressure actually changes sign as  $U_{\text{corr}}/NkT$  becomes negative, so one might imagine that during an adiabatic expansion the correlated plasma would actually heat rather than cool. However, this is not the case, although the rate of cooling during the expansion is reduced compared to Eq. (4.52) (Dubin and O'Neil, 1986b). In fact, using Eq. (4.35), we can express Eq. (4.51) succinctly in terms of the specific heat, which is non-negative:

$$\frac{\partial \ln T}{\partial \ln n_-} \bigg|_s = \frac{Nk}{c_{n-}} \left( 1 + \frac{c_{n-} - c_{\text{ideal}}}{3Nk} \right). \quad (4.53)$$

The technique of adiabatic expansion has been proposed as a method for cooling electron plasmas into the strongly correlated regime (Dubin and O'Neil, 1986b). The technique works best when the electron cyclotron motion is quantized, in the lowest Landau level, but the motion parallel to  $\mathbf{B}$  remains classical. In this case an adiabatic increase in the length of the plasma can be thought of as a one-dimensional adiabatic expansion, because the perpendicular degrees of freedom associated with cyclotron motion are “frozen out.” If the plasma is uncorrelated,  $c_{\text{ideal}} = Nk/2$  and Eq. (4.52) implies a much larger decrease in temperature than for a 3D expansion, where  $c_{\text{ideal}} = 3Nk/2$ . However, correlations reduce the cooling rate, because correlations increase  $c_{n-}$  above  $Nk/2$  (see Fig. 43). [As discussed in Sec. IV.A, Eq. (4.53) remains valid even if the cyclotron motion is quantized because correlations remain classical provided that  $\hbar \omega_p \ll kT$ .] Equation (4.53) shows that cooling is slowed by the strong-correlation state of the plasma; nevertheless, quantization of the cyclotron motion still makes the cooling rate larger than for the case of 3D expansions.

Finally, we consider the implications of Eq. (4.43) for the freezing transition in a large plasma. In the previous section, the freezing transition for an infinite homogeneous OCP was determined by finding the  $\Gamma$  value at which  $F^{\text{solid}}$  becomes smaller than  $F^{\text{fluid}}$ . One minimizes the Helmholtz free energy  $F$ , rather than the Gibbs free energy, because the neutralizing background charge fixes the plasma density (or volume). In Sec. V, we shall show that the free energy  $F_R$  must be a minimum for a trapped plasma that is in thermal contact with a heat and angular momentum reservoir. When the rotation frequency of the reservoir is fixed and the temperature is gradually lowered, a freezing transition occurs when  $F_R^{\text{solid}}$  becomes smaller than  $F_R^{\text{fluid}}$  (we assume that the plasma is large enough that the transition is sharp). Since  $E_R^{(0)}$  is independent of the temperature and of the correlation state of the plasma, the relation  $F_R = E_R^{(0)} + F$  shows that the freezing transition for a large plasma occurs at the same temperature (or  $\Gamma$  value) as it does for an infinite homogeneous OCP. There is no change in

bulk density just as for the infinite OCP phase transition, since  $n_-$  is fixed by the rotation frequency of the reservoir.

On the other hand, if the plasma is not connected to an angular momentum reservoir, so that angular momentum rather than rotation frequency is fixed as  $T$  varies through the transition, there now will be a change in rotation frequency and a concomitant change in density at the phase transition. However,  $F_R$  is not extensive, increasing with  $N$  more rapidly than the first power of  $N$ , and this implies that the density change is small, becoming negligible for a sufficiently large plasma. Physically, the cold mean-field energy renders negligible any density change at the transition, even if the correlation energy could be lowered by such a change. Since the correlation energy is small compared to the mean-field energy for large plasmas. [We shall discuss this density change more carefully in connection with Eq. (4.79).] We return again to the observation that large plasmas have correlation properties identical to the infinite OCP.

##### 5. Effect of correlations on the plasma edge

At the edge of the plasma the density falls from the bulk value  $n_-$  to zero with a characteristic functional form that depends on  $\Gamma$ . For a weakly correlated plasma this density profile can be derived from the solution of the Poisson-Boltzmann equation, Eq. (3.34), and is displayed in Fig. 9. For a strongly correlated plasma the density profile can be obtained numerically using the methods discussed in Sec. IV.B (see Figs. 22 and 23). However, a theoretical description of the strongly correlated plasma edge of comparable simplicity and accuracy to that of the weakly correlated edge has not yet been found. Nevertheless, some exact analytic results can be obtained.

We consider a large plasma, so Eqs. (4.42) and (4.43) apply. Also, for a large plasma, the edge region can be treated in slab geometry, that is, the density depends only on the coordinate  $x$  measured normal to the surface. Taking a derivative with respect to  $x$  in Eq. (4.5) and using Eq. (4.8) then leads to the first equation of the BBGKY hierarchy:

$$kT \frac{\partial n}{\partial x_1} = -en(x_1) \frac{\partial}{\partial x_1} [\phi_p + \phi_R] - e^2 n(x_1) \int d^3r_2 n(x_2) g(\mathbf{r}_1, \mathbf{r}_2) \frac{\partial}{\partial x_1} |\mathbf{r}_1 - \mathbf{r}_2|^{-1}. \quad (4.54)$$

This equation can be thought of as a generalization of the force balance relation for a fluid, Eq. (3.14), that includes the (nonlocal) pressure force due to correlations. The equation leads back to the Poisson-Boltzmann system if the correlation function  $g$  is neglected. However, in the strongly correlated limit the correlation pressure term involving  $g$  is not negligible, and since  $g$  is an unknown function both of  $\mathbf{r}_1$  and  $\mathbf{r}_2$  no exact solution for  $n$  can be found. This problem is well

known in the literature of fluid-vapor interfaces and metallic surfaces, and approximation schemes for the solution of such integral equations abound [see, for example, Hansen and McDonald (1986)]. Here, however, we shall focus on exact results.

Although the exact functional form of the density profile cannot be determined analytically, exact results for moments of the density profile can be derived. One exact result follows from the virial theorem:

$$\sum_i \left( \mathbf{r}_i \cdot \frac{\partial}{\partial \mathbf{r}_i} H_R \right) = 3NkT. \quad (4.55)$$

For a harmonic trap in which  $\phi_R$  is quadratic and  $G(\mathbf{r}_i|\mathbf{r}_j) = |\mathbf{r}_i - \mathbf{r}_j|^{-1}$ , this can be written as

$$Nm\omega_z^2(\langle z^2 \rangle + \beta \langle r^2 \rangle) - \varepsilon_c = 3NkT, \quad (4.56)$$

where  $\varepsilon_c = \langle \sum_{i>j} e^2 / |\mathbf{r}_i - \mathbf{r}_j| \rangle$  is the mean Coulomb energy of the cloud and  $\langle z^2 \rangle$  and  $\langle r^2 \rangle$  are the mean-square length and cylindrical radius, respectively, of the plasma.

We can use this relation to investigate the effect of temperature (Corngold, 1993) and correlations on the mean-square length and radius. [The  $\beta=1$  zero-temperature limit of Eq. (4.56) has also been employed to check that a zero-temperature equilibrium has been achieved in molecular dynamics simulations of spherical plasmas (Hasse and Avilov, 1991).] The average total energy  $E_R$  of a plasma in a harmonic trap in the rotating frame can be written as the sum of the average kinetic energy, the external trap potential, and the Coulomb interaction energy [see Eq. (4.37)]:

$$E_R = \frac{3}{2} NkT + \frac{1}{2} Nm\omega_z^2(\langle z^2 \rangle + \beta \langle r^2 \rangle) + NC + \varepsilon_c, \quad (4.57)$$

where  $C$  is the constant in Eq. (3.39). Substituting for  $\varepsilon_c$  from Eq. (4.56), using the large-plasma result  $E_R = E_R^{(0)} + U$ , and using expression (4.20) for  $U$  then yields the relation

$$\begin{aligned} & \frac{3}{2} Nm\omega_z^2(\langle z^2 \rangle + \beta \langle r^2 \rangle) \\ &= E_R^{(0)} - NC + NkT \left( 3 + \frac{U_{\text{corr}}}{NkT}(\Gamma) \right). \end{aligned} \quad (4.58)$$

By substituting Eq. (3.47) for  $E_R^{(0)}$ , we obtain the result

$$\begin{aligned} & \frac{3}{2} m\omega_z^2 \left[ \langle z^2 \rangle - \frac{Z_p^2}{5} + \beta \left( \langle r^2 \rangle - \frac{2R_p^2}{5} \right) \right] \\ &= kT \left( 3 + \frac{U_{\text{corr}}(\Gamma)}{NkT} \right). \end{aligned} \quad (4.59)$$

For a cold mean-field plasma,  $\langle z^2 \rangle = Z_p^2/5$  and  $\langle r^2 \rangle = 2R_p^2/5$ , so Eq. (4.59) describes how temperature and correlations affect  $\langle z^2 \rangle$  and  $\langle r^2 \rangle$  in a large plasma in a harmonic trap. Equation (4.58) has also been derived by Corngold for the special case of a weakly correlated infinitely long cylindrical plasma (Corngold, 1993).

More general results for moments of the density profile other than  $\langle z^2 \rangle$  and  $\langle r^2 \rangle$  and for plasmas trapped in

general geometries can be derived using the first equation of the BBGKY hierarchy, Eq. (4.54) (Dubin, 1996). We integrate Eq. (4.54) from a point  $x = x_{\text{in}}$  within the plasma where  $n(x) = n_-$ , to a point  $x = x_{\text{out}}$  where  $n(x) = 0$ :

$$\begin{aligned} -kTn_- = & -e \int_{x_{\text{in}}}^{x_{\text{out}}} dx_1 n(x_1) \frac{\partial}{\partial x_1} (\phi_p + \phi_R) \\ & - e^2 \int_{x_{\text{in}}}^{x_{\text{out}}} dx_1 \int d^3\mathbf{r}_2 n(x_1) n(x_2) g(\mathbf{r}_1, \mathbf{r}_2) \\ & \times \frac{\partial}{\partial x_1} |\mathbf{r}_1 - \mathbf{r}_2|^{-1}. \end{aligned} \quad (4.60)$$

For large plasmas the integrals involving the correlation function  $g(\mathbf{r}_1, \mathbf{r}_2)$  can be simplified. We split the integral involving  $g$  into two pieces,

$$\begin{aligned} e^2 \int_{x_{\text{in}}}^{x_{\text{out}}} dx_1 \int d^3\mathbf{r}_2 n(x_1) n(x_2) g \frac{\partial}{\partial x_1} |\mathbf{r}_1 - \mathbf{r}_2|^{-1} \\ = e^2 \int_{x_{\text{in}}}^{x_{\text{out}}} dx_1 \int_{-\infty}^{x_{\text{in}}} dx_2 \int d^2\mathbf{r}_{\perp 2} n(x_1) n(x_2) g(\mathbf{r}_1, \mathbf{r}_2) \\ \times \frac{\partial}{\partial x_1} |\mathbf{r}_1 - \mathbf{r}_2|^{-1} + e^2 \int_{x_{\text{in}}}^{x_{\text{out}}} dx_1 \int_{x_{\text{in}}}^{x_{\text{out}}} dx_2 \\ \times \int d^2\mathbf{r}_{\perp 2} n(x_1) n(x_2) g(\mathbf{r}_1, \mathbf{r}_2) \frac{\partial}{\partial x_1} |\mathbf{r}_1 - \mathbf{r}_2|^{-1}. \end{aligned} \quad (4.61)$$

However, if surface curvature is neglected, we can write  $g(\mathbf{r}_1, \mathbf{r}_2) = g(x_1, x_2; \mathbf{r}_{\perp 1} - \mathbf{r}_{\perp 2})$  where  $\mathbf{r}_1$  is the component of  $\mathbf{r}$  parallel to the surface. The second integral on the right-hand side of Eq. (4.61) then vanishes because  $g$  is symmetric on interchange of  $x_1$  and  $x_2$  but  $\partial|\mathbf{r}_1 - \mathbf{r}_2|^{-1}/\partial x_1$  is antisymmetric. Furthermore, since  $x_{\text{in}}$  is in the bulk, we can replace  $g$  and  $n$  by their bulk forms  $g(\mathbf{r}_1 - \mathbf{r}_2)$  and  $n_-$ , respectively, and we can replace  $x_{\text{out}}$  by  $\infty$  since  $g(\mathbf{r}) \rightarrow 0$  when  $|\mathbf{r}|$  is larger than a correlation length. Thus the integral involving  $g$  in Eq. (4.60) becomes

$$-e^2 \int_{x_{\text{in}}}^{\infty} dx_1 \int_{-\infty}^{x_{\text{in}}} dx_2 \int d^2\mathbf{r}_{\perp 2} n_-^2 g(\mathbf{r}_1 - \mathbf{r}_2) \frac{\partial}{\partial x_1} |\mathbf{r}_1 - \mathbf{r}_2|^{-1}.$$

This expression is merely the total force per unit area due to correlations in the  $x$  direction across a surface  $x = x_{\text{in}}$ , caused by plasma on one side of the surface,  $x < x_{\text{in}}$ . Since  $x_{\text{in}}$  is within the uniform bulk plasma, this correlation force per unit area equals the correlation pressure in an infinite homogeneous OCP, provided that the plasma is in the fluid phase, for which correlations are isotropic. One can show this directly by changing integration variables from  $\mathbf{r}_2$  to  $\mathbf{r} = \mathbf{r}_2 - \mathbf{r}_1$ , writing  $d^3\mathbf{r} = r^2 dr d\Omega$ , where  $d\Omega$  is an element of solid angle, and performing the integral over  $d\Omega$  as well as over  $dx_1$ . Assuming that  $g = g(r)$ , this leaves a single integral over  $g(r)$ , which is equal to  $n_- kT U_{\text{corr}} / (3NkT)$ , where the correlation energy  $U_{\text{corr}}$  is given in terms of  $g(r)$  by Eq.

(4.21). However, Eq. (4.35) shows that this equals the correlation contribution to the OCP pressure. Thus Eq. (4.60) becomes

$$p = e \int_{x_{\text{in}}}^{x_{\text{out}}} dx n(x) \frac{\partial}{\partial x} (\phi_p + \phi_R). \quad (4.62)$$

This is merely an expression for force balance across the surface  $x_{\text{in}}$ : plasma pressure  $p$  balances the mean-field electrostatic forces. However, this expression is exact only in the fluid phase, for a crystal  $g(\mathbf{r})$  is not isotropic and neither is the correlation pressure. Rather, the left-hand side of Eq. (4.62) is replaced by  $\hat{n} \cdot \boldsymbol{\pi} \cdot \hat{n}$ , where  $\hat{n}$  is a surface normal and  $\boldsymbol{\pi}$  is the equilibrium pressure tensor of the crystal. The thermodynamic pressure  $p$  of Eq. (4.35) is related to the diagonal elements of  $\boldsymbol{\pi}$  through  $p = \text{Tr}(\boldsymbol{\pi})/3$ ; for a cubic crystal such as bcc the diagonal elements are all equal to  $p$ . However, we shall see that the effect of anisotropy can often be neglected: Eq. (4.62) is an excellent approximation for the shell-structure phase of mesoscopic plasmas, since the crystal-line symmetry is imperfect.

It is a straightforward exercise to check that the uncorrelated equilibrium density profile of Fig. 9 satisfies Eq. (4.62) for  $p = n_- kT$ . Defining  $\bar{x} = x/\lambda_D$  and  $\psi = -e(\phi_p + \phi_i)/kT$ , we find that Eq. (4.62) becomes

$$-1 = \int_{-\infty}^{\infty} d\bar{x} \frac{n(\bar{x})}{n_-} \frac{\partial \psi}{\partial \bar{x}}. \quad (4.63)$$

However, since  $n = n_- e^{\psi}$ , the integral can be performed,

$$\int_{\psi=0}^{-\infty} d\bar{x} \frac{\partial}{\partial \bar{x}} e^{\psi} = e^{\psi}|_0^{-\infty} = -1, \quad (4.64)$$

verifying Eq. (4.62) for the uncorrelated density profiles.

Equation (4.62) can also be expressed in a form that depends only on the density profile (Dubin, 1996) and applies to any confinement geometry. The right-hand side of Eq. (4.62) is the net mean-field electrostatic force in the  $x$  direction on the plasma slab located between  $x_{\text{in}}$  and  $x_{\text{out}}$ , except for a minus sign. However, if we consider the plasma to be confined by a uniform background of charge density  $-en_-$ , this net mean-field force must be equal and opposite to the net electrostatic force exerted by the charges between  $x_{\text{in}}$  and  $x_{\text{out}}$  on the uniform background. Noting that the force on the background vanishes in the cold mean-field limit, we can write the expression for electrostatic force balance between the plasma charges between  $x_{\text{in}}$  and  $x_{\text{out}}$  and the background as

$$\int_{x_{\text{in}}}^{x_{\text{out}}} dx e n \frac{\partial}{\partial x} (\phi_p + \phi_R) = - \int_{-\infty}^{+\infty} e n_- \Delta E_x dx, \quad (4.65)$$

where  $\Delta E_x$  is the difference in the electric field due to the plasma charges and the charges of a cold mean-field plasma. Solving a 1D Poisson equation (in the edge region) yields

$$\Delta E_x(x) = 4\pi e \int_{x_{\text{in}}}^x \Delta n(x) dx, \quad (4.66)$$

where  $\Delta n(x) \equiv n(x) - n^{(0)}(x)$ , and  $n^{(0)}(x)$  is the density of the cold mean-field plasma. Since  $\Delta n(x)$  is nonzero only near the edge and since

$$\int_{x_{\text{in}}}^{x_{\text{out}}} dx \Delta n(x) = 0,$$

we see that  $\Delta E_x(x)$  is nonzero only in the interval  $x_{\text{in}}$  to  $x_{\text{out}}$ . Thus Eq. (4.62) can be rewritten as

$$p = -4\pi e^2 n_- \int_{x_{\text{in}}}^{x_{\text{out}}} dx \int_{x_{\text{in}}}^x dx' \Delta n(x'), \quad (4.67)$$

and integrating by parts yields the result

$$p = 4\pi e^2 n_- \int_{x_{\text{in}}}^{x_{\text{out}}} dx x \Delta n(x). \quad (4.68)$$

This form of Eq. (4.62) is useful because it allows one to evaluate the effects of temperature and correlations on equilibrium averages in large plasmas. For example, consider the average of any smooth function  $f(\mathbf{r})$ ,

$$\langle f \rangle = N^{-1} \int d^3 \mathbf{r} f(\mathbf{r}) n(\mathbf{r}). \quad (4.69)$$

Adding and subtracting the zero-temperature mean-field density  $n^{(0)}(\mathbf{r})$  to the integrand, we break the average up into the average taken with respect to the zero-temperature mean-field equilibrium,  $\langle f \rangle^{(0)} \equiv N^{-1} \int d^3 \mathbf{r} f n^{(0)}$ , and the difference due to correlation or thermal effects:

$$\langle f \rangle = \langle f \rangle^{(0)} + N^{-1} \int d^3 \mathbf{r} f \Delta n. \quad (4.70)$$

Since  $\Delta n$  is zero everywhere but near the plasma edge, we can Taylor expand  $f$ , keeping terms up to first order in the distance  $x$  from the edge:

$$\langle f \rangle - \langle f \rangle^{(0)} = N^{-1} \int d^2 r_{\perp} \hat{n} \cdot \nabla f \int dx x \Delta n, \quad (4.71)$$

where  $\hat{n}$  is a unit vector normal to the cold fluid surface and the area integral is over the fluid surface. Here we have employed the charge-conservation constraint  $\int \Delta n dx = 0$ . We can then substitute from Eq. (4.68) for the integral over  $x$  and employ the divergence theorem to obtain the result

$$\langle f \rangle - \langle f \rangle^{(0)} = \frac{p}{4\pi e^2 n_-^2} \langle \nabla^2 f \rangle^{(0)}. \quad (4.72)$$

This equation provides the temperature dependence of equilibrium averages (Dubin, 1996). For example, the mean-square length and cylindrical radius of the plasma are given by

$$\langle z^2 \rangle = \langle z^2 \rangle^{(0)} + \frac{p}{2\pi e^2 n_-^2}, \quad (4.73)$$

$$\langle r^2 \rangle = \langle r^2 \rangle^{(0)} + \frac{p}{\pi e^2 n_-^2}. \quad (4.74)$$

[Equation (4.74) was first derived for the special case of a weakly correlated, infinitely long cylindrical plasma (Davidson and Lund, 1993).]

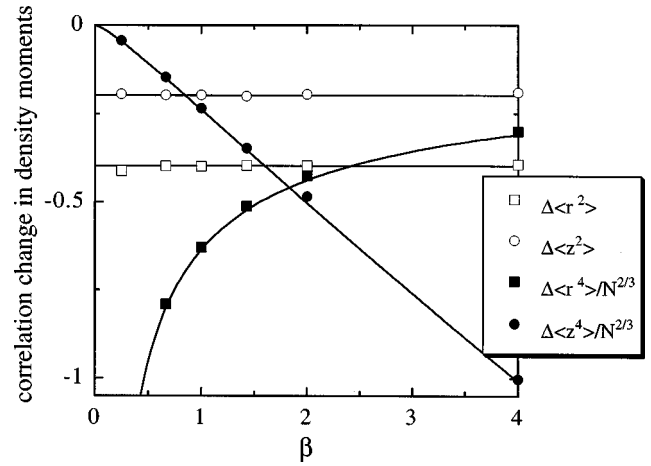


FIG. 44. Effect of correlations on density moments in crystalized plasmas as a function of the trap parameter  $\beta$ . Shown are differences between the actual value of a moment and its cold mean-field value, for several moments. Distances are in terms of the Wigner-Seitz radius,  $N$  is the number of trapped charges. Dots are the results of molecular dynamics simulations; lines are theory predictions [Eqs. (4.72)–(4.74)]. From Dubin (1996).

Thus an increase in  $p$  (or  $T$ ) at fixed  $\omega$  and  $N$  causes both  $\langle r^2 \rangle$  and  $\langle z^2 \rangle$  to increase, in accordance with our intuition that the plasma should expand as  $p$  increases. The effect of correlations on moments of the plasma density can be observed qualitatively in Figs. 22, 24, and 30. In the strongly correlated regime where  $p$  is negative, the density profile shrinks within the cold fluid surface, and moments such as  $\langle z^2 \rangle$  decrease in accord with Eqs. (4.73). However, in weakly correlated plasmas the profile extends beyond the fluid boundary and  $\langle z^2 \rangle$  is increased over its cold fluid value.

Although the derivation of Eq. (4.72) assumed that the edge region was small compared to the size of the plasma, which is a good approximation for large plasmas, for mesoscopic plasmas with  $\Gamma \gg 1$ , shells form throughout the plasma, and one would not expect Eq. (4.72) to hold. Nevertheless, Eq. (4.72) appears to work well even in the extreme limit of  $\Gamma \rightarrow \infty$  where the mesoscopic plasma is crystalized—see Fig. 44.

Equations (4.73) and (4.74) are also consistent with the virial theorem for the case of a harmonically trapped plasma. This can be verified by direct substitution of Eqs. (4.73) and (4.74), together with Eq. (4.35) and the harmonically trapped fluid values  $\langle z^2 \rangle^{(0)} = Z_p^2/5$ ,  $\langle r^2 \rangle^{(0)} = 2R_p^2/5$ , into Eq. (4.59).

We can also use Eq. (4.74) to determine the temperature dependence of the canonical angular momentum. In general Eq. (2.5) implies that

$$L = \langle P_{\theta} \rangle = \frac{Nm(\Omega_c - 2\omega)\langle r^2 \rangle}{2}. \quad (4.75)$$

Substituting for  $\langle r^2 \rangle$  from Eq. (4.74) yields the temperature and correlation correction to the angular momentum of a large plasma,

$$\frac{L - L^{(0)}}{N} = 2 \frac{(\Omega_c - 2\omega)}{\omega_p^2 n_-} p, \quad (4.76)$$

where  $L^{(0)}$  is the value of  $L$  for a cold mean-field plasma. This equation is analogous to Eq. (4.42), which describes the effect of correlations on the energy of the plasma.

Equation (4.76) is consistent with a Maxwell relation to be derived in Sec. V. According to Eq. (5.17),

$$\left( \frac{\partial L}{\partial T} \right)_{\omega, N} = - \left( \frac{\partial S}{\partial \omega} \right)_{T, N} = - \frac{\partial(n_-)^{-1}}{\partial \omega} T N \left( \frac{\partial p}{\partial T} \right)_{n_-}, \quad (4.77)$$

where in the second step we have employed Eq. (4.50) for  $S$ , which is valid for large plasmas. On the other hand, Eq. (4.76) implies

$$\left( \frac{\partial L}{\partial T} \right)_{\omega, N} = \frac{2N(\Omega_c - 2\omega)}{\omega_p^2 n_-} \left( \frac{\partial p}{\partial T} \right)_{\omega, N}, \quad (4.78)$$

and  $\partial n_- / \partial \omega$  can be evaluated using Eq. (3.19), showing that Eqs. (4.77) and (4.78) are identical. Thus Eq. (4.76) provides the correct temperature dependence for  $L$  for large plasmas. Nevertheless, Eq. (4.76) is exact only in the fluid phase where  $g = g(|\mathbf{r}|)$ . Although we have shown that it provides the correct temperature dependence for  $L$ , as discussed in connection with Eq. (4.62) there can be a temperature-independent correction to Eq. (4.76) in the crystalline phase where  $g(\mathbf{r})$  is not an isotropic function of  $\mathbf{r}$ .

Recall that there is a jump in the thermal pressure  $p$  at the fluid-solid phase transition [see Eqs. (4.35) and (4.33)]. If angular momentum is conserved during the transition, Eq. (4.76) implies that the rotation frequency must also jump at the transition. Since the angular momentum is dominated by  $L^{(0)}$ , Eq. (4.76) implies

$$\Delta \omega \simeq - \frac{2N(\Omega_c - 2\bar{\omega})\Delta p}{\omega_p^2 n_- \partial L^{(0)} / \partial \bar{\omega}}, \quad (4.79)$$

where  $\Delta p$  is the thermal pressure jump, equal to  $0.24 n_- kT$  from Eqs. (4.35) and (4.33), and  $\bar{\omega}$  is the average value of  $\omega$  at the transition. Equation (4.79), together with Eq. (3.19), implies that there is a change in density of the plasma at the phase transition when angular momentum is conserved. However, this density change is small since  $\partial L^{(0)} / \partial \omega$  is not extensive, increasing with  $N$  more rapidly than the first power of  $N$ . Thus a sufficiently large trapped plasma exhibits no density change at the phase transition, just as for an infinite OCP.

#### D. Analytic models of mesoscopic plasmas

As discussed in Sec. IV.B, mesoscopic plasmas are observed to crystallize into concentric shells of charge. These shells are approximately equally spaced by a distance of about  $n_-^{-1/3}$ , and the number of particles per unit area within each shell is roughly  $n_-^{2/3}$ , so that the average density of the plasma matches that of the uniform background. The shape of the outer shell follows

that of the cold mean-field plasma, while the shape of the inner shells is determined from the roughly equal spacing between shells.

These observations have been explored theoretically by consideration of idealized models of the plasma called shell models. In these models, the crystalline plasma is regarded as a series of thin concentric shells of charge, and the number of shells  $S$ , spacing  $D_i$  between shells, and charge  $Q_i$  on each shell is then determined by minimizing an approximate potential-energy function. Typically the approximation involves neglecting correlations between particles in different shells, but keeping correlations within a shell in some approximate fashion. The values of  $S$ ,  $D_i$ , and  $Q_i$  derived from these models are often found to match the simulation results with rather good accuracy. Shell models have been formulated for cylindrical plasmas (Totsuji and Barrat, 1988; Hasse and Schiffer, 1990), spherical plasmas (Hasse and Avilov, 1991; Tsuruta and Ichimaru, 1993), and plasmas in planar geometry (Dubin, 1989).

The most complex shell models also keep some effects of correlations between particles in different shells. This allows one to explore structural phase transitions as the external fields are varied and to obtain an estimate for how large a plasma must be in order to be described as a large plasma with the bcc structure of an infinite OCP.

##### 1. Cylindrical shell model

The first shell model was put forward by Totsuji and Barrat (1988) in order to explain the cylindrical shells observed in simulations of long cylindrical plasma columns confined by a harmonic potential (Rahman and Schiffer, 1986). The potential energy of this system is

$$E_R = \frac{1}{2} m \omega_r^2 \sum_{i=1}^N r_i^2 + \sum_{i>j}^N e^2 G(\mathbf{r}_i | \mathbf{r}_j), \quad (4.80)$$

where  $r_i$  is the cylindrical radius of charge  $i$  and  $\omega_r$  is the frequency of the harmonic confinement potential. As usual, the external potential can be thought of as being produced by a background charge of constant density  $n_- = m \omega_r^2 / 2 \pi e^2$ .

The simplest version of the shell model replaces the  $N$  particles by  $S$  uniform thin cylindrical shells with radii  $R_i$ , density  $n_i$  per unit length, and number per unit area  $\sigma_i = n_i / 2 \pi R_i$ . The energy per particle of this system is

$$\begin{aligned} \frac{E'_R}{N} = & \frac{1}{N_L} \\ & \times \left[ \sum_{i=1}^S \frac{1}{2} m \omega_r^2 R_i^2 n_i + \frac{1}{2} \sum_{i=1}^S \sum_{j=1}^S n_i n_j e^2 \phi(R_i | R_j) \right], \end{aligned} \quad (4.81)$$

where  $N_L = \sum_{i=1}^S n_i$  is the total number per unit length, and  $\phi(R_i | R_j)$  is a Green's function for the potential between cylinders:

$$\phi(R_i | R_j) = -2 \ln \left( \frac{R_{>}}{R_w} \right), \quad (4.82)$$



TABLE II. Results of cylindrical shell model for  $k=8 \times 10^{-5}$ .

Cold mean-field theory [Eqs. (4.88) and (4.89)] $k^{1/2}\bar{R}_p = \sqrt{2}$ , $E_R^{(0)}/N - e^2 N_L \ln(\bar{R}_\omega) = -4.3133e^2 N_L$						
Model 1, $S=4$				Model 2		
Shell no.	$f_i$	$\bar{n}_i$	$k^{1/2}\bar{R}_i$	$f_i$	$\bar{n}_i$	$k^{1/2}\bar{R}_i$
1	0.1510	0.1510	0.3886	0.0538	0.0538	0.1839
2	0.3795	0.2285	0.7283	0.2369	0.1831	0.5185
3	0.6658	0.2862	1.0224	0.5520	0.3151	0.8757
4	1.000	0.3343	1.2906	1.0000	0.4479	1.2369
$E_R/N - e^2 N_L \ln(\bar{R}_\omega) = -4.3054e^2 N_L$				$E_R/N - e^2 N_L \ln(\bar{R}_\omega) = -4.3468e^2 N_L$		

where  $R_> = \max(R_i, R_j)$  and  $R_w$  is the location of a cylindrical conducting wall at which the potential equals zero.

When we normalize distances and densities per unit length by  $N_L$ , Eq. (4.81) becomes

$$\frac{E'_R}{N} = e^2 N_L \times \left\{ \sum_{i=1}^S \bar{n}_i \left[ \frac{1}{2} k \bar{R}_i^2 - \left( \bar{n}_i + 2 \sum_{j<i} \bar{n}_j \right) \ln \bar{R}_i \right] + \ln \bar{R}_w \right\}. \quad (4.83)$$

Here  $\bar{R}_i = R_i N_L$ ,  $\bar{n}_i = n_i / N_L$ ,  $\bar{R}_w = R_w N_L$ , and the parameter  $k$  is defined as

$$k = \frac{m \omega_r^2}{e^2 N_L^3} = \frac{2 \pi n_-}{N_L^3}. \quad (4.84)$$

This parameter is a measure of the strength of the confinement field compared to that of the plasma self-field. Other authors employ the scaled density per unit length  $\lambda = N_L a$  rather than  $k$ , where  $a$  is the Wigner-Seitz radius. The two parameters are related by Eq. (4.84):

$$\lambda = \left( \frac{3}{2k} \right)^{1/3}. \quad (4.85)$$

Positions of the shells are now evaluated by minimization of  $E'_R$  with respect to the shell positions  $R_i$ , holding the charge on each shell fixed:

$$k \bar{R}_i^2 = 2 \sum_{j=1}^{i-1} \bar{n}_j + \bar{n}_i, \quad (4.86)$$

which is merely an expression of radial force balance. Substituting this result into Eq. (4.83) and defining

$$f_i \equiv \sum_{j=1}^i \bar{n}_j, \quad i=1, \dots, S,$$

and  $f_0 \equiv 0$  yields

$$\frac{E'_R}{N} = \frac{e^2 N_L}{2} \left\{ 1 - \sum_{i=1}^S (f_i^2 - f_{i-1}^2) \ln(f_i + f_{i-1}) + \ln(\bar{R}_w^2 k) \right\}. \quad (4.87)$$

Minimization of this expression with respect to the  $f_i$ 's, provides a nonlinear recurrence relation for the  $f_i$ 's

which can be solved numerically for a given number of shells  $S$ . The results of this procedure for the case  $S=4$  is shown in Table II as Model 1. Note that both the energy and the overall radius of the plasma are close to those of a cold mean-field plasma,

$$R_p N_L = \left( \frac{2}{k} \right)^{1/2}, \quad (4.88)$$

$$\frac{E_R^{(0)}}{N} = e^2 N_L \left[ \frac{3}{4} + \ln \left( \frac{R_w}{R_p} \right) \right]. \quad (4.89)$$

However, this shell model suffers from an important defect: the number of shells and the values of the  $f_i$ 's are independent of  $k$ , as can be seen from Eq. (4.87) where  $k$  enters only as an additive constant. This is physically incorrect; in fact one observes in experiments or simulations that the number of shells varies with the external field strength: the number of shells should decrease with increasing  $k$ . Furthermore, if one allows  $S$  to vary in the model, one finds that the minimum-energy state has infinite  $S$  and  $n_i \rightarrow 0$ , that is, one returns to the cold mean-field plasma [for example, in Table II, Model 1 has slightly higher energy than the cold mean-field limit  $S = \infty$  given by Eq. (4.89)].

This difficulty is related to the neglect of correlations between charges within the shells. Totsuji and Barrat (1988) overcame this problem by including in the energy the correlation energy between particles in a given shell and neglecting the correlation energy between particles in separate shells. The correlation energy of charges,  $U_{\text{corr}}$ , confined to a thin cylindrical shell of radius  $R_i$  is the difference between the Coulomb energy of the charges and the energy of a thin uniform cylindrical shell. Totsuji and Barrat show that for a crystalline system  $U_{\text{corr}}$  has the functional form

$$\frac{U_{\text{corr}}}{N} = n_i e^2 c(n_i R_i), \quad (4.90)$$

where the function  $c(\bar{R})$  is determined by the type of lattice on the cylinder. After comparing several helical lattices, Totsuji and Barrat observed that  $c(\bar{R})$  is well approximated by the following functional form:

$$c(\bar{R}) = \begin{cases} \gamma + \ln(\bar{R}/2), & \bar{R} < 0.153, \\ -\eta/(2\sqrt{2\pi\bar{R}}), & \bar{R} > 0.153, \end{cases} \quad (4.91a)$$

$$c(\bar{R}) = \begin{cases} \gamma + \ln(\bar{R}/2), & \bar{R} < 0.153, \\ -\eta/(2\sqrt{2\pi\bar{R}}), & \bar{R} > 0.153, \end{cases} \quad (4.91b)$$

TABLE III. Critical values of  $\lambda = N_L a$  for transitions between differing structures.

Structure	Model 2, Totsuji and Barrat (1988)	Hasse and Schiffer (1990)
1-D chain	...	$0 < \lambda < 0.709$
Zigzag	...	$0.709 < \lambda < 0.964$
Helix	...	$0.964 < \lambda < 1.25$
Single shell	$0 < \lambda < 3.35$	$1.25 < \lambda < 3.10$
Shell+1D chain	...	$3.10 < \lambda < 5.7$
2 shells	$3.35 < \lambda < 10.0$	$5.7 < \lambda < 9.5$
2 shells+string	...	$9.5 < \lambda < 13$
3 shells	$10.0 < \lambda < 20.3$	
4 shells	$20.3 < \lambda < 34.0$	
5 shells	$34.0 < \lambda < 51.6$	

where  $\gamma = 0.577 \dots$  is Euler's constant, and where  $\eta = 3.921 \dots$ .

The small  $\bar{R}$  form of  $c(\bar{R})$  is the normalized correlation energy per particle of a 1D Coulomb chain (sometimes also referred to as a Coulomb string)—a 1D lattice of uniformly spaced charges (Totsuji, 1988). The large  $\bar{R}$  form of  $c(\bar{R})$  is the normalized correlation energy per particle of a planar 2D hexagonal lattice (Totsuji, 1978). The 2D hexagonal lattice is the minimum-energy structure for a 2D planar system of charges, and so one would expect a system of charges confined to a cylinder to approach this lattice structure for cylinders of large radius.

The energy of the cylindrical shell model, including the correlation energy between particles within the same shell, is then

$$\frac{E''_R}{N} = \frac{E'_R}{N} + e^2 N_L \sum_{i=1}^S \bar{n}_i^2 c(\bar{n}_i \bar{R}_i), \quad (4.92)$$

where  $E'_R$  is the energy of the previous shell model, neglecting intrashell correlations, given by Eq. (4.83). Minimization of  $E''_R$  with respect to  $\bar{n}_i$ ,  $\bar{R}_i$ , and  $S$  for given  $k$  (subject to the constraint that  $\sum_i \bar{n}_i = 1$ ) yields predictions for the number of shells, their position, and their charge per unit length, as well as the energy of the configuration. An example is shown in Table II for  $k = 8 \times 10^{-5}$ , listed as Model 2, and compared to the results of the previous shell model, Model 1, as well as the cold mean-field approximation, which is given by the equation at the top of the table. Note that the energy of this shell model is now less than that of the cold mean-field limit. Furthermore, using  $\lambda = N_L a$  and Eq. (4.85) to convert energies to units of  $e^2/a$ , one finds that the difference between the shell-model energy of Model 2 and the cold mean-field energy is close to the ion-sphere value of  $-0.9e^2/a$  per particle.

Table III lists the values of  $\lambda$  [determined from  $k$  via Eq. (4.85)] at which transitions from one shell to two shells, two to three, etc., are expected to occur according to Eq. (4.92). The ranges of  $\lambda$  for which the inner shell was actually a Coulomb chain were not precisely determined. These results may be compared to those of a

more detailed model that compares the correlation energies of various helical patterns of charge within each shell (Hasse and Schiffer, 1990). In this work the ranges of  $\lambda$  over which the inner shell was a chain were accurately determined for the first few transitions; these ranges are shown in Table III. When  $k$  decreases beyond a critical value the 1D chain becomes linearly unstable and suffers a second-order structural phase transition to a zig-zag configuration [Fig. 47(b)]. The point of linear instability can be easily calculated (Totsuji and Barrat, 1988):

$$k = 4.2072 \dots \quad (\lambda = 0.7091 \dots). \quad (4.93)$$

As  $k$  decreases below this critical value a second critical point is reached where the zig-zag develops a helical twist [Fig. 47(c)]. The value of  $k$  (or  $\lambda$ ) at this critical point has also been evaluated (Hasse and Schiffer, 1990):

$$k = 1.67 \dots \quad (\lambda = 0.964 \dots). \quad (4.94)$$

As  $k$  decreases further, more complex helical arrangements are predicted to occur [on the basis of numerical simulations (Hasse and Schiffer, 1990)], and finally a second shell appears.

Experiments have been performed that can be compared to these predictions (Birkel, Kassner, and Walther, 1992). Shell structures were created in plasmas consisting of several hundred thousand laser-cooled ions confined in a quadrupole ring trap. Side-view pictures of the shell structures, observed via laser-induced fluorescence of the ions, are displayed in Fig. 45. As  $\lambda$  increased, the radius and number of the shells increased. Experimental data for the radius and number of shells are displayed in Fig. 46 as a function of the well depth  $e\psi_0 = (1/2)m\omega_z^2 r_0^2$ , where  $r_0 = 2.5$  mm is the radius of the confinement electrodes. The straight lines in Fig. 46 show critical  $\lambda$  values separating different numbers of shells taken from Table III. Sometimes the innermost shell is a Coulomb chain or string. Good agreement between theory and experiment is observed for the locations of these structural transitions.

There are some difficulties with the shell models presented so far. Although symmetric geometries such as cylindrical and spherical plasmas can be dealt with, the more general case of spheroidal plasmas is not analytically tractable, since spacing between shells and density within a shell should be allowed to vary as a function of position during the minimization procedure, and the potential arising from a surface of arbitrary shape and surface charge density must be evaluated numerically. The model then becomes more complex than the original system of isolated charges.

Another problem with the shell model of Eq. (4.92) is more fundamental. As  $k$  decreases, the number of shells increases and the model continues to predict that the lowest-energy state is a system of concentric shells with a 2D hexagonal lattice within each shell. However, this is not true as  $k \rightarrow 0$  since a sufficiently large system should exhibit the structural features of an infinite homogeneous system, i.e., a bcc lattice. This problem is

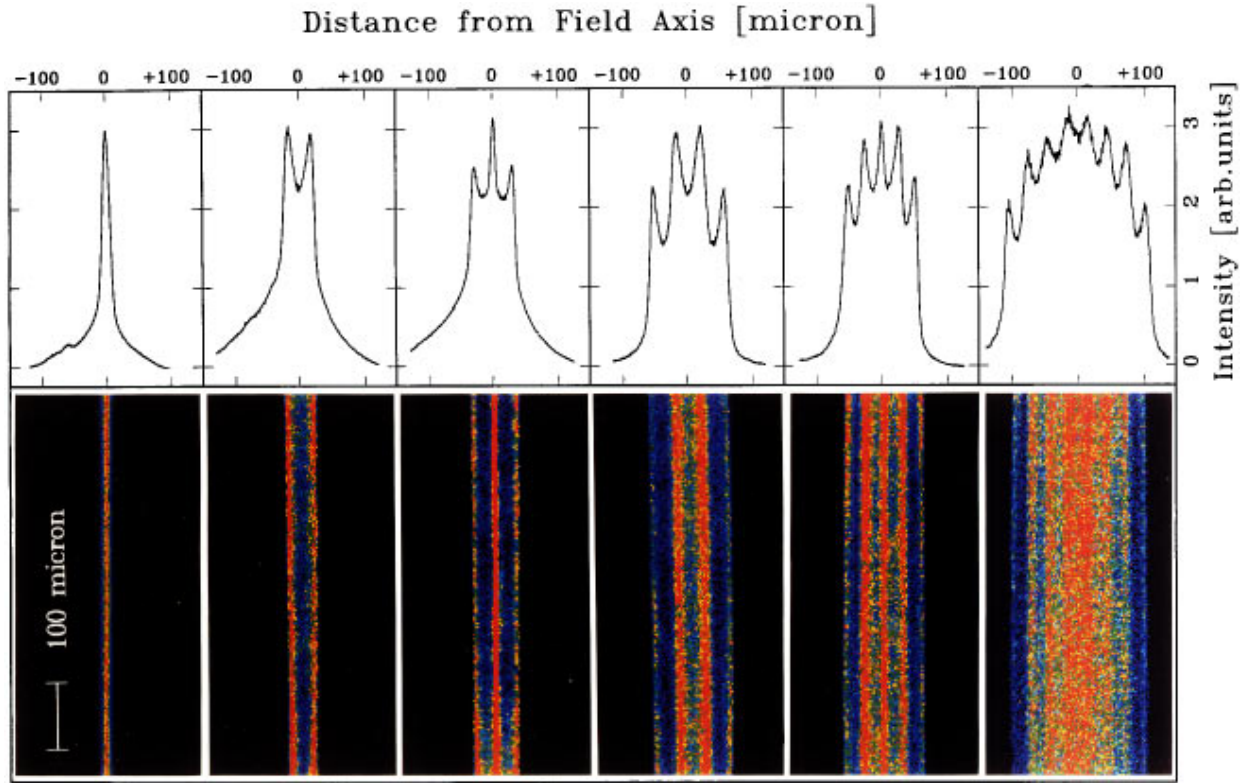


FIG. 45. (Color) Images and intensity profiles of ions in the ring trap, observed via laser fluorescence, as  $N$  increases: (a) 1D chain; (b) one shell,  $N=5 \times 10^4$ ; (c) one shell+chain,  $N=1 \times 10^5$ ; (d) two shells,  $N=2 \times 10^5$ ; (e) two shells+string,  $N=3 \times 10^5$ ; (f) four shells,  $N=8 \times 10^5$ . From Birkel, Kassner, and Walther (1992).

clearly related to the neglect of correlations between separate shells. In the next section we consider a shell model that can account for intershell correlations and that also addresses the issue of asymmetric geometries such as spheroidal plasmas.

## 2. Planar shell model

Consider a system of charges confined in the  $z$  direction by a uniform neutralizing background  $n_-$ . In the  $x$  and  $y$  directions the system is infinite and homogeneous. This system models the surface region of a spheroidal plasma with a sufficiently large radius that the curvature can be neglected. Thus the  $z$  direction can be thought of as the local normal to the surface of the plasma.

A shell model can be developed for this geometry (Dubin, 1989). This planar model has the advantage that it applies to systems of any shape, provided that the radius of curvature of the shells is large compared to the Wigner-Seitz radius. The shell model analogous to Eq. (4.92) consists of a series of  $S$  planes at positions  $z_i$  with number per unit area  $\sigma_i$ . The planes are ordered so that  $z_1 < z_2 < z_3 < \dots$ . The total number per unit area is

$$\sigma = \sum_{i=1}^S \sigma_i.$$

The planes are in a potential well of the form  $m\omega_p^2 z^2/2$ , where  $\omega_p = \sqrt{4\pi e^2 n_- / m}$  is the plasma frequency of the

effective neutralizing background charge. The energy per particle of this shell model is a sum of three terms:

$$\frac{E}{N} = \frac{1}{\sigma} \left[ \int_{-L}^L \frac{\varepsilon^2(z)}{8\pi} dz + \sum_{i=1}^S \left( \frac{1}{2} m \omega_p^2 z_i^2 \sigma_i - \frac{e^2 \eta}{2} \sigma_i^{3/2} \right) \right], \quad (4.95)$$

where  $\pm L$  are the positions of conducting walls. The first term is the self-energy of the set of  $S$  planes, written in terms of the space-charge electric field  $\varepsilon(z)$ . The second term in Eq. (4.95) is the energy associated with the external potential, and the last term is the correlation energy associated with each 2D hexagonal lattice plane. The constant  $\eta=3.921$  is the same as appears in Eq. (4.91b). As in the previous cylindrical shell model, no correlations between different shells are kept in this version of the model. These correlations will be considered presently.

Since the magnitude of the electric field due to a given plane  $j$  is constant, equal to  $2\pi e\sigma_j$ , the field due to all the planes can be written as a sum,

$$\varepsilon(z) = 2\pi e \left( 2 \sum_{j=1}^i \sigma_j - \sigma \right), \quad (4.96)$$

where  $i$  labels the plane nearest to  $z$  for which  $z_i < z$ . Substituting Eq. (4.96) into Eq. (4.95), the integral over  $z$  can be performed, yielding

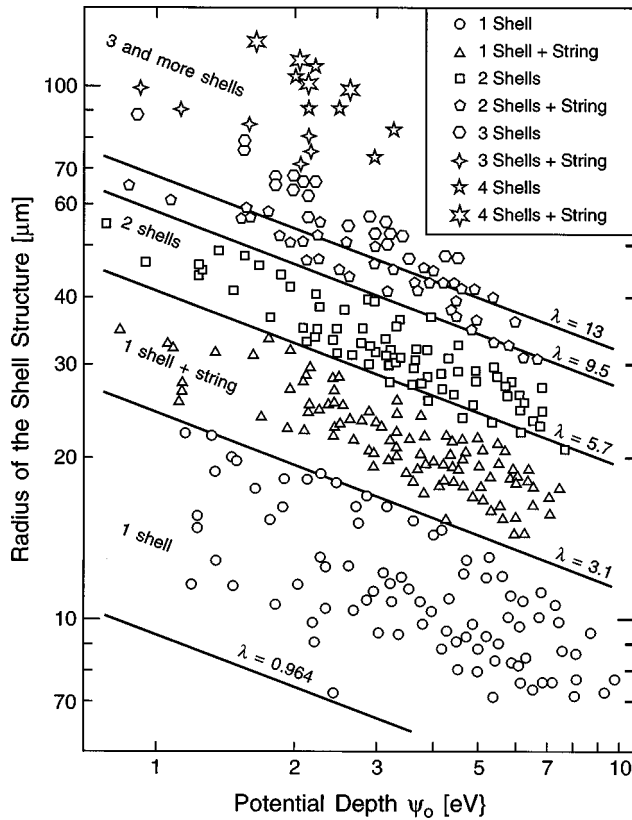


FIG. 46. Outer radius of the shell structure as a function of the potential depth  $\psi_0$  (in V) in a quadrupole ring trap. Different symbols denote different numbers of shells and/or central strings. From Birkel, Kassner, and Walther (1992).

$$\frac{E}{N} = \frac{e^2}{a} \left[ \frac{\pi}{2} \bar{\sigma} \sum_{i=1}^{S+1} (2f_{i-1} - 1)^2 (\bar{z}_i - \bar{z}_{i-1}) + \frac{3}{2\bar{\sigma}} \sum_{i=1}^S \bar{\sigma}_i \bar{z}_i^2 - \frac{\eta}{2\bar{\sigma}} \sum_{i=1}^S \bar{\sigma}_i^{3/2} \right], \quad (4.97)$$

where

$$\bar{\sigma}_i = \sigma_i a^2, \quad \bar{z}_i = z_i / a, \quad f_i = \sum_{j=1}^i \bar{\sigma}_j / \bar{\sigma},$$

$f_0 = 0$ , and  $z_{S+1} = L$  and  $z_0 = -L$ . [Note that in Dubin (1989), distances were normalized to  $n_-^{-1/3}$ ; here we normalize to the Wigner-Seitz radius  $a$ .]

The parameter  $\bar{\sigma}$  is the total number per unit area normalized by the Wigner-Seitz radius:

$$\bar{\sigma} = \sigma a^2. \quad (4.98)$$

This parameter plays the same role as the parameter  $\lambda$  (or  $k$ ) in the cylindrical shell model. It parametrizes the strength of the Coulomb repulsion between adjacent charges, of order  $e^2 \sigma$ , compared to the strength of the background confinement force, of order  $e^2/a^2$ . As  $\bar{\sigma}$  increases, we expect the number of lattice planes  $S$  to increase.

Minimization of Eq. (4.97) with respect to the position  $z_i$  and charge density  $\sigma_i$  of each lattice plane, holding  $S$  fixed, implies that the charge density on each lattice plane is identical,

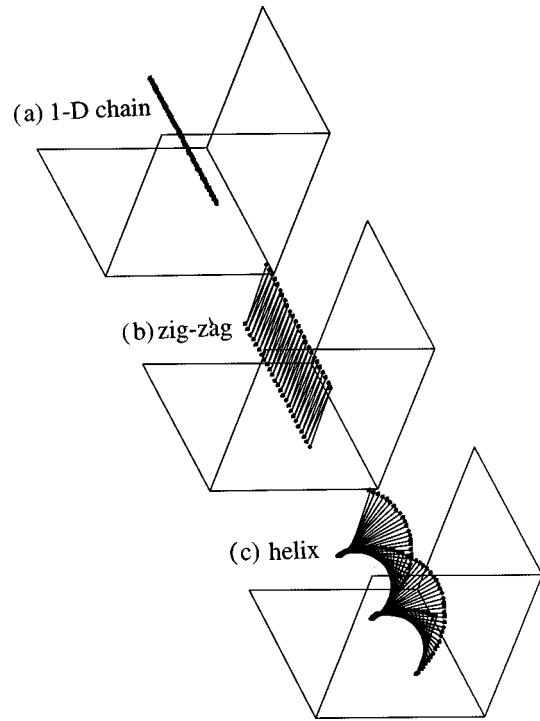


FIG. 47. Structure of infinitely long cylindrical plasma at low density per unit length ( $x-y$  dimensions magnified for clarity): (a)  $\lambda < 0.709$ : 1D Coulomb chain; (b)  $0.709 < \lambda < 0.964$ : zigzag; (c)  $0.964 < \lambda < \dots$ : helix.

$$\sigma_i = \frac{\sigma}{S}, \quad (4.99)$$

and that the lattice planes are spaced by a uniform distance  $D$ ,

$$z_i = z_i^{(0)} \equiv D \left( i - \frac{S+1}{2} \right), \quad i = 1, 2, \dots, S. \quad (4.100)$$

The spacing between planes is related by force balance to the charge on each lattice plane and the density of the background:

$$D = \frac{\sigma}{n_- S}. \quad (4.101)$$

As one might expect, the mean density of the system of planes,  $\sigma/D S$ , matches the background density  $n_-$ .

The energy per particle of the system is found by substituting Eqs. (4.99)–(4.101) into Eq. (4.97):

$$\frac{E}{N} = \pi e^2 \left[ L \sigma - \frac{1}{6} \frac{\sigma^2}{n} \right] + \frac{U_{\text{corr}}}{N}, \quad (4.102)$$

where the term in square brackets is the cold mean-field energy per particle of a uniform slab of density  $\sigma$  per unit area, and  $U_{\text{corr}}$  is the extra correlation energy of the shell model,

$$\frac{U_{\text{corr}}}{N} = \frac{e^2}{a} \left[ \frac{2\pi^2}{9} \left( \frac{\bar{\sigma}}{S} \right)^2 - \frac{\eta}{2} \left( \frac{\bar{\sigma}}{S} \right)^{1/2} \right]. \quad (4.103)$$

This extra energy arises because the system consists of  $S$  planes of charge rather than a uniform slab of charge (the first term), and correlations between particles within each plane are kept (the second term).

The first term in Eq. (4.103) is positive, indicating that a system of  $S$  parallel planes of charge has higher energy than a charge spread throughout a uniform slab, as one would expect intuitively. However, the second term, arising from intraplane correlations, is negative and this creates a tendency to form a finite set of ordered planes. The competition between these two terms determines how many planes form, just as in the previous cylindrical shell model.

For a given value of the parameter  $\bar{\sigma}$  we can determine the number of lattice planes  $S$  by minimizing  $U_{\text{corr}}$  with respect to  $S$ , from which one finds that the value of  $S$  giving the minimum energy is

$$S_{\text{min}} = [16\pi^2/(9\eta)]^{2/3} \bar{\sigma}. \quad (4.104)$$

The normalized distance between lattice planes is then determined by Eqs. (4.104) and (4.101),

$$\bar{D} \equiv \frac{D}{a} = \left( \frac{3\eta^2}{4\pi} \right)^{1/3} = 1.54, \quad (4.105)$$

where  $a$  is an average interparticle spacing, and the correlation energy is

$$\frac{U_{\text{corr}}}{N} = -\frac{3}{8} \left( \frac{9\eta^4}{16\pi^2} \right)^{1/3} \frac{e^2}{a} = -0.8923 \frac{e^2}{a}, \quad (4.106)$$

where we have used the value of  $\eta$  for a 2D hexagonal lattice,  $\eta = 3.921 \dots$ . Note that this  $\eta$  value yields the lowest possible energy since the 2D hexagonal lattice has the lowest Madelung energy of all 2D lattices.

Of course,  $S$  must be an integer, so Eq. (4.106) is actually the minimum possible correlation energy, occurring when  $\bar{\sigma}$  is chosen such that  $S_{\text{min}}$  is an integer. For other values of  $\bar{\sigma}$  the minimization procedure produces an integer value of  $S$  close to  $S_{\text{min}}$ , and a value of  $U_{\text{corr}}/N$  close to but slightly larger than Eq. (4.106). The actual solutions for  $S$ ,  $U_{\text{corr}}$ , and  $\bar{D}$  as a function of  $\bar{\sigma}$  are shown in Fig. 48. The cusps in  $U_{\text{corr}}$  as  $\bar{\sigma}$  increases arise as  $S$  increases by integer steps. For large  $\bar{\sigma}$  one can observe in Fig. 48 that  $S$  remains close to  $S_{\text{min}}$  and  $D$  is close to the value  $1.54 a$ .

Considering the results of this planar shell model as applied to a confined spheroidal plasma with large radius of curvature, we observe that simulations show the charge per unit area on each shell and the spacing between shells are approximately constant (see Table II, or Figs. 22, 24, and 30), and the spacings are close to the value  $1.54 a$  given by Eq. (4.105).

The shell spacing  $D$  can be used to estimate the number of spheroidal shells expected to be observed in a large spheroidal plasma (Dubin, 1989). Observing that the shells closely follow the surface of the cold mean-field spheroid, we find that the number of shells is simply determined by the number of equidistant concentric surfaces one can fit into a spheroid of given radius  $R_p$  and length  $2Z_p$ . Noting that  $N = 4\pi R_p^2 Z_p n_-/3$ , we obtain from this simple algorithm the following estimate for the number of shells as a function of  $N$  and the aspect ratio  $\alpha = Z_p/R_p$ :

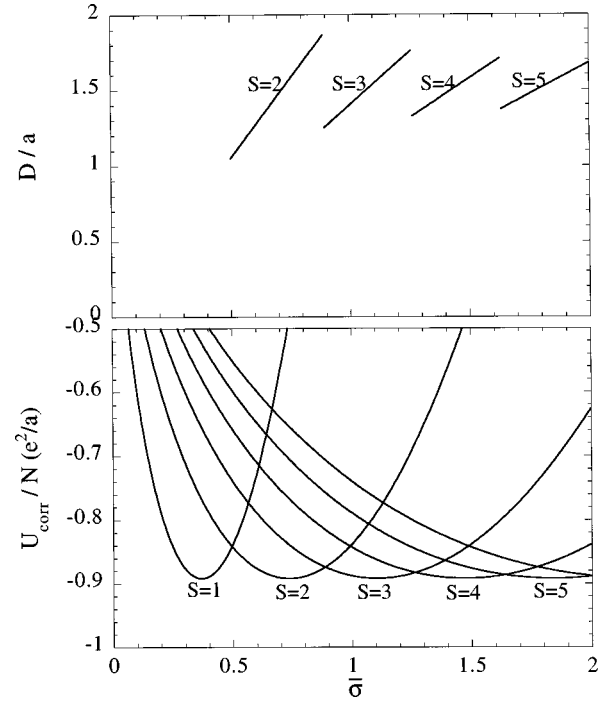


FIG. 48. Planar shell model neglecting interplane correlations: Upper plot: spacing  $D$  between adjacent lattice planes, number of planes  $S$ . Lower plot: correlation energy per particle  $U_{\text{corr}}/N$  as a function of  $\bar{\sigma} = \sigma a^2$ , where  $\sigma$  is the number of particles per unit area and  $a$  is the Wigner-Seitz radius.

$$S \approx \begin{cases} \left( \frac{N}{\alpha} \right)^{1/3} \frac{a}{D}, & \alpha \geq 1, \\ (N\alpha^2)^{1/3} \frac{a}{D}, & \alpha \leq 1. \end{cases} \quad (4.107)$$

For example, for a spherical cloud of  $N = 4096$  particles, Eqs. (4.107) and (4.105) imply that one should observe 10.4 shells, whereas Fig. 30 shows that such a cloud has 10 shells (and a central charge). For  $N = 1028$  charges, a cloud with  $\alpha = 1.75$  is predicted to have 5.4 shells, whereas Fig. 24 shows that such a cloud actually has five shells and a central Coulomb chain of four charges. Of course, this algorithm breaks down when  $N$  is small, or when  $\alpha$  is either much less or much greater than unity. The case of small  $N$  (Coulomb clusters) is considered in Sec. IV.E, while the cases of small and large  $\alpha$  are discussed in Sec. IV.D.5.

### 3. Intershell correlations

So far we have neglected correlations between particles in separate lattice planes. As a result the planar shell model discussed in Sec. IV.D.2 suffers from the same defect as the cylindrical shell model discussed in Sec. IV.D.1: as  $\bar{\sigma} \rightarrow \infty$  (or equivalently as  $S \rightarrow \infty$ ), the system becomes infinite and homogeneous, yet there is no transition to the bcc lattice as expected for an infinite homogeneous OCP. We shall now resolve this problem by introducing an improved model that keeps correlations between the shells (Dubin, 1989). We further generalize the previous model by relaxing the assumption

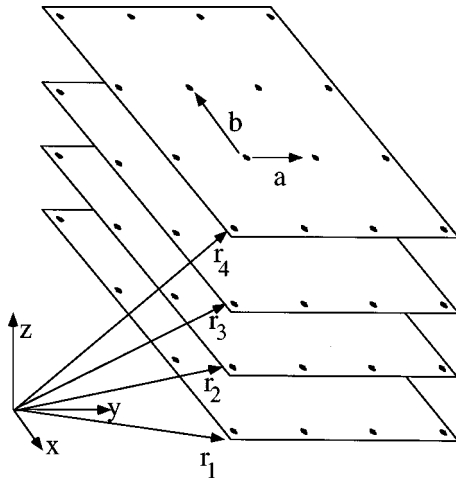


FIG. 49. Planar shell model including correlations between lattice planes.

that the planar lattice within each shell is 2D hexagonal; we shall see that this is crucial to our analysis. However, in order that the model be tractable we assume that each planar shell consists of the same 2D lattice, defined by primitive vectors  $\mathbf{a}$  and  $\mathbf{b}$ , and that these lattices are displaced in space from one another by  $\mathbf{r}_j = (x_j, y_j, z_j)$  (see Fig. 49). This necessarily implies that the number of charges per unit area  $\sigma_i$  in each planar shell is identical, equal to  $\sigma/S$ . However, the correlations between shells imply that the spacing between shells now varies:

$$\bar{z}_i = \bar{z}_i^{(0)} + \delta\bar{z}_i, \quad (4.108)$$

where  $\bar{z}_i^{(0)}$  is the shell position given by Eq. (4.100) and  $\delta\bar{z}_i$  is the variation in position. The correlation energy of the system, including intershell correlations, is then (Dubin, 1989)

$$\begin{aligned} \frac{U_{\text{corr}}}{N} = & \frac{e^2}{a} \left\{ \frac{2\pi^2}{9} \left( \frac{\bar{\sigma}}{S} \right)^2 - \frac{\hat{\eta}}{2} \left( \frac{\bar{\sigma}}{S} \right)^{1/2} \right. \\ & + \frac{\pi\bar{\sigma}}{S^2} \sum_{i=1}^S \sum_{j \neq i}^S \sum_{\mathbf{k}}' e^{-\bar{k}|\bar{z}_i - \bar{z}_j|} \\ & \left. \times \frac{\cos \bar{\mathbf{k}} \cdot (\bar{\mathbf{r}}_i - \bar{\mathbf{r}}_j)}{\bar{k}} + \frac{3}{2S} \sum_{i=1}^S \delta\bar{z}_i^2 \right\}, \quad (4.109) \end{aligned}$$

where distances are in units of  $a$ ,  $\hat{\eta}$  is the constant determining the 2D correlation energy of a given 2D lattice plane, and the sum over  $\mathbf{k}$  is a sum over the reciprocal lattice to the 2D lattice plane; the prime denotes neglect of the  $\mathbf{k}=0$  term. The constant  $\hat{\eta}$  depends on the angle between  $\mathbf{a}$  and  $\mathbf{b}$  and the ratio of their lengths. The reciprocal lattice is defined by primitive vectors

$$\left( \frac{2\pi S}{\sigma} \hat{\mathbf{z}} \times \mathbf{a}, \frac{2\pi S}{\sigma} \hat{\mathbf{z}} \times \mathbf{b} \right). \quad (4.110)$$

The first two terms of Eq. (4.109) are identical to Eq. (4.103) and provide the contribution to the correlation energy that arises from neglecting correlations between

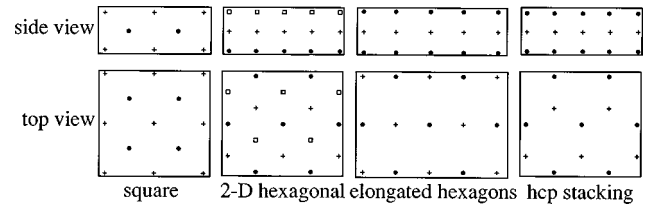


FIG. 50. Local minimum-energy planar-lattice structures: top view looks along  $z$  axis. Side view looks along  $x$  axis, showing three planes.

charges in different planes. The third and fourth terms account for interplane correlations. The third term provides the Coulomb interaction energy between two identical lattice planes separated by  $\mathbf{r}_i - \mathbf{r}_j$ , subtracting out the interaction energy of two uniform planes (the  $\mathbf{k}=0$  term in the sum) since this energy has already been accounted for in the first term. The last term is the extra energy due to the external potential because the planes are no longer spaced evenly.

In order to find the structure of the crystal for a given value of  $\bar{\sigma}$  one minimizes the correlation energy with respect to the lattice-plane positions  $\mathbf{r}_i$ , the structure of each plane as defined by the primitive vectors  $\mathbf{a}$  and  $\mathbf{b}$ , and the number of lattice planes  $S$ . For example,  $\delta\bar{z}_i$  is determined by the equation

$$\begin{aligned} \delta\bar{z}_i = & \frac{\bar{D}}{2} \sum_{i=1}^S \sum_{j \neq i}^S \sum_{\mathbf{k}}' \text{sgn}(\bar{z}_i - \bar{z}_j) e^{-k|z_i - z_j|} \\ & \times \cos \bar{\mathbf{k}} \cdot (\bar{\mathbf{r}}_i - \bar{\mathbf{r}}_j), \quad (4.111) \end{aligned}$$

which can be solved iteratively for  $\delta\bar{z}_i$  if  $S$ ,  $x_i$ ,  $y_i$ ,  $\mathbf{a}$ , and  $\mathbf{b}$  are known. However, rather than performing the full numerical minimization over all parameters, Dubin (1989) considered only a few symmetric lattice types, fixing  $\mathbf{a}$ ,  $\mathbf{b}$ ,  $x_i$ , and  $y_i$ . The choices were based on the intuition that these symmetric lattices could form bcc and fcc structures in the bulk. While this method does not guarantee that the true minimum-energy structure is found, it considerably simplifies the analysis. For a few values of  $\sigma$ , the full minimization was performed, and in each run the crystal settled into one of these symmetric lattices within the numerical accuracy of the procedure (however, see the *Note* on page 143). These symmetric lattices are displayed in Fig. 50 and Table IV and consist of square, 2D hexagonal, and elongated hexagonal lattice planes. Other cases, such as hcp stacking (Fig. 50), also consist of 2D hexagonal lattice planes, but the planes are stacked differently and have slightly higher energy than the 2D hexagonal stacking. From among this finite set of equilibria one chooses the value of  $S$  that provides the lowest energy for a given  $\bar{\sigma}$ . For example, when  $\bar{\sigma}$  is small the minimum energy state is a single 2D hexagonal lattice plane. As  $\bar{\sigma}$  increases beyond the critical value,

$$\sigma_1 a^2 = 0.427 \dots, \quad (4.112)$$

the single 2D hexagonal plane becomes unstable, as Coulomb repulsion forces charges out of the  $x$ - $y$  plane, and the system forms three interlocking 2D hexagonal

TABLE IV. Surface energies of bounded Coulomb lattices.

3D lattice type	Lattice plane parallel to surface	Type of lattice plane	<b>a</b> ←	<b>b</b> (arb. units)	$(x_j, y_j)$ →	$D/a$ for perfect lattice	$E_s(e^2/a)$
bcc	(111)	2D hexagonal	(1,0)	$(1/2, \sqrt{3}/2)$	$(0, 1/\sqrt{3})j$	0.5863	$4.6055 \times 10^{-2}$
bcc	(100)	square	(1,0)	(0,1)	$(1/2, 1/2)j$	1.016	$2.3395 \times 10^{-2}$
bcc	(110)	elongated hexagons	(1,0)	$(1/2, 1/\sqrt{2})$	$(1/2, 0)j$	1.436	$3.779 \times 10^{-3}$
fcc	(110)	rectangular	(1,0)	$(0, \sqrt{2})$	$(1/2, 1/\sqrt{2})j$	0.9046	$3.0370 \times 10^{-2}$
fcc	(100)	square	(1,0)	(0,1)	$(1/2, 1/2)j$	1.279	$1.0185 \times 10^{-2}$
fcc	(111)	2D hexagonal	(1,0)	$(1/2, \sqrt{3}/2)$	$(0, 1/\sqrt{3})j$	1.477	$2.147 \times 10^{-3}$
hcp		2D hexagonal	(1,0)	$(1/2, \sqrt{3}/2)$	$(0, 0), j \text{ even}$ $(0, 1/\sqrt{3}), j \text{ odd}$	1.477	$2.12 \times 10^{-3}$

lattice planes. The distance between the planes rapidly increases as  $\sigma$  increases, until at  $\sigma_2 a^2 = 0.442$  a different local minimum consisting of two square lattice planes takes over as the global energy minimum. As  $\sigma$  increases, this structure is replaced by another energy minimum consisting of two planes with elongated hexagonal symmetry (Dubin, 1993).

Figure 51 displays other equilibria further along in the sequence as  $\bar{\sigma}$  increases. One can see that for large  $\bar{\sigma}$  a symmetric lattice is created in the bulk with nearly evenly spaced lattice planes, spaced by the distance  $D = \sigma/(n_{\perp} S)$  predicted by the previous planar shell model [Eq. (4.101)].

Only near the surfaces are the lattice planes unevenly spaced. This is because, as Eq. (4.111) shows, the variation in spacing is caused by correlation forces between different planes. These correlation forces fall off expo-

ponentially with distance between the planes, with a characteristic exponentiation length of order  $1/k_{\min}$  where  $k_{\min}$  is the minimum magnitude of the reciprocal lattice vectors [see Eq. (4.111)]. Thus in the bulk the correlation force cancels and  $\delta \bar{z}_i$  vanishes.

#### 4. Mesoscopic to large-plasma transition

As  $\bar{\sigma}$  increases, the symmetry of the lattice continues to jump between 2D hexagonal lattice planes and elongated hexagonal planes. In the bulk, away from the surface, the 2D hexagonal lattice planes form an fcc lattice and the elongated hexagonal planes form a bcc lattice. The energies of these competing minima are displayed in Fig. 52. The energies of the fcc and bcc lattices show a similar cusp behavior to that in the previous shell model neglecting interplane correlations [Fig. 48(b)], along with an overall downward trend as  $\bar{\sigma}$  increases. The competing energy curves cross many times, so the lattice structure exhibits sensitive dependence on  $\bar{\sigma}$ .

As can be seen in Fig. 52, the sensitive dependence of the lattice structure on  $\bar{\sigma}$  persists until  $\bar{\sigma}$  becomes quite large. Only for  $\bar{\sigma} \gtrsim 20$ –21 is the bcc lattice the lowest-energy state without any further sensitive dependence on  $\bar{\sigma}$ ; this defines the large-plasma regime. Using Eq. (4.101) and the  $D/a$  values for perfect fcc and bcc lat-

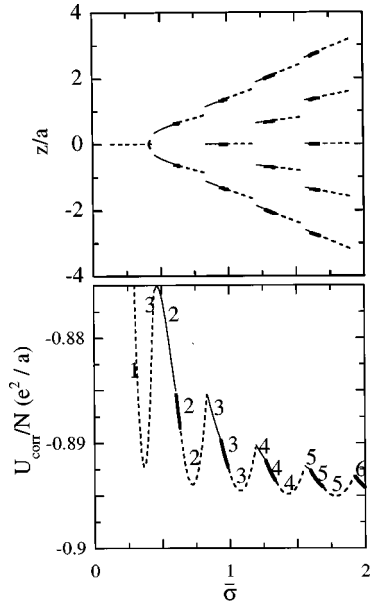


FIG. 51. Planar shell model keeping interplane correlations: Upper plot,  $z$  position, number, and type of lattice planes as normalized density per unit area  $\bar{\sigma} = \sigma a^2$  increases; dashed line, 2D hexagonal; thin solid line, square; heavy solid line, elongated hexagons. Lower plot, correlation energy per particle  $U_{\text{corr}}/N$  for these bounded lattices. Numbers refer to number of planes.

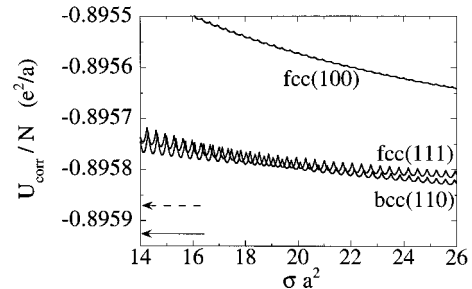


FIG. 52. Correlation energy per particle  $U_{\text{corr}}/N$  as a function of normalized density per unit area  $\bar{\sigma} = \sigma a^2$  values near the point where structural transitions between fcc and bcc order cease (continuation of Fig. 51 to large  $\bar{\sigma}$  values). Dashed and solid horizontal arrows show energies of infinite fcc and bcc lattices, respectively. fcc (100) corresponds to the square lattice of Fig. 51, while fcc (111) corresponds to the 2D hexagonal structure and bcc (110) corresponds to the elongated hexagons. From Dubin (1989).

tices in Table IV, we find that this range of  $\bar{\sigma}$  corresponds to  $S \approx 58$  bcc lattice planes or  $S \approx 57$  fcc planes.

For  $\bar{\sigma} \lesssim 20$  the many transitions between fcc and bcc structure can be understood as a competition between surface energy and bulk energy in each structure. For large  $S$  and  $\bar{\sigma}$ , the correlation energy per particle, Eq. (4.109), can be written as a sum of a bulk energy per particle  $E_b$  and a surface energy per particle  $2E_S/S$ :

$$\frac{U_{\text{corr}}}{N} = E_b + \frac{2E_S}{S}. \quad (4.113)$$

For given values of  $\bar{\sigma}$ ,  $S$ ,  $\mathbf{a}$ , and  $\mathbf{b}$ , the bulk energy is obtained from Eq. (4.109) by taking an infinite number of lattice planes spaced evenly by the normalized distance  $\bar{D}$  given by Eq. (4.101):

$$E_b = \frac{e^2}{a} \left[ \frac{\bar{D}^2}{8} + \frac{3\bar{D}}{2} \sum_{j=1}^{\infty} \sum_{\mathbf{k}}' \frac{e^{-\bar{D}\bar{k}j}}{\bar{k}} \times \cos \mathbf{k} \cdot (\bar{\mathbf{r}}_{j+1} - \bar{\mathbf{r}}_1) - \frac{\hat{\eta}}{2} \left( \frac{3}{4\pi} \bar{D} \right)^{1/2} \right]. \quad (4.114)$$

Certain values of  $\mathbf{a}$ ,  $\mathbf{b}$ ,  $\mathbf{r}_j$ , and  $\bar{D}$  minimize  $E_b$ . For example, for  $\mathbf{a}$  and  $\mathbf{b}$  corresponding to a 2D hexagonal lattice, and for the  $\mathbf{r}_j$ 's chosen as shown in Table IV,  $\bar{D} = 1.477$  makes a perfect fcc lattice, with a bulk energy per particle given in Table I. This 2D hexagonal lattice corresponds to the fcc (111) plane, so we call this lattice fcc (111). On the other hand, for  $\mathbf{a}$  and  $\mathbf{b}$  corresponding to the elongated hexagons,  $\bar{D} = 1.436$  creates a bcc (110) lattice [i.e., the (110) plane is parallel to the surface]. Since fcc and bcc lattices have the lowest energies, and these energies are nearly identical (see Table I), the values  $\bar{D} = 1.436$  and  $\bar{D} = 1.477$  are preferred and, for a given value of  $\bar{\sigma}$ ,  $S$  will be an integer as close as possible to  $4\pi\bar{\sigma}/(3\bar{D})$  [see Eq. (4.101)]. Each successive cusp in the correlation energy curves displayed in Fig. 52 corresponds to a unit increase in  $S$  and a concurrent jump in  $E_b$  as  $\bar{D}$  varies around the preferred value. Since the bulk bcc and bulk fcc energies are extremely close, with bcc lower by less than one part in  $10^4$  (see the horizontal arrows in Fig. 52), only a very small surface-energy contribution need be added in order to change the lattice structure. It is for this reason that the lattice structure displays sensitive dependence on  $\bar{\sigma}$  even for rather large values of  $\bar{\sigma}$ .

The bcc (110) and fcc (111) orientations are favored over the myriad other orientations since these orientations have low surface energies. For an infinite lattice any orientation is possible, but for a bounded lattice the surface energy depends on which lattice plane is parallel to the surface. The surface energy is given by the difference between the correlation energy, Eq. (4.109), and the bulk energy, Eq. (4.114). When  $S$  is large  $E_S$  becomes independent of  $S$ :

$$E_S = \frac{e^2}{a} \left[ \frac{3}{2} \sum_{j=1}^{\infty} (\delta \bar{z}_j)^2 + \frac{3\bar{D}}{4} \sum_{i=1}^{\infty} \sum_{j \neq i}^{\infty} \sum_{\mathbf{k}}' \times [e^{-\bar{k}|\bar{z}_i - \bar{z}_j|} - e^{-\bar{k}\bar{D}|i-j|}] \frac{\cos \mathbf{k} \cdot (\bar{\mathbf{r}}_i - \bar{\mathbf{r}}_j)}{\bar{k}} \right]. \quad (4.115)$$

For stable lattices  $E_S$  is positive (Landau and Lifshitz, 1980, p. 517). Values of  $E_S$  for bulk bcc and fcc lattices with different orientations are displayed in Table IV. As one can see from the table, the surface energy of a lattice with bulk bcc symmetry is minimized when the 110 plane (elongated hexagons) is parallel to the surface. For an fcc lattice the surface energy is minimized when the 111 plane (a 2D hexagonal lattice plane) is parallel to the surface, and this surface energy is slightly less than that of the bcc lattice. [The hcp surface energy is slightly lower than fcc (111), but the bulk energy of hcp structure is too high to make it a contender for the minimum-energy state.]

Thus the bcc (110) and fcc (111) orientations are favored; other orientations of the bcc and fcc lattices have larger surface energy, as can be seen in Fig. 52 for the fcc (100) lattice, which is the next lowest energy state. This is because the fcc (111) and bcc (110) lattice planes are the most widely separated lattice planes in fcc and bcc lattices, respectively. The wider the separation of the planes, the lower the correlation between them (the planes appear to one another as uniform sheets at large separation), and less interplane correlation implies less surface energy [recall that in the previous planar shell model, where interplane correlations were neglected, there was no surface energy term—see Eq. (4.106)].

*Note.* It has recently been discovered that the elongated hexagons deform into a slightly lower energy rhombic structure when full energy minimization is performed in the planar shell model [Eq. (4.109)] (Mitchell, Bollinger, Dubin, Huang, Itano, and Baughman, 1998). This has the effect of reducing the ranges of  $\sigma$  over which the square lattice is minimum energy compared to what is shown in Fig. 51, and of lowering energy of the bcc(110) lattice by a nearly imperceptible amount in Fig. 52. However, there is a negligible effect on the  $z$  positions of the lattice planes (Fig. 51) or on the mesoscopic to large-plasma transition.

The planar model neglects surface curvature and so applies in detail only to the central region of very oblate plasmas or to the surface region of large plasmas. However, it may be that certain aspects of the model can be applied to mesoscopic spheroidal plasmas. Numerical studies have been performed to determine the energies of spherical Coulomb crystals at zero temperature as a function of the number of particles  $N$  (Hasse and Avilov, 1991). The simulation results are shown in Fig. 53 as solid points. The correlation energy of mesoscopic spherical plasmas with  $N \lesssim 5000$  is observed to obey roughly a bulk-plus-surface-energy form:

$$\frac{U_{\text{corr}}}{N} = E_b + \frac{E_S}{N^{1/3}} + \frac{E_{cu}}{N^{2/3}}, \quad (4.116)$$



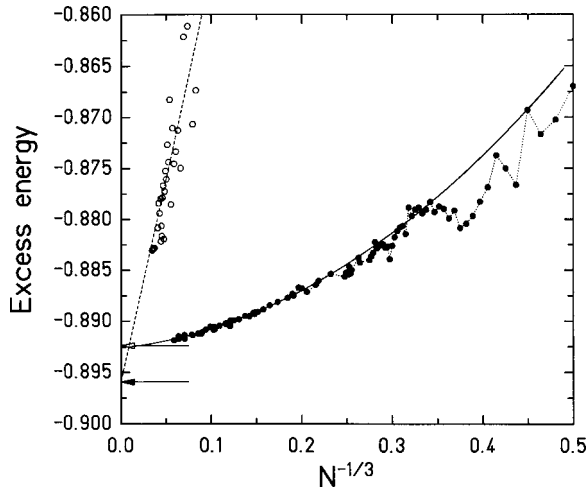


FIG. 53. Correlation energy per particle in spherical Coulomb crystals vs number of particles to the  $-1/3$  power: solid points, molecular dynamics simulations of mesoscopic plasmas; open circles, spherical fragments of bcc crystals. Lines are fits of the form given by Eq. (4.116). From Hasse and Avilov (1991).

where  $E_{cu}$  is a “curvature energy” term, and  $E_b$ ,  $E_S$ , and  $E_{cu}$  are determined by a numerical fit to the data (the solid curve in Fig. 53). The authors compare these computed energies to those of spherical fragments of a bcc crystal (the open circles), also fitting this data set using Eq. (4.116) (the dashed curve). The crossing point of these two fits provides an estimate that the mesoscopic shell-structure phase gives way to a bcc lattice when  $N \geq 10^6$ , corresponding to a diameter of roughly  $200 a$ . This is somewhat larger than what is suggested by the planar shell model, in which the thickness  $SD$  of the system (where  $S$  is the number of planes and  $D$  the spacing between adjacent planes) is about  $90 a$ . This follows from our previous estimate  $\bar{\sigma} \approx 20$  for the mesoscopic to large-plasma transition, together with Eq. (4.101). In a spherical plasma this thickness corresponds to  $N \sim 10^5$  charges, if we take the thickness of the planar system to correspond to the diameter of the spherical system (the number is somewhat larger if this thickness corresponds to the radius rather than the diameter of the sphere). For spheroidal plasmas, a minimum dimension of about  $90 a$  requires that the particle number exceed

$$N \geq 10^5 \alpha, \quad \alpha < 1, \quad (4.117a)$$

$$N \geq 10^5 / \alpha^2, \quad \alpha > 1. \quad (4.117b)$$

Bragg scattering experiments (Tan *et al.*, 1995a; 1995b; Itano *et al.*, 1998), discussed in Sec. IV.C, observe reproducible bcc order in crystals consisting of a few times  $10^5$  charges, consistent with the estimate of Eq. (4.117). However, a thickness equal to  $90 a$  across the minimum dimension must still be regarded as only a rough estimate for the minimum size of a crystal required to enter the regime of large plasmas.

The planar shell model discussed here neglects the effects of finite temperature on the structural transitions. At finite  $T$  free energies rather than correlation energies

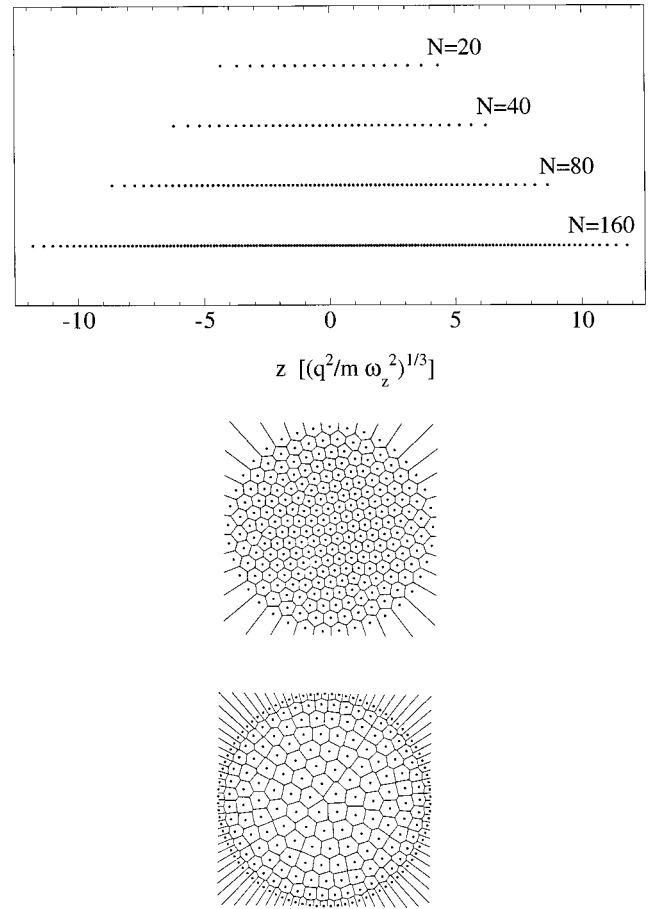


FIG. 54. Positions of charges in minimum-energy states in 1D and 2D systems: (a) 1D Coulomb chains of various sizes in a quadratic confinement potential (Dubin, 1997), (b) 2D systems in quadratic confinement (top) and hard-wall confinement (bottom). Lines show the Wigner-Seitz cells around each charge.  $N = 230$ . From Bedanov and Peeters (1994).

should be compared to determine the stable structure. This requires evaluation of the entropy associated with different crystalline configurations. Such an evaluation has been made in the harmonic lattice approximation, in which the phonons are treated as an ideal gas (Dubin and O'Neil, 1990). The phonon entropy [see Eq. (4.31)] is found to separate into a bulk and a surface contribution. For large  $\bar{\sigma}$  the most stable lattice structures are again fcc(111) and bcc(110), but the number of lattice planes required to enter the regime of large plasmas is found to decrease as temperature increases (the phonon entropy of the bcc lattice is larger than that of the fcc lattice because bcc is not as closely packed as fcc).

#### 5. Limits of large and small aspect ratio: Inhomogeneous Coulomb chains and discs

When the external fields and rotation frequency are chosen such that  $\beta \ll 1$  or  $\beta \gg 1$  the mesoscopic plasma can no longer be described as a system of concentric spheroidal shells. Rather, the charges are squeezed onto the  $z$  axis when  $\beta \gg 1$ , or are collapsed onto the  $x$ - $y$  plane when  $\beta \ll 1$ . Examples of the resulting 1D and 2D

configurations are shown in Fig. 54. Bedanov and Peeters have also analyzed hard-wall confinement potentials [Fig. 54(b, bottom)], but here we focus on the harmonic potential case both for simplicity and because of its experimental relevance. Unlike the shell-structure phase, the interparticle spacing varies with position, increasing with distance from the center of the system. For the 2D disc this variation can be understood from the highly oblate limit of the cold mean-field spheroid (Rafaele *et al.*, 1991; Dubin, 1993). The number of particles per unit area in a spheroid is

$$\sigma(r) = n_- \int_{-z_p(1-r^2/R_p^2)^{1/2}}^{z_p(1-r^2/R_p^2)^{1/2}} dz = \frac{3N}{2\pi R_p^2} \left[ 1 - \left( \frac{r}{R_p} \right)^2 \right]^{1/2}. \quad (4.118)$$

The disc radius  $R_p$  is determined by  $N$ ,  $\omega_z$ , and  $\beta$  using the  $\beta \ll 1$  limit of Eqs. (3.48) and (3.44):

$$R_p = \left( \frac{3\pi e^2 N}{4m\omega_z^2 \beta} \right)^{1/3}. \quad (4.119)$$

The average interparticle spacing in the 2D crystallized disc then varies with position as  $\sigma(r)^{-1/2}$ , which is in fact what is observed in the simulations when  $N$  is large.

However, if we attempt to explain the variation of the interparticle spacing of the 1D Coulomb chain using a similar cold mean-field model, we encounter a problem (Dubin, 1993). Describing the 1D chain as a highly prolate spheroid, the number of particles per unit length should vary as

$$N_L(z) = 2\pi n_- \int_0^{R_p(1-z^2/Z_p^2)^{1/2}} r dr = \frac{3}{4} \frac{N}{Z_p} \left( 1 - \frac{z^2}{Z_p^2} \right), \quad (4.120)$$

and the half-length  $Z_p$  of the spheroid is determined by the  $\beta \gg 1$  limit of Eqs. (3.48) and (3.44),

$$Z_p^3 = \frac{12\pi e^2 N}{m\omega_z^2} \left[ \ln \left[ \frac{8m\omega_z^2}{3e^2} Z_p^3 \beta \right] - 1 \right], \quad (4.121)$$

which is a nonlinear equation for  $Z_p$  that can be solved numerically for given values of  $\omega_z$ ,  $N$ , and  $\beta$ .

The problem with using Eqs. (4.120) and (4.121) as a model for the 1D Coulomb chain is apparent in Eq. (4.121), which says that for fixed  $N$  and  $\omega_z$  the length of the chain increases logarithmically with increasing  $\beta$ . In fact, the length of a 1D chain with all particles on the  $z$  axis should depend only on  $N$  and  $\omega_z$ , since only the confining force in the  $z$  direction should affect the equilibrium. This problem arises because the cold mean-field approximation does not work for a 1D system: a line charge has infinite energy.

This problem does not occur in the 2D disc limit because a 2D disc has finite energy in the mean-field limit, so discreteness of the 2D disc plasma can be safely ignored. In 2D as well as in 3D systems, correlations have only a small effect on the equilibrium. However, for the 1D Coulomb chain the discreteness of the constituent charges cannot be neglected; it has a large effect on the density, even on scales large compared to an interparticle spacing.

To see this another way, note that the total Coulomb energy of a system scales roughly as  $e^2 N^2 / Z_p$ , where  $Z_p$  is the size of the plasma. However, the correlation energy scales as  $Ne^2/a$ , where  $a$  is an average interparticle spacing, of order  $N^{1/D}/Z_p$  for a  $D$ -dimensional system. Thus correlation energy scales as  $N^{1+1/D}e^2/Z_p$ , which is of the same order of magnitude as the total Coulomb energy for a 1D system, but is only a small part of the energy when  $D > 1$ . Therefore the 1D chain equilibrium cannot be correctly determined without including correlation energy.

One can include the correlation energy by using an approximation useful in the limit  $N \gg 1$ , based on the local-density approximation (Dubin, 1993; Dubin, 1997). One writes the self-energy

$$\varepsilon_c = \sum_{i>j} e^2 / |z_i - z_j|$$

of the 1D chain as

$$\varepsilon_c = \varepsilon_0 + U_{\text{corr}}, \quad (4.122)$$

where  $\varepsilon_0$  is the cold mean-field energy of a globule of uniform-density charged fluid, with density per unit volume  $n_-$ , number density  $N_L(z)$  per unit length, and radius  $r_0(z) = [N_L(z)/\pi n_-]^{1/2}$ , and  $U_{\text{corr}}$  is the remaining correlation energy.

The energy  $\varepsilon_0$  of a thin uniform-density globule of arbitrary shape can be written as an integral over the density per unit length  $N_L$ :

$$\varepsilon_0 = \frac{e^2}{2} \int_{-\infty}^{\infty} dz \left\{ \frac{N_L(z)^2}{2} + N_L(z) \int_0^{\infty} dy \times \ln \left[ \frac{2y}{r_0(z)} \right] \frac{d}{dz} [N_L(z-y) - N_L(z+y)] \right\}. \quad (4.123)$$

This expression neglects image charges and assumes  $r_0(z) \ll (d \ln N_L/dz)^{-1}$ ; otherwise, it is valid for any shape  $r_0(z)$  [or number per unit length  $N_L(z)$ ]. [A generalization that includes image charges can be found in Dubin (1997).]

We now require a form for the correlation energy  $U_{\text{corr}}$ . Since the interparticle spacing is assumed to be small compared to the scale of variation of  $N_L$ , the plasma is locally homogeneous, and so we can approximate the correlation energy per particle by that of an infinite homogeneous 1D chain in a cylinder of uniform charge (the local-density approximation). The total correlation energy is then an integral over the correlation energy per particle of a Coulomb chain:

$$U_{\text{corr}} = \int dz N_L e^2 N_L \left[ c(r_0 N_L) - \frac{1}{4} \right] = \int_{-\infty}^{\infty} dz e^2 N_L^2 \left[ \gamma - \frac{1}{4} + \ln \left( \frac{r_0 N_L}{2} \right) \right], \quad (4.124)$$

where we have employed Eqs. (4.90) and (4.91a); the extra factor of  $-1/4$  compared to Eq. (4.91a) arises through the difference in energy between a uniform cyl-

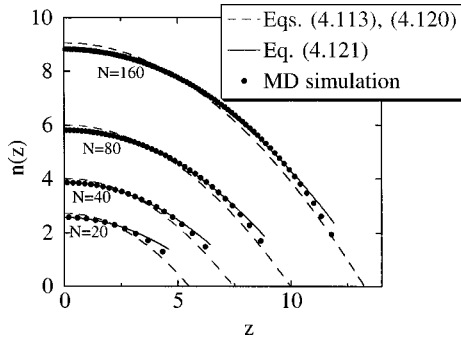


FIG. 55. Density per unit length  $n(z)$  vs position  $z$  in 1D Coulomb chains of different sizes: Dots, molecular-dynamics simulation results taken from Fig. 54(a). Dashed line: One-parameter variational solution of Eq. (4.126). Solid line: Two-parameter variational solution. Distance and density in units of  $(e^2/m\omega_z^2)^{1/3}$ . From Dubin (1997).

inder and a thin cylindrical shell with the same number of particles per unit length  $N_L$  and radius  $r_0$ .

Note that when  $N_L$  is fixed,  $U_{\text{corr}}$  depends on  $r_0$  and as  $r_0 \rightarrow 0$ ,  $U_{\text{corr}}$  diverges logarithmically. The mean-field energy  $\varepsilon_0$  also diverges as  $r_0 \rightarrow 0$  [see Eq. (4.123)]. However, the two divergences cancel when  $\varepsilon_0$  and  $U_{\text{corr}}$  are added together, and the resulting expression for the total self-energy of the Coulomb chain is independent of  $r_0(z)$ :

$$\varepsilon_c = e^2 \int_{-\infty}^{\infty} dz \left\{ \gamma N_L^2(z) + \frac{1}{2} N_L(z) \times \int_0^{\infty} dy \ln[N_L(z)y] \frac{d}{dz} [N_L(z-y) - N_L(z+y)] \right\}. \quad (4.125)$$

In order to determine  $N_L(z)$  we then minimize the total energy of the system with respect to  $N_L$ , including the external potential:

$$E_R[N_L] = \varepsilon_c[N_L] + \int dz N_L(z) \frac{1}{2} m \omega_z^2 z^2. \quad (4.126)$$

This functional minimization procedure yields an integral equation that must be solved numerically in general. An approximate analytic solution can be obtained by choosing a trial variational function for  $N_L(z)$ . One choice that works rather well is the quadratic form given by Eq. (4.120). One can then minimize  $E_R[N_L]$  with respect to the variational parameter  $Z_p$ . This yields the result

$$Z_p^3 = \frac{3e^2}{m\omega_z^2} N [\ln[6N] + \gamma - 13/5]. \quad (4.127)$$

The resulting density per unit length is shown in Fig. 55 and compared to the density per unit length as obtained from simulations of 1D chains. The fit is close, but one can see that Eq. (4.127) slightly overestimates the length of the chain. A much improved fit to the simulations is obtained by using a trial function with two variational parameters,  $Z_p$  and  $C$ :

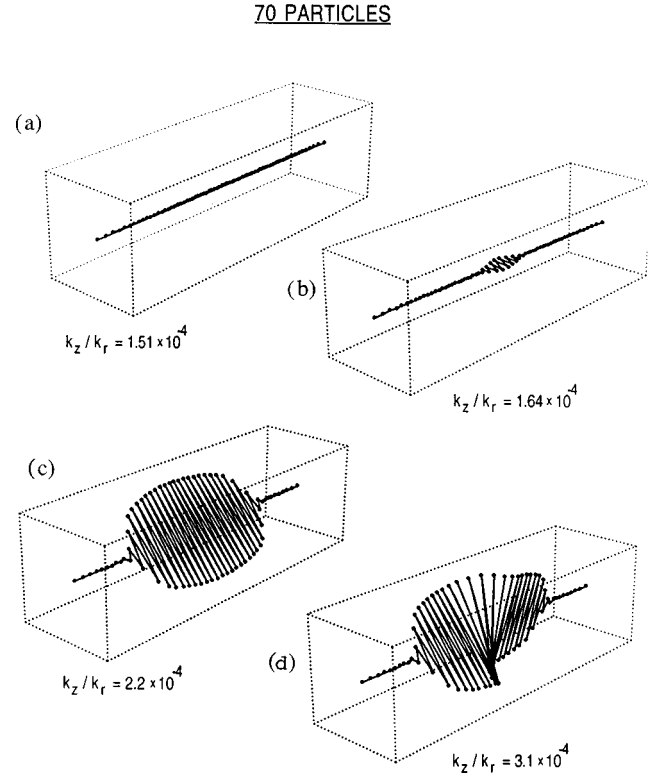


FIG. 56. Structural phase transitions in trapped plasmas for large  $\beta$  and for  $N=70$  charges: (a) 1D Coulomb chain; (b) and (c) zigzag; (d) helix.  $x-y$  scales magnified by a factor of 100 compared to  $z$  scale.  $k_z/k_r = 1/\beta$ . From Schiffer (1993).

$$N_L(z) = \begin{cases} \frac{N}{2Z_p(1-C/3)} (1 - Cz^2/Z_p^2) & |z| < Z_p \\ 0 & |z| > Z_p. \end{cases} \quad (4.128)$$

The form of the coefficients are chosen so that

$$\int_{-Z_p}^{Z_p} dz N_L(z) = N.$$

Minimization of  $E_R[N_L]$  with respect to  $Z_p$  and  $C$  is performed numerically, and the results are shown in Fig. 55 as solid lines, which closely match the simulations.

Although the equilibrium of the 1D chain is unaffected by the value of  $\beta$ , this equilibrium is stable only if  $\beta$  is sufficiently large. If  $\beta$  is too small, the radial confining force cannot overcome the Coulomb repulsion between charges and, just as for the infinite Coulomb chain, the charges move off the axis, forming a zig-zag as in Fig. 47(b). However, since the density of the inhomogeneous chain is largest in the center, the charges first form the zig-zag structure in the central region (Schiffer, 1993). This inhomogeneous zig-zag transition is displayed in Fig. 56. At lower values of  $\beta$  the next instability of an infinite system sets in, and a helical twist develops, which is shown in Fig. 47(c). The analogous transition in a finite system is shown in Fig. 56. As  $\beta$  decreases further, concentric shells eventually develop and we return to the regime of spheroidal shell structure.

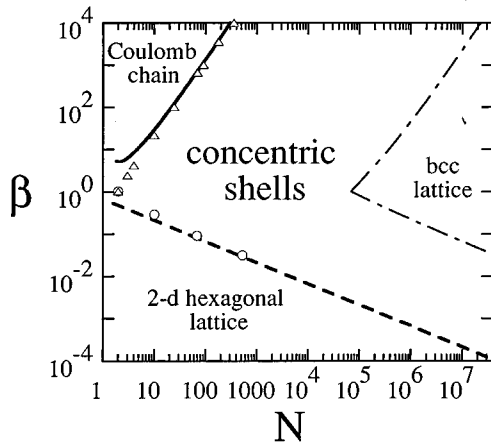


FIG. 57. Structural phase diagram of plasmas trapped in a harmonic potential. Adapted from Dubin (1993) and Schiffer, (1993).

Since the interparticle spacing is small compared to the scale of variation of  $N_L$ , the critical value of  $\beta$  below which the central part of the chain becomes unstable can be evaluated using the result for an infinite homogeneous chain, Eq. (4.93). According to this equation, instability sets in when the minimum value of  $k$ , attained at the center of the chain, falls below 4.2072:

$$\frac{2\pi n_-}{[N_L(z=0)]^3} < 4.2072 \dots \quad (4.129)$$

[here we have used the definition of  $k$ , Eq. (4.84)]. When we use the approximate analytic variational form for  $N_L(z)$ , Eqs. (4.120) and (4.127), together with Eqs. (3.19) and (3.40), then yield

$$\beta_{\text{crit}}(N) = \frac{0.591N^2}{\ln(6N) + \gamma - 13/5}. \quad (4.130)$$

The critical  $\beta$  value for stability of the 1D chain has also been investigated in simulations. Equation (4.130) is found to be a good match to the simulations (Schiffer, 1993) for large  $N$ . In Fig. 57, the triangles display where simulations find an instability of the 1D chain to a zig-zag phase, and the solid line is Eq. (4.130).

Similarly, the 2D disc equilibrium is stable only when  $\beta$  is sufficiently small. If  $\beta$  is too large, Coulomb repulsion overcomes the confining force, and particles near the center of the disc come out of the  $z=0$  plane, just as was discussed for the infinite homogeneous 2D plasma in Sec. IV.D.3. The critical  $\beta$  value for stability of the 2D disc follows from Eq. (4.112), in a manner analogous to the analysis leading to Eq. (4.130). One merely replaces  $\sigma$  in Eq. (4.112) by the maximum value of  $\sigma$  in the inhomogeneous disc, given by Eq. (4.118) at  $r=0$ . The result for  $\beta_{\text{crit}}$  is

$$\beta_{\text{crit}}(N) = \frac{0.665}{N^{1/2}}. \quad (4.131)$$

This critical value for stability of the 2D disc has also been determined in simulations for various values of  $N$ , shown by the open circles in Fig. 57. Again, Eq. (4.131),

the dashed line, provides a good match to the simulation data (Schiffer, 1993) for large  $N$ .

Figure 57 summarizes the results of this section. It can be regarded as the structural phase diagram for crystallized charges in a harmonic trap (Dubin, 1993). For large  $\beta$  values the charges form a 1D Coulomb chain along the  $z$  axis, and for small  $\beta$  values they form a 2D disc in the  $x$ - $y$  plane. For intermediate values of  $\beta$  the plasma consists of concentric shells if  $N$  is not too large. However, when  $N$  is sufficiently large, a bcc lattice forms within the plasma. An estimate for the size needed to enter this regime of large plasmas is provided by Eq. (4.117) and is shown in Fig. 57 as the dot-dashed lines. On the other hand, when  $N$  is very small the system enters the regime of Coulomb clusters. We consider properties of these clusters in the next section.

### E. Coulomb clusters

In this section we discuss some aspects of the thermal equilibrium properties of small numbers of trapped charges ( $N \leq 10$ ). When these ‘‘Coulomb clusters’’ are laser cooled to temperatures in the range of millidegrees Kelvin, they assume symmetric configurations that minimize their potential energy and are the analogs of the crystalline states observed in larger systems. These configurations of minimum energy (CME’s) can be observed in experiments and have been carefully studied using computer simulations (e.g., Itano, Bergquist, and Wineland, 1989, p. 241; Rafac *et al.*, 1991; Tsuruta and Ichimaru, 1993). In this section we review the behavior of the CME as system parameters are varied. We focus on the case of harmonic traps since most of the experimental work on Coulomb clusters has been carried out in such traps.

The theoretical problem of finding the CME of charges confined in a neutralizing background has a long history, going at least as far back as Thomson’s investigations of the plum-pudding model of the atom (Thomson, 1904). The related problem of determining the CME of charges trapped on the surface of a sphere has received somewhat more attention over the years, possibly because limiting the charges to a 2D surface simplifies the problem by reducing the number of local energy minima. Even so, the problem remains unsolved for arbitrary  $N$  and is a topic of current research (see, for example, Altschuler *et al.*, 1997, and references therein).

Most experimental work on Coulomb clusters has been carried out in Paul traps rather than Penning traps. When CME’s are considered in Paul traps it must be remembered that these configurations have neglected the jitter motion associated with the applied rf field. While the jitter motion has a negligible effect on CME’s for most experiments on Coulomb clusters, the jitter motion, together with the effect of the laser cooling, can in some circumstances cause chaotic motion of the trapped charges as well as transitions between chaotic and regular motion (Blümel, 1995; Hoffnagle and Brewer, 1995). These nonlinear dynamics effects are specific to Paul traps and lie beyond the scope of this

review. Here we consider only the CME's, which apply both to Paul and Penning traps.

### 1. Constant rotation frequency

We first consider the case in which the equilibrium rotation frequency is fixed by an angular momentum reservoir, or by entrapment in a Paul rather than a Penning trap. Later we shall compare this case to the situation that is more typical of Penning trap experiments, where the angular momentum is held fixed.

In the rotating frame the Hamiltonian takes the form of Eq. (2.8). If we cool the cluster to its minimum-energy state at fixed rotation frequency, we minimize the value of this Hamiltonian. This minimization implies that kinetic energy in the rotating frame is zero, which in turn implies that

$$\mathbf{v}_i + \omega \mathbf{r}_i \hat{\theta}_i = 0, \quad (4.132)$$

so the ion cluster rotates rigidly.

Minimization of the potential energy  $\Phi(\mathbf{r}_1, \dots, \mathbf{r}_N)$  determines the positions of the charges in the cluster.

The value of  $\Phi$  at the minimum is equal to the energy  $E_R$  of the crystallized charges as seen in the rotating frame [see Eq. (2.8)]. This energy is connected to the energy as seen in the laboratory frame  $E$ , through Eq. (2.6):

$$\Phi = E_R = E + \omega L, \quad (4.133)$$

where  $L$  is the angular momentum of the CME, given by Eq. (4.75),

$$L = \frac{Nm\Omega_v}{2} \langle r^2 \rangle,$$

and where  $\langle r^2 \rangle$  is the mean-square cylindrical radius of the CME:

$$\langle r^2 \rangle = \frac{1}{N} \sum_{i=1}^N r_i^2.$$

Some useful “thermodynamic” relations between these quantities can be derived using the fact that  $\Phi$  is minimized at the CME. Recalling that rotation frequency is fixed by an external angular momentum reservoir, consider a small interaction with the reservoir that changes the angular momentum by a small amount  $\Delta L$ , leading to a change in  $\Phi$ , which we Taylor expand in powers of  $\Delta L$  using Eq. (4.133):

$$\Delta \Phi = \left( \frac{\partial E}{\partial L} + \omega \right) \Delta L + \frac{1}{2} \frac{\partial^2 E}{\partial L^2} \Delta L^2 + \dots \quad (4.134)$$

Since the CME is an extremum of  $\Phi$ , the first-order term in  $\Delta L$  must vanish, so we obtain the relation

$$\omega = - \frac{\partial E}{\partial L}. \quad (4.135)$$

Furthermore, the CME is not just an extremum of  $\Phi$ , it is a local minimum, so the second-order term in  $\Delta L$  must be nonnegative, which, when combined with Eq. (4.135), implies that

$$\frac{\partial L}{\partial \omega} \leq 0. \quad (4.136)$$

Equation (4.135) can be manipulated into a useful form involving  $E_R$  rather than  $E$ . Substituting for  $E$  using Eq. (4.133) implies

$$\omega = - \frac{\partial E_R}{\partial L} + \omega + L \frac{\partial \omega}{\partial L}. \quad (4.137)$$

However  $\partial E_R / \partial L \partial L / \partial \omega = \partial E_R / \partial \omega$ , so Eq. (4.137) becomes

$$L = \frac{\partial E_R}{\partial \omega}. \quad (4.138)$$

Equations (4.135), (4.136), and (4.138), derived here for CME's, are actually the zero-temperature limits of more general relations that can be derived by minimizing the free energy of the plasma. These general relations are developed in Sec. V.

Minimization of  $\Phi$  has been carried out by several authors using both analytic and numerical methods (Mostowski and Gajda, 1985; Baklanov and Chebotayev, 1986; Casdorff and Blatt, 1988; Rafac *et al.*, 1991; Tsuruta and Ichimaru, 1993; Bedanov and Peeters, 1994). These authors have focused on the experimentally important case of a harmonic trap for which  $\Phi$  can be written as

$$\Phi(\mathbf{r}_1, \dots, \mathbf{r}_N) = \sum_{i>j} \frac{e^2}{|\mathbf{r}_i - \mathbf{r}_j|} + \sum_i \frac{1}{2} m \omega_z^2 (z_i^2 + \beta r_i^2). \quad (4.139)$$

If one scales distances by  $(e^2/m\omega_z^2)^{1/3}$ ,  $\Phi(\mathbf{r}_1, \dots, \mathbf{r}_N)$  depends only on the number of particles  $N$  and the trap parameter  $\beta$ . The minimum-energy configurations for systems with 3 to 18 ions in a spherically symmetric confining potential ( $\beta=1$ ) are shown in Fig. 58. Several of these configurations do not correspond with naive expectations. For example, when  $N=8$  the ions do not lie on the vertices of a cube (Mostowski and Gajda, 1985) but instead form two squares rotated by  $45^\circ$  with respect to each other. This configuration was first identified as a CME at the turn of the century by scientists investigating Thomson's model of the atom (Föppl, 1912; Thomson, 1921).

For  $N$  up to 12 the ions appear to lie on the surface of a sphere. In fact this is only exactly true for the symmetric configurations  $N=2, 3, 4, 6, 8$ , and 12. For  $N=5, 7, 9, 10$ , and 11 the radii differ slightly. For example, for  $N=5$  the two particles along the symmetry axis are at a distance  $r=1.1036$  from the origin, whereas the particles in the central triangle have radii  $r=1.0808$  [in units of  $(e^2/m\omega_z^2)^{1/3}$ ].

When  $N=13$  it becomes energetically favored for a single ion to be at the origin. For  $22 < N < 27$ , there are two ions inside the outer envelope. These inner ions are the beginnings of a second shell. As more ions are added, the ions form the concentric shell structures described in previous sections.

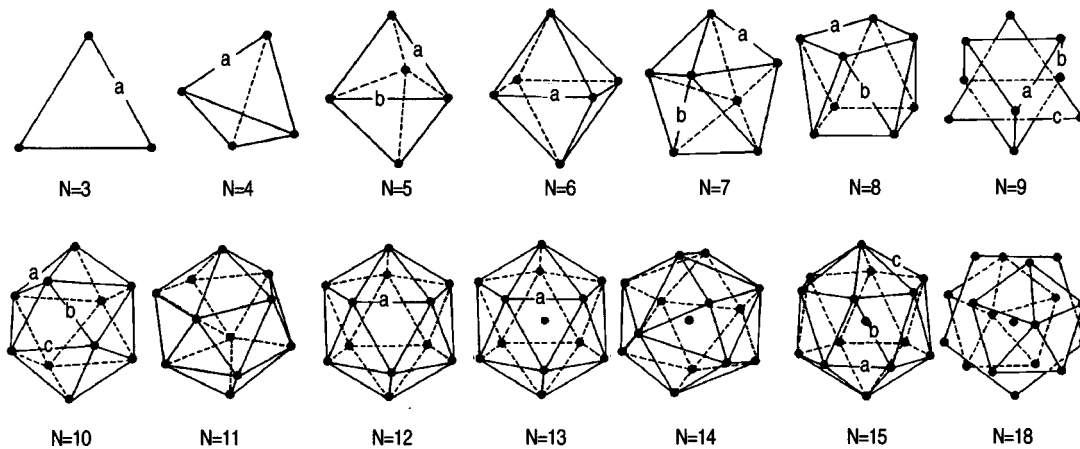


FIG. 58. Minimum-energy configurations of Coulomb clusters in a spherical harmonic potential. From Rafac *et al.* (1991).

For anisotropic confinement ( $\beta \neq 1$ ), the CME varies as  $\beta$  varies. It has been observed that as  $\beta$  is varied continuously (for example, by varying  $\omega_z$ ), the CME also changes continuously except at specific values of  $\beta$  at which discontinuous changes in the symmetry of the CME occur (Rafac *et al.*, 1991). These jumps are due to competing local energy minima, which become lowest energy at these  $\beta$  values. The transitions are the analogs of the structural transitions that were discussed for mesoscopic systems in Sec. IV.D. Some of the transitions

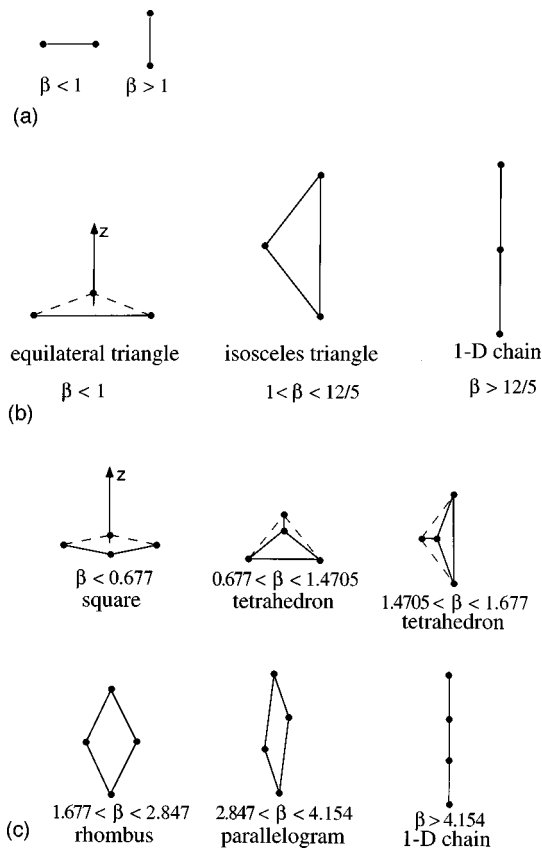


FIG. 59. Structural phase transitions in Coulomb clusters as  $\beta$  is varied: (a)  $N=2$ ; (b)  $N=3$ ; (c)  $N=4$ . The  $z$  axis is in the vertical direction in all cases.

are first order (an order parameter such as the mean-square radius has a discontinuous jump) and some behave like phase transitions of the second kind, where derivatives of the order parameter with respect to  $\beta$  are discontinuous. Some examples of these structural transitions are shown in Fig. 59, for the cases of  $N=2, 3$ , and 4.

For  $N=2$ , and  $\beta > 1$ , the ions sit on opposite sides of the origin in the  $x-y$  plane. When  $\beta > 1$ , the ions are aligned along the  $z$  axis; these are the only stable configurations [Fig. 59(a)]. The value  $\beta=1$  is special in that any rotation of the configuration around the origin is allowed; this rotational symmetry occurs for all  $N$  values.

For  $N=3$ , three configurations are stable, as shown in Fig. 59(b). Again, the ranges of  $\beta$  over which the configurations are the CME correspond to the ranges over which the configurations are stable local minima. When  $\beta < 1$  the CME is an equilateral triangle in the  $x-y$  plane. When  $1 < \beta < 12/5$  the CME is an isosceles triangle with the long side parallel to the  $z$  axis, and when  $\beta > 12/5$  the ions are squeezed into a line along the  $z$  axis.

For  $N=4$ , six distinct stable equilibria are found, two of which have overlapping regions of linear stability [see Fig. 59(c)]. When  $\beta < (1+2^{3/2})/2^{5/2} = 0.677$  the charges form a square in the  $x-y$  plane. When  $0.677 < \beta < 1.4705$  (stable for  $0.677 < \beta < 1.6279$ ) the configuration is no longer coplanar; it becomes a tetrahedron with two equal-length edges that are transverse to one another as well as the  $z$  axis. When  $1.4705 < \beta < 2 \times 3^{3/2}/(1+3^{3/2}) = 1.677$  (stable for  $1.4019 < \beta < 1.677$ ), the tetrahedron now has one edge parallel to the  $z$  axis and one perpendicular. When  $1.677 < \beta < 2.8468$  the configuration becomes coplanar, forming a rhombus parallelogram with two ions on the  $z$  axis and two ions in the  $x-y$  plane. When  $2.8468 < \beta < 4.1542$ , the ions that were in the  $x-y$  plane move out of the plane, one above and one below. For  $4.1542 < \beta$ , the ions are squeezed onto the  $z$  axis, forming a Coulomb chain.

Experiments on clusters of ions confined in a Paul trap have directly observed these structural transitions

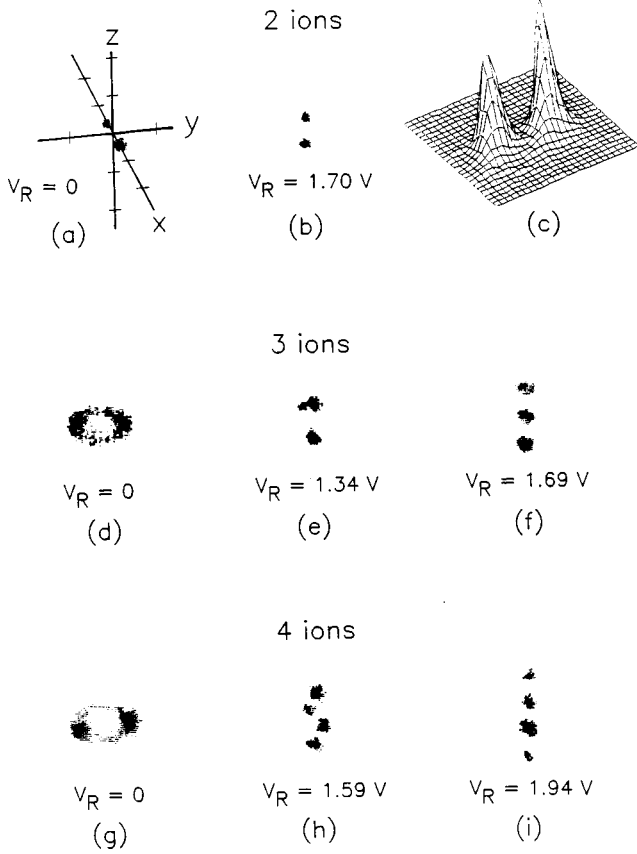


FIG. 60. Experimental images of clusters of two, three, and four trapped laser-cooled  $\text{Hg}^+$  ions in a Paul trap. The coordinate system of (a) applies to the remaining pictures except for (c). The tick marks on the axes are separated by  $10 \mu\text{m}$ . (c) A three-dimensional intensity plot for two ions pinned along the  $z$  axis with  $\beta=6$ . The voltage  $V_R$  is related to  $\beta$  through  $\beta = 0.5(1 + BV_R)/(2 - BV_R)$ , where  $B = 0.907 \text{ V}^{-1}$  (Wineland *et al.*, 1987).

(Deidrich *et al.*, 1987; Wineland *et al.*, 1987; Itano, Bergquist, and Wineland, 1989, p. 241). Using laser fluorescence techniques, one can image the ion positions directly. For example, Figs. 60(g),(h),(i) show three such images of four charges, with  $\beta=0.25$ ,  $2.2$ , and  $5.7$ . In each case the observed configuration (square, rhombus, Coulomb chain) corresponds to the expected theoretical CME shown in Fig. 59(c).

For larger values of  $N$  the CME's become more numerous and complex as a function of  $\beta$ . They have been determined numerically as a function of  $\beta$  for  $N \leq 10$ . Interactive animations of some of the CME's can be viewed over the world wide web at the nonneutral plasma home page at UCSD (<http://sdphca.ucsd.edu/Ioncryst.html>). Larger clusters have also been directly imaged in experiments. Figures of the CME's may be found in Itano, Bergquist, and Wineland, 1989, p. 241.

For sufficiently large  $\beta$  the ions are always compressed onto the  $z$  axis, forming an inhomogeneous 1D Coulomb chain, as discussed in Sec. IV.D. On the other hand, as  $\beta \rightarrow 0$  the ions always settle into the  $x-y$  plane. The structure of these 2D clusters has also been studied as a function of  $N$  (Rafac *et al.*, 1991; Bedanov and

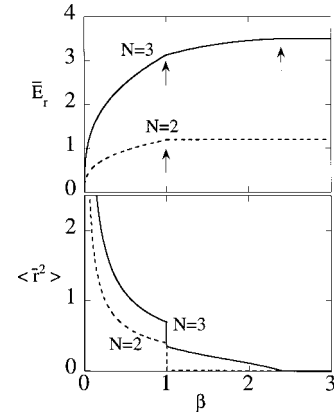


FIG. 61. Scaled energy  $\bar{E}_R$  and mean-square cylindrical radius  $\langle \bar{r}^2 \rangle$  as a function of the trap parameter  $\beta$  for Coulomb clusters in a harmonic trap, for  $N=2$  (dashed) and  $N=3$  (solid). Arrows denote the locations of structural phase transitions.

Peeters, 1994). For  $N \leq 5$  the ions lie on a circle, and for  $6 \leq N \leq 8$  a single ion sits in the center of the ring, while at  $N=9$  a second ion joins the first in an inner ring. These concentric rings are two-dimensional analogs of the concentric shell structures observed in spheroidal plasmas. For large  $N$  the ions form the distorted 2D hexagonal lattice discussed in Sec. IV.D.

The energy  $E_R$  as seen in the rotating frame [i.e., the value of  $\Phi$  at the minimum, given by Eq. (4.139)] and the mean-square radius of the clusters are shown in Figs. 61 and 62 as a function of  $\beta$  for  $N=2, 3$ , and  $4$ . Note that the mean-square radius jumps in value for various values of  $\beta$ . These jumps occur when a new configuration becomes the CME.

The curves in Figs. 61 and 62 are connected by Eq. (4.138),  $\partial E_R / \partial \omega = L$ . Using Eqs. (4.75) and (3.40) one can easily show that Eq. (4.138) can be written as

$$\frac{\partial(\bar{E}_R)}{\partial \beta}(\beta, N) = \frac{1}{2} N \langle \bar{r}^2 \rangle(\beta, N), \quad (4.140)$$

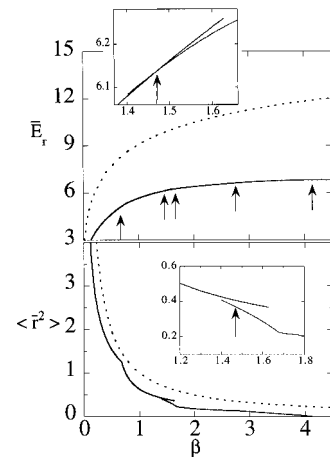


FIG. 62. Same as Fig. 61 but for  $N=4$ . Insets blow up the region around the first-order structural phase transition that occurs at  $\beta=1.47$  when  $\omega$  is held fixed during the transition. The dashed curves correspond to the results for a cold mean-field spheroid for which the total particle number equals 4.

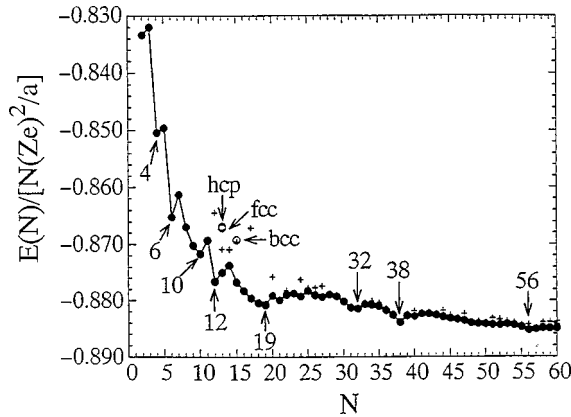


FIG. 63. Correlation energy  $U_{\text{corr}}$  vs particle number  $N$  in spherical Coulomb clusters. From Tsuruta and Ichimaru (1993).

where the overbars denote that distances are scaled by  $(e^2/m\omega_z^2)^{1/3}$  and that the energy is scaled by  $m\omega_z^2(e^2/m\omega_z^2)^{2/3}$ . Thus changes in the slope of the  $E_R$  vs  $\beta$  curves are connected to the discrete jumps in the mean-square radius that can be observed in Figs. 61 and 62.

Furthermore, when a new CME takes over from a previous CME, the new CME must have lower energy than the old CME. This implies that the slope of the energy curve decreases as  $\beta$  increases through a transition. Equation (4.140) then implies that the mean-square radius always decreases in the jump as  $\beta$  increases. One can also show that  $\partial\langle r^2 \rangle / \partial\beta < 0$  by considering fluctuations in  $\langle r^2 \rangle$  in the canonical ensemble [see Eq. (5.67)]. This explains the negative slope of the  $\langle r^2 \rangle$  versus  $\beta$  curves.

Also shown in Fig. 62 are the energy and mean-square radius one would obtain for a cold mean-field spheroid, as determined by Eqs. (3.41)–(3.44) and (3.47) [and taking  $C=0$  in Eq. (3.47)]. Even for very small numbers of charges, the mean-field approximation still provides the qualitatively correct dependence for the mean-square radius, although the jumps due to structural phase transitions are, of course, missed in the mean-field theory. However, cold mean-field theory does not provide a very good model for the energy of the cluster. Clearly, correlation energy plays an important role in the cluster equilibrium.

The difference between the exact cluster energy and the cold mean-field energy is the correlation energy of the cluster. The correlation energy per particle for spherical Coulomb clusters is plotted in Fig. 63 as a function of  $N$  (Tsuruta and Ichimaru, 1993). As  $N$  increases the correlation energy decreases as surface effects become less important (Fig. 63 is analogous to Fig. 53, which shows the same effect in mesoscopic plasmas with larger  $N$ ). Several dips in the  $U$  vs  $N$  curve can be observed. The values  $N=4, 6, 10, 12, 19, 32, 38$ , and  $56$  all have lower energy than nearby  $N$  values. Clusters with  $N=6, 12$ , and  $38$  have particularly low energies, prompting some authors to refer to these  $N$  values as “magic numbers” for spherical Coulomb clusters, borrowing the

terminology from nuclear physics. These  $N$  values all correspond to particularly symmetric configurations: an octahedron for  $N=6$ , a dodecahedron (icosahedron) for  $N=12$ , and a two-shelled structure consisting of an octahedron inside a face-centered icosahedron for  $N=38$ .

## 2. Constant angular momentum

In experiments involving isolated charges trapped in a Penning trap, angular momentum is a conserved quantity, not rotation frequency. In this section we determine the minimum-energy state holding angular momentum fixed rather than rotation frequency.

We will see that states of minimum energy at fixed angular momentum are identical to those obtained by holding rotation frequency fixed, except near first-order structural phase transitions. In the previous section we observed that when rotation frequency is fixed the mean-square cylindrical radius jumps in value at first-order transitions (see Figs. 61 and 62). Such jumps in radius are suppressed when angular momentum is constant, so one might imagine that these first-order transitions are disallowed. Actually, they still occur, but in a different fashion than for the case of constant rotation frequency. When  $L$  is fixed there is a jump in  $\omega$  at the transition, just as when  $\omega$  is fixed there is a jump in  $L$ . The jumps are related by the fact that  $-\omega$  and  $L$  are thermodynamically conjugate variables, as we shall see. This behavior is analogous to the physics of  $p$ - $V$  systems at a first-order phase transition.

First we consider the general problem of finding the CME while holding angular momentum fixed rather than rotation frequency. The Hamiltonian  $H(\mathbf{r}_1, \mathbf{v}_1, \dots, \mathbf{r}_N, \mathbf{v}_N)$  is then minimized subject to the constraint that the angular momentum  $P_\theta(\mathbf{r}_1, \mathbf{v}_1, \dots, \mathbf{r}_N, \mathbf{v}_N)$  is held constant. We employ the technique of Lagrange multipliers to carry out the minimization, constructing the function

$$H_R(\mathbf{x}_1, \mathbf{v}_1, \dots, \mathbf{x}_N, \mathbf{v}_N) = H + \omega P_\theta, \quad (4.141)$$

where  $\omega$  is a Lagrange multiplier. Extrema of  $H_R$  provide us with candidates for the CME. However, note that  $H_R$  is actually the Hamiltonian in a frame rotating with frequency  $-\omega$  [see Eq. (2.6)], so the extrema of  $H_R$  are identical to those discussed in the search for minima holding rotation frequency fixed. We are then led to curves of  $E_R$  vs  $\beta$  and  $\langle r^2 \rangle$  vs  $\beta$ , as in Figs. 61 and 62. From these curves we can construct the desired plots of  $E$  vs  $L$ .

An example of this procedure is shown in Fig. 64 for  $N=4$ , taking  $\omega_z/\Omega_c=0.2$ . First, we determine  $L$  vs  $\omega$  using Eq. (4.75) and the data of Fig. 62. The  $L$  vs  $\omega$  curve in Fig. 64(a) is antisymmetric about the Brillouin limit point  $L=0$ ,  $\omega=\Omega_c/2$ , as expected. However, for the choice  $\omega_z/\Omega_c=0.2$ , there is a rather large range of  $\omega$  values for which  $L=0$ . This range of  $\omega$  values corresponds to  $\beta > 4.1542$ , for which the four charges collapse to the  $z$  axis, forming a 1D Coulomb chain with  $\langle r^2 \rangle = 0$ . Also, for future reference note that the curve of  $L$  vs  $\omega$  is double valued near  $\omega/\Omega_c=0.1$  and  $0.9$ , where



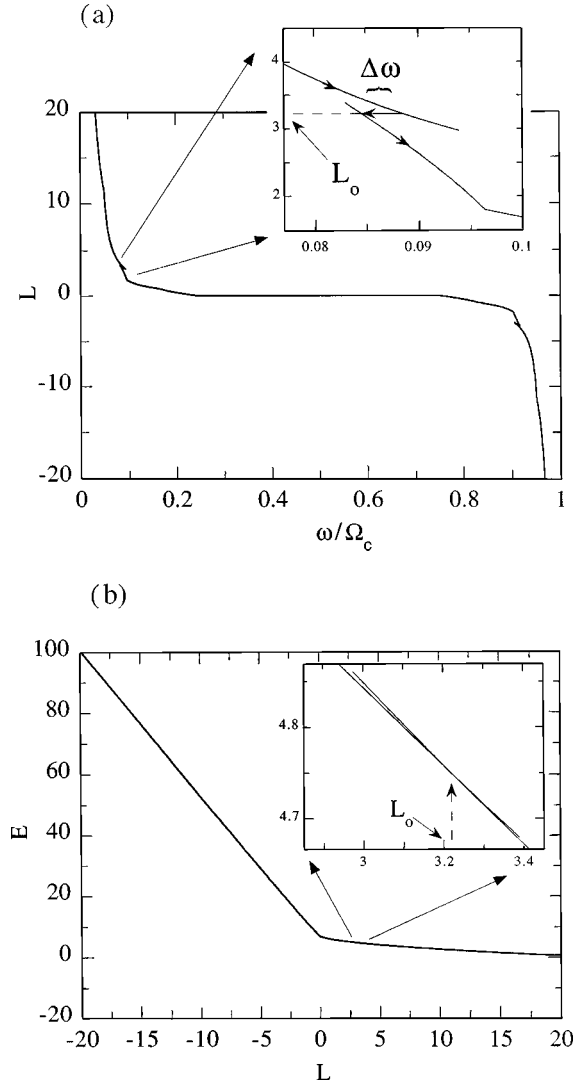


FIG. 64. Minimum energy state of  $N=4$  Coulomb cluster at fixed angular momentum,  $\omega_z/\Omega_c=0.2$ : (a) Angular momentum vs rotation frequency (b) Energy in the laboratory frame vs angular momentum. Energy is in units of  $m\omega_z^2(e^2/m\omega_z^2)^{2/3}$ , angular momentum is in units of  $m\omega_z(e^2/m\omega_z^2)^{2/3}$ . Inset blows up the location of the first-order structural phase transition that occurs at  $L_0 \approx 3.2$ .

there are two stable equilibria. One can easily see this in the inset to the figure, which shows the region around  $\omega/\Omega_c=0.1$ .

The information in this  $L-\omega$  plot can then be used to construct the  $E$  vs  $L$  curve, using the relation  $E=E_R-\omega L$  and the data in Figs. 62 and 64(a). There are two branches of the  $E$  vs  $L$  curve, which meet at  $L=0$ , as shown in the example in Fig. 64(b). The high-energy branch with negative angular momentum corresponds to rotation frequencies higher than  $\Omega_c/2$ . Most of the energy in this branch arises from rapid rotation. The low-energy branch occurs for positive angular momenta and corresponds to rotation frequencies below  $\Omega_c/2$ . Here most of the energy arises from Coulomb interactions between the charges as well as the external trap potential.

The slope of the  $E$  vs  $L$  curve is connected to the

rotation frequency through Eq. (4.135),  $\omega = -\partial E/\partial L$ . A jump in the slope of the curve occurs at  $L=0$ , and Eq. (4.135) then implies  $\omega$  changes discontinuously as  $L$  passes through zero. This jump in  $\omega$  corresponds to the range of  $\omega$  values for which the charges are squeezed onto the  $z$  axis and  $L=\langle r^2 \rangle=0$ . Only when  $\omega$  is above or below this range is  $L \neq 0$ .

The  $E$  vs  $L$  curve is double valued due to the existence of more than one stable local energy minimum, as discussed previously in relation to Eq. (4.139) (although the double-valued nature of the curve is very difficult to observe). For the example shown in Fig. 64(b) ( $N=4$  and  $\omega_z/\Omega_c=0.2$ ), the curve is double valued in two locations near  $L/m\omega_z a_0^2 \approx \pm 3.2$  (the region near 3.2 is blown up in the inset). Since angular momentum is now held fixed rather than rotation frequency, the structural transition now causes a jump in the rotation frequency of the cluster. This jump can be observed in the inset to Fig. 64(a).

Note that the curves shown in Fig. 64 are mapped directly from those shown in Fig. 62. However, the linear stability boundaries at fixed  $\omega$  (the end points of the curves in Fig. 62) will in general differ when  $L$  rather than  $\omega$  is fixed. Unconstrained fluctuations away from extrema of  $H_R$  are less stable than fluctuations constrained by fixed  $L$ . Therefore the actual stability boundaries at fixed  $L$  extend beyond the end points of the curves shown in Fig. 64, although the degree of extension is presently unknown. Nevertheless, one can show that the CME at fixed  $L$  always corresponds to a stable or neutrally stable configuration at fixed  $\omega$ , so the extensions to the curves are not needed to find the CME.

The behavior of the cluster near the transition between local energy minima can be understood analytically from the behavior of  $E_R(\omega)$ . For example, we can analytically determine the value of  $L_0$  at the transition between two structures  $A$  and  $B$  provided that the jump in  $\omega$  is not too large. These structures are assumed to have energy curves in the rotating frame labeled  $E_R^A(\omega)$  and  $E_R^B(\omega)$ . Expanding to second order in  $\omega$  around the point  $\omega=\omega_0$  where  $E_R^A=E_R^B=E_0$  (i.e., the location of the structural transition when  $\omega$  is fixed), we obtain

$$E_R^A = E_0 + L_0^A \Delta\omega + \frac{\partial L^A}{\partial \omega_0} \frac{\Delta\omega^2}{2}, \quad (4.142a)$$

$$E_R^B = E_0 + L_0^B \Delta\omega + \frac{\partial L^B}{\partial \omega_0} \frac{\Delta\omega^2}{2}, \quad (4.142b)$$

where

$$\Delta\omega = \omega - \omega_0, \quad L_0^A = L^A(\omega_0)$$

and where we have employed Eq. (4.138). Furthermore, to the same order of approximation, application of Eq. (4.138) to Eqs. (4.142) yields the cluster angular momenta:

$$L^A = L_0^A + \frac{\partial L^A}{\partial \omega_0} \Delta\omega, \quad (4.143a)$$

$$L^B = L_0^B + \frac{\partial L^B}{\partial \omega_0} \Delta \omega. \quad (4.143b)$$

Now we evaluate the energy in the laboratory frame,  $E = E_R - \omega L$ , using Eqs. (4.142) and (4.143):

$$E^A = E_0 - \omega_0 L - \frac{1}{2} \frac{(L - L_0^A)^2}{\partial L^A / \partial \omega_0}, \quad (4.144a)$$

$$E^B = E_0 - \omega_0 L - \frac{1}{2} \frac{(L - L_0^B)^2}{\partial L^B / \partial \omega_0}, \quad (4.144b)$$

where we have substituted for  $\Delta \omega$  in terms of  $L$  using Eqs. (4.143). Finally, we subtract Eq. (4.144b) from (4.144a) in order to determine the transition point  $L_0$  where  $E^A - E^B = 0$ . In this process the linear term in  $L$  vanishes, which is why we needed to keep second-order variations in  $E$  in Eqs. (4.142). The resulting equation for  $L_0$  has the solution

$$L_0 = \frac{L_0^A + L_0^B \sqrt{\partial L^A / \partial \omega_0 / \partial L^B / \partial \omega_0}}{1 + \sqrt{\partial L^A / \partial \omega_0 / \partial L^B / \partial \omega_0}}. \quad (4.145)$$

This equation exhibits the connection between structural transitions in the  $E-L$  plane and in the  $E_R-\omega$  plane. In the  $E_R-\omega$  plane a transition at  $\omega = \omega_0$  creates a jump between structures with different angular momenta,  $L_0^A$  and  $L_0^B$ . In the  $E-L$  plane a transition between the same two structures occurs at  $L = L_0$ , a weighted average of  $L_0^A$  and  $L_0^B$  given by Eq. (4.145). Furthermore, there is a jump in rotation frequency at the transition. This jump can be determined via Eqs. (4.143) and (4.145):

$$\omega_A - \omega_B = \frac{L_0^A - L_0^B}{\sqrt{\partial L^A / \partial \omega_0 \partial L^B / \partial \omega_0}}. \quad (4.146)$$

This shows that the jump in  $\omega$  that occurs in the  $E-L$  plane is proportional to the jump in  $L$  that occurs in the  $E_R-\omega$  plane. Equations (4.145) and (4.146) are valid provided that  $L_0^A$  and  $L_0^B$  are not too different, so that the Taylor expansions in Eq. (4.142) are valid.

In some cases the differences between competing cluster angular momenta are too large for the previous Taylor-expansion analysis to be accurate. A case in point is the transition that occurs for  $N=2$  at  $\beta=1$ . Now the behavior of the CME at fixed angular momentum differs qualitatively from the behavior at fixed  $\omega$ . When  $\omega$  is held fixed the two charges jump from the  $x-y$  plane ( $L$  finite) to locations along the  $z$  axis ( $L=0$ ) as  $\beta$  increases through  $\beta=1$  [Fig. 59(a)]. However, when  $L$  is fixed, instead of jumping between the two orientations, the cluster now rotates continuously from one orientation to the other, with the orientation controlled at all times by external parameters. The orientation is determined by Eq. (4.75):

$$L = \frac{mN}{2} \Omega_v \left( \frac{e^2}{m\omega_z^2} \right)^{2/3} \langle \bar{r}^2 \rangle (\beta=1, N, \theta, \psi), \quad (4.147)$$

where the overbar on  $\bar{r}$  denotes distances normalized to  $(e^2/m\omega_z^2)^{1/3}$  and the angles  $\theta$  and  $\psi$  determine the orien-

tation of the cluster. In Eq. (4.147) the vortex frequency  $\Omega_v$  is related to  $\Omega_c$  and  $\omega_z$  by the condition that  $\beta=1$ :

$$\Omega_v^2 = \Omega_c^2 - 6\omega_z^2. \quad (4.148)$$

For example, for two charges in the trap, the mean-square cylindrical radius of the cluster at  $\beta=1$  is

$$\langle \bar{r}^2 \rangle (\beta=1, N=2, \theta, \psi) = 2^{-4/3} \sin^2 \theta, \quad (4.149)$$

where  $\theta$  is the angle between the  $z$  axis and a line connecting the two charges. Equations (4.147)–(4.149) imply that for  $N=2$  the angle  $\theta$  satisfies

$$\sin \theta = \left[ \frac{2^{4/3} L}{m(\Omega_c^2 - 6\omega_z^2)^{1/2}} \left( \frac{m\omega_z^2}{e^2} \right)^{2/3} \right]^{1/2}. \quad (4.150)$$

Thus the orientation of the cluster varies continuously between  $\sin \theta=0$  and  $\sin \theta=1$  as  $\omega_z$  and/or  $\Omega_c$  are varied at fixed  $L$ . Similarly, for three charges, the mean-square radius at  $\beta=1$  is

$$\langle \bar{r}^2 \rangle = \frac{3^{1/3}(1 + \sin^2 \theta)}{2}, \quad (4.151)$$

where now  $\theta$  is the angle between the  $z$  axis and the plane of the three ions, which form an equilateral triangle. When angular momentum is held fixed and other parameters are varied,  $\theta$  satisfies

$$\sin^2 \theta = \frac{4L}{3^{2/3} m(\Omega_c^2 - 6\omega_z^2)^{1/2}} \left( \frac{m\omega_z^2}{e^2} \right)^{2/3} - 1. \quad (4.152)$$

On the other hand, for four ions, the tetrahedron has a mean-square cylindrical radius that is independent of orientation,  $\langle \bar{r}^2 \rangle = 2^{1/6}/3^{1/2}$ . It is also the case that, for  $N=6, 8, 12$ , and  $13$ ,  $\langle \bar{r}^2 \rangle$  is independent of orientation, so for these special values of  $N$  the orientation of the cluster is not fixed by external parameters when  $\beta=1$ , and the cluster can rotate freely, just as when  $\omega$  is held fixed.

## V. THERMODYNAMICS OF NONNEUTRAL PLASMAS

Various useful relations between quantities evaluated in thermal equilibrium can be derived using thermodynamic arguments. The relations are based on the expression of these quantities in terms of derivatives of thermodynamic potentials with respect to the thermodynamic variables of the system. For a nonneutral plasma in a Penning trap, a complete set of thermodynamic variables is the temperature  $T$ , total particle number  $N$ , the rotation frequency  $-\omega$ , the magnetic field  $B$ , and the voltages  $\{V_j\}$  on the surrounding electrode structure. This set of variables specifies the thermal equilibrium state of the plasma. However, it is by no means the only possible complete set. For example, depending on the circumstances one might wish to replace  $T$  by the energy  $E$  and  $\omega$  by the angular momentum  $L$ .

We have already considered some thermodynamic relations in Secs. IV.C.4 and IV.C.5. However, in those discussions we were concerned with correlation effects

in large plasmas. Here we consider more general relations that hold for any nonneutral plasma for which the Gibbs distribution describes the thermal equilibrium. For an isolated plasma this requires  $N \geq 100$ , as we have previously discussed.

The thermodynamic relations can be useful in several ways. For example, Maxwell relations connect seemingly unrelated physical quantities. Stability criteria place bounds on measurable quantities, such as the specific heat. These bounds are related to the magnitude of fluctuations which can be measured in experiments. We can also use thermodynamics to determine quantities that are easy to measure in terms of other quantities which are easier to calculate. Finally, a thermodynamic approach greatly simplifies the description of slow plasma evolution (transport) due to such effects as collisions with neutrals, interaction with field errors, and interaction with laser cooling and torque beams. As mentioned earlier, these effects gradually change the values of  $E$  and  $L$ . If the change is slow compared to the time required for Coulomb collisions to bring the plasma to thermal equilibrium, the plasma evolves through a sequence of thermal equilibrium states, and the slow change in  $E$  and  $L$  translates to a slow change in  $T$  and  $\omega$ . The thermodynamic approach describes the evolution using two first-order ordinary differential equations for the time evolution of  $T$  and  $\omega$ , which is a major simplification from the partial differential equations typically required to describe transport. The two equations provide a theoretical basis for the dynamic control of the plasmas (e.g., through laser cooling and torque beams).

### A. The $TdS$ equation

A modern theory of thermodynamics begins by defining the free energy in terms of the canonical partition function [see Eq. (4.3)]

$$F_R(T, \omega, B, \{V_j\}, N) = -kT \ln Z_c, \quad (5.1)$$

where the subscript  $R$  is a reminder that this is the free energy in the rotating frame of the plasma. By simply evaluating the following partial derivative one can show that (Landau and Lifshitz, 1980, p. 74)

$$-T^2 \frac{\partial}{\partial T} \left[ \frac{F_R}{T} \right]_{\omega, B, \{V_j\}, N} = \langle H_R \rangle \equiv E_R, \quad (5.2)$$

where the bracket indicates an average over the Gibbs distribution (4.2). The entropy  $S$  is defined through the relation

$$F_R = E_R - TS, \quad (5.3)$$

which, together with Eq. (5.2), implies the familiar result

$$\left( \frac{\partial F_R}{\partial T} \right)_{\omega, B, \{V_j\}, N} = -S. \quad (5.4)$$

Likewise, the partial derivatives of  $F_R$  with respect to the other thermodynamic variables are physically meaningful quantities. For example, the partial derivative with respect to  $\omega$  yields the angular momentum

$$\left( \frac{\partial F_R}{\partial \omega} \right)_{T, B, \{V_j\}, N} = \langle P_\theta \rangle \equiv L, \quad (5.5)$$

and the partial derivative with respect to  $N$  is by definition the chemical potential

$$\left( \frac{\partial F_R}{\partial N} \right)_{T, \omega, B, \{V_j\}} = \mu. \quad (5.6)$$

This function plays an important role in determining the thermal equilibrium of systems in which the number of particles can fluctuate.

The partial derivative of  $-F_R$  with respect to  $B$  is equal to the average magnetic moment of the plasma:

$$\begin{aligned} \left( \frac{\partial F_R}{\partial B} \right)_{T, \omega, \{V_j\}, N} &= \int d^3r_1 \dots d^3r_N \frac{e}{2c} \omega \sum_{i=1}^N r_i^2 f_c(\mathbf{r}_1, \dots, \mathbf{r}_N) \\ &= \frac{Ne}{2c} \omega \langle r^2 \rangle = -M, \end{aligned} \quad (5.7)$$

where the minus sign enters the last equality because  $-\omega$  is the rotation frequency of the plasma. Note that  $M$  is a negative quantity for a nonneutral plasma, indicating that the magnetization induced by rotation opposes the applied magnetic field: the plasma is diamagnetic. This appears to contradict the Bohr-van-Leeuwen theorem, which states that classical systems cannot display diamagnetism (Pathria, 1986). However, the theorem applies only to systems that do not rotate in thermal equilibrium. In a nonneutral plasma the magnetic moment arises from the current created by rotation.

The partial derivative of  $-F_R$  with respect to the electrode voltage  $V_j$  is equal to the average charge  $q_j$  induced on the electrode by the plasma:

$$\left( \frac{\partial F_R}{\partial V_j} \right)_{T, \omega, B, \{V_{k \neq j}\}, N} = -q_j. \quad (5.8)$$

To prove this relation we note that the voltages  $V_j$  enter the Hamiltonian  $H_R$  only through the trap potential  $\phi_T(\mathbf{r})$ , whose linear dependence on  $\{V_j\}$  can be expressed as

$$\phi_T(\mathbf{r}) = \sum_j V_j \hat{\phi}_T^{(j)}(\mathbf{r}),$$

where  $\hat{\phi}_T^{(j)}(\mathbf{r})$  is the potential caused by a unit voltage on electrode ( $j$ ). Then Eqs. (5.1), (4.3), (4.5), and (2.9) imply that

$$\begin{aligned} \left( \frac{\partial F_R}{\partial V_j} \right)_{T, \omega, B, N, \{V_{k \neq j}\}} &= \int d^3r_1 \dots d^3r_N \sum_i e \hat{\phi}_T^{(j)}(\mathbf{r}_i) f_c(\mathbf{r}_1 \dots \mathbf{r}_N) \\ &= \sum_i \langle e \hat{\phi}_T^{(j)}(\mathbf{r}_i) \rangle. \end{aligned}$$

This average can be related to  $q_j$  by using Poisson's equation for the electrostatic potential  $\phi$  induced by the  $N$  charges in the plasma,

$$\nabla^2 \phi = - \sum_i 4\pi e \delta(\mathbf{r} - \mathbf{r}_i),$$

with the boundary condition that  $\phi=0$  on the electrodes. Multiplying each side by  $\hat{\phi}_T^{(j)}(\mathbf{r})$  and integrating over  $\mathbf{r}$  implies

$$\int d^3r [\hat{\phi}_T^{(j)}(\mathbf{r}) \nabla^2 \phi] = - \sum_i 4\pi e \hat{\phi}_T^{(j)}(\mathbf{r}_i).$$

Now we add  $-\phi(\mathbf{r}) \nabla^2 \hat{\phi}_T^{(j)}$  to the integrand on the left-hand side, which makes no change since  $\nabla^2 \hat{\phi}_T^{(j)}=0$  except on the wall where  $\phi=0$ . However, this allows us to apply Green's theorem:

$$\int d^3r [\hat{\phi}_T^{(j)} \nabla^2 \phi - \phi \nabla^2 \hat{\phi}_T^{(j)}] = \int d\mathbf{S} \cdot [\hat{\phi}_T^{(j)} \nabla \phi - \phi \nabla \hat{\phi}_T^{(j)}],$$

where the surface integral runs over the electrodes. On the electrodes  $\phi=0$ , while  $\hat{\phi}_T^{(j)}$  equals 1 on electrode  $j$  and 0 on the other electrodes, so we have

$$\int_{s_j} d\mathbf{S} \cdot \nabla \phi = - \sum_i 4\pi e \hat{\phi}_T^{(j)}(\mathbf{r}_i),$$

where the surface integral runs only over electrode  $j$ . Taking the average of this equation and using the relation

$$\int_{s_j} d\mathbf{S} \cdot \nabla \phi = 4\pi q_j$$

yields Eq. (5.8).

The partial derivatives of the free energy expressed in Eqs. (5.4)–(5.8) can be summarized by the total differential

$$dF_R = -SdT + Ld\omega - \sum_j q_j dV_j - MdB + \mu dN. \quad (5.9)$$

$F_R$  is an example of a thermodynamic potential for the system. By making Legendre transformations, we obtain the total differential of other thermodynamic potentials. For example, using Legendre transformation (5.3) to eliminate  $F_R$  in favor of  $E_R$  yields the total differential

$$dE_R = TdS + Ld\omega - \sum_j q_j dV_j - MdB + \mu dN. \quad (5.10)$$

Likewise, using the Legendre transformation  $E=E_R - \omega L$  to exchange  $E_R$  for the energy in the laboratory frame  $E$  [see Eq. (2.6)] yields

$$dE = TdS - \omega dL - \sum_j q_j dV_j - MdB + \mu dN. \quad (5.11)$$

Obviously, this procedure can be continued to generate many such total differentials.

Simply by rearranging terms, one can rewrite Eqs. (5.10) and (5.11) in the traditional form  $TdS = \dots$ . For many situations, the trap parameters and the particle number are constant (i.e.,  $dB=dV_j=dN=0$ ), so Eq. (5.11) reduces to the form

$$TdS = dE + \omega dL. \quad (5.12)$$

This equation is formally equivalent to the well-known  $TdS$  equation for a gas,

$$TdS = dE + p dV, \quad (5.13)$$

where  $p$  corresponds to  $\omega$  and  $V$  to  $L$ . We shall make use of this formal correspondence from time to time as we proceed.

It is instructive to compare Eqs. (5.10) and (5.11) to Eq. (4.50), the  $TdS$  equation for a large plasma. Note that the mean-field energy  $E_R^{(0)}$  makes large contributions to  $\mu$ ,  $M$ ,  $q_j$ ,  $L$ , and  $E$  [see Eq. (4.43)]. However, recall that Eq. (4.50) implies that there is no mean-field energy contribution to  $S$ ; it remains an extensive variable for a large plasma. Cancellations between large mean-field energy terms must therefore occur in Eqs. (5.10) and (5.11), leaving the relatively small extensive variation in  $S$  apparent in Eq. (4.50). These cancellations follow from the differential relation

$$0 = dE_R^{(0)} - L^{(0)} d\omega + \sum_j q_j^{(0)} dV_j + M^{(0)} dB - \mu^{(0)} dN, \quad (5.14)$$

where  $L^{(0)}$ ,  $q_j^{(0)}$ ,  $M^{(0)}$ , and  $\mu^{(0)}$  are the mean-field limits of  $L$ ,  $q_j$ ,  $M$ , and  $\mu$ , obtained by replacing  $F_R$  with  $E_R^{(0)}$  in Eqs. (5.5)–(5.8). Equation (5.14) is the cold mean-field limit of the general  $TdS$  equations. Equation (5.14) summarizes several useful differential relations for cold-fluid equilibria. For example, the charge induced on the electrodes can be found from a derivative of the cold mean-field energy:

$$q_j^{(0)} = - \left. \frac{\partial E_R^{(0)}}{\partial V_j} \right|_{\omega, B, N, \{V_{k \neq j}\}}. \quad (5.15)$$

With knowledge of the cold mean-field energy, explicit expressions can be derived for the induced charge. For example, using the cold mean-field expression for the energy of a plasma in a hyperbolic trap, Eq. (3.47), along with Eqs. (3.38)–(3.44), one finds that the induced charge on the ring and cap electrodes satisfies  $q_{\text{ring}}^{(0)} + q_{\text{cap}}^{(0)} = Ne$ , as one would expect, and that

$$q_{\text{ring}}^{(0)} - q_{\text{cap}}^{(0)} = Ne \frac{\left[ z_0^2 - \frac{r_0^2}{2} + \frac{6}{5} (R_p^2 - Z_p^2) - \frac{4}{5} (2\beta + 1)(\beta R_p^2 - Z_p^2) d \ln \alpha / d\beta \right]}{z_0^2 + r_0^2/2}. \quad (5.16)$$

Since the plasma is assumed to be far from the electrodes, one can see that the plasma shape has little effect on the induced charge, as expected. Furthermore, the induced charge is completely independent of the plasma radius when the plasma is spherical (i.e.,  $R_p = Z_p$ ), which also follows from symmetry arguments.

## B. Maxwell relations

By taking cross derivatives of the coefficients in the total differentials, we obtain many Maxwell relations (hundreds). Some examples that follow from Eq. (5.9) are the following:

$$\left( \frac{\partial L}{\partial T} \right)_{\omega, B, \{V_j\}, N} = \frac{\partial^2 F_R}{\partial T \partial \omega} = - \left( \frac{\partial S}{\partial \omega} \right)_{T, B, \{V_j\}, N} \quad (5.17)$$

$$\left( \frac{\partial L}{\partial B} \right)_{T, \omega, \{V_j\}, N} = \frac{\partial^2 F_R}{\partial B \partial \omega} = - \left( \frac{\partial M}{\partial \omega} \right)_{T, B, \{V_j\}, N} \quad (5.18)$$

$$\left( \frac{\partial q_j}{\partial V_k} \right)_{T, \omega, B, \{V_{l \neq k}\}, N} = - \frac{\partial^2 F_R}{\partial V_k \partial V_j} = \left( \frac{\partial q_k}{\partial V_j} \right)_{T, \omega, B, \{V_{l \neq j}\}, N}. \quad (5.19)$$

Equations (5.17) and (5.18) are typical of Maxwell relations in that they connect quantities that at first glance seem unrelated. Of course, the relations are general. Equation (5.19) might seem to be a simple reciprocal relation from electrostatics but, in fact, is more general since it involves the plasma response.

As a simple application of Maxwell relations, we evaluate the rate at which charge flows onto (or off of) an electrode as the temperature of a large plasma is varied. The starting point is the two Maxwell relations

$$\left( \frac{\partial q_j}{\partial T} \right)_{\omega, B, \{V_k\}, N} = - \frac{\partial^2 F_R}{\partial T \partial V_j} = \left( \frac{\partial S}{\partial V_j} \right)_{T, \omega, B, N, \{V_{k \neq j}\}} \quad (5.20)$$

$$\left( \frac{\partial q_j}{\partial T} \right)_{L, B, \{V_k\}, N} = - \frac{\partial (F_R - \omega L)}{\partial T \partial V_j} = \left( \frac{\partial S}{\partial V_j} \right)_{T, L, B, \{V_{k \neq j}\}, N}. \quad (5.21)$$

For a plasma that is large compared to the correlation length, we have already observed that  $s = s(T, n_-)$ , so Eqs. (5.20) and (5.21) become

$$\left( \frac{\partial q_j}{\partial T} \right)_{\omega \text{ or } L} = \frac{\partial S}{\partial n_-} \left( \frac{\partial n_-}{\partial V_j} \right)_{\omega \text{ or } L}. \quad (5.22)$$

Since  $n_- = n_-(\omega, \Omega_c)$ , we observe that, at constant  $\omega$ ,  $\partial q_j / \partial T|_{\omega} = 0$  in large plasmas, but for  $L = \text{const}$  we find

$$\left( \frac{\partial q_j}{\partial T} \right)_L = - \frac{N}{n_-} \frac{\partial p}{\partial T} \left( \frac{2\Omega_v}{\omega_p^2} \frac{\partial \omega}{\partial V_j} \right)_{T, L}, \quad (5.23)$$

where we have used Eqs. (4.49) and (3.19). The derivative  $\partial \omega / \partial V_j|_{L, T}$  is nonzero and can be evaluated for large plasmas by dropping surface corrections and using the zero-temperature uncorrelated form. Equation (5.23) implies that the image charge on the conductors is a function of temperature in large plasmas at fixed  $L$ . However, if  $\omega$  is fixed instead,  $\partial q_j / \partial T = 0$ , because fixing  $\omega$  fixes the background density  $n_-$ .

As a specific example, for an uncorrelated plasma in a hyperbolic trap, Eq. (5.23) can be used with Eqs. (3.38)–(3.45) to obtain

$$\begin{aligned} \left( \frac{dq_{\text{ring}}}{dT} \right)_L &= - \left( \frac{dq_{\text{cap}}}{dT} \right)_L \\ &= \frac{d \ln \alpha / d\beta}{d \ln \alpha / d\beta + 2\omega_z^2 / \omega_p^2 + 3\omega_z^2 / \Omega_v^2} \frac{Nk}{V_0}, \end{aligned} \quad (5.24)$$

where  $V_0$  is the potential difference between the ring and cap electrode [see Eq. (3.38)]. Since  $d\alpha/d\beta > 0$ , Eq. (5.24) implies that charge flows off the cap electrode and onto the ring electrode as temperature increases at constant  $L$ . Consequently, measurements of  $q_j$  might possibly provide useful temperature information, although the effect is small: for  $V_0 = 1$  V in a spherical plasma for which  $\Omega_v \gg \omega_z$ , Eq. (5.24) predicts that a temperature change of 1 K produces a charge  $\Delta q$  on the electrodes of magnitude  $|\Delta q / eN| = 5 \times 10^{-5}$ .

## C. Derivatives at constant $T$ and $\omega$ vs derivatives at constant $E$ and $L$

It is convenient to work theoretically with the variables  $T$  and  $\omega$  since these variables enter the Gibbs distribution explicitly. However, these may not be the easiest variables to manipulate experimentally;  $E$  and  $L$  may be easier to control than  $T$  and  $\omega$ . For example, it may be easier to calculate the specific heat at constant rotation frequency

$$c_\omega = T \left( \frac{\partial S}{\partial T} \right)_\omega, \quad (5.25)$$

but easier to measure the specific heat at constant angular momentum

$$c_L = T \left( \frac{\partial S}{\partial T} \right)_L, \quad (5.26)$$

where  $B$ ,  $\{V_j\}$ , and  $N$  are held constant in both cases. Fortunately, Maxwell relations (or combinations of Maxwell relations) provide general relations between such quantities.

Rather than develop these relations explicitly, we make use of the formal correspondence between the  $TdS$  equation for a gas and the  $TdS$  equation for a rotating plasma [see Eqs. (5.12) and (5.13)]. Recalling that  $\omega$  corresponds to  $p$  and  $L$  to  $V$ , we see that  $c_L$  corresponds to the specific heat at constant volume  $c_v$  and  $c_\omega$  to the specific heat at constant pressure  $c_p$ . Simply transcribing the well-known relation between  $c_v$  and  $c_p$  (Landau and Lifshitz, 1980, p. 53) through the replacements  $p \rightarrow \omega$  and  $V \rightarrow L$  yields the relation

$$c_\omega - c_L = -T \frac{(\partial L / \partial T)_\omega^2}{\partial L / \partial \omega}_T. \quad (5.27)$$

In the next section, we shall show that  $\partial L / \partial \omega)_T \leq 0$  and that  $c_L \geq 0$ , so Eq. (5.27) implies that  $c_\omega \geq c_L \geq 0$ . However, in the large- $N$  limit, the relative difference between  $c_\omega$  and  $c_L$  vanishes. To understand why, first recall that  $L$  increases with  $N$  more rapidly than the first power of  $N$ , since  $L$  is dominated by the cold mean-field contribution. However,  $\partial L / \partial T)_\omega$  is extensive [see Eq. (4.78)], since the temperature affects only the plasma edge. Thus  $\partial L / \partial T)_\omega$  is small compared to  $\partial L / \partial \omega$  in the limit  $N \rightarrow \infty$ , and so

$$\lim_{N \rightarrow \infty} \frac{c_L}{Nk} = \frac{c_\omega}{Nk}. \quad (5.28)$$

Other useful general relations linking derivatives at constant  $T$  and  $\omega$  to those at constant  $E$  and  $L$  can also be borrowed from the standard  $p$ - $V$  system:

$$\left( \frac{\partial E}{\partial T} \right)_L = c_L, \quad (5.29)$$

$$\left( \frac{\partial E_R}{\partial T} \right)_\omega = c_\omega, \quad (5.30)$$

$$\left( \frac{\partial E}{\partial L} \right)_T = T \left( \frac{\partial \omega}{\partial T} \right)_L - \omega, \quad (5.31)$$

$$\left( \frac{\partial E}{\partial \omega} \right)_T = -T \left( \frac{\partial L}{\partial T} \right)_\omega - \omega \left( \frac{\partial L}{\partial \omega} \right)_T, \quad (5.32)$$

$$\left( \frac{\partial E}{\partial T} \right)_\omega = c_\omega - \omega \left( \frac{\partial L}{\partial T} \right)_\omega. \quad (5.33)$$

The properties of Jacobians (Landau and Lifshitz, 1980, p. 53) can be used to relate the derivative of any quantity  $G$  with respect to another quantity  $H$  at fixed  $E$  to a derivative at fixed  $T$ . For example,

$$\begin{aligned} \left( \frac{\partial G}{\partial H} \right)_E &= \frac{\partial(G, E)}{\partial(H, E)} = \frac{\partial(G, E) / \partial(G, T) \partial(G, T) / \partial(H, T)}{\partial(H, E) / \partial(H, T)} \\ &= \left( \frac{\partial G}{\partial H} \right)_T \frac{\left( \frac{\partial E}{\partial T} \right)_G}{\left( \frac{\partial E}{\partial T} \right)_H}. \end{aligned} \quad (5.34)$$

A similar relation between derivatives at fixed  $L$  and fixed  $\omega$  can be derived by substituting  $L$  for  $E$  and  $\omega$  for

$T$  in Eq. (5.34). Finally, the Jacobian of the transformation from  $(E, L)$  to  $(T, \omega)$  can be written as

$$\frac{\partial(E, L)}{\partial(T, \omega)} = \frac{\partial L}{\partial \omega}_T c_L. \quad (5.35)$$

#### D. Thermodynamic inequalities

The stability of a system in thermal equilibrium against fluctuations away from equilibrium provides several useful inequalities. We begin the derivation of these inequalities by defining the system energy

$$E' = E + \sum_j q_j V_j + MB,$$

which differs from the plasma (or particle) energy  $E = \langle H \rangle$  through the addition of the energy associated with the induced image charges and the plasma magnetic moment.  $E'$  is the total work, including that done by external circuits, required to construct a plasma out of individual charges brought in from infinity to a trap with fixed electrode voltages  $V_j$  and fixed vacuum magnetic field  $B$  (i.e., the current in the solenoid is held fixed). As the plasma is assembled in the trap, image charges  $q_j$  run onto the electrodes and the voltage sources for the electrodes do work

$$\sum_j q_j V_j.$$

Likewise the current source that maintains a constant  $B$  field does work  $MB$ , the energy associated with mutual inductance between the plasma and the surrounding solenoid. For future reference, we write Eq. (5.11) in terms of  $E'$  rather than  $E$ :

$$dE' = TdS - \omega dL + \sum_j V_j dq_j + BdM + \mu dN. \quad (5.36)$$

We consider a plasma that is confined in a trap with fixed electrode voltages  $V_j = V_{j0}$ , and fixed magnetic field  $B = B_0$ , and that is in contact with a heat, angular momentum, and particle reservoir parametrized by temperature  $T_0$ , rotation frequency  $-\omega_0$ , and chemical potential  $\mu_0$ . Initially, we postulate that the system is slightly out of equilibrium; it does not have the values of  $E$ ,  $L$ ,  $q_j$ ,  $M$ , or  $N$  that would correspond to  $(T_0, \omega_0, V_{j0}, B_0, \mu_0)$  in thermal equilibrium. The system adjusts itself by interacting with the reservoir, exchanging energy, angular momentum, and particles, and by also interacting with the external circuits that fix the electrode voltages and magnetic field. In what follows these circuits are assumed to have no entropy associated with them, and the plasma and heat reservoir constitute a thermally isolated system (no heat is exchanged with the circuits, but work may be done on them). For example, a constant voltage can be maintained by a homopolar generator that consists of a massive conducting flywheel that rotates through a transverse magnetic field. The state of the wheel is described by a single degree of freedom, the rotation angle, so the generator has negligible entropy.

The second law then implies that the total entropy of the plasma and the reservoir must be nonnegative in this equilibration process:

$$\Delta S + \Delta S_{\text{res}} \geq 0. \quad (5.37)$$

Furthermore, the entropy change of the reservoir is related to the heat  $Q$  absorbed into the system from the reservoir,

$$\Delta S_{\text{res}} = \frac{-Q}{T_0}. \quad (5.38)$$

However, the first law for the plasma states that

$$Q = \Delta E' + W, \quad (5.39)$$

where  $\Delta E'$  is the change in energy of the system (including the energy of image charges and the magnetic energy associated with  $M$ ) and  $W$  is the work done by this system. The system can do work as it comes to equilibrium in a number of ways: for instance, induced image charges can flow onto or off of the electrodes, which requires the system to do work

$$-\sum_j V_{0j} \Delta q_j$$

against the circuits that hold the electrode voltages fixed; angular momentum and particle exchange with the reservoir causes work  $\omega_0 \Delta L - \mu_0 \Delta N$  to be performed; and a change in magnetic moment  $\Delta M$  of the plasma does work  $-B_0 \Delta M$  against the power supply that fixes the current in the magnetic-field solenoid. Adding these contributions yields the relation

$$W = \omega_0 \Delta L - \sum_j V_{0j} \Delta q_j - B_0 \Delta M - \mu_0 \Delta N. \quad (5.40)$$

This relation can also be obtained directly from Eq. (5.36) by considering the change in  $E'$  at constant entropy and setting  $W = -\Delta E'$ .

Substitution of Eqs. (5.38)–(5.40) into Eq. (5.37), and then multiplying by the negative constant  $-T_0$ , implies

$$\Delta \Omega_R \leq 0, \quad (5.41)$$

where

$$\Omega_R \equiv E' - T_0 S + \omega_0 L - \sum_j V_{0j} q_j - B_0 M - \mu_0 N \quad (5.42)$$

is a thermodynamic potential for the plasma. When  $\omega = \omega_0$ ,  $V_j = V_{0j}$ , and  $B = B_0$ ,  $\Omega_R = E_R - T_0 S - \mu_0 N$  is the grand potential of the plasma as seen in a rotating frame (Landau and Lifshitz, 1980, p. 72). From Eq. (5.41) we conclude that the thermal equilibrium state achieved by a nonneutral plasma connected to a heat, angular momentum, and particle reservoir and confined by constant electrode voltages and constant external magnetic field is the state for which the thermodynamic potential  $\Omega_R$  is minimized.

Let us now examine the consequences of this result by considering small fluctuations of the system away from thermal equilibrium to some nearby state, under the conditions that  $T_0$ ,  $\omega_0$ ,  $V_{0j}$ ,  $B_0$ , and  $\mu_0$  are fixed. Since the system started in thermal equilibrium, the thermodynamic potential  $\Omega_R$  must increase away from equilibrium, and we can use this fact to determine thermodynamic inequalities. Say that there are  $P$  electrodes. Then let  $\{\lambda_k\}$ ,  $k=1, \dots, P+4$ , be any complete set from the  $P+4$  conjugate pairs of thermodynamic variables

$$\{(T, S), (-\omega, L), \{(V_j, q_j)\}, (B, M), (\mu, N)\}. \quad (5.43)$$

Note that the plasma rotation frequency  $-\omega$  is the variable conjugate to  $L$ . Here the term “conjugate” has the usual meaning in thermodynamics: conjugate variables are related through derivatives of the system energy  $E'$  [see Eq. (5.36)]. The nearby state to which the system has been perturbed is assumed to be characterized by changes in the  $\lambda_k$ 's by small amounts  $\delta \lambda_k$ . The change in  $\Omega_R$  compared to the minimum equilibrium value is then

$$\delta \Omega_R = \sum_k \frac{\partial \Omega_R}{\partial \lambda_k} \delta \lambda_k + \frac{1}{2} \sum_{j,k} \frac{\partial^2 \Omega_R}{\partial \lambda_j \partial \lambda_k} \delta \lambda_j \delta \lambda_k \geq 0, \quad (5.44)$$

where the inequality follows from the fact that  $\Omega_R$  is minimized in the thermal equilibrium for which  $\delta \lambda_k = 0$ .

Now since  $\delta \lambda_k$  can be either positive or negative, the first variation of  $\Omega_R$  must vanish, implying

$$\frac{\partial \Omega_R}{\partial \lambda_k} = 0.$$

We can rewrite this equation by using the definition of  $\Omega_R$  in Eq. (5.42) and substituting for  $\partial E' / \partial \lambda_j$  from Eq. (5.36):

$$\begin{aligned} \frac{\partial \Omega_R}{\partial \lambda_k} = & (T - T_0) \frac{\partial S}{\partial \lambda_k} - (\omega - \omega_0) \frac{\partial L}{\partial \lambda_k} + \sum_j (V_j - V_{0j}) \frac{\partial q_j}{\partial \lambda_k} \\ & + (B - B_0) \frac{\partial M}{\partial \lambda_k} + (\mu - \mu_0) \frac{\partial N}{\partial \lambda_k} = 0. \end{aligned} \quad (5.45)$$

Equation (5.45) implies that the thermal equilibrium state is such that

$$\begin{aligned} T &= T_0, \quad \omega = \omega_0, \quad V_j = V_{0j}, \\ B &= B_0, \quad \text{and} \quad \mu = \mu_0. \end{aligned} \quad (5.46)$$

For example, suppose that  $\{\lambda_k\} = \{S, L, \{q_j\}, M, N\}$  and that  $\lambda_k = S$ . Then in Eq. (5.45),  $\partial S / \partial \lambda_k$  is unity and the remaining partial derivatives are zero, so we obtain  $T = T_0$ . The other results in Eq. (5.46) follow from setting  $\lambda_k = L$ ,  $\{q_j\}$ ,  $M$ , and  $N$  one after the other.

When conditions (5.46) are satisfied, only the term quadratic in the  $\delta \lambda_k$ 's survives and inequality (5.44) implies that this term must be nonnegative. In other words, in the space of  $\{\delta \lambda_k\}$  the surfaces of constant  $\delta \Omega_R$  are closed and nested so that  $\delta \Omega_R = 0$  is a local minimum.

Since this is a statement concerning the topology of the constant  $\delta\Omega_R$  surfaces, it remains true for any complete set of  $\lambda_k$ 's that we choose. Therefore we lose no information by choosing any particular set of  $\lambda_k$ 's. A convenient set is  $\{\lambda_k\} = \{S, L, \{q_j\}, M, N\}$ , because we have al-

ready determined the first derivatives of  $\Omega_R$  with respect to these variables [see Eq. (5.45)]. For example,  $\partial^2\Omega_R/\partial S^2)_{L,\{q_j\},M,N} = \partial T/\partial S)_{L,\{q_j\},M,N}$ . The entire set of second derivatives forms a matrix of dimensions  $P+4$  by  $P+4$ :

$$\frac{\partial^2\Omega_R}{\partial\lambda_j\partial\lambda_k} = \begin{pmatrix} \frac{\partial T}{\partial S} \bigg|_{L,\{q_j\},M,N} & \frac{\partial T}{\partial L} \bigg|_{S,\{q_j\},M,N} & \left\{ \frac{\partial T}{\partial q_k} \right\}_{S,L,\{q_{j \neq k}\},M,N} & \frac{\partial T}{\partial M} \bigg|_{S,L,\{q_j\},N} & \frac{\partial T}{\partial N} \bigg|_{S,L,\{q_j\},M} \\ & -\frac{\partial\omega}{\partial L} \bigg|_{S,\{q_j\},M,N} & \left\{ -\frac{\partial\omega}{\partial q_k} \right\}_{S,L,\{q_{j \neq k}\},M,N} & -\frac{\partial\omega}{\partial M} \bigg|_{S,L,\{q_j\},N} & -\frac{\partial\omega}{\partial N} \bigg|_{S,L,\{q_j\},M} \\ & & \left\{ \frac{\partial V_j}{\partial q_k} \right\}_{S,L,\{q_{j \neq k}\},M,N} & \frac{\partial V_j}{\partial M} \bigg|_{S,L,\{q_j\},N} & \frac{\partial V_j}{\partial N} \bigg|_{S,L,\{q_j\},M} \\ & \dots & & \frac{\partial B}{\partial M} \bigg|_{S,L,\{q_j\},N} & \frac{\partial B}{\partial N} \bigg|_{S,L,\{q_j\},M} \\ & & & & \frac{\partial\mu}{\partial N} \bigg|_{S,L,\{q_j\},M} \end{pmatrix}, \quad (5.47)$$

where only the top half of the matrix is displayed because it is symmetric:  $\partial^2\Omega_R/\partial\lambda_j\partial\lambda_k = \partial^2\Omega_R/\partial\lambda_k\partial\lambda_j$ . This symmetry provides a set of Maxwell relations for the system.

Stability implies that the eigenvalues of this matrix are nonnegative, which yields  $P+4$  thermodynamic inequalities. These inequalities form a necessary and sufficient set of criteria for stability of the equilibrium against fluctuations in any of the thermodynamic variables.

However, the eigenvalues are quite complicated in form, so we consider a simpler set of inequalities, which only form a necessary set of criteria for stability (they are not sufficient). Considering fluctuations in only one of the  $\lambda_k$ 's at a time implies that each diagonal element,  $\partial^2\Omega_R/\partial\lambda_k^2$ , must be nonnegative. For example, we find

$$\frac{\partial T}{\partial S} \bigg|_{L,\{q_j\},M,N} \geq 0, \quad (5.48)$$

which implies that the specific heat at constant  $L$ ,  $\{q_j\}$ ,  $M$ , and  $N$  is nonnegative, provided that  $T \geq 0$ . It is also worthwhile to write out the other inequalities explicitly:

$$-\frac{\partial\omega}{\partial L} \bigg|_{S,\{q_j\},M,N} \geq 0, \quad (5.49)$$

$$\frac{\partial V_k}{\partial q_k} \bigg|_{S,L,\{q_{j \neq k}\},M,N} \geq 0, \quad (5.50)$$

$$\frac{\partial B}{\partial M} \bigg|_{S,L,\{q_j\},N} \geq 0, \quad (5.51)$$

$$\frac{\partial\mu}{\partial N} \bigg|_{S,L,\{q_j\},M} \geq 0. \quad (5.52)$$

The fact that these inequalities are necessary but not sufficient for stability can be seen by allowing variations in more than one parameter. For example, consider variations in both  $S$  and  $L$ . Then the determinant of the  $2 \times 2$  matrix composed of the upper left-hand side of  $\partial^2\Omega_R/\partial\lambda_j\partial\lambda_k$  must be non-negative, which implies that

$$-\frac{\partial T}{\partial S} \bigg|_{L,\{q_j\},M,N} \frac{\partial\omega}{\partial L} \bigg|_{S,\{q_j\},M,N} \geq \left( \frac{\partial T}{\partial L} \bigg|_{S,\{q_j\},M,N} \right)^2,$$

providing more stringent bounds for both  $\partial T/\partial S$  and  $\partial\omega/\partial L$  than are provided by Eqs. (5.48) and (5.49).

Equations (5.48)–(5.52) reflect stability along one particular set of directions, given by  $\lambda_k = \{S, L, \{q_j\}, M, N\}$ , but more information may be uncovered by considering other directions. The inequalities so obtained take the simplest forms when only one of each conjugate pair in Eq. (5.43) is employed as a  $\lambda_k$ . For example, choose  $\{\lambda_k\} = \{T, L, \{V_j\}, B, N\}$ , and take  $\lambda_k = L$  in Eq. (5.45). Then taking another derivative with respect to  $L$  yields

$$\frac{\partial^2\Omega_R}{\partial L^2} \bigg|_{T,\{V_j\},B,N} = -\frac{\partial\omega}{\partial L} \bigg|_{T,\{V_j\},B,N} \geq 0, \quad (5.53)$$

where we have employed the equilibrium conditions, Eq. (5.46), after taking the derivative. Similarly, taking  $\lambda_k = T$  in Eq. (5.45) yields  $\partial S/\partial T)_{L,\{V_j\},B,N} \geq 0$ . Assuming that  $T > 0$ , and using definition (5.26), we then obtain

$$c_L \geq 0. \quad (5.54)$$

This equation, together with Eq. (5.27), shows that  $c_\omega$  must also be non-negative. Analogous arguments show



that any other choice for the set of  $\{\lambda_k\}$ 's consisting of one variable from each of the conjugate pairs in Eq. (5.43) can be employed without changing the basic form of Eqs. (5.48)–(5.52). For example,  $\partial M/\partial B)_{T,\omega,\{V_j\},N} \geq 0$  and  $\partial V_j/\partial q_j)_{T,L,\{V_{k \neq j}\},B,\mu} \geq 0$  as well.

The inequalities  $c_L \geq 0$  and  $\partial\omega/\partial L)_{T \leq 0}$  are the analogs of the inequalities  $c_v \geq 0$  and  $\partial p/\partial V)_{T \leq 0}$  for a gas. The latter two inequalities can be understood physically as the conditions for temperature and mechanical stability when the gas is in contact with a reservoir characterized by fixed temperature and pressure. Likewise, the inequalities  $c_\omega \geq 0$  and  $\partial\omega/\partial L)_{T \leq 0}$  are necessary for temperature and rotation frequency stability when the plasma is in contact with a reservoir characterized by fixed temperature and fixed rotation frequency. In thinking about frequency stability, it is necessary to remember that  $-\omega$  is the rotation frequency, so it may be useful to rewrite  $\partial\omega/\partial L)_{T \leq 0}$  as  $\partial(-\omega)/\partial L)_{T \geq 0}$ . Suppose, for example, that a fluctuation makes  $-\omega$  larger (more positive) than the rotation frequency of the reservoir. The reservoir will then exert a negative torque on the plasma, opposing the differential rotation. The two inequalities  $\Delta L < 0$  and  $\partial(-\omega)/\partial L)_{T > 0}$  then imply that  $\Delta(-\omega) < 0$ , which is a frequency change of the sign required to restore equilibrium.

The inequality  $\partial V_j/\partial q_j)_{T,L,\{V_{k \neq j}\},B,\mu} \geq 0$  also follows from a straightforward physical picture. As  $V_j$  is increased (holding the other parameters fixed), a plasma consisting of positive charges is pushed away from electrode  $j$ , so the (negative) image charge on that electrode is decreased in magnitude.

The inequality  $\partial M/\partial B)_{T,\omega,\{V_j\},N} \geq 0$  implies that the magnitude of the plasma's (negative) magnetic moment  $M$  decreases as  $B$  increases, which may be counterintuitive at first glance since the plasma is diamagnetic, so one expects the magnitude of the plasma magnetization to increase as  $B$  increases. However, the average magnetization is the magnetic moment divided by the plasma volume, and as  $B$  increases the plasma volume decreases, since the plasma radius tends to shrink. The decrease in plasma volume allows the magnetization to increase in magnitude even though the magnetic moment decreases in magnitude.

Finally, we may wish to fix  $E$  rather than  $S$  or  $T$ . For example, consider variations of  $L$  at fixed  $E$ ,  $\{V_j\}$ ,  $B$ , and  $N$ . Taking  $\lambda_k = L$  in Eq. (5.45), and then taking another derivative with respect to  $L$ , yields the inequality

$$\left. \frac{\partial^2 \Omega_R}{\partial L^2} \right)_{E,\{V_j\},B,N} = \left. \frac{\partial T}{\partial L} \right)_{E,\{V_j\},B,N} \left. \frac{\partial S}{\partial L} \right)_{E,\{V_j\},B,N} - \left. \frac{\partial \omega}{\partial L} \right)_{E,\{V_j\},B,N} \geq 0. \quad (5.55)$$

However, Eq. (5.11) implies that  $T \partial S/\partial L)_{E,\{V_j\},B,N} = \omega$ , so we can write Eq. (5.55) as

$$-T \left. \frac{\partial}{\partial L} \left( \frac{\omega}{T} \right) \right)_{E,\{V_j\},B,N} \geq 0. \quad (5.56)$$

Note that this inequality does not imply that  $(\partial\omega/\partial L)_{E,\{V_j\},B,N} \leq 0$ . In fact, thermodynamic stability does not disallow the possibility that  $(\partial\omega/\partial L)_{E,\{V_j\},B,N} > 0$ . Nevertheless, for a large classical plasma one can show that the inequality is satisfied. By using Eqs. (5.34) and (5.29), we obtain the relation

$$\left. \frac{\partial \omega}{\partial L} \right)_E = \frac{\left. \frac{\partial E}{\partial T} \right)_\omega \left. \frac{\partial \omega}{\partial L} \right)_T}{c_L}, \quad (5.57)$$

where  $\{V_j\}$ ,  $B$ , and  $N$  are held fixed throughout. Now,  $c_L \geq 0$  and  $\partial\omega/\partial L)_{T \leq 0}$ , so the sign of  $\partial\omega/\partial L)_E$  hinges on the sign of  $\partial E/\partial T)_\omega$ . Since  $E = E_R - \omega L$ , Eq. (5.30) implies that

$$\left. \frac{\partial E}{\partial T} \right)_\omega = c_\omega - \omega \left. \frac{\partial L}{\partial T} \right)_\omega. \quad (5.58)$$

Unfortunately, this is as far as we can go in general because we do not have a general expression for  $\partial L/\partial T)_\omega$ . However, for a large plasma, this derivative is given by Eq. (4.78) and also  $c_\omega = c_L = c_{n-}$ , the specific heat of a one-component-plasma. Employing these results in Eq. (5.57), and using Eq. (4.35) to evaluate  $\partial p/\partial T)_\omega$ , yields

$$\left. \frac{\partial \omega}{\partial L} \right)_{E,\{V_j\},B,N} = \left. \frac{\partial \omega}{\partial L} \right)_{T,\{V_j\},B,N} \frac{c_{\text{ideal}} - Nk \left( 1 - \frac{2\omega^2}{\omega_p^2} \right) + \frac{2}{3} \left( 1 + \frac{\omega^2}{\omega_p^2} \right) (c_{n-} - c_{\text{ideal}})}{c_{n-}}. \quad (5.59)$$

For an OCP consisting of classical point charges,  $c_{n-} - c_{\text{ideal}}$ , the specific heat due to correlation effects, is non-negative (see Fig. 43) and  $c_{\text{ideal}} = 3Nk/2$ , so  $\partial\omega/\partial L)_E \leq 0$ . However, for a cryogenic electron plasma for which the cyclotron motion is quantized and in the lowest Landau level,  $c_{\text{ideal}} = Nk/2$ . In this case Eq. (5.59)

implies that  $\partial\omega/\partial L)_E$  can be greater than zero, depending on the rotation frequency and the degree of correlation. For example, for a weakly correlated plasma with quantized cyclotron motion, Eq. (5.59) implies  $\partial\omega/\partial L)_E = -[(\Omega_c - 3\omega)/(\Omega_c - \omega)] \partial\omega/\partial L)_T$ , which is greater than zero provided that  $\Omega_c > 3\omega$ .

### E. Fluctuations

The thermodynamic inequalities discussed in the previous section can be related to the magnitude of fluctuations in the plasma, and some of these relations may be of physical interest. For example, consider a fluctuation  $\delta q_i = q_i - \langle q_i \rangle$  in the charge on a sector  $i$  at fixed  $N$ ,  $\omega$ ,  $T$ ,  $B$ , and  $\{V_j\}$ . (Here we employ the notation  $\langle q_i \rangle$  for the equilibrium average, and  $q_i$  is the value of a particular realization of the canonical ensemble, which fluctuates by  $\delta q_i$  about  $\langle q_i \rangle$ .) Standard thermodynamic arguments allow us to express the average  $\langle \delta q_i \delta q_j \rangle_{T,\omega}$  in terms of thermodynamic derivatives. We first express this average in terms of  $\langle q_i q_j \rangle_{T,\omega}$ ,  $\langle q_i \rangle$ , and  $\langle q_j \rangle$ :

$$\langle \delta q_i \delta q_j \rangle_{T,\omega} = \langle q_i q_j \rangle_{T,\omega} - \langle q_i \rangle \langle q_j \rangle. \quad (5.60)$$

These averages can be expressed as derivatives of the canonical partition function  $Z_c$ . Using Eqs. (5.8) and (5.1), one finds

$$\langle q_i \rangle = (kT/Z_c) \partial Z_c / \partial V_j \Big|_{T,\omega,B,N}, \quad (5.61)$$

and a modification of the argument that led to Eq. (5.8) yields  $\langle q_i q_j \rangle_{T,\omega} = [(kT)^2/Z_c] \partial^2 Z_c / \partial V_i \partial V_j \Big|_{T,\omega,B,N}$ . Putting these averages together in Eq. (5.60) yields

$$\begin{aligned} \langle \delta q_i \delta q_j \rangle_{T,\omega} &= \frac{1}{Z_c} (kT)^2 \frac{\partial^2}{\partial V_i \partial V_j} Z_c \Big|_{T,\omega,B,N} - \left( \frac{kT}{Z_c} \right)^2 \frac{\partial Z_c}{\partial V_i} \frac{\partial Z_c}{\partial V_j} \\ &= (kT)^2 \frac{\partial^2 \ln Z_c}{\partial V_i \partial V_j} \Big|_{T,\omega,B,N} = kT \frac{\partial q_i}{\partial V_j} \Big|_{T,\omega,B,N} \\ &= kT \frac{\partial q_j}{\partial V_i} \Big|_{T,\omega,B,N}, \end{aligned} \quad (5.62)$$

where in the last two steps we used Eq. (5.61) and the Maxwell's relation, Eq. (5.19). The subscripts on  $\langle \delta q_i \delta q_j \rangle_{T,\omega}$  point out that the average is performed in a constant  $T$  and  $\omega$  ensemble (the canonical ensemble). Averages over the microcanonical ensemble will be discussed presently.

When  $i=j$ , the fact that  $\langle \delta q_i^2 \rangle_{T,\omega}$  must be non-negative provides us with an inequality similar to Eq. (5.50). Furthermore, fluctuations in image charge may be of some interest since Eq. (5.62) shows that they provide a measure of the temperature of the plasma.

A similar relation can be derived involving the magnetic moment  $M$  of the plasma:

$$\langle \delta M^2 \rangle_{T,\omega} = kT \frac{\partial M}{\partial B} \Big|_{T,\omega,\{V_j\},N}, \quad (5.63)$$

which provides us with an inequality similar to that given by Eq. (5.51). Measurements of fluctuations in  $M$ , through use of a circuit connected to an external inductance coupled to the plasma, for example, could also provide a temperature diagnostic.

Another useful relation follows from consideration of fluctuations in the function

$$1/N \sum_i r_i^2.$$

The thermal equilibrium average of this function is the mean-square cylindrical radius,  $\langle r^2 \rangle$ , and this average can be obtained by taking a derivative of the free energy with respect to  $\omega$ :

$$\langle r^2 \rangle = \frac{2}{Nm\Omega_v} \frac{\partial F_R}{\partial \omega} \Big|_{T,\{V_j\},B,N}. \quad (5.64)$$

Equation (5.64) can be obtained directly using Eqs. (5.1) and (4.3) or indirectly via Eq. (5.5) and the definition of  $L$ , Eq. (4.75). Furthermore, fluctuations in

$$(1/N) \sum_i r_i^2$$

can be related to a derivative of  $\langle r^2 \rangle$  using arguments analogous to those that led to Eq. (5.62):

$$\left\langle \left( \delta \frac{1}{N} \sum_i r_i^2 \right)^2 \right\rangle_{T,\omega} = - \frac{2kT}{Nm\Omega_v} \frac{\partial \langle r^2 \rangle}{\partial \omega} \Big|_{T,\{V_j\},B,N}. \quad (5.65)$$

This relation implies that

$$\frac{1}{\Omega_v} \frac{\partial \langle r^2 \rangle}{\partial \omega} \Big|_{T,\{V_j\},B,N} \leq 0. \quad (5.66)$$

When  $\Omega_v$  is positive, the mean-square radius shrinks as  $\omega$  increases, but when  $\Omega_v$  becomes negative  $\langle r^2 \rangle$  expands, as one can see in Fig. 15, for example. For a harmonic trap Eq. (5.66) can be written as

$$\frac{\partial \langle r^2 \rangle}{\partial \beta} \Big|_{T,\omega_z,N} \leq 0, \quad (5.67)$$

where the trap parameter  $\beta$  is defined by Eq. (3.40). Note that  $B$  need not be held fixed in Eq. (5.67) since  $\langle r^2 \rangle$  depends on  $B$  only through  $\beta$ . Inequality (5.67) was observed to hold in Coulomb clusters at zero temperature (see Sec. IV.E.1 and Figs. 61 and 62).

Equation (5.66) can be employed to obtain an improved bound on  $\partial L / \partial \omega$ . A derivative with respect to  $\omega$  of Eq. (4.75) implies

$$\frac{Nm}{2} \Omega_v \frac{\partial \langle r^2 \rangle}{\partial \omega} \Big|_{T,\{V_j\},B,N} = \frac{\partial L}{\partial \omega} \Big|_{T,\{V_j\},B,N} + Nm \langle r^2 \rangle. \quad (5.68)$$

Since Eq. (5.66) implies that the left-hand side of Eq. (5.68) is less than or equal to zero, we find

$$\frac{\partial L}{\partial \omega} \Big|_{T,\{V_j\},B,N} \leq -Nm \langle r^2 \rangle, \quad (5.69)$$

which is an improvement over Eq. (5.53). Note that the right-hand side of Eq. (5.69) is the negative of the rotational inertia of the plasma.

It is important to point out that the fluctuations in Eqs. (5.62), (5.63), and (5.65) are assumed to occur in a system at fixed  $\omega$  and  $T$ . We have added subscripts to

the averages in order to point this out explicitly. However, it is presumably fluctuations at fixed  $L$  and  $E$  that are of interest in many experimental measurements. Although we have said that averages in the microcanonical (fixed  $L$  and  $E$ ) and canonical (fixed  $\omega$  and  $T$ ) ensembles are identical for large systems, this statement must be modified when fluctuations are considered. A more precise statement is that averages of intensive quantities in the two ensembles are identical to  $O(1/N)$ . However, for fluctuations these  $O(1/N)$  corrections are important, and the two ensembles may provide different results in the thermodynamic limit. One trivial example is that in the microcanonical ensemble  $\langle \delta P_\theta^2 \rangle_{E,L} = 0$ , whereas in the canonical ensemble  $P_\theta$  fluctuates. The reason that the  $O(1/N)$  corrections are important can be understood from the following argument. Consider the fluctuation  $\delta G$  of an extensive quantity  $G$ . We evaluate  $\langle \delta G^2 \rangle$  by taking the difference  $\langle \delta G^2 \rangle = \langle G^2 \rangle - \langle G \rangle^2$ . Since  $G$  is extensive,  $\langle G^2 \rangle$  and  $\langle G \rangle^2$  scale as  $N^2$ . The  $O(1/N)$  difference between an evaluation of the averages using different ensembles will therefore scale as  $N$ . However, typical fluctuations  $\langle \delta G^2 \rangle$  are also of  $O(N)$ ; the  $O(N^2)$  terms cancel after  $\langle G \rangle^2$  is subtracted from  $\langle G^2 \rangle$ . We therefore cannot necessarily neglect the  $O(1/N)$  difference between evaluations of rms fluctuations using different ensembles.

Fortunately, it is possible to relate the fluctuations in different ensembles (Leibowitz, Percus, and Verlet, 1967). Given any two quantities  $G$  and  $H$  with average values  $\langle G \rangle, \langle H \rangle$  and fluctuations  $\delta G$  and  $\delta H$  about their average values, the fluctuations in a constant  $E, L, B, \{V_j\}$ , and  $N$  ensemble are related to the fluctuations in a constant  $T, \omega, B, \{V_j\}$ , and  $N$  ensemble by

$$\begin{aligned} \langle \delta G \delta H \rangle_{E,L} = & \langle \delta G \delta H \rangle_{T,\omega} - kT^2 \frac{\partial T}{\partial E} \left( \frac{\partial \langle G \rangle}{\partial T} \right)_{(\omega/T)} \\ & \times \frac{\partial \langle H \rangle}{\partial T} \Big|_{(\omega/T)} + k \frac{\partial T}{\partial L} \Big|_E \left\{ \frac{\partial \langle G \rangle}{\partial T} \right\}_{(\omega/T)} \\ & \times \frac{\partial \langle H \rangle}{\partial (\omega/T)} \Big|_T + \frac{\partial \langle G \rangle}{\partial (\omega/T)} \Big|_T \frac{\partial \langle H \rangle}{\partial T} \Big|_{(\omega/T)} \Big\} \\ & + k \frac{\partial (\omega/T)}{\partial L} \Big|_E \frac{\partial \langle G \rangle}{\partial (\omega/T)} \Big|_T \frac{\partial \langle H \rangle}{\partial (\omega/T)} \Big|_T, \end{aligned} \quad (5.70)$$

where  $B, \{V_j\}$ , and  $N$  are also held fixed throughout. For the mean-square fluctuations  $\langle \delta q_i \delta q_j \rangle_{E,L}$  and  $\langle \delta M^2 \rangle_{E,L}$ , we have evaluated the derivatives in Eq. (5.70). To do so we note that  $\partial \langle G \rangle / \partial T \Big|_{(\omega/T)} = \partial \langle G \rangle / \partial T \Big|_\omega + (\omega/T) \partial \langle G \rangle / \partial \omega \Big|_T$ . In the large-plasma limit, one can use Eqs. (5.28), (5.29), (5.34), and (4.78), along with the fact that  $\partial L / \partial \omega \Big|_T$  increases with  $N$  more rapidly than the first power of  $N$ , to show that

$$\langle \delta M^2 \rangle_{E,L} = kT \partial M / \partial B \Big|_{T,L,\{V_j\},N} \quad (5.71)$$

$$\begin{aligned} \langle \delta q_i \delta q_j \rangle_{E,L} &= kT \partial q_j / \partial V_i \Big|_{T,L,B,N} \\ &= kT \partial q_i / \partial V_j \Big|_{T,L,B,N}. \end{aligned} \quad (5.72)$$

The derivatives in these equations differ from those of Eqs. (5.62) and (5.63) because  $L$  is held fixed rather than  $\omega$ .

Another example of a fluctuation for which there is a difference between ensembles in the large-plasma limit is the rms fluctuation in the  $z$  component of the kinetic energy,

$$K_z = \sum_i \frac{1}{2} m v_z^2.$$

This quantity can be followed in computer simulations and may also be observable using laser diagnostics in actual experiments, since these diagnostics can determine components of the particle velocities. In the canonical ensemble straightforward integrals over the Maxwellian velocity distribution imply that  $\langle K_z \rangle = NkT/2$ , so measurement of  $\langle K_z \rangle$  provides one with the temperature. Fluctuations in  $K_z$  are also related to  $T$  through averages over a Maxwellian:

$$\langle \delta K_z^2 \rangle_{T,\omega} = \frac{1}{2} N(kT)^2. \quad (5.73)$$

However, using Eq. (5.70) one finds that in the constant  $E$  and  $L$  ensemble the mean-square fluctuation is different:

$$\langle \delta K_z^2 \rangle_{E,L} = \frac{1}{2} N(kT)^2 \left[ 1 - \frac{Nk}{2c_L} \right]. \quad (5.74)$$

There can be a considerable difference between Eq. (5.73) and Eq. (5.74). For example, for a large weakly correlated electron plasma for which the cyclotron motion is quantized and in the ground state (but motion parallel to  $\mathbf{B}$  remains classical),  $c_L \rightarrow \frac{1}{2} Nk$ . Equation (5.74) then implies that  $\langle \delta K_z^2 \rangle_{E,L}$  vanishes. However, Eq. (5.73) implies that  $\langle \delta K_z^2 \rangle_{T,\omega}$  remains finite. In the microcanonical ensemble the fluctuation in  $K_z$  is non-zero only by virtue of correlations that raise  $c_L$  above  $\frac{1}{2} Nk$ .

## F. Adiabatic processes

Some experiments involve adiabatic processes for which  $S = \text{const}$ . We have already discussed the rate of temperature change in adiabatic processes for large plasmas [see Eqs. (4.52) and (4.53)], but here we consider general relations which hold even for plasmas that include surface effects. For example, the rate of work done on the plasma due to different adiabatic processes is given by Eq. (5.11):

$$\begin{aligned} \frac{\partial E}{\partial V_j} \Big|_{S,L,\{V_{k \neq j}\},B,N} &= -q_j, & \frac{\partial E}{\partial B} \Big|_{S,L,\{V_j\},N} &= -M \\ \frac{\partial E}{\partial L} \Big|_{S,\{V_j\},B,N} &= -\omega. \end{aligned} \quad (5.75)$$

Typically, adiabatic expansions are carried out by varying a sector voltage  $V_j$  at constant  $L$ . The temperature change in such a process is

$$\begin{aligned}
\left. \frac{\partial T}{\partial V_j} \right)_{S,L,\{V_{k \neq j}\},B,N} &= -\partial S / \partial V_j \Big|_{T,L,\{V_{k \neq j}\},B,N} / \partial S / \partial T \Big|_{L,\{V_j\},B,N} \\
&= -\frac{T}{c_L} \left. \frac{\partial q_j}{\partial T} \right)_{L,\{V_j\},B,N}, \quad (5.76)
\end{aligned}$$

where we have employed the Maxwell relation, Eq. (5.21), and definition (5.26).

Adiabatic expansions can also be carried out by varying the magnetic field. The temperature change would then be given by

$$\left. \frac{\partial T}{\partial B} \right)_{S,L,B,N} = -\frac{T}{c_L} \left. \frac{\partial M}{\partial T} \right)_{L,\{V_j\},B,N}. \quad (5.77)$$

For large plasmas, Eqs. (5.76) and (5.77) are equivalent to Eq. (4.53).

### G. Thermodynamic approach to transport

For a collection of point charges that interact electrostatically in an ideal trap for which the electrode structure is cylindrically symmetric and the trap fields are time independent,  $E$  and  $L$  are constants (see Sec. II.B). However, for a real plasma in a real trap, such effects as collisions with neutrals, radiation, and interaction with small (but unavoidable) field errors produce slow changes in  $E$  and  $L$ . Furthermore, laser beams and rotating field asymmetries are often applied to produce changes in  $E$  and  $L$ . We assume that these changes are slow compared to the time for collisions to bring the plasma to thermal equilibrium, so the plasma evolves through a sequence of thermal equilibrium states, and the slow evolution of  $E$  and  $L$  translates to a slow evolution of  $T$  and  $\omega$ . Thermodynamics provides a simple framework for the description of this late time transport. Throughout this section we assume that the particle number and trap parameters are held constant (i.e.,  $dN=dV_j=dB=0$ ), so the  $TdS$  equation reduces to the simple form in Eq. (5.12).

#### 1. Direction of evolution

In some cases, thermodynamics alone can tell us the sign of the change in quantities and the direction of evolution. As a simple example, consider the sign of the torque that a static-field error (asymmetry) exerts on a rotating plasma. Of course, one's intuition suggests that the torque is a drag that opposes the rotation, but how can we prove this? Fundamentally, the intuition is an expression of the second law of thermodynamics. Since the field asymmetry is static,  $E$  remains constant and we can set  $dE=0$  in Eq. (5.12) to obtain the result

$$0 \leq TdS = \omega dL = -(-\omega)dL, \quad (5.78)$$

where the inequality expresses the second law. Thus the plasma rotation frequency  $(-\omega)$  and  $dL$  have opposite signs, that is, the torque  $\dot{L}=dL/dt$  opposes the rotation.

For a plasma of positive charges, the rotation frequency is negative (i.e.,  $\omega > 0$ ) so  $\dot{L}$  is positive.

Although the torque opposes the rotation, it is not necessarily true that this torque causes  $\omega$  to decrease monotonically toward zero: a static-field error can in some circumstances actually cause the rotation frequency to increase in magnitude. This rather surprising result follows from the fact that thermodynamics does not fix the sign of  $\partial\omega/\partial L)_E$ . In some regimes  $\partial\omega/\partial L)_E$  can be greater than zero. One example is the case of a cryogenic pure electron plasma in the lowest Landau level, which we discussed previously in connection with Eq. (5.59). When  $\partial\omega/\partial L)_E > 0$ , the fact that  $\dot{L} > 0$  implies  $\dot{\omega} = \dot{L} \partial\omega/\partial L)_E > 0$ , so the plasma spins more rapidly due to the application of the static-field error.

Of course, this cannot continue indefinitely, otherwise the system would never approach thermal equilibrium (which corresponds to  $\omega=0$  when a static error is applied). For example, for the case of the cryogenic pure electron plasma, the field error causes an increase in temperature [due to the entropy increase expressed in Eq. (5.78) and inequality (5.54)]. This eventually causes the system to leave the lowest Landau level, so  $\partial\omega/\partial L)_E$  changes sign and  $\omega$  begins to decrease toward zero.

Next, let us suppose that some other effect, say, laser cooling, maintains the plasma temperature at a constant value without exerting a torque. Then the relation  $\dot{\omega} = (\partial\omega/\partial L)_T \dot{L}$  plus the inequalities  $(\partial\omega/\partial L)_T \leq 0$  and  $\dot{L} > 0$  imply that  $\dot{\omega}$  is negative. The stationary field asymmetry slows the plasma rotation much as a caliper brake slows the rotation of a freely spinning bicycle wheel.

For fixed  $T$ , the direction of evolution of  $\omega$  determines the direction of evolution of all other quantities. For example, Eq. (5.66) implies that  $\partial\langle r^2 \rangle / \partial \omega)_T$  is positive for  $\omega < \Omega_c/2$  and negative for  $\omega > \Omega_c/2$ . Thus, if  $\omega$  starts off at a large value and decreases monotonically,  $\langle r^2 \rangle$  decreases until  $\omega = \Omega_c/2$  and then begins to increase. For the special case of a quadratic trap potential, this behavior can be seen in Fig. 15.

A more succinct argument treats the field asymmetry and the process that maintains the temperature at a fixed value as a heat and angular momentum reservoir. The reservoir is assumed to be fixed at the initial temperature  $T$  of the plasma and the rotation frequency  $-\omega_0$  of the field error. Here, we allow for the more general case of a rotating-field asymmetry (see the discussion of the "rotating-wall" field in Sec. III.H.2). The heat transfer is assumed to be sufficiently effective that the plasma remains in temperature equilibrium with the reservoir even though it is not in frequency equilibrium with the reservoir. The thermodynamic potential  $\Omega_R$ , which was defined in Eq. (5.42), must decrease as the plasma evolves toward frequency equilibrium with the reservoir. Thus we obtain

$$0 \geq \Delta \Omega_R = \left. \frac{\partial \Omega_R}{\partial L} \right)_{T,N,B,\{V_j\}} \Delta L = -(\omega - \omega_0) \Delta L, \quad (5.79)$$

where the partial derivative was evaluated by setting  $\lambda_k = L$ ,  $T = T_0$ ,  $V_j = V_{j0}$ , and  $B = B_0$  in Eq. (5.45). Again, we find that the torque opposes the differential rotation, which together with the inequality  $\partial\omega/\partial L)_T \leq 0$  implies that the rotation frequency of the plasma evolves toward that of the field asymmetry.

## 2. Evolution equations

If the plasma passes through a sequence of thermal equilibrium states characterized by fixed values of  $N$ ,  $\{V_j\}$ , and  $B$ , the temperature and rotation frequency at any instant can be expressed as  $T = T(E, L)$  and  $\omega = \omega(E, L)$ . The time derivative of these equations,

$$\dot{T} = \left( \frac{\partial T}{\partial E} \right)_L \dot{E}(\omega, T, \chi_j) + \left( \frac{\partial T}{\partial L} \right)_E \dot{L}(\omega, T, \chi_j), \quad (5.80)$$

$$\dot{\omega} = \left( \frac{\partial \omega}{\partial E} \right)_L \dot{E}(\omega, T, \chi_j) + \left( \frac{\partial \omega}{\partial L} \right)_E \dot{L}(\omega, T, \chi_j), \quad (5.81)$$

governs the plasma evolution, where  $\dot{E} = \dot{E}(\omega, T, \chi_j)$  and  $\dot{L} = \dot{L}(\omega, T, \chi_j)$  are functions that describe the rate of energy and angular momentum exchange with various external agencies. For example, suppose that the plasma energy and angular momentum were changing as a result of collisions with neutrals.  $\dot{E}$  and  $\dot{L}$  would depend on the plasma state (i.e., on  $\omega$  and  $T$ ) and on some parameters  $\chi_j$  that characterize the neutrals, such as the neutral density and temperature. Likewise, for interaction with a laser beam,  $\dot{E}$  and  $\dot{L}$  would be determined by the plasma state (i.e.,  $\omega$  and  $T$ ) and by parameters  $\chi_j$  such as the intensity and frequency of the laser light. Assuming that the parameters  $\chi_j$  are constant, or known functions of time, the plasma evolution is governed by two ordinary differential equations for the time evolution of  $T$  and  $\omega$ . This reduction in complexity from the partial differential equations typically required to describe transport is possible because the plasma passes through a sequence of thermal equilibrium states.

With the aid of Eqs. (5.29), (5.30), and (5.31), Eqs. (5.80) and (5.81) can be rewritten as

$$c_L \dot{T} = A \omega \dot{L} + \dot{E}, \quad (5.82)$$

$$c_L \dot{\omega} = \left[ c_\omega \left( \frac{\partial \omega}{\partial L} \right)_T + \omega \left( \frac{\partial \omega}{\partial T} \right)_L \right] \dot{L} + \left( \frac{\partial \omega}{\partial T} \right)_L \dot{E}, \quad (5.83)$$

where

$$A = 1 - \frac{T}{\omega} \left( \frac{\partial \omega}{\partial T} \right)_L. \quad (5.84)$$

It is often more convenient to write Eq. (5.83) as

$$\dot{\omega} \left( \frac{\partial L}{\partial \omega} \right)_T = \dot{L} - \left( \frac{\partial L}{\partial T} \right)_\omega \dot{T}, \quad (5.85)$$

where use has been made of Eqs. (5.27) and (5.82). This equation could have been written down directly by taking the time derivative of the mixed function  $\omega = \omega(L, T)$ . By using Maxwell relations, the coefficients

of Eqs. (5.82)–(5.85) can be written in many ways. However, one can see that only  $c_\omega$  and the function  $L = L(\omega, T)$  are needed to evaluate the coefficients.

For the case of a large plasma, only one of the coefficients in the evolution equations depends on the plasma shape. The other coefficients can be written out as explicit functions of  $T$  and  $\omega$  with no reference to plasma shape. For example,  $c_L = c_\omega = c_{n_-}$ , the specific heat of a one-component plasma at constant density, is given by Eq. (4.48). When the density is written as a function of  $\omega$  using  $\omega_p^2 = 2\omega(\Omega_c - \omega)$ , we obtain an expression for  $c_L(\omega, T) = c_\omega(\omega, T)$  that is independent of plasma shape. Likewise,  $\partial L / \partial T)_\omega$  is given by Eq. (4.78) in terms of the pressure  $p(n_-, T)$  for an OCP, which in turn is given by Eq. (4.35). One can also check that  $T \partial \omega / \partial T)_L$  is negligible compared to  $\omega$  so that  $A \approx 1$ .

For the simple case of a large and weakly correlated plasma of point charges, the specific heat reduces to  $c_n = (3/2)Nk$  and the pressure to  $p = n_- kT$ , so evolution equations (5.82) and (5.85) reduce to the simple form

$$\frac{3}{2} Nk \dot{T} = \omega \dot{L} + \dot{E} \quad (5.86)$$

$$\left( \frac{\partial L}{\partial \omega} \right)_T \dot{\omega} = \dot{L} - \frac{Nk(\Omega_c - 2\omega)}{\omega(\Omega_c - \omega)} \dot{T}. \quad (5.87)$$

The coefficient  $\partial L / \partial \omega)_T$  depends on plasma shape. For a large plasma,  $\partial L / \partial \omega)_T$  is determined principally by the cold mean-field contribution to the angular momentum [see Eq. (4.76)] and can be evaluated explicitly for two common trap geometries. For example, for a long cylindrical plasma column of radius  $R_p$  and fixed length, one can show that

$$\left( \frac{\partial L}{\partial \omega} \right)_T = - \frac{NmR_p^2}{4} \left[ \frac{(\Omega_c - \omega)^2 + \omega^2}{\omega(\Omega_c - \omega)} \right], \quad (5.88)$$

while for a spheroidal plasma in a harmonic trap, Eqs. (3.40)–(3.45) imply that

$$\left( \frac{\partial L}{\partial \omega} \right)_T = - \frac{2NmR_p^2}{5} \left[ 1 + \frac{\Omega_v^2}{3\omega_p^2} \left( 2 + \frac{d \ln \alpha(\beta)}{d\beta} \right) \right], \quad (5.89)$$

where the radius  $R_p$  is determined by  $N$ ,  $\omega$ ,  $\omega_z$ , and  $\Omega_c$  through Eq. (3.48). Note that in both cases the inequality  $\partial L / \partial \omega)_T \leq 0$  is satisfied.

As a simple example, consider the case of a pure electron plasma that is cooled by cyclotron radiation (Beck, Fajans, and Malmberg, 1996). This is a process that removes energy from the plasma but has negligible effect on the angular momentum. Thus Eqs. (5.86) and (5.87) reduce to the form

$$\dot{T} = \frac{\dot{E}}{3Nk/2} \quad (5.90)$$

$$\frac{\dot{\omega}}{\omega} = \frac{NkT(\Omega_c - 2\omega)}{\omega^2 \partial L / \partial \omega)_T (\Omega_c - \omega)} \frac{\dot{T}}{T}. \quad (5.91)$$

In Eq. (5.91) the coefficient of  $\dot{T}/T$  is small; for example, from either Eq. (5.88) or (5.89) one estimates that

$$\frac{NkT(\Omega_c - 2\omega)}{\omega^2 \partial L / \partial \omega}_T (\Omega_c - \omega) \leq O\left(\frac{\lambda_D}{R_p}\right)^2 \ll 1.$$

Thus the plasma cools with little change in the rotation frequency.

As another example, let us return to the interaction of the plasma with a static-field asymmetry. As was discussed in Sec. V.G.1, for this case  $\dot{E}=0$  and  $\omega\dot{L}>0$ . Thus Eqs. (5.86) and (5.87) reduce to the form

$$\dot{T} = \frac{\omega\dot{L}}{(3Nk/2)} > 0 \quad (5.92)$$

$$\frac{\dot{\omega}}{\omega} = \frac{NkT}{2\partial L / \partial \omega}_T \omega^2 \left( \frac{\Omega_c + \omega}{\Omega_c - \omega} \right) \frac{\dot{T}}{T}, \quad (5.93)$$

where the coefficient of  $\dot{T}/T$  in Eq. (5.93) is again small [i.e.,  $O(\lambda_D^2/R_p^2)$ ], and we may conclude that the plasma undergoes rapid heating with relatively slow change in the rotation frequency.

In Sec. V.G.1 we postulated that some effect such as laser cooling maintains the temperature at a constant value without exerting a torque on the plasma. One can see from Eqs. (5.86) and (5.78) that cooling, rather than heating, is required (i.e.,  $\dot{E} = -\omega\dot{L} < 0$ ). Note that energy must be extracted whether  $\langle r^2 \rangle$  is decreasing (for  $\omega > \Omega_c/2$ ) or increasing (for  $\omega < \Omega_c/2$ ). When  $\langle r^2 \rangle$  is decreasing, the electrostatic energy is increasing, but the rotational kinetic energy is decreasing fast enough that the total energy is decreasing.

### 3. Temperature and frequency stability

Often there is a competition between various effects. For example, radiation pressure from a laser exerts a torque that compensates the torque from collisions with neutrals or interaction with field errors. In addition, cyclotron radiation or laser cooling may balance various heating effects. We search for stable stationary states, that is, states for which  $\dot{T} = \dot{\omega} = 0$  and for which small deviations from equilibrium,  $\delta\omega$  and  $\delta T$ , are damped.

As we shall see, the issue of stability is important. Instabilities are observed when a parameter  $\chi_j$ , characterizing an applied torque or cooling process, is slowly varied and the equilibrium location evolves in  $(\omega, T)$  space. When the location enters an unstable region, either  $\omega$  or  $T$  (or both) can vary rapidly ("jump") across the region to the next stable equilibrium.

Suppose that  $\dot{E}(\omega, T)$  and  $\dot{L}(\omega, T)$  are known functions and that  $(\omega', T')$  is an equilibrium point where  $\dot{E} = \dot{L} = 0$  and, therefore, where  $\dot{T} = \dot{\omega} = 0$ . To investigate stability near this point, we set  $\delta\omega = \omega - \omega'$  and  $\delta T = T - T'$ , linearize Eqs. (5.82) and (5.85) with respect to  $\delta\omega$  and  $\delta T$ , and assume that these quantities vary in time as  $e^{\nu t}$ . The result is

$$\left[ c_L \nu - A \omega \frac{\partial \dot{L}}{\partial T} \right]_{\omega} \left[ -\frac{\partial \dot{E}}{\partial T} \right]_{\omega} \delta T = \left[ A \omega \frac{\partial \dot{L}}{\partial \omega} \right]_T \left[ \frac{\partial \dot{E}}{\partial \omega} \right]_T \delta \omega, \quad (5.94)$$

$$\left[ \frac{\partial \dot{L}}{\partial \omega} \right]_T \left[ \nu - \frac{\partial \dot{L}}{\partial \omega} \right]_T \delta \omega = \left[ \frac{\partial \dot{L}}{\partial T} \right]_{\omega} \left[ -\frac{\partial \dot{L}}{\partial T} \right]_{\omega} \nu \delta T. \quad (5.95)$$

Setting the determinant of the coefficients equal to zero yields a quadratic equation for  $\nu$ :

$$a\nu^2 + b\nu + c = 0, \quad (5.96)$$

where

$$a = c_L \left[ \frac{\partial \dot{L}}{\partial \omega} \right]_T, \quad (5.97)$$

$$b = \left\{ -\frac{\partial \dot{L}}{\partial \omega} \right]_T \left[ c_L - \frac{\partial \dot{L}}{\partial \omega} \right]_T \left[ A \omega \frac{\partial \dot{L}}{\partial T} \right]_{\omega} + \frac{\partial \dot{E}}{\partial T} \right]_{\omega} \left[ A \omega \frac{\partial \dot{L}}{\partial \omega} \right]_T + \frac{\partial \dot{E}}{\partial \omega} \right]_T \right\}, \quad (5.98)$$

$$c = \frac{\partial \dot{L}}{\partial \omega} \right]_T \left[ \frac{\partial \dot{E}}{\partial T} \right]_{\omega} - \frac{\partial \dot{L}}{\partial T} \right]_{\omega} \left[ \frac{\partial \dot{E}}{\partial \omega} \right]_T. \quad (5.99)$$

The two solutions to Eq. (5.96) are

$$\nu = \frac{-b \pm \sqrt{b^2 - 4ac}}{2a}, \quad (5.100)$$

and stability requires  $\text{Re}(\nu) \leq 0$  for both solutions. Inequalities (5.53) and (5.54) imply  $a \leq 0$ , so stability requires  $b < 0$  and  $c < 0$ .

As a simple example, consider the case in which the angular momentum may be considered constant on the time scale required for significant changes in the energy. Setting  $\dot{L} = 0$  in Eqs. (5.98) and (5.99) yields  $c = 0$  and

$$b = -\frac{\partial \dot{L}}{\partial \omega} \right]_T \left[ \frac{\partial \dot{E}}{\partial T} \right]_{\omega} + \frac{\partial \dot{L}}{\partial T} \right]_{\omega} \left[ \frac{\partial \dot{E}}{\partial \omega} \right]_T = -\frac{\partial \dot{L}}{\partial \omega} \right]_T \left[ \frac{\partial \dot{E}}{\partial T} \right]_L. \quad (5.101)$$

The nonzero root is  $\nu = -b/a$ , which is stable for  $b < 0$  or  $\partial \dot{E} / \partial T)_L < 0$  since  $\partial \dot{L} / \partial \omega)_T < 0$ . Temperature fluctuations about the equilibrium are damped for  $\partial \dot{E} / \partial T)_L < 0$ , since a positive  $\delta T$  leads to a negative  $\delta \dot{E} = \partial \dot{E} / \partial T)_L \delta T$ , which restores the equilibrium. From Eq. (5.95) one can see that the fluctuations  $\delta T$  and  $\delta \omega$  are coupled and vary in such a way that  $0 = \delta \dot{L} = \partial \dot{L} / \partial \omega)_T \delta \omega + \partial \dot{L} / \partial T)_\omega \delta T$ .

Of course, for this case of constant  $L$ , it is simpler to replace the evolution equations (5.82) and (5.85) with  $c_L \delta \dot{T} = \dot{E}(T, L)$  and  $L(\omega, T) = \text{const}$ . This separates out the temperature evolution at the outset and the stability results follow trivially from the Taylor expansions:  $c_L \delta \dot{T} = \partial \dot{E} / \partial T)_L \delta T$  and  $0 = \partial \dot{L} / \partial \omega)_T \delta \omega + \partial \dot{L} / \partial T)_\omega \delta T$ .

As an illustration, we suppose that a plasma of partially ionized atoms is heated by some ambient process

at the rate  $\dot{E}_a(T, L)$  and laser cooled at the rate  $\dot{E}_l(T, \omega, \chi_l)$ . The laser light is assumed to be directed along the trap magnetic field and the intensity to be uniform over the cross section of the plasma. In this case, the laser light does not exert a torque on the plasma, and the cooling rate does not depend on the plasma rotation frequency. The laser frequency is tuned close to but slightly lower than an electric dipole transition of the partially ionized atoms that constitute the plasma. The transition is characterized by the cross section at resonance  $\sigma_0$ , the frequency  $\omega_0/2\pi$ , and the line width  $\gamma_0$ . The distribution of ion velocities parallel to  $\mathbf{B}$  is Maxwellian, with thermal spread  $u = \sqrt{2kT/m}$ . In this case the cooling rate is given by the expression

$$\dot{E}_l(T, I, \omega_l) = \frac{NI\sigma_0}{\hbar\omega_l} \times \int_{-\infty}^{+\infty} \frac{dv_x (\hbar k_l v_x + 2R) \exp[-v_x^2/u^2]}{[1 + (\omega_l - \omega'_0 - k_l v_x)^2/(4\gamma_0^2)] \sqrt{\pi} u}, \quad (5.102)$$

where  $I$ ,  $\omega_l$ , and  $k_l = \omega_l/c$  are the intensity, frequency, and wave number of the laser light,  $\omega'_0 = \omega_0 + R/\hbar$  and  $R = (\hbar k_l)^2/2m$  (Wineland and Itano, 1979).

We define the thermal Doppler width  $\omega_D = k_l u$  and for simplicity work in the limit where  $\gamma_0$ ,  $R/\hbar \ll \omega_D$ . Equation (5.102) then reduces to the form

$$\dot{E}_l(T, I, \omega_l) \approx \frac{NI\sigma_0}{\hbar\omega_l} \frac{\sqrt{\pi}\gamma_0}{2} \frac{\hbar(\omega_l - \omega_0)}{\omega_D} e^{-[(\omega_l - \omega_0)^2/\omega_D^2]}. \quad (5.103)$$

From this form one can see that  $\dot{E}_l$  can be negative and substantial only if  $\omega_l - \omega_0$  is negative but  $|\omega_l - \omega_0|$  is not too large compared to  $\omega_D$ .

In Fig. 65, the solid curve is a plot of  $\dot{E}_l$  versus  $\omega_D^2/(\omega_l - \omega_0)^2 \propto T$ . The dashed and dotted curves are plots of  $\dot{E}_a(T, L)$  and  $-\dot{E}_a(T, L)$ , respectively, assumed here to be constant for simplicity. The intersections A and B are equilibrium points where  $\dot{E}_l + \dot{E}_a = 0$ . Point A is stable, since  $\partial\dot{E}_l/\partial T)_L + \partial\dot{E}_a/\partial T)_L < 0$ , and point B is unstable, since  $\partial\dot{E}_l/\partial T)_L + \partial\dot{E}_a/\partial T)_L > 0$ . From the evolution equation  $c_L \dot{T} = \dot{E}_l + \dot{E}_a$ , one can see that the temperature will evolve to point A if it is started off at any point to the left of B. When started off at any point to the right of B, the temperature increases indefinitely.

In experiments, the temperature for a plasma in stable equilibrium A is gradually reduced by slowly decreasing  $|\omega_l - \omega_0|$  (Wineland and Itano, 1979). One can see from Eq. (5.103) that  $\omega_D$  tracks  $|\omega_l - \omega_0|$ . If the slow decrease in  $|\omega_l - \omega_0|$  is made through increments, one must be careful not to leave the temperature to the right of point B after the increment—that is, the increments should be smaller than  $O(\omega_D)$ . This can be restrictive for small  $\omega_D$ . Of course, for sufficiently small  $\omega_D$ , Eq. (5.103) does not accurately represent an integral (5.102).

As another example of a stability criterion that is easy to understand physically, consider the case in which there is a strongly stable mechanism for temperature control, that is,  $(\partial\dot{E}/\partial T)_\omega$  is negative and substantially larger in magnitude than the other terms to which it is compared in Eqs. (5.98) and (5.99). The solution for the plus sign,

$$\nu_+ = \left. \frac{\partial\dot{E}}{\partial T} \right|_\omega \bigg/ c_L, \quad (5.104)$$

$$\left. \frac{\partial L}{\partial \omega} \right|_T \delta\omega + \left. \frac{\partial L}{\partial T} \right|_\omega \delta T = 0, \quad (5.105)$$

describes strongly damped temperature and frequency fluctuations that conserve the angular momentum. In effect, this is the solution that we considered in the previous example. The solution for the minus sign,

$$\nu_- = \frac{\partial\dot{L}/\partial\omega)_T}{\partial L/\partial\omega)_T}, \quad (5.106)$$

$$\delta T \approx 0, \quad \delta\omega \neq 0, \quad (5.107)$$

describes weakly damped or growing ( $|\nu_-| \ll |\nu_+|$ ) frequency fluctuations that are decoupled from the temperature fluctuations. Since  $\partial L/\partial\omega)_T < 0$ , stability requires that  $\partial\dot{L}/\partial\omega)_T > 0$ . This result is well known from the analysis of induction electric motors as the condition for frequency stability; recall, here, that  $-\omega$  is the frequency of rotation.

Again, the analysis can be simplified at the outset by noting that the temperature is effectively fixed at the equilibrium value where  $\partial\dot{E}/\partial T)_L$  is negative and large in magnitude. The time derivative of  $L(\omega, T)$ , holding  $T$  fixed, yields the evolution equation  $\dot{\omega} \partial L/\partial\omega)_T = \dot{L}(\omega, T)$ , and Taylor expansion about the equilibrium yields solution (5.106).

As a specific illustration, we suppose that two laser beams act on the plasma. The first is an intense cooling beam that is directed along  $\mathbf{B}$  and provides strongly stable temperature control, that is, provides a large and negative  $\partial\dot{E}/\partial T)_\omega$ . We suppose that this beam effectively fixes  $T$  at some low value. The second is a narrow beam that is directed transverse to  $\mathbf{B}$  and passes through the plasma at a distance  $d$  from the axis. The direction of propagation is in the same sense as the plasma rotation; so the torque due to the radiation pressure can balance an ambient torque, say, due to a static-field error: Of course, the ambient torque opposes the rotation. The second beam can heat or cool the plasma depending on how frequencies are adjusted.

For the simple case in which  $\gamma_0$ ,  $R/\hbar \ll \omega_D$ , the torque is given by (Wineland *et al.*, 1985)

$$\dot{L}_l \approx \frac{-I\sigma_0\sqrt{\pi}\gamma_0}{\hbar\omega_l 2\omega_D} \bar{n}_x(T, \omega, d) a \hbar k_l d e^{-[(\omega_l - \omega_0 - k_l d)^2/\omega_D^2]}, \quad (5.108)$$

where  $a$  is the cross-sectional area of the narrow laser beam, and

$$\bar{n}_x(T, \omega, d) = \int d^3\mathbf{r} \delta(y-d) \delta(z) n(\mathbf{r}, \omega, T) \quad (5.109)$$

is the line integral of the plasma density along the beam. In writing Eq. (5.108), we used the fact that the  $x$  component of the plasma rotation velocity is given by  $\hat{x} \cdot \omega \mathbf{r}_\perp \hat{\theta} = \omega r_\perp \cos \theta = \omega d$  all along the beam.

We have already discussed an experiment in which this kind of two-laser system was used to vary the rotation frequency of a plasma through the full range of allowed values (see Fig. 15). Further results from this experiment can be understood from the criterion for frequency stability. Figure 66 shows a plot of the plasma rotation frequency versus the frequency of the torque laser (Heinzen *et al.*, 1991). Interestingly, the function  $\omega = \omega(\omega_l)$  exhibits hysteresis behavior, with different values of  $\omega$  obtained for the same value of  $\omega_l$  depending on whether  $\omega_l$  is slowly increasing or slowly decreasing. It is this behavior that we shall explain.

The condition for frequency equilibrium is that the laser torque just balance the ambient torque

$$\dot{L}_l(\omega, I, \omega_l) + \dot{L}_a(\omega) = 0, \quad (5.110)$$

and the condition for frequency stability is that

$$\frac{\partial \dot{L}_l}{\partial \omega} + \frac{\partial \dot{L}_a}{\partial \omega} > 0. \quad (5.111)$$

Dependence on  $T$  (or  $\omega_D$ ) is not denoted, since we assume that the intense cooling laser effectively fixes the value of  $T$ .

The experiments (Heinzen *et al.*, 1991) suggest that the ambient torque is due to a field error (tilt in the magnetic field relative to the axis of the cylindrical electrode structure) and that the ambient torque becomes large (exhibits a resonance) near a particular value of the plasma rotation frequency ( $\omega = \omega^*$ ). At this frequency, a tilt mode, which rotates backwards on the rotating plasma, has zero frequency in the laboratory frame and is driven secularly by the static-field error. The amplitude of this mode presumably is limited by viscous effects, which also set the frequency width of the resonance. The solid curve in the upper half of Fig. 67 is a sketch of an ambient torque  $\dot{L}_a(\omega)$  with a resonance peak at  $\omega = \omega^*$ , and the dashed curve in the lower half is  $-\dot{L}_a(\omega)$ , which is introduced for construction purposes. The three solid curves in the lower half of the figure are plots of  $\dot{L}_l(\omega, I, \omega_l)$  as given by Eq. (5.108) for three values of  $\omega_l$  (i.e.,  $\omega_{lA} < \omega_{lB} < \omega_{lC}$ ). To avoid confusion, the full Maxwellian is not shown for curves A, B, and C.

Each intersection of a solid curve with the dashed curve is an equilibrium point, that is, a solution of Eq. (5.110). For curve A, one can see graphically that equilibrium 1 is stable, that is, that  $\partial \dot{L}_l / \partial \omega + \partial \dot{L}_a / \partial \omega > 0$ . Recall, here, that the dashed curve is  $-\dot{L}_a(\omega)$ . This equi-

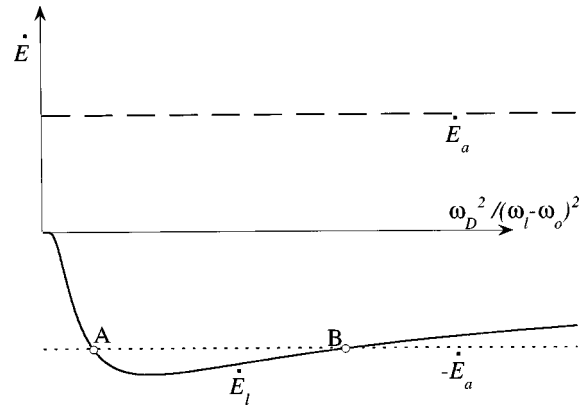


FIG. 65. A construction used to determine temperature equilibrium and stability. The solid curve is a plot of the laser cooling rate  $\dot{E}_l(T, I, \omega_l)$  vs  $\omega_D^2 / (\omega_l - \omega_0)^2 \propto T$ , assuming that the angular momentum  $L$  is constant on the time scale of interest. The dashed curve is an ambient heating rate,  $\dot{E}_a(T, L)$ , assumed constant for simplicity, and the dotted curve is  $-\dot{E}_a$ . Points A and B are equilibria since  $\dot{E}_l + \dot{E}_a = 0$  at these points. Equilibrium A is stable since  $\partial \dot{E}_l / \partial T)_L + \partial \dot{E}_a / \partial T)_L < 0$ , whereas B is unstable since  $\partial \dot{E}_l / \partial T)_L + \partial \dot{E}_a / \partial T)_L > 0$ .

librium is indicated by point 1 in Fig. 66. When the laser frequency is increased to  $\omega_{lB}$ , equilibrium 1 evolves to equilibrium 2, which also is stable. Here, the equilibrium point is climbing the resonance peak, so an increase in  $\omega_l$  produces relatively little change in  $\omega$ ; see point 2 in Fig. 66. Curve B has two other equilibria; one can see graphically that 2' is unstable and 5 is stable. When the laser frequency is increased to  $\omega_{lC}$ , the equilibrium evolves to point 3, which is on the edge of the stability boundary. A slight increase in  $\omega_l$  produces instability, and the equilibrium jumps to equilibrium 4, the next stable equilibrium. This jump produces the nearly vertical section (3→4) of the curve in Fig. 66. For further increase in  $\omega_l$ ,  $\omega$  simply tracks  $\omega_l$  as before the resonance. When the process is reversed by decreasing  $\omega_l$ , only a small jump is encountered. Note that for decreasing  $\omega_l$ , equilibrium 4 evolves into equilibrium 5, which is stable. For a sufficiently narrow resonance, the small jump encountered for decreasing  $\omega_l$ , would not be apparent in Fig. 66.

## VI. DISCUSSION

This review has focused on our current understanding of nonneutral plasmas in thermal equilibrium. However, the study of thermal equilibrium states forms an active area of research, and new advances are being made almost on a daily basis. For example, the rotating-wall technique described in Sec. III.H.2 is being carefully studied due to both its usefulness in plasma control and its fundamental importance in understanding the manner by which external fields can inject angular momentum into a rotating plasma. The ellipsoidal rotating-wall equilibria discussed theoretically in Sec. III.H.2 have recently been observed in experiments (Huang, Bollinger,



Mitchell, and Itano, 1998b). New results on rotating-wall equilibria with multispecies plasmas have also recently been reported (Huang *et al.*, 1998a), and both theoretical and experimental studies of the torque applied to the plasma by the rotating wall are underway. In addition, analytic studies of thermal equilibria in highly oblate plasmas have recently been carried out (Paulson and Spencer, 1998). New off-axis and oscillating thermal equilibria have been discovered, and the thermodynamics of these states and their connection to previous experiments has been studied (O'Neil and Dubin, 1998).

Several topics that were not addressed in the previous sections could easily have been included in a review of thermal equilibrium states, but were neglected for lack of space. These topics are briefly discussed below, including a few of the more important references.

(1) *Variational principles in the decay of 2D turbulence.* For certain initial conditions, a nonneutral plasma column is unstable to the growth of diocotron modes (Davidson, 1990). In experiments with pure electron plasmas (Huang and Driscoll, 1994), such modes were observed to grow to large amplitude and generate a complicated turbulent flow. Ultimately the turbulence decayed, leaving the plasma in a stable and quiescent meta-equilibrium state, which then persisted essentially unchanged until collisional transport drove the plasma to a true thermal equilibrium state. We emphasize that the meta-equilibrium state was produced by collective, not collisional, processes and was not a thermal equilibrium state. Nevertheless, the experiments observed that this meta-equilibrium state could be quite robust, varying in a reproducible manner as experimental parameters (such as the initial density profile) were varied.

It is interesting to ask if there is a theoretical principle that predicts the structure of the meta-equilibrium state just as maximum entropy predicts the structure of the thermal equilibrium state. To a good approximation the turbulence can be described by 2D bounce-average  $\mathbf{E} \times \mathbf{B}$  drift dynamics, since the important frequencies are ordered as  $\Omega_c \gg \omega_B \gg \omega_D$ . Here,  $\omega_B$  is the characteristic axial bounce frequency for an electron and  $\omega_D$  is the characteristic cross-field drift frequency. The plasma column is also sufficiently long that Poisson's equation for the electric potential is effectively two dimensional [i.e.,  $\phi = \phi(r, \theta)$ ].

It turns out that the 2D drift Poisson equations are formally equivalent to the Euler equations for the 2D evolution of an ideal (incompressible and inviscid) fluid (Levy, 1965), so the 2D plasma turbulence models the 2D turbulence of an ideal fluid. For example, Kelvin-Helmholtz instabilities are the analog of the diocotron instabilities. There has been much theoretical effort over many years to predict the final state arising from the decay of 2D turbulence in an ideal fluid, and prediction of the meta-equilibrium state is part of that larger effort.

Some authors have represented the plasma as a 2D system of charged rods that undergo  $\mathbf{E} \times \mathbf{B}$  drifts due to mutual interaction and, equivalently, the fluid as a 2D system of interacting point vortices (Onsager, 1949; Montgomery, 1972; Edwards and Taylor, 1974; Mont-

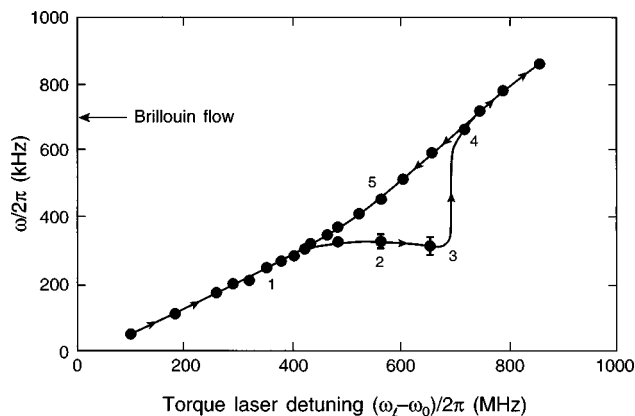


FIG. 66. Observed plasma rotation frequency vs frequency of torque laser. The laser frequency was gradually increased then gradually decreased, and the arrows indicate the direction of evolution when the plasma rotation frequency was measured. The interesting feature is the hysteresis loop. This result is from Heinzen *et al.* (1991).

gomery and Joyce, 1974; Seyler, 1976; Pointin and Lundgren, 1976; Smith and O'Neil, 1990; Smith, 1991; Eyink and Spoon, 1993). The turbulence is assumed to mix the system ergodically and the relaxed state is predicted to be the maximum-entropy state for the 2D dynamics. These 2D thermal equilibria are quite different from the full three-degree-of-freedom thermal equilibria discussed in previous sections. For the case of a 2D guiding-center drift plasma, only the guiding-center degrees of freedom are assumed to be ergodically mixed. There is no equipartition with the degrees of freedom associated with the axial bounce motion and the cyclotron motion. This is a useful approximation only if effects that couple these motions to the guiding-center motions (such as collisions) are negligible on the timescale of the experiments.

These 2D thermal equilibria have several interesting features not found in 3D thermal equilibria. For example, for energies above a certain threshold, the temperature of the 2D plasma is negative. This can occur because in the 2D system there are no terms in the Hamiltonian associated with kinetic energy. Furthermore, at a second (higher) energy threshold the thermal equilibria do not share the underlying cylindrical symmetry of the confinement geometry (Smith and O'Neil, 1990). However, this symmetry breaking has not yet been observed in experiments.

Several attempts to improve this kind of theory have been developed over the years. One approach involves including the constraint that  $\mathbf{E} \times \mathbf{B}$  flow is incompressible (Lynden-Bell, 1967; Miller, Weichman, and Cross, 1992; Robert and Sommeria, 1992); another applies the maximum entropy theory only to regions of the flow that are well mixed (Jin and Dubin, 1998). Other authors choose to extremize functionals other than the entropy, such as enstrophy (Bretherton and Haidvogel, 1976; Matthaeus and Montgomery, 1980; Leith, 1984; Huang and Driscoll, 1994; Taylor, 1997). These theories have met with varying degrees of success depending on the experi-

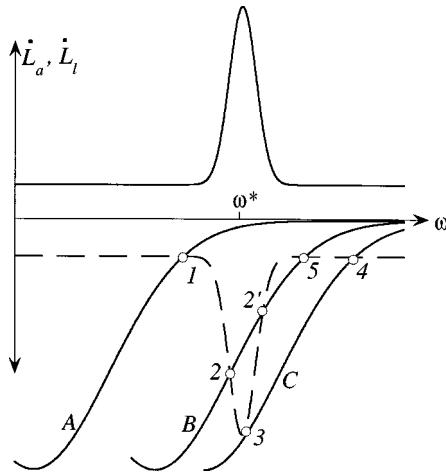


FIG. 67. A construction used to determine frequency equilibria and stability when the temperature is fixed. The solid curve in the upper half of the figure is a plot of an ambient torque  $\dot{L}_a(\omega)$  assumed to have a resonance peak, and the dashed curve in the lower half is its negative  $-\dot{L}_a(\omega)$ . The three solid curves in the lower half of the figure are plots of a laser torque  $\dot{L}_l(\omega, \omega_l)$  for three values of  $\omega_l$  (i.e.,  $\omega_{lA} < \omega_{lB} < \omega_{lC}$ ). Each intersection of the dashed curve with a solid curve is an equilibrium, where  $\dot{L}_l(\omega, \omega_l) + \dot{L}_a(\omega) = 0$ . Equilibria 1, 2, 3, 4, and 5 are stable since  $\partial \dot{L}_l / \partial \omega + \partial \dot{L}_a / \partial \omega > 0$ , whereas 2' is unstable since  $\partial \dot{L}_l / \partial \omega + \partial \dot{L}_a / \partial \omega < 0$ . The equilibria are realized sequentially when  $\omega_l$  is first increased and then decreased, and this gives rise to the hysteresis loop in Fig. 66.

mental regime. A complete and rigorous description of the relaxed state of 2D turbulence remains an elusive goal.

(2) *Stability theorems.* The variational equation,  $\delta S - \beta(\delta H + \omega \delta P_\theta) - \gamma \delta N \geq 0$ , that is used to find maximum-entropy states can be given a different interpretation to yield a stability theorem (Gardner, 1963; Rosenbluth, 1965; Arnold, 1969). A generalized entropy is introduced that is constant under a general constraint on the dynamics, for example, under incompressible flow in phase space. For a change of state that is allowed under the dynamics,  $\delta S = 0$ . Setting  $\delta N = 0$  reduces the variational equation to  $\beta \delta H_R \leq 0$ . Thus the variational equation can be reinterpreted as the statement that the energy is a minimum (for  $\beta > 0$ ) or a maximum (for  $\beta < 0$ ) relative to neighboring states that are accessible under the dynamics. If  $H_R$  is a constant of the motion, the fact that  $H_R$  is a local minimum (or maximum) means that no change in state is possible. The plasma is in a state of stable equilibrium. There are many examples of this kind of stability theorem in the literature, and the review article by Holm *et al.* (1985) has an extensive bibliography.

For the case of a trapped nonneutral plasma, Davidson and Krall (1970) established a sufficient condition that  $H_R$  be a local minimum. Examples in which the energy is a local maximum are less common. For general dynamics it is not possible to find states of maximum energy because there is always a neighboring state with

larger kinetic energy. However, for 2D  $\mathbf{E} \times \mathbf{B}$  drift dynamics the kinetic energy does not enter the Hamiltonian because the kinetic energy is bound up in adiabatic invariants  $\mu = mv_\perp^2/2B$  and  $I = \oint v_\parallel dl$ . It is then possible to find states in which the electrostatic energy is maximum, subject to the constraint of incompressible flow (O'Neil and Smith, 1992, 1994). The plasma cannot change out of such states because there is no place to deposit the electrostatic energy that would be liberated under the change.

The advantage of the minimum-energy stability theorem is that the dynamics can be general—that is, no frequency ordering is required to ensure that  $\mu$  and  $I$  are good adiabatic invariants. The disadvantage is that minimum energy can be established only in a rapidly rotating frame, and this requires cylindrical symmetry of the trap and equilibrium, at least for the case of time-independent trap fields. The advantage of the maximum-energy stability theorem is that cylindrical symmetry is not required; maximum-energy states can be realized in the laboratory frame. This allows us to explore new confinement geometries, for example, toroidal traps. The disadvantage is that the dynamics are restricted, so the theorem only provides stability against low-frequency drift perturbations such as diocotron modes (Davidson, 1990). However, one expects (and experiment seems to confirm) that these commonly observed modes are the most dangerous (Driscoll and Fine, 1990).

(3) *Cross-magnetic-field transport.* Nonneutral plasmas confined in Penning traps are excellent systems for the study of collisional transport. Because these systems can be confined quiescently for long periods of time, collisional effects can be observed without being masked by the large fluctuations inherent in most neutral laboratory plasmas. The signature of the transport is a slow relaxation of the plasma toward a confined thermal equilibrium state, involving cross-magnetic-field fluxes of particles, energy, and angular momentum.

Recent experiments have observed collisional fluxes that are orders of magnitude larger than the predictions of the classical theory of transport in magnetized plasmas. This is because the classical theory was developed for plasmas for which the cyclotron radius  $r_c$  was large compared to the Debye length, but nonneutral plasmas typically operate in the opposite regime. The observed transport is in agreement with new theories developed for the regime  $r_c \ll \lambda_d$ . For a recent review of cross-magnetic-field collisional transport in nonneutral plasmas, see Dubin (1998).

Externally applied fields can also induce cross-field transport. An example of this is the rotating-wall field discussed in Sec. III.H.2, used to inject angular momentum into the plasma and change its radial density profile. Static-field errors with azimuthal asymmetries also change the angular momentum, causing the plasma slowly to expand, as discussed previously in Secs. II.B and V.G. The precise mechanism for this external transport is still an outstanding question, but several experimental papers have determined an approximate scaling

law (the “Driscoll curve”) for the transport rate (de-Grassie and Malmberg, 1977; Driscoll and Malmberg, 1983; Eggleston, 1997).

(4) *Strong magnetization.* For plasmas confined in sufficiently strong magnetic fields the cyclotron radius  $r_c$  can become smaller than the mean distance of closest approach  $e^2/kT$ . For an electron plasma this happens when  $B$  exceeds  $13 (T/100 \text{ K})^{3/2} \text{ kGauss}$ . In this regime of strong magnetization, Coulomb collisions are strongly modified by the magnetic field. Collisional equipartition between particle velocities parallel and perpendicular to the magnetic field is suppressed by a many particle adiabatic invariant associated with the fast cyclotron motion, and the equipartition rate becomes exponentially small (O’Neil and Hjorth, 1985; Glinsky, O’Neil, Rosenbluth, Tsuruta, and Ichimaru, 1992). This effect has been observed in experiments (Beck, Fajans, and Malmberg, 1996).

(5) *Collective modes.* The spheroidal thermal equilibrium discussed in Sec. III.F has an important and useful property: the linear cold-fluid electrostatic normal modes of this thermal equilibrium state can be determined analytically (Dubin, 1991). This is the only known realistic three-dimensionally confined plasma equilibrium for which all of the electrostatic modes can be obtained analytically. The modes have been employed as a diagnostic of the plasma shape and density for situations where no other nondestructive diagnostic is available (Weimer, Bollinger, Moore, and Wineland, 1994). The modes have been observed in experiments by several groups (Heinzen, Bollinger, Moore, Itano, and Wineland, 1991; Bollinger, Heinzen, Moore, Itano, Wineland, and Dubin, 1993; Tinkle *et al.*, 1994; Greaves, Tinkle, and Surko, 1995; Higaki and Mohri, 1997; see also the short review in Bollinger, Wineland, and Dubin, 1994, and the upcoming article by Mitchell, Bollinger, Huang, and Itano, 1998).

There is also a large body of work on nonneutral plasma modes that are not directly related to thermal equilibrium states, including work on diocotron instabilities (White, Malmberg, and Driscoll, 1982; Driscoll, 1990; Smith and Rosenbluth, 1990), spatial Landau damping (Briggs, Daugherty, and Levy, 1970; Pillai and Gould, 1994; Corngold, 1995; Spencer and Rasband, 1997), nonlinear effects; Crawford and O’Neil, 1987; Fine, Driscoll, and Malmberg, 1989; Mitchell and Driscoll, 1994, and cyclotron and Bernstein modes (Gould and LaPointe, 1991). The effect of modes on transport caused by field errors is also of continuing interest in several groups (see, for example, Bollinger, Heinzen, Moore, Itano, Wineland, and Dubin, 1993).

(6) *Other areas.* Finally, we should mention that there are a number of active areas of research in nonneutral plasma physics that have little to do with the study of thermal equilibrium states, but are of practical importance and scientific interest. Some of these areas were alluded to in previous sections. Among these areas are antimatter plasmas (see the review by Greaves and Surko, 1997), fusion in Penning traps via nonthermal velocity distributions (Barnes, Mitchell, and Schauer,

1997), trapping of partially neutralized nonneutral plasmas (Walz, Ross, Zimmerman, Ricci, Prevedelli, and Hansch, 1995; Hall and Gabrielse, 1996), nonneutral plasmas employed in radiation sources and relativistic beams (Davidson, 1990), and 2D turbulence and vortex dynamics (Mitchell, Driscoll, and Fine, 1993; Huang and Driscoll, 1994; Fine, Flynn, Cass, and Driscoll, 1995; Huang, Fine, and Driscoll, 1995; Lansky, O’Neil, and Schecter, 1997).

## ACKNOWLEDGMENTS

This work was supported by National Science Foundation grants PHY87-06358 and 91-20240, Department of Energy grant DE-FG03-85ER53199, and Office of Naval Research grants N00014-89-J-1714 and N00014-96-1-0239.

## REFERENCES

- Alder, B. J., and T. E. Wainwright, 1957, *J. Chem. Phys.* **27**, 1208.
- Altschuler, E. L., T. J. Williams, E. R. Ratner, R. Tipton, R. Strong, F. Dowla, and F. Wooten, 1997, *Phys. Rev. Lett.* **78**, 2681.
- Arnold, V. I., 1969, *Am. Math. Soc. Trans.* **79**, 267.
- Arnold, V. I., 1978, *Mathematical Methods of Classical Mechanics* (Springer, New York).
- Baklanov, E., and V. P. Chebotayev, 1986, *Appl. Phys. B: Photophys. Laser Chem.* **39**, 179.
- Barnes, D. C., T. B. Mitchell, and M. M. Schauer, 1997, *Phys. Plasmas* **4**, 1745.
- Beck, R. B., J. Fajans, and J. H. Malmberg, 1996, *Phys. Plasmas* **3**, 1250.
- Bedanov, V. M., and F. M. Peeters, 1994, *Phys. Rev. B* **49**, 2667.
- Bergström, I., C. Carlberg, and R. Schuch, 1995, Eds., *Proceedings of Nobel Symposium 91 on Trapped Charged Particles and Fundamental Physics*, *Phys. Scr.* **T59**.
- Binney, J., and S. Tremaine, 1987, *Galactic Dynamics* (Princeton University, Princeton, N.J.).
- Birkel, G., S. Kassner, and H. Walther, 1992, *Nature (London)* **357**, 310.
- Blümel, R., 1995, *Phys. Scr.* **T59**, 369.
- Bollinger, J. J., D. J. Heinzen, F. L. Moore, W. M. Itano, D. J. Wineland, and D. H. E. Dubin, 1993, *Phys. Rev. A* **48**, 525.
- Bollinger, J. J., and D. J. Wineland, 1984, *Phys. Rev. Lett.* **53**, 348.
- Bollinger, J. J., D. J. Wineland, and D. H. E. Dubin, 1994, *Phys. Plasmas* **1**, 1403.
- Bollinger, J. J., *et al.* 1995, in *Proceedings of Nobel Symposium 91 on Trapped Charged Particles and Fundamental Physics*, edited by I. Bergström, C. Carlberg, and R. Schuch, *Phys. Scr.* **T59**, 352.
- Bretherton, F. P., and D. B. Haidvogel, 1976, *J. Fluid Mech.* **78**, 129.
- Brewer, J. R., J. D. Prestage, J. J. Bollinger, W. M. Itano, D. J. Larson, and D. J. Wineland, 1988, *Phys. Rev. A* **38**, 859.
- Briggs, R. J., J. D. Daugherty, and R. H. Levy, 1970, *Phys. Fluids* **13**, 421.
- Brillouin, L., 1945, *Phys. Rev.* **67**, 260.

- Britannica Online, 1998 (accessed Jan. 16, 1998), "Euler's theorem on polyhedrons," Encyclopedia Britannica.
- Brown, L. S., and G. Gabrielse, 1986, *Rev. Mod. Phys.* **58**, 233.
- Brueckner, K. A., and S. Jorna, 1974, *Rev. Mod. Phys.* **46**, 325.
- Brush, S. G., H. L. Sahlin, and E. Teller, 1966, *J. Chem. Phys.* **45**, 2102.
- Campbell, L. J., and R. M. Ziff, 1979, *Phys. Rev. B* **20**, 1886.
- Casdorff, R., and R. Blatt, 1988, *Appl. Phys. B: Photophys. Laser Chem.* **45**, 175.
- Ceperley, D. M., and P. M. Alder, 1980, *Phys. Rev. Lett.* **45**, 566.
- Chabrier, G., N. Ashcroft, and H. DeWitt, 1992, *Nature (London)* **360**, 48.
- Chace, W. G., and H. K. Moore, 1959, in *Exploding Wires*, edited by W. G. Chace and H. K. Moore (Plenum, New York).
- Chu, R., J. S. Wurtele, J. Notte, A. Peurrung, and J. Fajans, 1993, *Phys. Fluids B* **5**, 2378.
- Cole, M. W., 1974, *Rev. Mod. Phys.* **46**, 451.
- Corngold, N. R., 1993, *Phys. Fluids B* **5**, 3847.
- Corngold, N. R., 1995, *Phys. Plasmas* **2**, 620.
- Cowan, T. E., B. R. Beck, J. H. Hartley, R. H. Howell, R. R. Rohatgi, J. Fajans, and R. Gopalan, 1993, *Hyperfine Interact.* **76**, 135.
- Crawford, J. D., 1991, *Rev. Mod. Phys.* **63**, 991.
- Crawford, J. D., and T. M. O'Neil, 1987, *Phys. Fluids* **30**, 2076.
- Craxton, R. S., R. L. McCrory, and J. M. Soures, 1986, *Sci. Am.* **255**, 60.
- Davidson, R. C., 1974, *Theory of Nonneutral Plasmas* (Benjamin, Reading, MA).
- Davidson, R. C., 1990, *Physics of Nonneutral Plasmas* (Addison-Wesley, Redwood City, CA).
- Davidson, R. C., and N. A. Krall, 1970, *Phys. Fluids* **13**, 1543.
- Davidson, R. C., and S. M. Lund, 1993, in *Advances in Plasma Physics, Thomas H. Stix Symposium*, edited by N. J. Fisch (AIP, New York), p. 1.
- deGrassie, J. S., and J. H. Malmberg, 1977, *Phys. Rev. Lett.* **39**, 1077.
- deGrassie, J. S., and J. H. Malmberg, 1980, *Phys. Fluids* **23**, 63.
- Dehmelt, H. G., 1967, *Adv. At. Mol. Phys.* **3**, 53.
- Deidrich, F., *et al.* 1987, *Phys. Rev. Lett.* **59**, 2931.
- DeSilva, A. W., and H.-J. Kunze, 1993, in *Strongly Coupled Plasma Physics*, edited by H. M. Van Horn and S. Ichimaru (University of Rochester, Rochester, NY), p. 191.
- Driscoll, C. F., 1990, *Phys. Rev. Lett.* **64**, 645.
- Driscoll, C. F., and K. S. Fine, 1990, *Phys. Fluids B* **2**, 1359.
- Driscoll, C. F., and J. H. Malmberg, 1983, *Phys. Rev. Lett.* **50**, 167.
- Driscoll, C. F., J. H. Malmberg, and K. S. Fine, 1988, *Phys. Rev. Lett.* **60**, 1290.
- Dubin, D. H. E., 1989, *Phys. Rev. A* **40**, 1140.
- Dubin, D. H. E., 1990, *Phys. Rev. A* **42**, 4972.
- Dubin, D. H. E., 1991, *Phys. Rev. Lett.* **66**, 2076.
- Dubin, D. H. E., 1993, *Phys. Rev. Lett.* **71**, 2753.
- Dubin, D. H. E., 1996, *Phys. Rev. E* **53**, 5268.
- Dubin, D. H. E., 1997, *Phys. Rev. E* **55**, 4017.
- Dubin, D. H. E., 1998, *Phys. Plasmas* **5**, 1688.
- Dubin, D. H. E., and T. M. O'Neil, 1986a, *Phys. Fluids* **29**, 11.
- Dubin, D. H. E., and T. M. O'Neil, 1986b, *Phys. Rev. Lett.* **56**, 728.
- Dubin, D. H. E., and T. M. O'Neil, 1988, *Phys. Rev. Lett.* **60**, 511.
- Dubin, D. H. E., and T. M. O'Neil, 1990, in *Strongly Coupled Plasma Physics*, edited by S. Ichimaru (Elsevier Science Publishers B.V./Yamada Science Foundation, Amsterdam) p. 189.
- Edwards, S. F., and J. B. Taylor, 1974, *Proc. R. Soc. London, Ser. A* **336**, 257.
- Eggleston, D. L., 1997, *Phys. Plasmas* **4**, 1196.
- Eyink, G. L., and H. Spoon, 1993, *J. Stat. Phys.* **70**, 833.
- Fajans, J. R., and D. H. E. Dubin, Eds., 1995, *Non-neutral Plasma Physics II*, AIP Conf. Proc. No. 331 (AIP, New York).
- Fajans, J., R. Gopalan, and C. Hansen, 1996, *Bull. Am. Phys. Soc.* **41**, 1521.
- Farouki, R. T., and S. Hamaguchi, 1993, *Phys. Rev. E* **47**, 4330.
- Fine, K. S., C. F. Driscoll, and J. H. Malmberg, 1989, *Phys. Rev. Lett.* **63**, 2232.
- Fine, K. S., W. G. Flynn, A. C. Cass, and C. F. Driscoll, 1995, *Phys. Rev. Lett.* **75**, 3277.
- Föppl, L., 1912, in *Proceedings of the International Congress of Mathematicians*, Vol. 11, edited by E. W. Hobson and A. E. H. Love (Cambridge University Press, Cambridge), p. 188.
- Gabrielse, G., X. Fei, L. A. Orozco, R. L. Tjoelker, J. Haas, H. Kalinowsky, T. A. Trainor, and W. Kells, 1989, *Phys. Rev. Lett.* **63**, 1360.
- Gardner, C. S., 1963, *Phys. Fluids* **6**, 839.
- Gilbert, S. L., J. J. Bollinger, and D. J. Wineland, 1988, *Phys. Rev. Lett.* **60**, 2022.
- Glinzsky, M. E., T. M. O'Neil, M. N. Rosenbluth, K. Tsuruta, and S. Ichimaru, 1992, *Phys. Fluids B* **4**, 1373.
- Goldstein, H., 1980, *Classical Mechanics* (Addison-Wesley, Reading, MA).
- Gould, R. W., and M. A. LaPointe, 1991, *Phys. Rev. Lett.* **67**, 3685.
- Gradshteyn, I. S., and I. M. Ryzhik, 1980, *Table of Integrals, Series and Products* (Academic, New York).
- Greaves, R. G., and C. M. Surko, 1997, *Phys. Plasmas* **4**, 1528.
- Greaves, R. G., M. D. Tinkle, and C. M. Surko, 1994, *Phys. Plasmas* **1**, 1439.
- Greaves, R. G., M. D. Tinkle, and C. M. Surko, 1995, *Phys. Rev. Lett.* **74**, 90.
- Hall, D. S., and G. Gabrielse, 1996, *Phys. Rev. Lett.* **77**, 1962.
- Hansen, J. P., 1973, *Phys. Rev. A* **8**, 3096.
- Hansen, J. P., and I. McDonald, 1986, *Theory of Simple Liquids* (Academic, London).
- Hansen, J. P., and P. Vieillefosse, 1975, *Phys. Lett. A* **53**, 187.
- Hart, G. W., 1991, *Phys. Fluids B* **3**, 2987.
- Hasse, R. W., and V. V. Avilov, 1991, *Phys. Rev. A* **44**, 4506.
- Hasse, R. W., and J. P. Schiffer, 1990, *Ann. Phys. (N.Y.)* **203**, 419.
- Heinzen, D. J., J. J. Bollinger, F. L. Moore, W. M. Itano, and D. J. Wineland, 1991, *Phys. Rev. Lett.* **66**, 2080.
- Higaki, H., and A. Mohri, 1997, *Phys. Lett. A* **235**, 504.
- Hoffnagle, J. A., and R. G. Brewer, 1995, *Phys. Scr.* **T59**, 380.
- Holm, D. D., J. E. Marsden, T. Ratiu, and A. Weinstein, 1985, *Phys. Rep.* **123**, 1.
- Holzschneider, M. H., X. Feng, T. Goldman, N. S. P. King, R. A. Lewis, M. M. Nieto, and G. A. Smith, 1996, *Phys. Lett. A* **214**, 279.
- Huang, X.-P., F. Anderegg, E. M. Hollmann, T. M. O'Neil, and C. F. Driscoll, 1997, *Phys. Rev. Lett.* **78**, 875.
- Huang, X.-P., J. J. Bollinger, T. B. Mitchell, W. M. Itano, and D. H. E. Dubin, 1998a, *Phys. Plasmas* **5**, 1656.

- Huang, X.-P., J. J. Bollinger, T. B. Mitchell, and W. M. Itano, 1998b, *Phys. Rev. Lett.* **80**, 73.
- Huang, X.-P., J. J. Bollinger, W. M. Itano, and D. J. Wineland, 1996, *Bull. Am. Phys. Soc.* **41**, 1606.
- Huang, X.-P., and C. F. Driscoll, 1994, *Phys. Rev. Lett.* **72**, 2187.
- Huang, X.-P., K. S. Fine, and C. F. Driscoll, 1995, *Phys. Rev. Lett.* **74**, 4424.
- Ichimaru, S., 1973, *Basic Principles of Plasma Physics* (W. A. Benjamin, London).
- Ichimaru, S., 1982, *Rev. Mod. Phys.* **54**, 1017.
- Ichimaru, S., 1992, *Statistical Plasma Physics, Vol. 1: Basic Principles* (Addison-Wesley, Redwood City, CA).
- Ichimaru, S., H. Iyetomi, and S. Tanaka, 1987, *Phys. Rep.* **149**, 92.
- Iida, K., and S. Ichimaru, 1995, *Phys. Rev. B* **53**, 7278.
- Imajo, H., K. Hayasaka, R. Ohmukai, U. Tanaka, M. Watanabe, and S. Urabe, 1997, *Phys. Rev. A* **55**, 1276.
- Itano, W. M., J. C. Bergquist, and D. J. Wineland, 1989, in *Proceedings of the Workshop on Crystalline Ion Beams*, edited by R. W. Hasse, I. Hofmann, and D. Liese (GSI Report GSI-89-10, ISSN 0170-4546), p. 241.
- Itano, W. M., J. J. Bollinger, J. N. Tan, B. Jelenkovic, X.-P. Huang, and D. J. Wineland, 1998, *Science* **279**, 686.
- Ivanov, Y. V., V. B. Mintsev, V. E. Fortov, and A. N. Drenia, 1976, *Sov. Phys. JETP* **44**, 112.
- Jin, D. Z., and D. H. E. Dubin, 1998, *Phys. Rev. Lett.* **80**, 4434.
- Kittel, C., 1976, *Introduction to Solid State Physics*, 5th Ed. (Wiley, New York).
- Kingdon, K. H., 1923, *Phys. Rev.* **21**, 408.
- Landau, L. D., and E. M. Lifshitz, 1960, *Electrodynamics of Continuous Media* (Pergamon, Oxford).
- Landau, L. D., and E. M. Lifshitz, 1976, *Mechanics*, 3rd ed. (Pergamon, Oxford).
- Landau, L. D., and E. M. Lifshitz, 1980, *Statistical Physics*, 3rd ed. (Pergamon, Oxford).
- Lansky, I., T. M. O'Neil, and D. A. Schecter, 1997, *Phys. Rev. Lett.* **79**, 1479.
- Larson, J. D., J. C. Bergquist, W. M. Itano, and D. J. Wineland, 1986, *Phys. Rev. Lett.* **57**, 70.
- Leibowitz, J. L., J. K. Percus, and L. Verlet, 1967, *Phys. Rev.* **153**, 250.
- Leith, C. E., 1984, *Phys. Fluids* **27**, 1388.
- Levy, R. H., 1965, *Phys. Fluids* **8**, 1288.
- Levy, R. H., J. D. Daugherty, and O. Buneman, 1969, *Phys. Fluids* **12**, 2616.
- Lynden-Bell, D., 1967, *Mon. Not. R. Astron. Soc.* **136**, 101.
- Malmberg, J. H., *et al.*, 1988, in *Nonneutral Plasma Physics*, edited by C. W. Roberson and C. F. Driscoll (AIP, New York), p. 28.
- Malmberg, J. H., and T. M. O'Neil, 1977, *Phys. Rev. Lett.* **39**, 1333.
- Matthaeus, W. H., and D. Montgomery, 1980, *Ann. N.Y. Acad. Sci.* **357**, 203.
- Miller, J., P. B. Weichman, and M. C. Cross, 1992, *Phys. Rev. A* **45**, 2328.
- Mitchell, T. B., J. J. Bollinger, D. H. E. Dubin, X.-P. Huang, W. M. Itano, and R. H. Baughman, 1998, *Science* **282**, 290.
- Mitchell, T. B., J. J. Bollinger, X.-P. Huang, and W. M. Itano, 1998, *Opt. Express* (in press).
- Mitchell, T. B., and C. F. Driscoll, 1994, *Phys. Rev. Lett.* **73**, 2196.
- Mitchell, T. B., C. F. Driscoll, and K. S. Fine, 1993, *Phys. Rev. Lett.* **71**, 1371.
- Mochkovitch, R., and J. P. Hansen, 1979, *Phys. Lett. A* **73**, 35.
- Mohri, A., H. Tanaka, T. Michishita, Y. Yuyama, Y. Kawase, and T. Takami, 1995, in *Elementary Processes in Dense Plasmas*, edited by S. Ichimaru and S. Ogata (Addison-Wesley, New York), p. 477.
- Montgomery, D., 1972, *Phys. Lett. A* **39**, 7.
- Montgomery, D., and G. Joyce, 1974, *Phys. Fluids* **17**, 1139.
- Montgomery, D., and D. Tidman, 1964, Eds., *Plasma Kinetic Theory* (McGraw-Hill, New York).
- Mostowski, J., and M. Gajda, 1985, *Acta Phys. Pol. A* **67**, 783.
- Nagara, H., Y. Nagata, and T. Nakamura, 1987, *Phys. Rev. A* **36**, 1859.
- O'Neil, T. M., 1980, *Phys. Fluids* **23**, 2216.
- O'Neil, T. M., 1981, *Phys. Fluids* **24**, 1447.
- O'Neil, T. M., 1988, in *Nonneutral Plasma Physics*, edited by C. W. Roberson and C. F. Driscoll (AIP, New York), p. 1.
- O'Neil, T. M., and C. F. Driscoll, 1979, *Phys. Fluids* **22**, 266.
- O'Neil, T. M., and D. H. E. Dubin, 1998, *Phys. Plasmas* **5**, 2163.
- O'Neil, T. M., and P. G. Hjorth, 1985, *Phys. Fluids* **28**, 3241.
- O'Neil, T. M., and R. A. Smith, 1992, *Phys. Fluids B* **4**, 2720.
- O'Neil, T. M., and R. A. Smith, 1994, *Phys. Plasmas* **1**, 2430.
- Onsager, L., 1949, *Nuovo Cimento Suppl.* **6**, 279.
- Pathria, R. K., 1986, *Statistical Mechanics* (Pergamon, Oxford).
- Paul, W., and H. Steinwedel, 1953, *Naturforsch.* **8**, 448.
- Paulson, D., and R. Spencer, 1998, *Phys. Plasmas* **5**, 345.
- Penning, F. M., 1936, *Physica* (Amsterdam) **3**, 873.
- Peurrung, A. J., and J. Fajans, 1990, *Phys. Fluids B* **2**, 693.
- Pillai, N. S., and R. W. Gould, 1994, *Phys. Rev. Lett.* **73**, 2849.
- Pointin, Y. B., and T. S. Lundgren, 1976, *Phys. Fluids* **19**, 1459.
- Pollock, R. E., and F. Anderegg, 1994, in *Nonneutral Plasma Physics II*, AIP Conf. Proc. No. 331, edited by J. Fajans and D. H. E. Dubin (AIP, New York), 139.
- Prasad, S. A., and T. M. O'Neil, 1979, *Phys. Fluids* **22**, 278.
- Rafac, R., *et al.* 1991, *Proc. Natl. Acad. Sci. USA* **88**, 483.
- Rahman, A., and J. P. Schiffer, 1986, *Phys. Rev. Lett.* **57**, 1133.
- Reif, F., 1965, *Fundamentals of Statistical and Thermal Physics* (McGraw-Hill, New York).
- Roberson, C. W., and C. F. Driscoll, Eds. 1988, *Non-neutral Plasma Physics*, AIP Conf. Proc. No. 175 (AIP, New York).
- Robert, R., and J. Sommeria, 1992, *Phys. Rev. Lett.* **69**, 2776.
- Rosenbluth, M. N., 1965, in *Plasma Physics*, Lectures presented at the seminar on Plasma Physics organized by and held at the ICTP, Trieste, Italy, 1964 (IAEA, Vienna), p. 489.
- Schatzman, E., 1958, *White Dwarfs* (North-Holland, Amsterdam).
- Schiffer, J. P., 1993, *Phys. Rev. Lett.* **70**, 818.
- Schiffer, J. P., 1995, in *Nonneutral Plasma Physics II*, edited by J. Fajans and D. H. E. Dubin (AIP, New York), p. 191.
- Seyler, Jr., C. E., 1976, *Phys. Fluids* **19**, 1336.
- Slattery, W. L., G. D. Doolen, and H. E. DeWitt, 1980, *Phys. Rev. A* **21**, 2087.
- Slattery, W. L., G. D. Doolen, and H. E. DeWitt, 1982, *Phys. Rev. A* **26**, 2255.
- Smith, R. A., 1991, *Phys. Rev. A* **43**, 1126.
- Smith, R. A., and T. M. O'Neil, 1990, *Phys. Fluids B* **2**, 2961.
- Smith, R. A., and M. N. Rosenbluth, 1990, *Phys. Rev. Lett.* **64**, 649.
- Spencer, R. L., and S. N. Rasband, 1997, *Phys. Plasmas* **4**, 53.
- Stringfellow, G. S., H. E. DeWitt, and W. L. Slattery, 1990, *Phys. Rev. A* **41**, 1105.

- Surko, C. M., and T. J. Murphy, 1990, *Phys. Fluids B* **2**, 1372.
- Tan, J. N., J. J. Bollinger, B. Jelenkovic, and D. J. Wineland, 1995a, *Phys. Rev. Lett.* **75**, 4198.
- Tan, J., and G. Gabrielse, 1993, *Phys. Rev. A* **48**, 3105.
- Tan, J. N., J. J. Bollinger, B. Jelenković, W. M. Itano, and D. J. Wineland, 1995b, in *Proceedings of the International Conference on the Physics of Strongly Coupled Plasma Physics*, edited by W. D. Kraeft and M. Schlanges (World Scientific, Singapore), p. 387.
- Taylor, J. B., 1997, *Plasma Phys. Controlled Fusion* **39**, 1.
- Thomson, J. J., 1904, *Philos. Mag. S.6* **7**, 237.
- Thomson, J. J., 1921, *Philos. Mag. S.6* **41**, 510.
- Tinkle, M. D., R. G. Greaves, C. M. Surko, R. L. Spencer, and G. W. Mason, 1994, *Phys. Rev. Lett.* **72**, 352.
- Totsuji, H., 1978, *Phys. Rev. A* **17**, 399.
- Totsuji, H., 1987, in *Strongly Coupled Plasma Physics*, edited by F. Rogers and H. DeWitt (Plenum, New York), p. 19.
- Totsuji, H., 1988, *Phys. Rev. A* **38**, 5444.
- Totsuji, H., and J. L. Barrat, 1988, *Phys. Rev. Lett.* **60**, 2484.
- Tsuruta, K., and S. Ichimaru, 1993, *Phys. Rev. A* **48**, 1339.
- Turner, L., 1987, *Phys. Fluids* **30**, 3196.
- Turner, L., 1991, *Phys. Fluids B* **3**, 1355.
- Walz, J., S. B. Ross, C. Zimmerman, L. Ricci, M. Prevedelli, and T. W. Hansch, 1995, *Phys. Rev. Lett.* **75**, 3257.
- Weimer, C. S., J. J. Bollinger, F. L. Moore, and D. J. Wineland, 1994, *Phys. Rev. A* **49**, 3842.
- Weurker, R. F., H. Shelton, and R. V. Langmuir, 1959, *J. Appl. Phys.* **30**, 342.
- White, W. D., J. H. Malmberg, and C. F. Driscoll, 1982, *Phys. Rev. Lett.* **49**, 1822.
- Wigner, E., 1934, *Phys. Rev.* **46**, 1002.
- Wineland, D. J., J. J. Bollinger, W. M. Itano, and J. D. Prestage, 1985, *J. Opt. Soc. Am. B* **2**, 1721.
- Wineland, D. J., and W. M. Itano, 1979, *Phys. Rev. A* **20**, 1521.
- Wineland, D. J., C. S. Weimer, and J. J. Bollinger, 1993, *Hyperfine Interact.* **76**, 115.
- Wineland, D. J., *et al.* 1987, *Phys. Rev. Lett.* **59**, 2935.
- Zemansky, M. W., 1968, *Heat and Thermodynamics*, 5th ed. (McGraw-Hill, New York).